

**"Unstoppable" hypersonic weapons
ignite new arms race** p. 134

**New bird species found on remote
Indonesian islands** pp. 140 & 167

**The force behind
hair loss** p. 161

Science

\$15
10 JANUARY 2020
sciencemag.org

 AAAS

GAMMA-RAY FLASH

How lightning drives emission in
the upper atmosphere p. 183

CONTENTS

10 JANUARY 2020 • VOLUME 367 • ISSUE 6474

134

NEWS

IN BRIEF

126 News at a glance

IN DEPTH

128 Study disputes carbon dioxide-fish behavior link

Three-year effort fails to replicate alarming findings about effects of ocean acidification
By M. Enserink

129 Articles in 'predatory' journals receive few or no citations

Study counters fears that mediocre or misleading papers contaminate the literature
By J. Brainard

130 China delivers verdict on gene editing of babies

He Jiankui gets prison sentence, but legal proceedings fail to satisfy calls for transparency
By J. Cohen and D. Normile

131 How safe is a popular gene therapy vector?

Dog study suggests virus-delivered DNA can invade chromosomes near cancer genes
By J. Kaiser

132 Russian academy probe triggers more than 800 retractions

Fraud commission's work causes "tension and conflict"
By D. Singh Chawla

133 In two-person MRI, brains socialize at close range

In pursuit of natural interactions, researchers push the limits of neuroimaging
By K. Servick
PODCAST

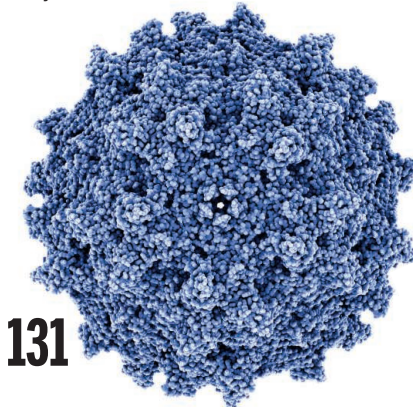
FEATURES

134 Need for speed

Despite hype and technological hurdles, a hypersonic arms race is accelerating
By R. Stone

136 In Russia, hypersonic rivalry feeds suspicions and arrests

By R. Stone



131

INSIGHTS

PERSPECTIVES

140 Completing Wallace's journey

A global inventory of species diversity is critical for understanding the evolution of life on Earth
By J. D. Kennedy and J. Fjeldså
RESEARCH ARTICLE p. 167

141 Tolerance to antibiotics affects response

Bacterial tolerance to antibiotics reduces the ability to prevent resistance
By A. D. Berti and E. B. Hirsch
REPORT p. 200

143 Improving cancer screening programs

Evaluating diagnostic tests in learning screening programs could improve public health
By M. Kalager and M. Bretthauer

145 Counting on Majorana modes

Quantized conductance is a prerequisite of a topologically robust Majorana qubit
By J. Sau
REPORT p. 189

146 A sugary input to leucine sensing

Glucose channels the amino acid leucine into synthetic versus degradative pathways
By E. Lehman and R. T. Abraham
REPORT p. 205

147 A younger “earliest human migration” to Southeast Asia

New dating suggests that hominids arrived at the Sangiran dome later than had been thought *By B. Brasseur*
REPORT p. 210

148 Flipping carbon monoxide on a salt surface

Advanced mid-infrared techniques identify orientational isomers
By S. Wu
REPORT p. 175

POLICY FORUM

150 Waiting for data: Barriers to executing data use agreements

Delays stem from institutional factors and negotiating challenges, some of which appear amenable to reform *By M. M. Mello et al.*

BOOKS ET AL.

153 People-powered discovery

A physicist reveals how citizen science is reshaping research
By L. A. Shanley

154 Fun and games and ecosystems

Video games—even those without explicit educational goals—can offer insights into ecology *By S. LeMenager*

LETTERS

155 Retraction

By I. Cho et al.

Brazil oil spill response

155 Time for coordination

By M. O. Soares et al.

155 Government inaction

By H. D. Brum et al.

156 Protect rhodolith beds

By M. Nasri Sissini et al.

RESEARCH

IN BRIEF

158 From Science and other journals

RESEARCH ARTICLES

161 Stem cell biology

Dermal sheath contraction powers stem cell niche relocation during hair cycle regression
N. Heitman et al.



167 Biodiversity

A lost world in Wallacea: Description of a montane archipelagic avifauna
F. E. Rheindt et al.
PERSPECTIVE p. 140

REPORTS

171 Metallurgy

Observation of hydrogen trapping at dislocations, grain boundaries, and precipitates
Y.-S. Chen et al.

175 Quantum chemistry

Observation of an isomerizing double-well quantum system in the condensed phase
J. A. Lau et al.

PERSPECTIVE p. 148

179 Chemical physics

Observation of the fastest chemical processes in the radiolysis of water
Z.-H. Loh et al.

183 Lightning

A terrestrial gamma-ray flash and ionospheric ultraviolet emissions powered by lightning
T. Neubert et al.

186 Quantum simulation

Time-resolved observation of spin-charge deconfinement in fermionic Hubbard chains
J. Vijayan et al.

189 Topological matter

Nearly quantized conductance plateau of vortex zero mode in an iron-based superconductor
S. Zhu et al.

PERSPECTIVE p. 145

193 Catalysis

Hydrophobic zeolite modification for in situ peroxide formation in methane oxidation to methanol
Z. Jin et al.

197 Developmental biology

Programmed cell death along the midline axis patterns ipsilaterality in gastrulation
L. Maya-Ramos and T. Mikawa

200 Antibiotic resistance

Effect of tolerance on the evolution of antibiotic resistance under drug combinations
J. Liu et al.
PERSPECTIVE p. 141

205 Signal transduction

Glucose-dependent control of leucine metabolism by leucyl-tRNA synthetase 1
I. Yoon et al.
PERSPECTIVE p. 146

210 Paleoanthropology

Age control of the first appearance datum for Javanese *Homo erectus* in the Sangiran area
S. Matsu'ura et al.
PERSPECTIVE p. 147

DEPARTMENTS

125 Editorial

Stick to science *By H. Holden Thorp*

222 Working Life

A refreshing change *By Lila Westreich*

ON THE COVER



An artist's impression of multiwavelength emission above a thunderstorm, based on data from the Atmosphere-Space Interactions Monitor on the International Space Station. The high electric field associated with

lightning (light blue) generates a terrestrial gamma-ray flash (magenta). The resulting electromagnetic pulse causes an elve—an expanding ring of ultraviolet emission (red and white). See page 183. Image: Birkeland Centre for Space Science, Daniel Schmelling/Mount Visual

New Products..... 218
Science Careers 219

SCIENCE (ISSN 0036-8075) is published weekly on Friday, except last week in December, by the American Association for the Advancement of Science, 1200 New York Avenue, NW, Washington, DC 20005. Periodicals mail postage (publication No. 484460) paid at Washington, DC, and additional mailing offices. Copyright © 2020 by the American Association for the Advancement of Science. The title SCIENCE is a registered trademark of the AAAS. Domestic individual membership, including subscription (12 months): \$165 (\$74 allocated to subscription). Domestic institutional subscription (51 issues): \$2148; Foreign postage extra: Air assist delivery: \$98. First class, airmail, student, and emeritus rates on request. Canadian rates with GST available upon request. GST #R123456789. Publications Mail Agreement Number 1069624. Printed in the U.S.A.
Change of address: Allow 4 weeks, giving old and new addresses and 8-digit account number. Postmaster: Send change of address to AAAS, P.O. Box 96178, Washington, DC 20090-6178. Single-copy sales: \$15 each plus shipping and handling; bulk rate on request. Authorization to reproduce material for internal or personal use under circumstances not falling within the fair use provisions of the Copyright Act can be obtained through the Copyright Clearance Center (CCC), www.copyright.com. The identification code for Science is 0036-8075. Science is indexed in the Reader's Guide to Periodical Literature and in several specialized indexes.

Stick to science

Just stick to science.” This is a common admonition that *Science* receives when we publish commentaries and news stories on policies that readers disagree with (rather, we should “stay in our lane” and focus on research). It turns out that “stick to science” is a tired-but-very-much-still-alive political talking point used to suppress scientific advice and expertise. According to a recent issue of *The Washington Post*, “stick to science” is what the U.S. Environmental Protection Agency (EPA) administrator said in chastising and silencing its own Scientific Advisory Board, of which two-thirds of the members were appointed by the current administration. The EPA is planning to pat these folks on the head while the administration does what suits its political goals. Sadly, this pattern is not new—the administration declares something outrageous, goes through the motions of consulting scientists, and then does the outrageous thing, regardless. The scientific community should not let this cycle continue because facts that have stood up to, in some cases, years of scrutiny are being suppressed in the service of politics.

The latest go-round is one of the most egregious. On New Year’s Eve, the EPA posted four reports from its Scientific Advisory Board commenting on upcoming changes in EPA rules. Three of the four consensus reports from the administration’s own panel are highly critical of upcoming EPA rule changes. These will be discussed in four January conference calls next week (beginning on 17 January).

One of the four proposed rules addresses data transparency, which was the subject of a statement that I was proud to sign with my counterparts from five major scientific journals (*Nature*, *Public Library of Science*, *The Lancet*, *Cell*, and *Proceedings of the National Academy of Sciences of the United States of America*). The EPA Scientific Advisory Board agreed with our statement that the proposal’s push for transparency would suppress the use of relevant scientific evidence in policy-making. The Board articulated, among other criticisms, that the

EPA’s proposed rule was “vague, and as a result, can be interpreted in different ways.” In other words, the rule is ripe for markup by the administration’s Sharpies, allowing it to do whatever it wants.

The scientific community needs to step out of its labs and support evidence-based decision-making in a much more public way. The good news is that over the past few years, scientists have increasingly engaged with the public and policy-makers on all levels, from participating in local science cafes, to contacting local representatives and protesting in the international March for Science in 2017 and 2018. *Science* and the American Association for the Advancement of Science (AAAS,

the publisher of *Science*) will continue to advocate for science and its objective application to policy in the United States and around the world, but we too must do more.

Scientists must speak up. In June 2019, Patrick Gonzalez, the principal climate change scientist of the U.S. National Park Service, testified to Congress on the risks of climate change even after he was sent a cease-and-desist letter by the administration (which later agreed that he was free to testify as a private citizen). That’s the kind of gumption that deserves the attention of the greater scientific community. There are many more examples of folks leading federal agencies and working on science throughout the government.

When their roles in promoting science to support decision-making are diminished, the scientific community needs to raise its voice in loud objection.

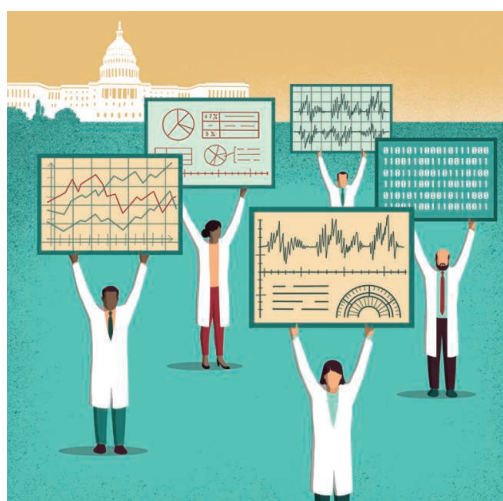
The upcoming EPA public conference calls on the scientific and technical basis of the four proposed rules are an excellent opportunity for the scientific community to mobilize. All who value evidence and inductive reasoning should support the conclusions of the Scientific Advisory Board through feedback to the EPA, local representatives, scientific societies, and other science advocacy organizations.

Because we need to make the science stick.

—H. Holden Thorp



H. Holden Thorp
Editor-in-Chief,
Science journals.
hthorp@aaas.org;
@hholdenthorp



“...facts that have stood up to, in some cases, years of scrutiny are being suppressed in the service of politics.”

“Targeting cultural sites for military activity is a war crime ... and cannot be justified.”

The American Anthropological Association and other scientific societies, protesting President Donald Trump's proposal to bomb cultural sites in Iran, later ruled out by the military as unlawful.

IN BRIEF

Edited by Jeffrey Brainard

PUBLIC HEALTH

Mystery illness hits city in China



Reported cases of pneumonia in Wuhan, China, 690 kilometers west of Shanghai, doubled in 1 week.

Health authorities in China suspect a novel virus jumped from animals to humans at a market in the central city of Wuhan, causing at least 59 unusual cases of pneumonia. No deaths have been reported since the first cases were reported on 31 December 2019, but some people remain critically ill; patients are reported to be responding to standard medical treatments. Some of the cases in the city of 11 million have been linked to the wholesale market, which sells seafood and live animals. The Wuhan Municipal Health Commission has since ruled out several possible causes, among them adenovirus, avian flu, influenza, Middle East respiratory syndrome, and severe acute respiratory syndrome (SARS). Close contacts of patients are under surveillance, although the health commission has so far found no evidence of human-to-human transmission. China was criticized for its slow action and a lack of transparency when SARS, caused by a previously unknown virus, emerged in 2002 in southern China. In response, the country beefed up disease surveillance and response efforts. But a dearth of details about the Wuhan cases has left scientists in China and around the world frustrated again.

EPA panel knocks draft rules

POLICY | In four draft reports released in late December 2019, the U.S. Environmental Protection Agency's (EPA's) external Science Advisory Board strongly criticized the agency for ignoring research findings when writing a quartet of new regulations. The move is significant in part because a majority of the board's 44 members were appointed by the Trump administration. An agency proposal to narrow protections for small waterways and wetlands is "in conflict with established science," one report concludes. Others fault draft rules on mercury pollution and auto emissions and a measure barring the agency from considering studies that don't make their underlying data fully public (*Science*, 15 November 2019, p. 783). EPA is under no obligation to follow the panel's suggestions.

Open-access rumor sows worry

PUBLISHING | More than 125 scientific societies and journal publishers, as well as an influential U.S. senator, warned the Trump administration last month not to move forward with a rumored executive order that would make all articles produced by federally funded research immediately free to the public. In three separate letters, they argue such a move would be costly and could bankrupt many scientific societies that rely on income from journal subscriptions. The White House wouldn't comment on whether the administration is considering the change, and society officials say they have learned no details—nor been asked for input. But if the murmuring is accurate, the order would represent a major change from current U.S. policy, which allows publishers to keep papers that report the results of federally funded studies behind a paywall for up to 1 year.

China sentences animal scientist

CRIMINAL JUSTICE | A court in China last week sentenced a leading animal genetics researcher to 12 years in prison for embezzling research funds and reaping illegal gains totaling more than \$4 million. Li Ning had been a professor and director of a prestigious biotechnology laboratory



Wildfires on Australia's mainland, like this one in Lake Conjola, have killed more than 480 million animals, by one estimate.

CONSERVATION

Australia's wildfires devastate an island haven for biodiversity

The blazes sweeping Australia last week ravaged 30% of Kangaroo Island, a 4400-square-kilometer wildlife sanctuary off the continent's southern coast. They destroyed conservation reserves and research field sites for endangered species and subspecies, including the Kangaroo Island glossy black cockatoo, which had numbered fewer than 400 birds. The entire fenced reserve for the Kangaroo Island dunnart—a mouse-size marsupial carnivore—was also

incinerated. There are now grave concerns for this critically endangered species, which the Australian government had flagged as one of the nation's 20 highest priority mammals for conservation. Up to half the island's 50,000 koalas are feared dead. Fueled by unprecedented drought and record temperatures, bushfires have continued to devastate other parts of Australia, razing 84,000 square kilometers so far—an area bigger than the country of Ireland.

at China Agricultural University when he was arrested in 2014; his work focused on animal breeding and cloning and genetic engineering. A court found Li guilty of transferring funds as “investments” to several companies he controlled, according to local press reports. Li told the court he meant to avoid a funding gap created by a government policy that required research institutions to return unused state funding at the end of each year, local press reported. The government suspended the policy soon after Li's arrest. More than 15 senior members of the Chinese Academy of Engineering, of which Li was a member, and the Chinese Academy of Sciences requested clemency for him.

Permanent NOAA head picked

LEADERSHIP | The acting administrator of the U.S. National Oceanic and Atmospheric Administration (NOAA), Neil Jacobs, was nominated by President Donald Trump last month to lead the agency on a permanent basis. A meteorologist, Jacobs has pushed to unify federal and academic weather research with the goal of returning the country's weather model to preeminence after it fell behind

its European peers. In September 2019, however, Jacobs found himself in the middle of the “Sharpiegate” controversy that followed Hurricane Dorian; at the behest of the Trump administration, he helped draft an unsigned memo castigating federal weather forecasters for dismissing the president's storm track prediction. Multiple investigations into the memo, which was roundly rejected by the scientific community, are ongoing. NOAA has been without a permanent leader for the entirety of the Trump administration.


Yangtze River fishing banned

CONSERVATION | China on 1 January launched a 10-year fishing ban on the Yangtze River to allow fish stocks and biodiversity to recover. The ban initially applies to 332 previously designated conservation areas, but will be extended to cover the entire river and its major tributaries by January 2021. The annual catch on the Yangtze has dropped from 420,000 tons in the 1950s to less than 100,000 tons now because of overfishing, pollution, and changes wrought by dams. Scientists have been calling for a fishing ban for more than 10 years. The river's ecological

collapse is blamed for driving the Chinese paddlefish, one of the world's largest freshwater fishes, to extinction.

U.S. proposes principles for AI

COMPUTER SCIENCE | The Trump administration this week proposed principles on how federal agencies should regulate the use of artificial intelligence (AI) by the private sector. The principles, released for public comment, seek to balance innovation with individuals' privacy rights; agencies would have to base new rules on scientific evidence and seek comment from the academic community and others. Without offering specifics, the White House memo encourages agencies to consider whether AI programs are flawed by bias and subjectivity. AI-powered facial recognition programs, for example, have been found to have a disproportionately high false-positive rate for dark-skinned people. Writing for Bloomberg Opinion, U.S. Chief Technology Officer Michael Kratsios promised a “light-touch regulatory approach” and said the government would continue to work with other countries to harmonize oversight. Agencies have 180 days to submit their plans, which will not apply to the U.S. government's own use of AI.



Studies of reef fish like these in Australia suggested acidification might leave them disoriented and vulnerable.

IN DEPTH

CLIMATE SCIENCE

Study disputes carbon dioxide-fish behavior link

Three-year effort fails to replicate alarming findings about effects of ocean acidification

By **Martin Enserink**

Over the past decade, marine scientists published a series of studies warning that humanity's burgeoning carbon dioxide (CO₂) emissions could cause yet another devastating problem. They reported that seawater acidified by rising CO₂—already known to threaten organisms with carbonate shells and skeletons, such as corals—could also cause profound, alarming changes in the behavior of fish on tropical reefs. The studies, some of which made headlines, found that acidification can disorient fish, make them hyperactive or bolder, alter their vision, and lead them to become attracted to, rather than repelled by, the smell of predators. Such changes, researchers noted, could cause populations to plummet.

But in a *Nature* paper published this week, researchers from Australia, Canada, Norway, and Sweden challenge a number of those findings. In a major, 3-year effort that studied six fish species, they could not replicate three widely reported behavioral effects of ocean acidification. The replication team notes that many of the original studies came from the same relatively small group of researchers and involved small sam-

ple sizes. That and other “methodological or analytical weaknesses” may have led the original studies astray, they argue.

“It’s an exceptionally thorough replication effort,” says Tim Parker, a biologist and an advocate for replication studies at Whitman College in Walla Walla, Washington. Marine scientist Andrew Esbaugh of the University of Texas, Austin, agrees that it’s “excellent, excellent work.”

But marine biologist Philip Munday of James Cook University, Townsville, in Australia, a co-author of most of the papers the *Nature* study tried to replicate, says there are “fundamental methodological differences” between the original and replication studies. “Replication of results in science is critically important, but this means doing things in the same way, not in vastly different ways,” he wrote in an email.

Munday helped launch research on the behavioral impacts of ocean acidification together with Danielle Dixon, now at the University of Delaware. In 2009, their paper in the *Proceedings of the National Academy of Sciences* showing that orange clownfish (*Amphiprion percula*) reared in seawater with elevated CO₂ levels no longer recognized the chemical cues that could help them find a suitable habitat on

the reef. (“Losing Nemo” was a popular headline for stories about the paper.) That study was followed by dozens of others showing similarly striking, and often large, behavioral effects in clownfish and other species, mostly from tropical waters.

Timothy Clark, the first author on the *Nature* paper and a marine scientist at Deakin University, Geelong, in Australia, says he initially set out to probe the physiological mechanisms behind those behavior changes. But after he failed to reproduce the changes—let alone explain them—he invited other scientists to set up a systematic replication attempt. It focused on three reported effects of acidified waters: making reef fish prone to swim toward their predators’ chemical cues rather than fleeing them, increasing their activity, and altering the fish’s tendency to favor either their left or right sides in some behaviors.

Overall, the group reports, exposing fish to seawater with acidification levels predicted for the end of the century had “negligible” effects on all three behaviors. The *Nature* paper also reports the results of a statistical analysis called a bootstrapping simulation, designed to calculate the probability that Munday and co-authors could have found the striking data on chemical

PHOTO: DAVID DOUBILET/NATIONAL GEOGRAPHIC IMAGE COLLECTION

signal preference presented in seven papers. The authors say the odds are exceedingly low: “0 in 10,000,” as they put it.

Clark declined to elaborate on the implications of the bootstrap finding, but says he “would encourage any other avenues of investigation to find out what has caused the stark differences between our findings and theirs.” Esbaugh calls the bootstrap analysis “a little concerning,” but he objects to the “somewhat nefarious undercurrent” in the *Nature* paper. “I know both of these research groups,” he says, “and they’re both very, very good.”

Dixon—who presented her findings at a 2015 White House meeting—and three other researchers involved in the previous studies did not respond to interview requests from *Science*. Munday stands by his papers and plans to detail many “critically important” differences in the designs of the two sets of experiments in a response to the *Nature* paper. For instance, he notes the replication group didn’t study clownfish, used different water volumes and experiment durations, and used a different setup to study chemical cue avoidance. The *Nature* authors say some methods had to be adapted because they didn’t work as described in the original papers. They add that they could not catch enough clownfish, so used six other species also used in the previous studies.

Replication studies often cause quibbles about methods, Parker says. But, he argues, “If the original finding is reasonably robust,” then researchers using even somewhat different methods should be able to replicate it. And he notes that the replication team went to great lengths to be transparent. Unlike the original authors, the team released video of each experiment, for example, as well as the bootstrap analysis code. “That level of transparency certainly increases my confidence in this replication,” Parker says.

Researchers say the *Nature* paper allays one fear about the impact of ocean acidification. But Josefin Sundin of Uppsala University in Sweden, the *Nature* paper’s last author, stresses that climate change still poses a serious threat to sea life. “If the oceans were as acidic as we have been testing, it would also be much warmer, and that’s a huge issue,” she says.

Although replication efforts have blossomed in psychology, biomedicine, and other fields, they’re still rare in ecology, says biologist Shinichi Nakagawa of the University of New South Wales in Sydney. The new paper “sets a great example,” says Nakagawa, who hopes it “will instigate and inspire more replication studies—not to prove previous results wrong but to make our science more robust and trustworthy.” ■

PUBLISHING

Articles in ‘predatory’ journals receive few or no citations

Study counters fears that mediocre or misleading papers contaminate the literature

By Jeffrey Brainard

Six of every 10 articles published in a sample of “predatory” journals attracted not one single citation over a 5-year period, according to a new study. Like many open-access journals, predatory journals charge authors to publish, but they offer little or no peer review or other quality controls and often use aggressive marketing tactics. The new study found that the few articles in predatory journals that received citations did so at a rate much lower than papers in conventional, peer-reviewed journals.

The authors say the finding allays concerns that low-quality or misleading studies published in these journals are getting undue attention. “There is little harm done if nobody reads and, in particular, makes use of such results,” write Bo-Christer Björk of the Hanken School of Economics in Finland and colleagues in a preprint posted 21 December 2019 on arXiv.

But Rick Anderson, an associate dean at the University of Utah who oversees collections in the university’s main library, says the finding

that 40% of the predatory journal articles drew at least one citation “strikes me as pretty alarming.”

The number of predatory journals has ballooned in recent years, raising alarm among researchers. Previous studies found that their authors are predominantly in Africa and Asia and that some turn to predatory journals for speed and ease of publication, or to satisfy institutional requirements to publish. But some observers fear these journals enable a proliferation of mediocre or flawed research. Others worry authors may use them to spread misinformation—for example, about climate change or vaccine safety—knowing that reputable refereed journals would not accept it.

Björk and his colleagues randomly selected 250 journals from a list of 10,000 such titles compiled by the information

service Cabell’s International. The team then selected one paper in each journal published in 2014. Most papers were in the natural and social sciences. For comparison, the researchers randomly selected 250 articles from 2014 from Elsevier’s Scopus database, which includes science journals that meet quality standards.

Scopus and other widely used citation databases don’t list most predatory journals, so the team used Google Scholar to count citations. Fully 60% of the articles in predatory journals attracted no citations, compared with just 9% of those in the peer-reviewed journals. On average, the predatory articles drew about two citations each, compared with 18 for the traditional papers. (Because of limited staff resources, the team did not count how many of those citations came from an article’s own authors, a practice some scholars use to inflate their citation counts.)

“There is little harm done if nobody reads and, in particular, makes use of such results.”

Bo-Christer Björk and colleagues,
Hanken School of Economics

“It’s great to see this,” says Kelly Cobey, a researcher in clinical epidemiology at the Ottawa Hospital Research Institute. But she notes that variations in citation rates by field might affect the comparisons, and that Cabell’s list may

not capture all predatory journals. (Cobey and 34 colleagues from multiple institutions last month proposed a definition of these journals that researchers could apply without relying on a list.)

Björk doesn’t think those factors would change the results much. But he and his colleagues say other studies should examine how often predatory journal articles are referenced outside the scholarly literature, for example on social media. Their study found that among the 17 most cited articles in its sample, none was cited in a Wikipedia entry.

Even if no one reads them, predatory journals are a problem, Cobey says. “I’d argue that the average member of the public doesn’t want their tax dollars going to pay for article-processing charges for predatory journals that may not be read,” she says. ■

REPRODUCTIVE MEDICINE

China delivers verdict on gene editing of babies

He Jiankui gets prison sentence, but legal proceedings fail to satisfy calls for transparency

By **Jon Cohen** and **Dennis Normille**

When China sentenced biophysicist He Jiankui and two colleagues to fines and prison time last month, it may have hoped to close the door on a national embarrassment: He's announcement in late 2018 that he had created gene-edited babies, a claim that drew widespread condemnation. But after the state news agency Xinhua revealed on 30 December 2019 that a Shenzhen court had found He and two embryologists he collaborated with guilty of "illegal medical practices," many scientists and ethicists were far from satisfied. They debated the merits of the punishment and decried the opaque Chinese legal process and the lack of information about the altered children.

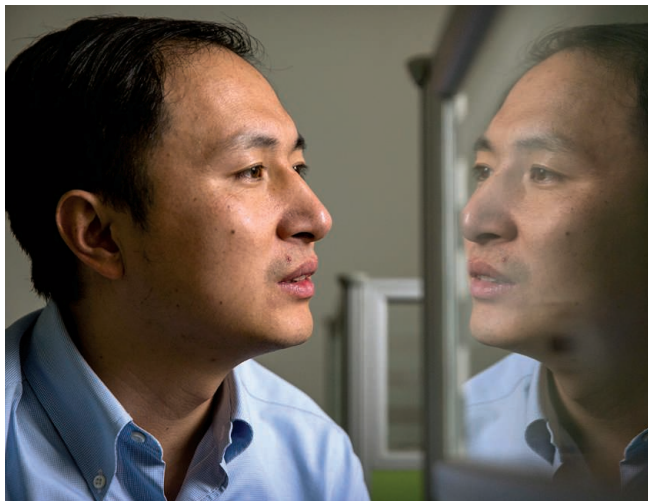
Some critical of He, inside and outside of China, deem the penalties appropriate or even light for subjecting babies to the potential dangers of editing their embryonic genomes with CRISPR. Plant researcher Gao Caixia, who has done path-breaking CRISPR studies at a Beijing branch of the Chinese Academy of Sciences, calls the punishment "reasonable." And Nobel laureate David Baltimore of the California Institute of Technology, who has chaired two human genome editing congresses, says He's 3-year prison term is "a minimal sentence for such a brazen action."

But bioethicist William Hurlbut at Stanford University argues that the secrecy surrounding the trial obscured He's large network of support, which included prominent scientists and even some in the Chinese government. "It really is hanging someone out to dry when he was being encouraged and cooperative with the spirit of his society," says Hurlbut, who had attempted to convince He not to pursue the research (*Science*, 2 August 2019, p. 430).

In an essay posted this week on the Hastings Center website, two Chinese bioethicists said it was "ridiculous" that this "notorious scandal" had been reduced to a case of illegal medical practices. They also expressed disappointment at their government's restrictions on information. "We believe that the

public has the right to know more," wrote Lei Ruipeng of Huazhong University of Science and Technology and Qiu Renzong of Renmin University of China. "[T]he reported words of the sentence are so ambiguous as to leave room for different interpretations." One charge, for example, is that the three were guilty of "deliberate violence of China's relevant regulations and medical ethics."

Chinese bioethicist Jing-Bao Nie of the University of Otago in New Zealand adds that because China "politically censored and censored" information even before the trial, "no adequate public discussion on the case has ever occurred in China."



He Jiankui's "illegal medical practices" landed him a 3-year prison term.

Xinhua said the court proceedings were closed to protect the privacy of the eight families involved in the experiments. It reported nothing about the health of the twin girls described in He's announcement, who were born in October 2018. Xinhua did confirm suspicions that a third gene-edited embryo had resulted in the birth of another baby by a different mother. It also revealed that He's group had edited and implanted embryos in Thailand, but none resulted in live births. The news agency reported that physical and documentary evidence and witness and expert testimony were presented to the court, but it gave no details.

Many suspect that He, who was fired from his position at Southern University of Science and Technology in Shenzhen, has been in detention for much of 2019. According to Xinhua, charges were filed against

him and his colleagues in July and a hearing was held on 27 December. Although editing embryos to produce children was not illegal in China in 2018, Xinhua reported that the scientists admitted to offenses that included practicing medicine without a license, falsifying ethical review documents, using reagents not approved for humans, and concealing information from those who implanted the embryos.

In addition to his prison sentence, He, who is also known as JK, was fined 3 million Chinese yuan (\$429,000). One of the embryologists, Zhang Renli, received a 2-year prison sentence and was fined 1 million yuan. The

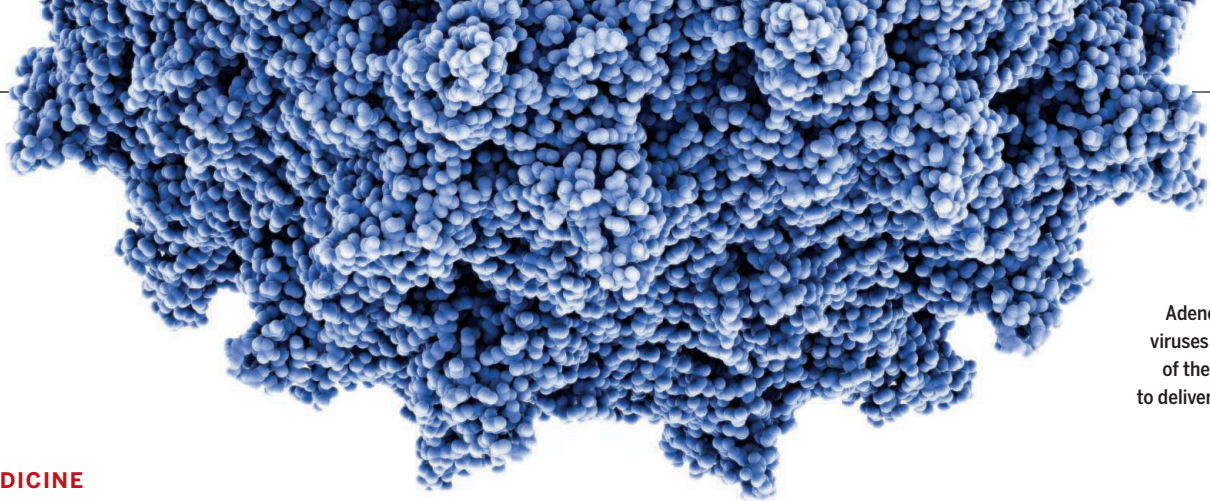
other, Qin Jinzhou, was given a 500,000 yuan fine and sentenced to prison for 18 months, although the court included a "reprieve" of 2 years that presumably will allow him to seek a shorter time behind bars. According to Xinhua, Zhang and Qin injected the genome editor into the human embryos.

Baltimore urges China to now reveal details about the status of the three children, whose genes were altered in an attempt to make them resistant to the AIDS virus. "The Chinese owe it to the rest of the world to make material from the children available for analysis under conditions where the source of the materials is unambiguously known." Scientists would like to confirm that

He indeed altered their genomes and look for any off-target effects.

Other loose ends include whether bio-engineer Michael Deem of Rice University, who was He's Ph.D. adviser and collaborated with him to some extent after He returned to China, will face any punishment. In late 2018, Rice said it was investigating Deem's role in the embryo editing but has since refused to answer questions about him. His lawyers also had no comment when contacted by *Science*. Deem remains listed as a faculty member on the school's website.

Hurlbut is struggling to find some silver lining in the whole affair. "Sad story—everyone lost in this, JK, his family, his colleagues, and his country," he says. "But the one gain is that the world is awakened to the seriousness of our advancing genetic technologies." ■



Adeno-associated viruses are stripped of their own genes to deliver therapeutic human DNA.

BIOMEDICINE

How safe is a popular gene therapy vector?

Dog study suggests virus-delivered DNA can invade chromosomes near cancer genes

By **Jocelyn Kaiser**

Just as gene therapy finally seems to be living up to its promise, a study has revived a lingering worry about the viral vessel that many efforts rely on to ferry therapeutic genes into patients. This “vector,” a stripped-down version of adeno-associated virus (AAV), was thought to be safe because it rarely knits its cargo of human DNA into a cell’s chromosomes, where it might activate cancer-causing genes. But a study of dogs with hemophilia, treated with AAV up to 10 years earlier, has shown that the vector can readily insert its payload into the host’s DNA near genes that control cell growth.

The new data, described in a conference talk last month by a Philadelphia-based research team, are “good news and bad news,” says gene therapy researcher Charles Venditti of the National Human Genome Research Institute. By slipping into the chromosomes rather than floating free, the therapeutic DNA might have longer lasting benefits. Integration “happens and it may actually be essential for long-term expression” of a needed protein, says physician-scientist David Lillicrap of Queen’s University, who attended the 9 December 2019 talk at the annual meeting of the American Society of Hematology (ASH) in Orlando, Florida. But the findings are also fueling a debate about whether AAV vectors could pose an unacceptable cancer risk. “We don’t know enough yet” to say, according to Lillicrap.

Another viral vector, used in the late 1990s in some early gene therapy trials, caused cancer in a few children after it integrated its DNA package into the chromosomes. AAV seemed to be a safer alternative because genes introduced by the modified virus generally become a free-floating loop, known as an episome, in the cell’s nucleus.

AAV vectors have helped drive the recent surge of successful gene therapies. These include one approved by the U.S. Food and Drug Administration last year for spinal muscular atrophy, a fatal childhood neurological disease, and a treatment for the blood-clotting disorder hemophilia B that’s expected to receive FDA approval this year. In the hemophilia treatment, AAV infects liver cells and turns the organ into a factory for making the clotting protein that patients depend on.

Yet doubts about AAV’s safety have simmered for nearly 20 years, since a study found that in newborn mice given high doses of the virus, it could integrate its genetic cargo into the animals’ DNA and cause liver cancer. Many gene therapists argued that findings in newborn mice are not relevant to human adults. But the new warning comes from larger, older animals: adult dogs with hemophilia A, in which a clotting protein called factor VIII is missing.

In seven of nine such dogs, AAV vectors successfully supplied a replacement copy of the gene for factor VIII and restored stable production of the molecule. In two of those dogs, however, blood levels rose further after about 3 years, reaching about four times the original level by 7 to 8 years, gene therapy researcher Denise Sabatino of the Children’s Hospital of Philadelphia reported at the ASH meeting.

After ending the experiment and studying the livers of six dogs, her team found that in every one of them, AAV-ferried DNA—the factor VIII gene or, more often, fragments of regulatory sequences—had integrated in many spots across the genome in the dogs’ liver cells, sometimes near genes affecting cell growth. Some of those cells had divided more than other cells, forming pockets of multiple cells, or “clones,” in some animals. Sabatino’s team suspects—although it can’t

prove—that the insertions activated growth genes, explaining both the clones and the rise in blood levels of factor VIII in the two dogs. (Sabatino declined to discuss the results because they have not yet been published.)

To some researchers, the results are encouraging: The integration levels were relatively low, the dogs had seemingly healthy livers, and their factor VIII levels held steady. “I don’t think there was anything too unexpected,” says Andrew Davidoff of St. Jude Children’s Research Hospital, which sponsored the first successful gene therapy trial in people with hemophilia B, which also used an AAV vector. Indeed, integration of AAV’s therapeutic DNA could explain why levels of clotting protein appear stable in that trial’s patients after as many as 9 years. DNA carried in episomes, in contrast, could be lost over time as the cells divide, because only one daughter cell would inherit the replacement gene.

But others in the gene therapy field worry that it’s only a matter of time before such clones acquire another growth-driving mutation and become tumors: “What if the dog lived another 5 years?” Venditti asks. Such a risk could arise not only in the liver, but in other tissues targeted with AAV treatments, such as neurons and muscle cells, some researchers say.

Sabatino’s data give new urgency to plans to look for integration of AAV-carried genes in other long-term dog studies and in planned liver biopsies from the St. Jude hemophilia patients, says Lillicrap, who is now studying the phenomenon in his group’s dogs. Meanwhile, researchers emphasize that people receiving AAV-delivered gene therapy should be monitored for signs of liver cancer for longer than the 5 years of follow-up now required by FDA. A spokesperson for the agency said only that it is “aware of” the Sabatino findings. ■



The Russian Academy of Sciences in Moscow is trying to improve ethical standards in publishing.

SCIENTIFIC INTEGRITY

Russian academy probe triggers more than 800 retractions

Fraud commission's work causes "tension and conflict"

By Dalmeet Singh Chawla

Academic journals in Russia are retracting more than 800 papers following a probe into unethical publication practices by a commission appointed by the Russian Academy of Sciences (RAS). The moves come in the wake of several other queries suggesting the vast Russian scientific literature is riddled with plagiarism, self-plagiarism, and so-called gift authorship, in which academics become a co-author without having contributed any work.

The RAS commission's preliminary report documenting the problems and journals' responses to them is "a bombshell," says Gerson Sher, a former staffer at the U.S. National Science Foundation and the author of recent book on U.S.-Russia science cooperation. The report, released on 7 January, "will reinforce the suspicions and fears of many—that their country is not going down the right path in science and that it's damaging its own reputation," says Sher, who applauds RAS for commissioning the investigation.

Russia's roughly 6000 academic journals, the vast majority published in Russian, are popular among the country's academics. A 2019 study found that Russian authors publish far more in domestic journals than, for instance, their counterparts in Poland, Germany, or Indonesia. But standards are often low. In March 2018, for instance, Dissernet, a network aimed at cleaning up the Russian

literature, identified more than 4000 cases of plagiarism and questionable authorship among 150,000 papers in about 1500 journals.

And Russian authors frequently republish their own work, says Yury Chekhovich, CEO of Antiplagiat, a plagiarism detection company. In September 2019, after sifting through 4.3 million Russian-language studies, Antiplagiat found that more than 70,000 were published at least twice; a few were published as many as 17 times. Chekhovich believes most instances are due to self-plagiarism. Meanwhile, the website 123mi.u claims to have brokered authorships for more than 10,000 researchers by selling slots on manuscripts written by others that were already accepted by journals.

The RAS commission, formally known as the Commission for Counteracting the Falsification of Scientific Research, investigated the problem independently. It has experienced fraud busters on board. Dissernet co-founder Andrew Zayakin, a physicist at the Institute for Theoretical and Experimental Physics, is the commission's secretary; it also includes several other "academic activists," Zayakin says, including representatives of the Society for Evidence-Based Medicine, the Russian Association of Scientific Editors and Publishers (RASEP), and Russia's Scientific Electronic Library (eLibrary). The commission used software to search hundreds of Russian-language journals—ranging from natural sciences, agronomy, psychology, and medicine to economics and law—for text overlap.

Suspicious papers were checked manually to verify that they counted as plagiarism or self-plagiarism. By comparing the author lists of papers that had been published twice or more, the commission also identified apparent cases of "obscure authorship"—academics who were an author on one version of the paper but not the other.

Last summer, the commission asked 541 journals to retract a total of 2528 papers. In its interim report, the commission writes that 390 journals have so far responded to the inquiry, 265 of which have agreed to retract all suspicious papers; others agreed to retract some of the highlighted papers but not others, or gave legitimate reasons why the papers shouldn't be pulled.

Eight journals explicitly refused to address the problems; the report urges that five of them be removed from the Russian Science Citation Index, a database run by eLibrary. (Because publication in indexed journals is often a prerequisite for promotions and funding in Russia, delisted journals are thought to be less attractive to authors.) Victor Glukhov, eLibrary's deputy director, says the group's own expert council will look into the matter, but is likely to agree. Zayakin emphasizes that the exercise is a work in progress; he hopes the threat of being delisted will persuade journals that haven't yet responded—or have refused to pull papers on flimsy grounds—to take the commission's findings seriously.

The same RAS commission caused a stir in September 2019, when it recommended not voting for 56 candidates—out of a total of more than 1800—during the academy's membership elections, because of their alleged involvement in plagiarism and other types of misbehavior. That "caused a lot of tension over how the commission is organized and who pulls the strings in it," says Dmitry Malkov, a science communication scholar at ITMO University in St. Petersburg. (The academy had about 200 new memberships available; only a few of the 56 were elected.)

The new investigation "caused tension and conflict" as well, says commission member Anna Kuleshova, chair of RASEP's Council on the Ethics of Scientific Publications. Kuleshova says some Russian journals were unaware of internationally accepted standards around ethical publishing and retractions. "I hope that our work will not only reduce scientometric distortions, and help us to get rid of garbage publications," she says, "but will also draw attention to issues related to the management of science." ■

Dalmeet Singh Chawla is a science journalist in London.

NEUROSCIENCE

In two-person MRI, brains socialize at close range

In pursuit of natural interactions, researchers push the limits of neuroimaging

By **Kelly Servick**

The dark, thumping cavern of an MRI scanner can be a lonely place. How can scientists interested in the neural activity underlying social interactions capture an engaged, conversing brain while its owner is so isolated? Two research teams are advancing a curious solution: squeezing two people into one scanner.

One such MRI setup is under development with new funding from the U.S. National Science Foundation (NSF), and another has undergone initial testing described in a preprint last month. These designs have yet to prove that their scientific payoff justifies their cost and complexity, plus the requirement that two people endure a constricted almost-hug, in some cases for 1 hour or more. But the two groups hope to open up new ways to study how brains exchange subtle social and emotional cues bound up in facial expressions, eye contact, and physical touch. The tool could “greatly expand the range of investigations possible,” says Winrich Freiwald, a neuroscientist at Rockefeller University. “This is really exciting.”

Functional magnetic resonance imaging (fMRI), which measures blood oxygenation to estimate neural activity, is already a common tool for studying social processes. But compared with real social interaction, these experiments are “reduced and artificial,” says Lauri Nummenmaa, a neuroscientist at the University of Turku in Finland. Participants often look at static photos of faces or listen to recordings of speech while lying in a scanner. But photos can’t show the subtle flow of emotions across people’s faces, and recordings don’t allow the give and take of real conversation.

So researchers have crafted real-time encounters in the scanner. In 2002, neuroscientist Read Montague and colleagues at Baylor College of Medicine published the first of many studies to record simultaneously from people in separate, linked MRI machines. The approach can capture neural activity as people play an online game or communicate through an audio or video feed.

Even with that approach, “There’s a huge amount of interpersonal information filtered out,” says Ray Lee, a neuroscientist and MRI physicist at Columbia University. So over the past decade, he has been refining an fMRI setup for two. It requires a specialized pair

of head coils that allows researchers to read separate signals from two adjacent brains. These cage-like metal coils encircle participants’ heads as they lie on their sides with their legs touching in the MRI magnet and gaze at each other through a window. In 2012, while at Princeton University, Lee and colleagues published the first paper on the device, which he estimates would cost \$200,000 to provide to another lab.

A second two-person fMRI scanner, developed by Nummenmaa and colleagues in

sponding to both the touch of the taps and the sight of the tapping finger—along with the sound of recorded instructions.

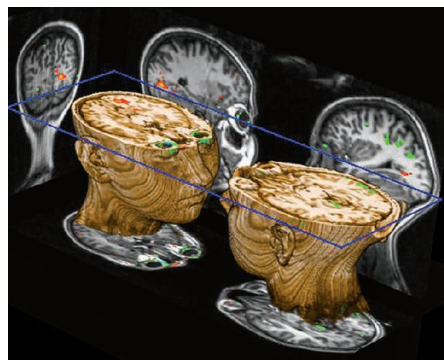
Lee’s first research questions are also relatively simple: How does brain activity in the shared scanner differ from activity during a remote video connection? What brain networks light up when people make eye contact? He is still analyzing data and submitting publications from his 2012 setup, but in the fall of 2019, his team received nearly \$1 million from NSF to design a coil with improved signal quality and scan more brains.

“If Ray can get this system working ... he’s got a lot of room to grow,” says Ellen Carpenter, a neuroscientist and program director at NSF. Future studies could, for example, observe the brain as it picks up social cues and decides when and how to convey empathy to a scanner mate, she says.

Of course, researchers can already observe socializing brains by imaging them one at a time. A person being scanned can talk with or even touch a person directly outside the scanner. “Do you actually gain something from observing in real time how the activity is changing in the two brains?” Freiwald wonders. One issue is that fMRI is slow. The changes in blood oxygen that it measures happen on the scale of seconds, which means that in some cases, the precise relationship between the timing of neural firing in the two brains could elude the scanner.

Others say the cozy MRI setup itself could limit the research. “This is more than face to face,” says Uri Hasson, a neuroscientist at Princeton. “You lie next to very particular people in your life.” With other people, the experience could feel threatening. “Have you ever stood in front of a stranger 3 inches from their nose? Probably not on purpose,” says Montague, now at Virginia Polytechnic Institute and State University. “I don’t know where it’s going,” he says of the approach. “On the other hand, I’m a big proponent of the renegade maverick that [does] what they want to do.”

Despite their limitations, Lee thinks two-person MRI scanners will capture aspects of socializing brains long overlooked by neuroimaging. He plans to look at differences in the brain dynamics of children with and without autism as they make eye contact and interact with a parent in the scanner. He expects his first subjects will be sliding into the magnet together by this fall. ■



A two-person fMRI setup captured brain activity (top) while people made eye contact (bottom).

the lab of neuroscientist Riitta Hari at Aalto University in Finland, uses a different type and shape of head coil, but places participants in the same near-cuddling pose. (The team tried a less intimate, sphinxlike pose: bellies down, face to face. But it was “pretty bad for the neck,” Hari notes.)

In a 10 December 2019 bioRxiv preprint, the team describes an early test of the technology: recording neural activity while pairs of friends or intimate partners took turns tapping each other on the lips. With that task, the researchers could verify that the scanner picked up brain activity corre-

An illustration showing several hypersonic missiles and a waverider aircraft flying through a sky filled with white, puffy clouds. One missile is in the upper left, another in the upper right, and a third in the lower left. A large, sleek, orange and white waverider aircraft is in the lower right. The background is a deep blue sky with scattered clouds.

NEED FOR SPEED

Despite hype and technological hurdles, a hypersonic arms race is accelerating

High in the sky over northwestern China, a wedge-shaped unmanned vehicle separated from a rocket. Coasting along at up to Mach 6, or six times the speed of sound, the Xingkong-2 “waverider” hypersonic cruise missile (HCM) bobbed and weaved through the stratosphere, surfing on its own shock waves. At least that’s how the weapon’s developer, the China Academy


By **Richard Stone**

of Aerospace Aerodynamics, described the August 2018 test. (China did not release any video footage.) The HCM’s speed and maneuverability, crowed the Communist Party’s *Global Times*, would enable the new weapon to “break through any current generation anti-missile defense system.”

For decades, the U.S. military—and its adversaries—have coveted missiles that

travel at hypersonic speed, generally defined as Mach 5 or greater. Intercontinental ballistic missiles (ICBMs) meet that definition when they re-enter the atmosphere from space. But because they arc along a predictable ballistic path, like a bullet, they lack the element of surprise. In contrast, hypersonic weapons such as China’s waverider maneuver aerodynamically, enabling them to dodge defenses and keep an adversary guessing about the target.

ILLUSTRATION: DARPA



Bullet-shaped interceptors defend the United States against attacking hypersonic weapons in an artist's concept. Such defenses remain hypothetical.

U.S. Department of Defense (DOD). “The community was underfunded and largely forgotten for many years,” adds Daniel DeLaurentis, director of Purdue University’s Institute for Global Security and Defense Innovation.

Now, DOD is leading a new charge, pouring more than \$1 billion annually into hypersonic research. Competition from ambitious programs in China and Russia is a key motivator. Although hype and secrecy muddy the picture, all three nations appear to have made substantial progress in overcoming key obstacles, such as protecting hypersonic craft from savage frictional heating. Russia recently unveiled a weapon called the Kinzhal, said to reach Mach 10 under its own power, and another that is boosted by a rocket to an astonishing Mach 27. China showed off a rocket-boosted hypersonic glide vehicle (HGV) of its own, the Dongfeng-17, in a recent military parade. The United States, meanwhile, is testing several hypersonic weapons. “It’s a race to the Moon sort of thing,” says Iain Boyd, an aerospace engineer at the University of Colorado, Boulder. “National pride is at stake.”

This new arms race promises to upend strategic calculations. Russian officials have cast nuclear-armed hypersonic craft as a hedge against future U.S. prowess at shooting down ICBMs, which could undermine nuclear deterrence.

China’s military, in contrast, sees hypersonic weapons (as well as cyberwarfare and electromagnetic pulse strikes) as an “assassin’s mace”: a folklore term for a weapon that gives an advantage against a better-armed foe, says Larry Wortzel, a senior fellow at the American Foreign Policy Council who serves on the U.S.-China Economic and Security Review Commission. If tensions were to spike over Taiwan or the South China Sea, for instance, China might be tempted to launch preemptive strikes with conventional hypersonic weapons that could cripple U.S. forces in the Pacific Ocean, Wortzel says. China’s hypersonic weapons, he warns, “seem deliberately targeted at upending the tenuous strategic stability that has been in place since the end of the Cold War.”

For now, maneuverability at hypersonic speeds makes the weapons nearly impossible to shoot down—“unstoppable,” as a headline in *The New York Times* put it last summer. But, “Unstoppable today does not mean unstoppable tomorrow,” says Shari Feth, a materials engineer at the U.S. Missile Defense Agency (MDA). She’s at the

vanguard of U.S. efforts to field countermeasures against hypersonic weapons. “There are technologies that could be developed that could be used for a more robust defense,” Feth says. “But we have more work to do to get there.”

THE UNITED STATES has spent decades trying to get hypersonic flight right. The first vehicle to exceed Mach 5 was a two-stage rocket, dubbed Project Bumper, launched in 1949. After four failed tests, the V-2 rocket lifted off from a missile range in New Mexico, releasing a second-stage sounding rocket that attained Mach 6.7.

Project Bumper and subsequent efforts laid bare the daunting challenges. “This is a very unforgiving realm,” says Lewis, who served as chief scientist of the U.S. Air Force from 2004 to 2008. “You’re flying under extraordinary conditions”—extreme velocities, forces, and temperatures. The hypersonic threshold of Mach 5 is arbitrary, but at those speeds, he says, “temperatures start to get high enough to worry about.”

The heating depends on factors such as the vehicle’s speed and contours. When a space shuttle returning from orbit hit the upper atmosphere at Mach 25, its blunt leading edges heated to 1400°C, which a skin of carbon-carbon composites helped it withstand. Newer hypersonic craft tend to have sharper edges—in part to assist with maneuverability—that can exceed 2000°C. Turbulence can make things worse. At hypersonic speeds, the boundary layer around the vehicle thickens, and a smooth, laminar flow can suddenly break up into eddies and swirls that cause temperature spikes on the vehicle’s skin. “We’ve devoted a lot of fundamental research to figure out when that occurs,” Lewis says. A vehicle’s survival, he says, requires resilient superalloys and ultra-high-temperature ceramics. And perhaps novel coolants. For example, a team at the U.S. Naval Research Laboratory has devised a liquid sodium system that drains heat from a leading edge through continuous evaporation and condensation.

High air speeds also pose challenges for engines on HCMs, which unlike HGVs have their own power plants. HCMs use a supersonic combustion ramjet, or “scramjet,” to accelerate. “It’s the simplest type of jet engine you could ever imagine ... just an open tube” in which air mixes with fuel, Lewis says. “It’s also perhaps the most complicated type you can imagine because of the extreme conditions under which it operates.”

At hypersonic speeds, air molecules spend milliseconds in the engine tube—scant time for fuel and air to mix properly. And when a vehicle pitches and yaws, airflow into the engine changes, which can result in uneven

Since the dawn of the Cold War, the Pentagon has periodically thrown its weight behind the development of maneuverable hypersonic weapons, only to shy away when technological hurdles such as propulsion, control, and heat resistance proved daunting. “You see a flurry of activity, a lot of investment, and then we conclude it’s a bridge too far,” says aerospace engineer Mark Lewis, director of defense research and engineering for modernization at the

In Russia, hypersonic rivalry feeds suspicions and arrests

As the hypersonic arms race escalates, international collaborations are crumbling—sometimes with dire consequences for researchers. Almost 10 years ago, Russian aerospace engineer Victor Kudryavtsev collaborated with Europe on Transhyberian, a €565,000 hypersonic project funded largely by the European Union. But in the summer of 2018, Russia's Federal Security Service (FSB) arrested him and, several months later, a colleague, physicist Roman Kovalev. Both have been charged with high treason for allegedly leaking hypersonic secrets to "a NATO research center." If found guilty, they each face up to 20 years in prison.

The charges dismay observers, who point out that a military review panel had approved the release of Russia's contribution to Transhyberian. (The project's coordinating institution, the von Karman Institute for Fluid Dynamics in Belgium, is affiliated with NATO but does no classified research.) FSB's decision to classify the work came 5 years after the EU project ended. The "absolutely illicit retroactive approach ... increases the vulnerability" of Russian scientists working in areas that might have military or other sensitive applications, says Boris Altshuler, a theoretical physicist and human rights activist at the Russian Academy of Sciences's P.N. Lebedev Physical Institute.

Launched in June 2011, the 2-year project examined a phenomenon that bedevils spacecraft re-entering Earth's atmosphere. At hypersonic speeds, laminar air flow over a surface can suddenly turn turbulent, creating intense temperature spikes on the vehicle's surface. To study those heat fluctuations, the Transhyberian team performed wind tunnel experiments and computer simulations at the Belgian institute, the German Aerospace Center, and three Russian institutions—including the Central Research Institute of Machine Building, or TsNIIMash, a spacecraft and missile design center in Korolyov where both arrested scientists work. The research showed that locally heating or cooling the surface could help control the temperature spikes—a finding that could improve the design of hypersonic aircraft.

As project coordinator for TsNIIMash, Kudryavtsev transmitted research findings to the foreign partners. The reports were approved by the military's Federal Service for Technical and Export Control, says Kudryavtsev's attorney, Ivan Pavlov, a prominent human rights lawyer. Herman Deconinck, who handles the von

Karman Institute's foreign relations, notes that all references in the Russian reports had been published in the open literature.

The project aimed to strengthen collaboration between Russia and the European Union in hypersonics, Deconinck says. But the amity faded in 2014 after Europe condemned Russia's invasion of Crimea. Relations cooled further in 2018, when Western analysts greeted Russian claims about the country's hypersonic weapons skeptically, citing test failures. Russia then classified much of its hypersonic research, and Kudryavtsev was hauled off to Moscow's Lefortovo Prison.

In November 2018, he was denied prison visits after rejecting a plea bargain requiring him to admit guilt and "frame a colleague," Pavlov says. The European Court of Human Rights weighed in in April 2019, ordering Russia to provide medical treatment for

Kudryavtsev, who is 76 and ailing. He was released from prison on 27 September 2019 after being diagnosed with metastatic lung cancer, says his son, Yaroslav Kudryavtsev, a polymer scientist. "They just put him outside with all his things," Victor Kudryavtsev was told not to leave the Moscow region before his trial.

"Mentally Victor is strong, not cooperating with the investigators," his son says. After failing to squeeze a confession out of Victor Kudryavtsev, FSB arrested Kovalev in June. He has also reportedly refused to plead guilty or incriminate colleagues and is confined in Lefortovo. In July 2019, the security service arrested a third TsNIIMash scientist, Sergey Mesh-

cheryakov, who had participated in a different international project. He, too, is accused of high treason and is under home detention after suffering a heart attack following his arrest. Authorities have not signaled when the three researchers will face trial.

Voices outside Russia need to speak up, Altshuler says. "Strong reaction in the West is an effective practical instrument to raise the level of decision-making on the case," he says. The Committee of Concerned Scientists, a human rights nonprofit, has worked to draw attention to the scientists' plight. And on 29 October 2019, the von Karman Institute declared it "could not find any trace of disclosing secret information" by Kudryavtsev's team. It asked the European Commission to pursue the matter with Russia.

The support is welcome, Yaroslav Kudryavtsev says. The von Karman Institute's "simple public declaration," he says, could persuade many academics to take a stand. —R.S.



Taking part in international hypersonic research landed Russian engineer Victor Kudryavtsev in prison.

combustion and thrust. Tweaks to get a better burn have ramifications for, say, how the aircraft withstands shock waves. "Everything is incredibly coupled. You are designing a fully integrated vehicle," Lewis says. It took the United States 46 years to realize its first working scramjet: NASA's \$230 million X-43a, an uncrewed vehicle that flew in 2004.

HGVs pose other challenges. The rocket that carries the glider reaches speeds far greater than those of an HCM, meaning engi-

neers must use materials that are even more resistant to heat. Still, HGVs are easier to maneuver because they lack a scramjet, with its acute sensitivity to pitch and yaw. "It almost becomes a religious discussion—rockets versus air breathing," Lewis says. "The ultimate answer is we probably want both."

The United States has not yet fielded either. After decades of fits and starts, any advantage that U.S. hypersonic R&D once held has largely eroded away. Its wind tunnels

and other testing infrastructure are aging. And challenges such as tweaking designs to ensure engine walls don't melt have slowed progress on scramjets, Lewis says. "Today we are further away from routine scramjet flight than we were 10 years ago."

FROM A BASE in the Ural Mountains on 26 December 2018, Russia's armed forces launched a ballistic missile carrying an HGV called Avangard. After separating

from its carrier in the stratosphere, the HGV zigzagged 6000 kilometers across Siberia at a searing Mach 27, Russian officials claimed, then smashed into a target on the Kamchatka Peninsula. Afterward, a beaming Russian President Vladimir Putin called Avangard “the perfect New Year’s gift for the country.” Russia’s defense ministry announced last month that it has put the nuclear-armed HGV into combat duty—allowing Putin to claim that Russia is the first country armed with hypersonic weapons.

Russian boasts along with Chinese advances have sounded the alarm in the United States. Congress will pour more than \$1 billion into military hypersonic research this year and has created a new university consortium to do basic studies. “Our work on hypersonics has really ramped up,” says Jonathan Poggie, an aerospace engineer at Purdue. His team models low-frequency shock waves “that pound on a vehicle like a hammer.”

The rising military stakes have prompted the Pentagon to consider classifying some basic hypersonic research. DOD “is very concerned about educating our enemies,” Poggie says. “They are in the middle of trying to draw these red lines,” Boyd adds. But, “If we overclassify,” he warns, “there are a number of domino effects. You’d be stifling innovation. Inevitably, that means fewer new ideas.”

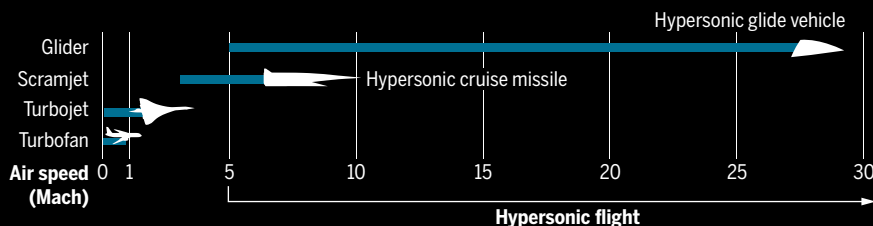
A veil of secrecy is also descending in Russia, which has produced “a rich body of hypersonic literature,” Lewis says. Security officials there recently charged two scientists with treason for sharing findings with European collaborators; the data had been approved for release but then declared secret 5 years later (see sidebar, p. 136).

China, in contrast, has been surprisingly open about its research. “The Chinese are trying to establish prestige in the field,” Lewis says. The nation has invested heavily in facilities, including sophisticated wind tunnels and shock tubes that use blast waves to study hypersonic flows. “Ten years ago, they were duplicating what others had done,” Boyd says. “Now, they’re publishing innovative ideas.” At a 2017 hypersonic conference in Xiamen, China, Chinese scientists presented more than 250 papers—about 10 times the number presented by U.S. researchers.

“You see papers you’d think they wouldn’t publish in the open literature,” Poggie says. One is a recent analysis from the China Aerodynamics Research and Development Center showing that the plume of ionized gas, or plasma, left by a hypersonic vehicle is more visible on radar than the vehicle

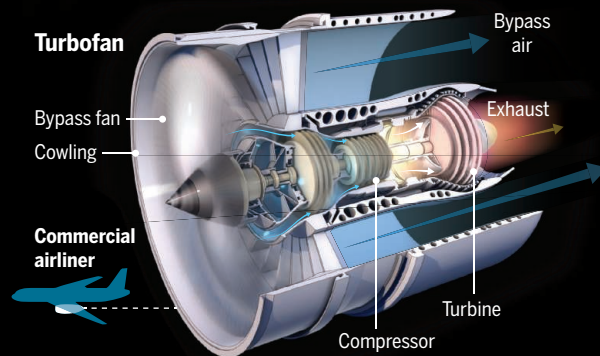
Fast strike

Since the dawn of the Cold War, militaries have strived for weapons that can maneuver at hypersonic speed, defined as Mach 5 (five times the speed of sound) or greater. Although hype and secrecy muddy the picture, China, Russia, and the United States all appear to have made big strides in overcoming key obstacles.

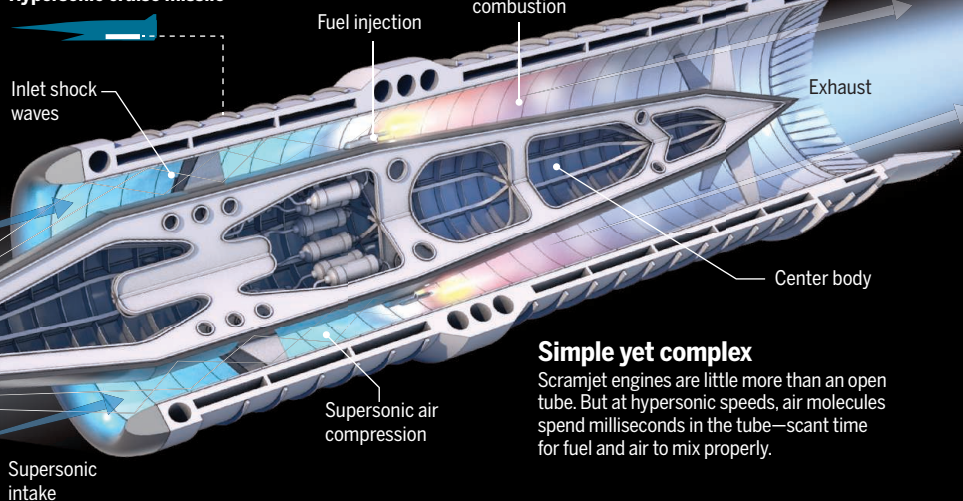


From fans to scrams

In the turbofan engines of commercial jetliners, thrust comes from the jet exhaust and from air swept past the combustion chamber by fans. Such engines are not designed to handle shock waves generated by air moving faster than sound. Hypersonic cruise missiles instead use a supersonic combustion ramjet, or scramjet.



Hypersonic cruise missile

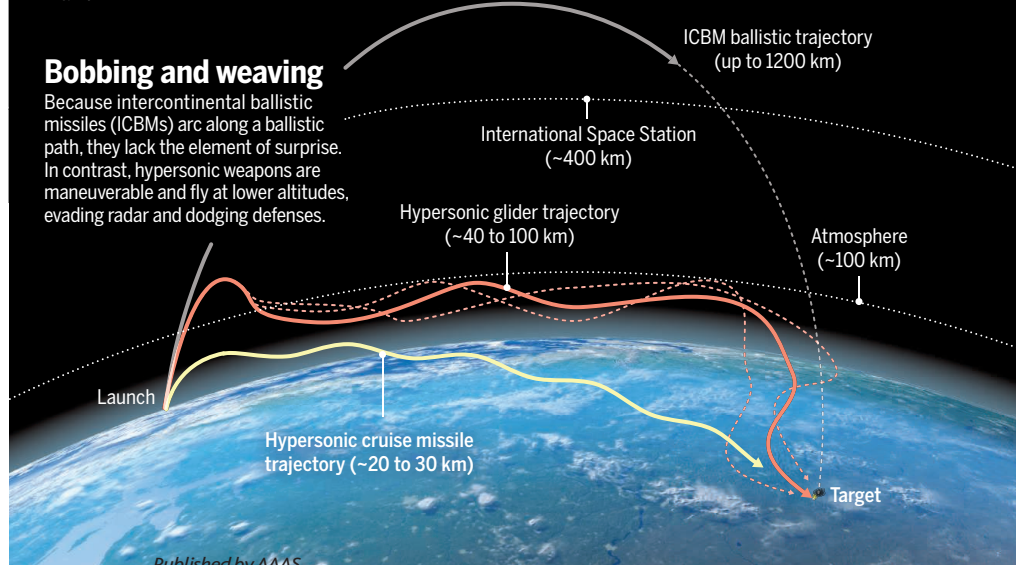


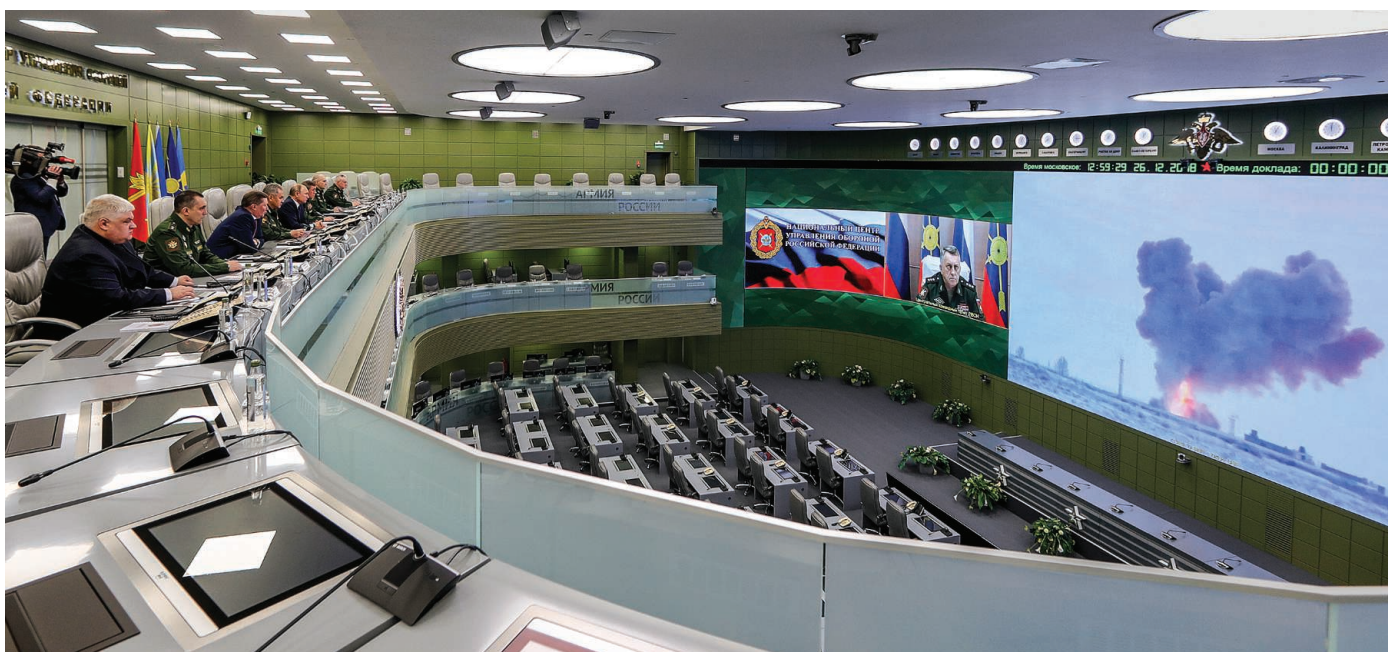
Simple yet complex

Scramjet engines are little more than an open tube. But at hypersonic speeds, air molecules spend milliseconds in the tube—scant time for fuel and air to mix properly.

Bobbing and weaving

Because intercontinental ballistic missiles (ICBMs) arc along a ballistic path, they lack the element of surprise. In contrast, hypersonic weapons are maneuverable and fly at lower altitudes, evading radar and dodging defenses.





Russia's Avangard is launched aboard a rocket in a 2018 test. Spectators include Russian President Vladimir Putin, who has declared the hypersonic weapon is now in service.

itself. That implies radar could give early warning of an incoming weapon.

Other nations are chasing the trio of leaders—or teaming up with them. Australia is collaborating with the United States on a Mach 8 HGV, and India with Russia on a Mach 7 HCM. France intends to field an HCM by 2022, and Japan is aiming for an HGV in 2026, the U.S. Congressional Research Service noted in a July 2019 report.

THE UNITED STATES is largely defenseless against such weapons, at least for now, in part because it can't track them. U.S. military satellites are vigilant for flashes that reveal launches of ICBMs and cruise missiles. But they would probably lose track of even a rocket-boosted hypersonic weapon soon after it detaches from its booster, analysts say. To avoid "shooting blindly ... you need to continue to track it when it starts doing these maneuvers in the atmosphere," says Thomas Karako, director of the Missile Defense Project at the Center for Strategic & International Studies.

To remedy that shortcoming, the Pentagon plans to launch hundreds of small satellites with sensors capable of tracking heat sources an order of magnitude cooler than rocket boosters. "By proliferating them, you make it impossible to take them all out," Karako says. The full Hypersonic and Ballistic Tracking Space Sensor network could be up and running by 2030, he adds. (The

satellites would also be used to help guide U.S. hypersonic weapons.)

Once you have such sensors, "we can find a way to build the interceptors," Karako says. Current missile defense interceptors aim to destroy ICBMs near their apex in the upper atmosphere, much higher than a hypersonic weapon flies, and they aren't maneuverable enough to hit a swerving target. "You'll need interceptors with more divert capability than we have," Karako says.

MDA is exploring various approaches that would enable interceptors to "overmatch" incoming weapons, Feth says. One possibility, she says, is to fly faster—a tall order that would demand new lightweight, heat-resistant composites and alloys.

Interceptors could destroy a hypersonic vehicle either by colliding with it or by detonating a warhead nearby. But MDA is also

exploring using directed energy: lasers, neutral particle beams, and microwaves or radio waves. Directed-energy countermeasures were floated in the 1980s as elements of the United States's "Star Wars" missile defense shield—then abandoned. Four decades later, "They are more plausible," Karako says. Still, MDA recently scrapped plans to test a prototype 500-kilowatt airborne laser by 2025 and to develop a space-based neutral particle beam.

Even as defense scientists search for ways to thwart a hypersonic attack, diplomats and nonproliferation experts are discussing how to limit—or even outlaw—the disruptive technology. "Hypersonic weapons are primed for arms control," argues Ankit Panda, senior fellow on the Defense Posture Project at the Federation of American Scientists, a think tank. The United Nations Office for Disarmament Affairs weighed in last year with a report exploring arms control scenarios, blasting what it called a "blinkered pursuit of a novel technology with as-yet-unproven military utility."

Arms control treaties, however, are hardly in vogue these days. And with China, Russia, and the United States egging each other on with one high-profile test after another, the hypersonic arms race seems likely to accelerate. ■


Richard Stone is senior science editor at the Howard Hughes Medical Institute's Tangled Bank Studios in Chevy Chase, Maryland.



China has flaunted its hypersonic prowess, including the Dongfeng-17 hypersonic glider, seen in a military parade last year.

INSIGHTS

PERSPECTIVES



The majority of Earth's species diversity remains to be discovered and described, particularly from its most remote regions (such as the Andes Mountains in Ecuador).

BIODIVERSITY

Completing Wallace's journey

A global inventory of species diversity is critical for understanding the evolution of life on Earth

By **Jonathan D. Kennedy**¹ and **Jon Fjeldså**^{2,3}

British naturalist Alfred Russel Wallace developed the theory of evolution as a consequence of the taxonomic discoveries made during his expeditions across the Indonesian archipelago in the 19th century. From his collections, thousands of new species have been described, including around 2% of all living bird species. Birds are one of the most

comprehensively documented organismal groups, but multiple new species continue to be described yearly, and at an increasing rate. Nearly all recent avian species discoveries come from disjunct geographic locations. However, on page 167 of this issue, Rheindt *et al.* (1) describe five new species and five subspecies from three islands off the eastern coast of Sulawesi, Indonesia. This is the largest number of new species descriptions from a restricted geographic locality in over a century and highlights the importance of documenting biodiversity today, given the environmental threats that could condemn many as yet unidentified taxa to extinction.

Knowing how many species are present on Earth remains a fundamental scientific question whose answer is essential to generating

a reliable benchmark from which current and future biodiversity losses can be gauged. Currently, as much as 86% of the world's overall species diversity is undescribed (2). Even for a well-known group such as birds, some estimates suggest that overall numbers could be substantially higher than the ~10,500 presently recognized species (3). The taxonomic description of bird species has benefited from their relative ease of observation. In addition, numerous clearly defined characters signify that lineages are evolving independently from one another [e.g., differentiation in plumage coloration, acoustic signaling, and genomic characters (4)]. Because of this progress, present-day avian species discoveries tend to represent relatively shallow levels of evolutionary distinctiveness. Although phenotypic and genetic evidence convincingly suggests that all 10 forms described by Rheindt *et al.* are independently evolving populations, these data also indicate that they represent lineages that are members of well-known genera, with close relatives distributed on nearby islands. Descriptions of deeper and more distinctive evolutionary branches of the avian tree

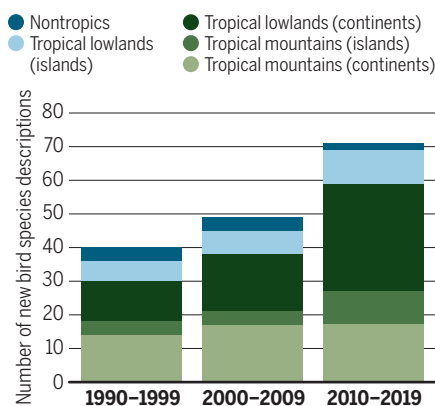
¹Department of Animal and Plant Sciences, University of Sheffield, Sheffield S10 2TN, UK. ²Center for Macroecology, Evolution and Climate, GLOBE Institute, University of Copenhagen, Universitetsparken 15, DK-2100 Copenhagen, Denmark. ³Natural History Museum of Denmark, University of Copenhagen, Universitetsparken 15, DK-2100 Copenhagen, Denmark. Email: jonathan.kennedy@sheffield.ac.uk

of life are rare, the most recent noteworthy example being the *Xenoperdix* forest partridges discovered in the mid-1990s (5).

Between 1990 and 2019, approximately 160 new bird species descriptions were made worldwide (see the figure), so the discovery of five bird species from a relatively small geographic locality is impressive, driven by the local aggregation of small-ranged species. This suggests that many biologically underexplored places likely still exist across Earth. Formal species descriptions, such as those by Rheindt *et al.*, are a necessary step toward initiating conservation actions that aim to preserve these little-known biotas.

New bird species descriptions

The total number of new species descriptions increased over the past three decades (9, 10).



In comparison to birds, global knowledge of other vertebrate, invertebrate, plant, fungal, and microorganismal life is far more limited, particularly in tropical regions. Millions of unknown species, likely representing more distinctive portions of the tree of life, remain to be discovered (2, 6). To discover these taxa most efficiently, geographic areas with high promise should first be targeted. It is thus notable that most new bird species discoveries in the past 30 years have been from localities that reside in tropical or subtropical latitudes. These areas tend to have complex landscapes, geologies, soil conditions (such as ultramafic soils), and topographic or aquatic barriers (such as mountains and river systems, respectively). Most problematically, these locations are poorly accessible, resulting in historically limited biological exploration. Limited access reflects not only geographic barriers but also political and commercial obstacles. Mountainous areas in the tropics, both in island and continental settings, hold great promise for discovering new species because they are environments that tend to harbor little-studied biological communities, where range-restricted spe-

cies can evolve (endemism) (7). Bird descriptions arising from these areas (especially in Indochina, Malesia, eastern Africa, Brazil, and the tropical Andes) are highly indicative of generally poorly known terrestrial biotas.

Extensive population growth and human consumption over the past century have caused substantial habitat degradation, primarily due to urban development, logging, mining, and wildlife trade and exploitation. These combined threats continue unabated and are driving the global extinction crisis, with current rates of extinction estimated to exceed background rates by a factor of 100 to 1000 (8). Much of the world's biodiversity is under considerable risk of being lost before it is ever scientifically known. For these reasons, Wallace's journey to find, describe, and study taxonomic diversity should continue today with increased vigor and resources, as this will ultimately increase knowledge about the most effective way to preserve nature. Achieving this will require more extensive international collaborative efforts by governments, academics, and local communities. To thoroughly explore and describe the poorly known parts of the terrestrial, subterranean, and aquatic world will also necessitate increased recognition of the value that taxonomic discovery has toward our general understanding of the natural world. To secure increased funding, scientists must better explain to their colleagues, the public, policy-makers, and funding agencies why biological exploration should be seen as a pressing issue today, not just a historical activity of Wallace's time. Without knowing how many species there are in the world, and their distributions, our understanding of how ecological and evolutionary processes have generated the full diversity of life on Earth is incomplete, limiting our capacity to successfully maintain biodiversity into the future. ■

REFERENCES AND NOTES

1. F. Rheindt *et al.*, *Science* **367**, 167 (2020).
2. C. Mora *et al.*, *PLOS Biol.* **9**, e1001127 (2011).
3. G. F. Barrowclough *et al.*, *PLOS ONE* **11**, e0166307 (2016).
4. G. Sangster, *Proc. Biol. Sci.* **276**, 3185 (2009).
5. L. Dinesen *et al.*, *Ibis* **136**, 2 (1994).
6. M. J. Costello *et al.*, *Science* **339**, 413 (2013).
7. C. Rahbek *et al.*, *Science* **365**, 1114 (2019).
8. A. D. Barnosky *et al.*, *Nature* **471**, 51 (2011).
9. J. del Hoyo, N. J. Collar, *HBW and BirdLife International Illustrated Checklist of the Birds of the World. Volume 1: Non-Passerines* (Lynx Edicions, 2014).
10. J. del Hoyo, N. J. Collar, *HBW and BirdLife International Illustrated Checklist of the Birds of the World. Volume 2: Passerines* (Lynx Edicions, 2016).

ACKNOWLEDGMENTS

J.F. thanks the Danish National Research Foundation for supporting the Center for Macroecology, Evolution and Climate (DNRF96). J.D.K. was supported by an individual fellowship from Marie Skłodowska-Curie actions (MSCA-792534).

INFECTIOUS DISEASE

Tolerance to antibiotics affects response

Bacterial tolerance to antibiotics reduces the ability to prevent resistance

By Andrew D. Berti¹ and Elizabeth B. Hirsch²

Antimicrobial resistance is increasing worldwide (1). More than 2.8 million antibiotic-resistant infections were identified in the United States in 2019, resulting in more than 35,000 deaths (2). Prior to the development of antimicrobial resistance, bacteria frequently develop enhanced antimicrobial tolerance (3). Antimicrobial resistance is the ability of a microbe to grow in an inhibitory concentration of an antibiotic, whereas tolerance is a reduced rate of antimicrobial killing (4). Antibiotic combinations are often used to improve efficacy (5) and to prevent the emergence of antibiotic resistance (6). However, it is unclear if antibiotic combinations prevent the emergence of tolerance. On page 200 of this issue, Liu *et al.* (7) examine sequential *Staphylococcus aureus* isolates from patients treated with daptomycin plus rifampin. Although this combination of antibiotics delayed the emergence of tolerant populations, once tolerance was established, the benefits of combination therapy in preventing resistance were lost.

Antibiotic tolerance is a natural phenomenon that occurs as a spontaneous "hibernation-mode" phenotypic switch within a small subset of a microbial population. Transient microbial growth arrest is induced by stressful conditions, such as a sudden decrease in nutrient availability, when continued rapid growth would threaten viability. Once the insult is removed, bacteria can resume typical microbial growth (8). Phenotypically tolerant microbes are genetically indistinguishable from other nontolerant, growing bacteria. However, mutations in one of sev-

¹Department of Pharmacy Practice, Wayne State University, Detroit, MI, USA. ²Department of Experimental and Clinical Pharmacology, University of Minnesota, Minneapolis, MN, USA. Email: andrew.berti@wayne.edu; ebhirsch@umn.edu

eral independent pathways can substantially increase the proportion of phenotypically tolerant cells within a population (9).

Pathways implicated in tolerance development are diverse and include inorganic phosphate metabolism, nucleotide signaling, transfer RNA (tRNA) charging, and toxin-antitoxin systems. Such mutations are heritable and typically alter either the threshold at which a given stressor can induce tolerance or the ease by which tolerant microbes can emerge from the tolerant state and resume growth. Although antibiotics are effective against actively growing bacteria, phenotypically tolerant microbes are often highly resilient to antimicrobial killing (10). These persister cells that survive antibiotic exposure are then able to cause recurrence or relapse of infection after completion of antibiotic treatment.

Liu *et al.* demonstrate that daptomycin tolerance consistently precedes the development of rifampin resistance. This is consistent with the overall poor performance of rifampin as a combination agent for severe staphylococcal infections (11). It also aligns with a model of resistance prevention whereby each antibiotic in combination exerts a counterselective pressure against the development of resistance to its partner agent. The authors found that development of resistance to rifampin enhanced daptomycin killing because rifampin-mediated restrictions on bacterial growth were removed. Thus, in mixed populations of resistant and susceptible microbes, only the susceptible populations survived under combined antibiotic exposure. However, once tolerance was established, the selective pressure against resistance development was lost (see the figure).

If this effect were specific to staphylococci, it would be concerning but probably manageable because of its limited impact. Unfortunately, Liu *et al.* demonstrate that the phenomenon is generalizable to Gram-negative bacteria and applies to other antimicrobial combination therapies. The implications of this finding are profound. Modern clinical microbiology laboratories determine antimicrobial resistance through phenotypic susceptibility testing that establishes the minimal antibiotic concentration necessary to inhibit visible growth (minimal inhibitory concentration, MIC). This assessment fails to capture the prevalence of antimicrobial tolerance because isolates enriched in tolerant cells would have the same MIC as isolates consisting only of rapidly growing cells.

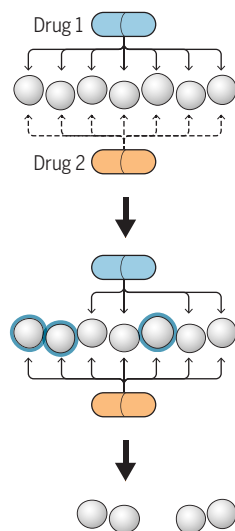
Tolerance compromises antibiotics

Antibiotics target dividing bacteria. In some antibiotic combinations, the development of resistance to one drug restores growth and thus the efficacy of the other agent, preventing the establishment of resistance. However, if an antibiotic induces bacterial tolerance (growth arrest), then resistance to the other drug will not be overcome by the combination.

○ Antibiotic-resistant bacteria ◐ Tolerant bacteria

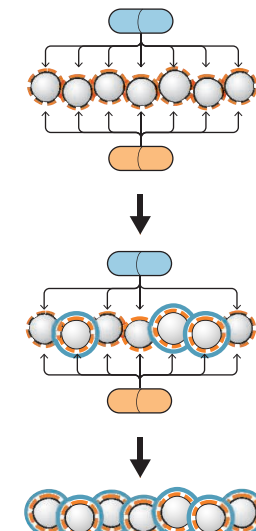
Effective treatment

Drug 1 inhibits growth and limits the effect of drug 2. Resistance to drug 1 restores growth, and thus drug 2 kills dividing cells and establishment of resistance to drug 1 is avoided.



Resistance establishment

Drug 1 inhibits growth. Resistance to drug 1 restores growth but drug 2 induces tolerance, not bacterial killing. Thus, resistance to drug 1 is favored.



The standard method for defining tolerance, a change in the minimum duration of exposure necessary to kill a defined percentage of the population (MDK), is labor- and time-intensive and would be challenging to implement clinically (4). Recently, phenotypic testing methods have been proposed to screen for tolerance, such as a modified two-step Kirby-Bauer disk diffusion assay, in which a nutrient disk is placed in the zone of inhibition after exposure and subsequent removal of an antibiotic-containing disk (12). However, these research-use-only tests have not been widely adopted in the clinical laboratory because they lack established reference standards for comparison and are not approved for clinical use. Without robust screening, the burden of antimicrobial tolerance in clinical isolates remains unknown.

In addition to genetic changes that result in more antibiotic-tolerant microbes, health system interventions may themselves be encouraging antimicrobial tolerance. The topical antibiotic ointment mupirocin is frequently used to treat staphylococcal skin infection, in antimicrobial stewardship interventions and in infection control measures such as nasal decolonization (13). Unfortunately, mupirocin is a potent chemi-

cal inducer of antimicrobial tolerance, inhibiting isoleucyl-tRNA synthetase and altering microbial perception of isoleucine bioavailability. This significantly increases the MDK of multiple antistaphylococcal antibiotic classes (14).

Antimicrobial tolerance has been identified as a risk factor for poor clinical outcome in staphylococcal bacteremia (15). The study of Liu *et al.* establishes that some combination antimicrobial therapies are of limited value in the presence of tolerant bacteria. There is clearly an unmet need to identify antibiotic therapies that maintain potency against antibiotic-tolerant microbes, either alone or in combination. Although phenotypic screens provide value, the development and implementation of more rapid diagnostics for antimicrobial tolerance will be necessary to provide timely information to clinicians as they determine whether combination therapy is warranted. Although these results suggest that many benefits of combination therapy are lost when microbes become tolerant, additional studies assessing clinical outcomes in patients with antimicrobial-tolerant infections will be necessary to guide clinical decision-making. In the meantime, when

choosing combination antibiotic therapies, perhaps ensuring adherence to a zero-tolerance policy is best. ■

REFERENCES AND NOTES

1. P. R. S. Lagacé-Wiens *et al.*, Canadian Antimicrobial Resistance Alliance (CARA) and CANWARD, *J. Antimicrob. Chemother.* **74** (suppl. 4), iv22 (2019).
2. CDC, www.cdc.gov/DrugResistance/Biggest-Threats.html (2019).
3. I. Levin-Reisman *et al.*, *Science* **355**, 826 (2017).
4. A. Brauner, O. Fridman, O. Gefen, N. Q. Balaban, *Nat. Rev. Microbiol.* **14**, 320 (2016).
5. W. E. Rose, A. D. Berti, J. B. Hatch, D. G. Maki, *Antimicrob. Agents Chemother.* **57**, 3450 (2013).
6. A. D. Berti *et al.*, *Antimicrob. Agents Chemother.* **56**, 5046 (2012).
7. J. Liu *et al.*, *Science* **367**, 200 (2020).
8. B. Van den Bergh, M. Fauvart, J. Michiels, *FEMS Microbiol. Rev.* **41**, 219 (2017).
9. H. S. Girgis, K. Harris, S. Tavazoe, *Proc. Natl. Acad. Sci. U.S.A.* **109**, 12740 (2012).
10. A. R. Coates, Y. Hu, *Trends Pharmacol. Sci.* **29**, 143 (2008).
11. G. E. Thwaites *et al.*, *Health Technol. Assess.* **22**, 1 (2018).
12. O. Gefen, B. Chekol, J. Strahilevitz, N. Q. Balaban, *Sci. Rep.* **7**, 41284 (2017).
13. A. Sakr, F. Brégeon, J.-M. Rolain, O. Blin, *Expert Rev. Anti Infect. Ther.* **17**, 327 (2019).
14. M. Singh *et al.*, *Antimicrob. Agents Chemother.* **61**, e01154 (2017).
15. N. S. Britt *et al.*, *J. Antimicrob. Chemother.* **72**, 535 (2017).

ACKNOWLEDGMENTS

We thank W. E. Rose (University of Wisconsin-Madison) for his critical review of this manuscript.

10.1126/science.aba0150

Improving cancer screening programs

Evaluating diagnostic tests in learning screening programs could improve public health

By **Mette Kalager** and **Michael Bretthauer**

National cancer screening programs, such as mammography for breast cancer, are widely implemented to reduce cancer incidence and mortality in high-income countries. Their introduction is also being considered in low- and middle-income countries. For many cancer types, the benefits and harms of different screening tests and the intervals at which they should be implemented are unknown. Thus, randomized comparison testing is warranted. However, this is not possible because most people in high-income countries have already undergone screening or have refused screening and are not comparable (1). There is an ethical, medical, economic, and societal imperative for continuous evaluation of cancer screening programs to ensure that their benefits outweigh any harms. This may be achievable if the screening programs can become the arena for clinical testing through the implementation of learning screening programs.

Every year, ~46 million individuals (126,000 people each day) are offered cancer screening worldwide (2). The most commonly used screening tests include the Pap smear for cervical cancer; fecal immunochemical test (FIT), fecal occult blood test (FOBT), colonoscopy, or sigmoidoscopy for colorectal cancer; prostate-specific antigen (PSA) testing for prostate cancer; mammography for breast cancer; and computed tomography (CT) for lung cancer. The effects of such screening tests on cancer incidence and mortality need to be balanced against their harms, such as possible medical complications of screening procedures and subsequent treatment, and psychological distress. Cancer screening targets whole populations rather than individual patients, and each cancer occurs rarely. Thus, many people undergo testing without benefit. Recently, it has also become evident that some screening tests, such as PSA, mammography, and lung CT, lead to increased cancer incidence rates as a result of overdiagnosis—that is, the detection of cancers

and cancer precursors that would not have progressed to symptoms or death in the absence of screening (3). Because overdiagnosed lesions cannot be distinguished from lesions that will progress, all patients are treated. Therefore, overdiagnosed patients only experience harms and do not gain any benefit from screening.

For many cancers, not only are the comparative benefits and harms of available screening tests unknown, there is also a lack of consensus regarding the appropriate choice of test interval and threshold for a positive diagnosis. Screening programs in different countries use different tests, intervals, and thresholds. For example, the UK National Health Service (NHS) offers a screening sigmoidoscopy at age 55 and FIT from age 60 in England, whereas in Scotland the NHS does not offer sigmoidoscopy and has a higher cutoff for FIT positivity than in England (4). No new prescription drug enters the market without rigorous testing in randomized controlled trials (RCTs); by contrast, many cancer screening tests and strategies have been introduced without such rigorous clinical trials. For the few tests that have been evaluated in RCTs, such as mammography and FOBT screening, the data are often outdated and there is controversy about whether the tests are beneficial in current screening programs. Because of the enormous improvements in treatment of many cancers, early detection through screening may not be as important to achieving improved cancer mortality rates today as it was 20 to 30 years ago when the screening trials were performed.

Future tests such as panels of genetic markers for prostate and breast cancer screening are expected to enter national screening programs soon (5). In the United States, a fecal DNA marker panel for colorectal cancer is recommended by some organizations on the basis of microsimulation modeling data (6) and not RCTs. When screening is widespread and everybody is exposed, traditional RCTs of screening tests outside of national screening programs are not possible because there is no control group for comparison.

A learning screening program continuously and systematically generates knowledge about what works—that is, which test is most effective to reduce mortality, has the optimal balance between benefits and

harms, and is most likely to be acceptable in the population. Individuals in national screening programs are asked to be randomized to receive either a new screening test, interval, or threshold, or the standard option. Testing thus involves randomized comparisons of thousands or even tens of thousands of participants with clinically relevant end points, such as cancer incidence or mortality. After the testing phase is over, it will be possible to make valid estimates of benefits and harms. For example, overdiagnosis can be measured in terms of the difference between numbers of cancers detected in individuals randomized to one screening test versus those randomized to another. Then, the best test or method will be introduced to all. When a new test or method becomes available, the cycle begins again. This continuous cycle of testing, treatment, and evaluation ensures that the public receives optimal cancer screening (see the figure).

Finland, Norway, and Poland have started to apply learning screening programs (7–9). The Finnish colorectal cancer screening program was designed as a randomized comparison of FOBT versus no screening, using the entire population of 60- to 69-year-olds in Finland (8). The program did not find a mortality benefit of screening versus no screening. FOBT screening was stopped, and half the Finnish population was prevented from undergoing an ineffective screening test. This year, Finland is starting the learning screening program cycle again to test FIT screening. The Norwegian cervical cancer screening program currently invites women with even-numbered dates of birth to be tested for human papilloma virus (HPV, a cause of cervical cancer) with Pap smears, whereas women born on odd-numbered dates receive the standard Pap smear. Women with negative tests in the two groups are offered new testing every 5 and 3 years, respectively, and compared for cancer incidence (9). The Polish colorectal cancer screening program has started to randomize individuals to immediate or delayed colonoscopy screening, or to no screening, and will assess cancer incidence and mortality (7).

Learning screening program activities that could be established immediately include assessment of colorectal cancer, cervical cancer, and breast cancer screening

Clinical Effectiveness Group, Institute of Health and Society, University of Oslo, Oslo, Norway, and Department of Transplantation Medicine, Oslo University Hospital, Oslo, Norway. Email: mette.kalager@medisin.uio.no

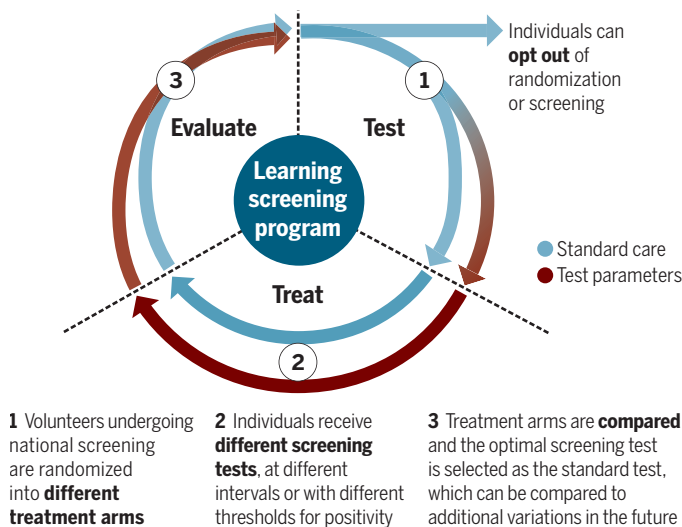
tests. The NHS colorectal cancer screening program in England offers FIT screening with a positivity threshold of 20 μg of hemoglobin per gram of feces (μg Hb/g) for further diagnostic assessment with colonoscopy, whereas NHS Scotland offers FIT screening with a positivity threshold of 80 μg Hb/g (4). It is unknown whether colorectal cancer incidence and mortality rates differ with these thresholds and whether cases of early colorectal cancer are being missed in Scotland (10). A learning screening program could randomize individuals to the two thresholds. After 10 years of follow-up, the data from the program will establish the optimum thresholds for reduction of colorectal cancer incidence and mortality, as well as for harms and burdens (e.g., number of false positives, burden of further testing by colonoscopy, and side effects from further testing such as colon perforations or hemorrhage), and could be established and implemented to all. Then, the program could continue and, for example, women could be randomized to colonoscopy versus FIT, because there is evidence from RCTs that women have less benefit from FIT and sigmoidoscopy screening to reduce colorectal cancer risk (11).

The cervical cancer screening program in Norway could be expanded to a true learning screening program (with continuous cycles of testing) by randomizing women with HPV-negative cytology to a 10-year screening interval in the next testing cycle. Furthermore, HPV-vaccinated women could be randomized to Pap smear screening perhaps every 10 years versus every 15 years, because it is unknown how frequently HPV-vaccinated women should be screened, if at all (12). In a learning screening program, it is possible to find out.

Although mammography screening resulted in reduced breast cancer mortality in RCTs carried out 30 years ago, recent improvements in therapy and care may have reduced this effect (13). The balance of benefits and harms of cancer screening is delicate and may shift with better quality of clinical service and improved cancer treatment and diagnostics (13). In a learning screening program, women could be randomized to mammography screening that is currently offered (every 1 to 3 years) or to screening, for example, every 5 years. If screening every 5 years is as effective in reducing mortality and also reduces overdiagnosis, then screening every

Learning screening programs

Patients enrolled in national screening programs agree to be randomized into testing arms that assess different tests, intervals, or thresholds to identify the optimal screening test that improves population mortality without overdiagnosing patients for additional treatment.



1 to 3 years could be phased out by randomizing women to screening every 5 years or to longer intervals, or even to no screening.

There are important challenges to consider for learning screening programs: All individuals in these programs must be informed about the randomized comparisons. Information needs to include descriptions of the uncertainty of current tests and strategies that are tested. Information needs to be easily accessible without overselling and promoting the new test. Eligible individuals should be given the opportunity to consent to testing and evaluation. Opt-out may be considered to facilitate the need for testing large numbers of individuals. The opportunity to consent also means that individuals who do not want to participate (that is, do not provide consent) need an alternative screening option, the standard screening test. The screening program will hence be similar to any RCT with a pre-randomization consent. Independent ethical oversight must also be provided, as occurs with clinical trials for therapeutics. Screening has been strongly advocated and many individuals overestimate the effect of screening. Hence, an independent review should focus on the individual's ability to give informed consent and may require evidence that the individuals are informed properly.

Randomized testing in learning screening programs requires the application of different trial methodologies depending on the settings and feasibility. For example, cluster-randomized trials may be applicable where individual randomization is deemed difficult to implement. Stepped-

wedge cluster-randomized trials, where new interventions are implemented in a randomized order between clusters, may facilitate the implementation of learning screening programs, because this design combines the desired implementation of new tests and strategies with the advantage of randomized comparison. Platform clinical trials that combine multiple new strategies with a joint standard-of-care group may also be considered.

Learning screening programs need new funding mechanisms because they are operating between public health and research. Ideally, funding should be through public health programs rather than research budgets. Randomization does not increase costs in already functioning, conventional screening

programs. Learning screening programs may also be applicable to other areas of public health and clinical practice such as diagnostic disease assessment; for example, radiology and endoscopy techniques could be compared for inflammatory bowel disease diagnosis.

The traditional divide between clinical trials and disease detection has become an obstacle to evidence-based screening programs. The establishment of learning screening programs may provide high-quality evidence for screening strategies with the most favorable benefit-to-harm ratio. ■

REFERENCES AND NOTES

1. R. J. Connor, P. C. Prorok, D. L. Weed, *J. Clin. Epidemiol.* **44**, 1215 (1991).
2. World Population Review, *Western Countries* 2019; <http://worldpopulationreview.com/countries/western-countries/>.
3. M. Bretthauer, M. Kalager, *Br. J. Surg.* **100**, 55 (2013).
4. U. K. Bowel Cancer, *Bowel Cancer Screening*; www.bowelcanceruk.org.uk/about-bowel-cancer/screening/.
5. J. D. Cohen et al., *Science* **359**, eaar3247 (2018).
6. U.S. Preventive Services Task Force, *JAMA* **315**, 2564 (2016).
7. M. F. Kaminski et al., *Endoscopy* **47**, 1144 (2015).
8. J. Pitkääniemi et al., *BMJ Open Gastroenterol.* **2**, e000034 (2015).
9. Cancer Registry of Norway, *HPV i primærskanning*; www.kreftregisteret.no/en/screening/Cervical-Cancer-Screening-Programme/Helsepersonell/screeningstrategi-og-nasjonale-retningslinjer/hpv-i-primarscreening/.
10. S. Moss et al., *Gut* **66**, 1631 (2017).
11. Ø. Holme et al., *BMJ* **356**, i6673 (2017).
12. P. G. Rossi et al., *Prev. Med.* **98**, 21 (2017).
13. H. G. Welch, P. C. Prorok, A. J. O'Malley, B. S. Kramer, *N. Engl. J. Med.* **375**, 1438 (2016).

ACKNOWLEDGMENTS

Supported by Norwegian Research Council grant 250256 and Norwegian Cancer Society grants 6741288 and 190345.

10.1126/science.aay3156

Counting on Majorana modes

Quantized conductance is a prerequisite of a topologically robust Majorana qubit

By Jay Sau

Systems with robust quantum states that are immune to external noise are essential to forming qubits, the basic unit of a large scalable quantum computer. A special type of superconductor in which quantum information is confined to the surfaces or the edges provides an accessible route to realizing robust qubits. These topological superconductors may host Majorana modes, which are related to Majorana fermions, which can be their own antiparticle. Direct evidence for Majorana modes does not yet exist, but several observations are consistent with their existence (1, 2). Majorana modes are also predicted to be characterized by an electrical conductance peak with a definite “quantized” value (3). On page 189 of this issue, Zhu *et al.* (4) used tunneling spectroscopy to find evidence for this quantized conductance in an iron tellurium selenide. Another recent study found similar behavior (5).

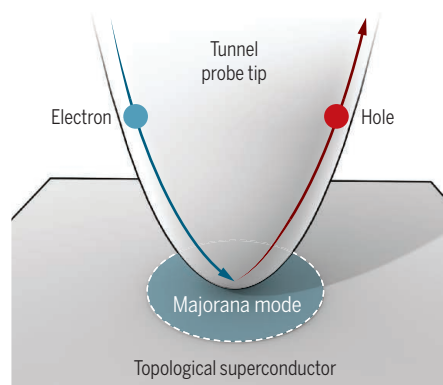
The realization of Majorana modes would demonstrate the existence of a solid-state analog of the excitations that were first imagined by Ettore Majorana in the context of the physics of fundamental particles (6). Majorana surmised the possibility that fermionic particles are their own antiparticles. This means that a pair of these particles could annihilate and dump their energy into light. Solid-state systems such as superconductors innately break symmetries like rotation. This removes constraints on Majorana modes and allows a pair of such excitations in certain superconductors to annihilate without leaving anything behind. Thus, the addition of two Majorana excitations returns the system back to the initial state without adding any energy. This forces the energy associated with a Majorana excitation to be zero. Thus, the single application of the Majorana changes the quantum state of the topological superconductor to a different state with exactly the same energy. The proposal for the qubit is a pair of quantum states at the same energy, which makes the qubits immune to dephasing errors.

The recent observations of quantized tun-

neling conductance into Majorana modes (1, 2, 4, 5) provide quantitative evidence for the existence of Majorana modes (see the figure). The particle-antiparticle symmetric nature of the mode envisioned by Majorana ensures that an incident electron at zero energy can only be reflected back as a hole, which is its antiparticle. This phenomenon, referred to as the “perfect Andreev reflection,” even in the presence of a strong obstruction to transport, is another way to characterize the topology of the superconducting state (7). Because the hole has the opposite charge as an electron, the reflection process transfers two electron charges from the tunnel probe to the superconductor. This results in the

A perfect match

A completely robust perfect Andreev reflection of an injected electron into an antiparticle (hole) from a Majorana mode is a signature characteristic of the Majorana being its own antiparticle.



observation of quantized conductance (3). Assuming that the temperature and the contact is under control, the only way to avoid perfect Andreev reflection from a Majorana mode would be to lose the electron in a spurious low-energy state on the superconductor. Such processes in which electrons are absorbed into or emitted from spurious bound states in a superconductor are called “quasiparticle poisoning.” Thus, the quantization of the measured conductance is an indicator of both the Majorana character of the excitation being probed and the isolation from other conventional electronic excitations.

Quasiparticle poisoning limits the quantization of conductance and the lifetime of

quantum information that can be stored in a Majorana mode. Although the topological nature of a Majorana-based qubit protects it from dephasing, it does not protect against qubit flip errors. The escape or entry of an electron from a conventional bound state in the superconductor into a Majorana mode can flip a qubit based on these modes. Ideally, such electrons should be removed by superconductivity unless they are siphoned off by quasiparticle poisoning. Quantized tunneling conductance measurements at 50 mK can, in principle, set an upper bound on the quasiparticle poisoning time of the order of a nanosecond or longer, and might allow for ns up the time-domain observation of the states of such a qubit. Thus, any Majorana mode promising for use as a qubit would need to show quantized tunneling conductance as a necessary, but not a sufficient, condition (8).

The recent observation of quantized conductance (1, 2, 4, 5) in at least two different platforms for Majorana modes is promising for the prospect of a topologically robust qubit. Platforms like the iron-based superconductor (4, 5, 9) and the semiconductor nanowire for which quantized conductance was also observed (1, 2, 10, 11) have different challenges and advantages. The semiconductor nanowire system offers a large parameter space and compatibility with device technology. However, this also makes it difficult to tune parameters of the nanowire systems that enter a topological superconducting phase with Majorana modes. The iron-based superconductors can be grown to have the topological superconducting phase but with less parameters to tune. The Majorana systems that show quantized conductance should be ready to demonstrate a Majorana qubit for which quantum information can be stored and read out. Beyond this, improving the quality of the device will hopefully push the lifetime of Majorana qubits past the sub-millisecond regime by taking advantage of the topological origin of the protection. This would make them competitive with existing quantum bits. Ultimately, the various mechanisms that limit a topological qubit fundamentally are expected to scale exponentially in their respective limiting parameters, such as finite size and temperature. ■

REFERENCES AND NOTES

1. H. Zhang *et al.*, *Nature* **556**, 74 (2018).
2. F. Nichele *et al.*, *Phys. Rev. Lett.* **119**, 136803 (2017).
3. K. T. Law *et al.*, *Phys. Rev. Lett.* **103**, 237001 (2009).
4. S. Zhu *et al.*, *Science* **367**, 189 (2020).
5. C. Chen *et al.*, *Chin. Phys. Lett.* **36**, 057403 (2019).
6. F. Wilczek, *Nature* **486**, 195 (2012).
7. M. Wimmer *et al.*, *New J. Phys.* **13**, 053016 (2011).
8. S. Das Sarma *et al.*, *Phys. Rev. B* **94**, 035143 (2016).
9. L. Fu, C. L. Kane, *Phys. Rev. Lett.* **100**, 096407 (2008).
10. R. M. Lutchyn, J. D. Sau, S. Das Sarma, *Phys. Rev. Lett.* **105**, 077001 (2010).
11. Y. Oreg, G. Refael, F. von Oppen, *Phys. Rev. Lett.* **105**, 177002 (2010).

10.1126/science.aaz9589

Condensed Matter Theory Center and Joint Quantum Institute, Department of Physics, University of Maryland, College Park, College Park, MD 20742, USA.
Email: jaysau@umd.edu

METABOLISM

A sugary input to leucine sensing

Glucose channels the amino acid leucine into synthetic versus degradative pathways

By Elyssa Lehman¹ and Robert T. Abraham²

Mammalian cell growth is tightly linked to adequate supplies of growth factors and nutrients, including glucose and amino acids. The mechanistic target of rapamycin complex 1 (mTORC1) functions as a coincidence detector that supports anabolic metabolism when convergent growth factor- and nutrient-derived signals trigger mTORC1 kinase activation. Conversely, nutrient starvation suppresses mTORC1 activity and triggers a shift to catabolic pathways, such as autophagy, to support cell survival under austere conditions. An elaborate signaling apparatus has evolved to harmonize mTORC1 kinase activation and protein synthesis with supplies of leucine and other amino acids (1). Earlier findings implicated the leucyl-transfer RNA (tRNA) synthetase 1 (LARS1) as a proximate sensor of leucine availability (2). On page 205 of this issue, Yoon *et al.* (3) report that glucose modulates the functions of LARS1 in leucine sensing and disposition, thereby coordinating leucine-dependent mTORC1 activation and protein synthesis with cellular energy stores.

Nutrient-derived signals are transmitted to mTORC1 by the Rag guanosine triphosphatases (GTPases), which reside on the cytoplasmic face of the lysosome, an organelle that functions in the degradation and recycling of cellular macromolecules. Four Rag isoforms, RagA to RagD, are expressed as obligate heterodimers of RagA or RagB bound to RagC or RagD. Like other small GTPases, the Rag proteins function as guanine nucleotide-regulated binary switches, with the “on” state conferred by the RagA/B-GTP-RagC/D-GDP configuration. The on-off status of each Rag subunit is governed by guanine nucleotide exchange factors (GEFs)

that load the Rag subunits with guanosine triphosphate (GTP) or by GTPase-activating proteins (GAPs) that promote the hydrolysis of the bound GTP to guanosine diphosphate (GDP) (4, 5). The activities of these Rag-GEFs and -GAPs are regulated in turn by amino acids, and the accumulation of RagA/B-GTP-RagC/D-GDP heterodimers on the lysosomal membrane triggers recruitment of mTORC1 and its juxtaposition to its direct activator RHEB (Ras homolog enriched in brain), another small GTPase that assumes the active, RHEB-GTP state in response to growth factor-derived signals (6).

the presence of leucine, Sestrin-2 is uncoupled from the RagB-GAP activity and favors the buildup of active RagA/B-GTP, which, when partnered with RagC/D-GDP, attracts mTORC1 to the lysosome for subsequent activation (7). The formation of active Rag heterodimers is an ordered process, with LARS1-dependent RagD activation preceding RagA/B-GTP formation, which is enabled by leucine-dependent Sestrin-2 inactivation (8). Collectively, these results suggest that parallel operation of the Sestrin-2- and LARS1-dependent pathways in leucine-replete cells provokes the formation of active RagA/B-GTP-RagC/D-GDP heterodimers and, in turn, mTORC1 activation, protein synthesis, and cell growth.

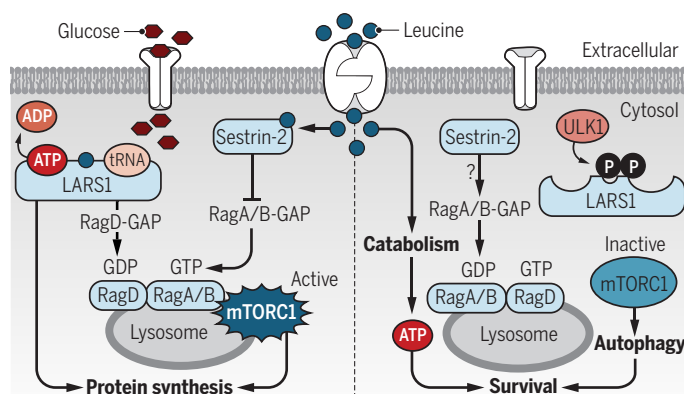
Protein synthesis is an energy-intensive process and, therefore, is not driven solely by amino acid availability. 5'-adenosine monophosphate-activated protein kinase (AMPK) is a pivotal coordinator of cellular metabolism based on the availability of bioenergy in the form of adenosine triphosphate (ATP). When ATP concentrations are limiting, AMPK is activated and suppresses energy-consuming processes, including mTORC1-stimulated protein synthesis. The inhibitory effects of AMPK on mTORC1 function occur primarily through the inhibition of RHEB-dependent mTORC1 activation and phosphorylation of the Raptor subunit of mTORC1 (5, 9, 10). The findings of Yoon *et al.*

indicate that the leucine-sensing function of LARS1 is influenced by the availability of glucose, the primary fuel for ATP production. They found that binding of LARS1 to RagD is gated by glucose availability. In the absence of glucose, cellular metabolism shifts toward energy preservation, leading to activation of Unc-51 like autophagy activating kinase 1 (ULK1), an apical activator of autophagy (11). Activated ULK1 phosphorylates LARS1 at two sites and thereby blocks binding of leucine and ATP. Decreased leucylation of LARS1 suppresses both mTORC1 signaling and protein synthesis, which pushes the cell into an energy-conserving mode.

In the absence of glucose, amino acids such as leucine can be catabolized to gener-

Regulating leucine metabolism

Leucine binds to Sestrin-2 and LARS1, thereby stimulating mTORC1 and protein synthesis, with energy supplied by glucose (left). During glucose starvation (right), ULK1 phosphorylates (P) LARS1, which promotes leucine catabolism and cell survival.



ADP, adenosine diphosphate; ATP, adenosine triphosphate; GAP, guanosine triphosphatase-activating protein; GDP, guanosine diphosphate; GTP, guanosine triphosphate; LARS1, leucyl-tRNA synthetase 1; mTORC1, mechanistic target of rapamycin complex 1; tRNA, transfer RNA; ULK1, Unc-51 like autophagy activating kinase 1.

In addition to its canonical role as a protein building block, the essential amino acid leucine is a central player in the amino acid-sensing limb of the mTORC1 pathway. Previously, LARS1 was identified as a leucine sensor and upstream regulator of mTORC1 (2). In leucine-replete conditions, LARS1 interacts directly with inactive RagD-GTP and functions as a RagD-GAP, converting this Rag subunit to the active RagD-GDP state (see the figure). The GAP activity of LARS1 is RagD-specific and does not target the highly homologous RagC-GTP isoform. Sestrin-2 was subsequently identified as a leucine-binding protein that negatively regulates mTORC1 in leucine-depleted cells by unleashing a downstream, RagA/B-GAP-selective activity (7). In

¹Oncology Research and Development Group, 401 North Middletown Road/PRL-200/4502D, Pfizer Worldwide Research and Development, Pearl River, NY 10965, USA.

²Oncology Research and Development Group, 10646 Science Center Drive/CB4, Pfizer Worldwide Research and Development, San Diego, CA 92121, USA.
Email: robert.abraham@pfizer.com

ate acetyl-coenzyme A, which supports the tricarboxylic acid (TCA) cycle and subsequent ATP production. Yoon *et al.* uncovered an additional function for ULK1-mediated LARS1 phosphorylation in the shuttling of leucine into a catabolic pathway. They found that glucose depletion led to increased leucine catabolism and entry of leucine-derived carbon into the TCA cycle. Although the mechanism was not clarified, these findings suggest that phosphorylation of LARS1 in glucose-starved cells converts this enzyme into an activator of leucine catabolism and allows the cell to consume leucine to maintain adequate ATP. Moreover, expression of a LARS1 phosphomimetic mutant partially protected cells from death during glucose starvation. Collectively, the results indicate that LARS1 functions as a glucose-dependent switch that shifts metabolism between growth-promoting and cellular maintenance pathways in accordance with the pool of bioenergetic precursors.

This report raises several key questions to be addressed in future studies. The mechanism underlying activation of ULK1 during glucose starvation requires further clarification. Yoon *et al.* present evidence suggesting that AMPK is primarily responsible for the stimulation of ULK1 activity and subsequent LARS1 phosphorylation, but additional experiments are needed to establish a temporal correlation between AMPK activation and LARS1 phosphorylation during glucose deprivation. The biological importance of the selective activation of RagD by LARS1, as well as the potential tissue selectivity of LARS1-dependent leucine degradation (for example, is it muscle specific?), requires further clarification. The tRNA synthetases are ATP- and amino acid-binding proteins and thus well poised to act as metabolic sensors and regulators, in addition to their core functions in translation. The findings of Yoon *et al.*, together with previous observations (2, 12), suggest that more moonlighting functions for the tRNA synthetases are on the horizon. ■

REFERENCES AND NOTES

1. K. J. Condon, D. M. Sabatini, *J. Cell Sci.* **132**, jcs222570 (2019).
2. J. M. Han *et al.*, *Cell* **149**, 410 (2012).
3. I. Yoon *et al.*, *Science* **367**, 205 (2020).
4. Y. Sancak *et al.*, *Science* **320**, 1496 (2008).
5. E. Kim *et al.*, *Nat. Cell Biol.* **10**, 935 (2008).
6. K. Inoki *et al.*, *Genes Dev.* **17**, 1829 (2003).
7. R. L. Wolfson *et al.*, *Science* **351**, 43 (2016).
8. M. Lee *et al.*, *Proc. Natl. Acad. Sci. U.S.A.* **115**, E5279 (2018).
9. K. Inoki, T. Zhu, K.-L. Guan, *Cell* **115**, 577 (2003).
10. D. M. Winnin *et al.*, *Mol. Cell* **30**, 214 (2008).
11. J. Kim *et al.*, *Nat. Cell Biol.* **13**, 132 (2011).
12. X. D. He *et al.*, *Cell Metab.* **27**, 151 (2018).

ACKNOWLEDGMENTS

The authors are employees and shareholders of Pfizer, Inc.

10.1126/science.aba2335

PALEOANTHROPOLOGY

A younger “earliest human migration” to Southeast Asia

New dating suggests that hominids arrived at the Sangiran dome later than had been thought

By Boris Brasseur

The fossiliferous Sangiran dome in Central Java contains the oldest human remains in Southeast Asia and is thus considered to be one of the most important sites in human paleoanthropology. Researchers have discovered more than 100 hominid remains from at least three different early to middle Pleistocene hominid species (1). Although numerous dating studies have been conducted at this site, the accepted date of earliest hominin migration is controversial. On page 210 of this issue, Matsu'ura *et al.* (2) describe their combined use of uranium/lead (U/Pb) dating (crystallization age) and fission-track dating (volcano eruption age) on zircons from three key strata in the hominid-bearing layers of Sangiran.

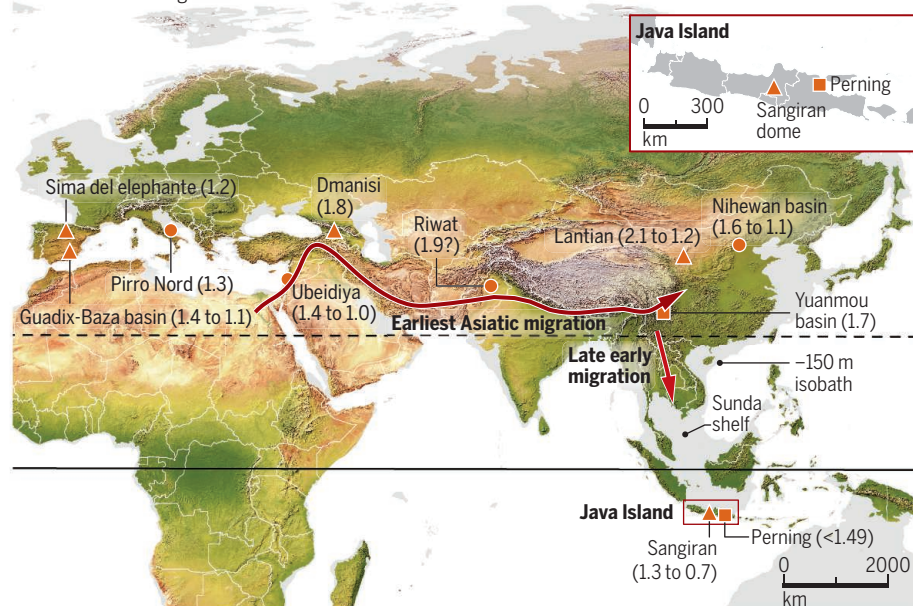
UMR7058 EDYSAN, Université de Picardie Jules Verne Pôle Santé, Amiens, France. Email: boris.brasseur@u-picardie.fr

The Sangiran dome is a recently (Upper Pleistocene) uplifted tectonic dome in a fossil-filled ~55-km² area with 250-m-thick Quaternary outcroppings. One of the world's first potassium/argon (K/Ar) datings of a hominid-bearing layer occurred on an Australasian tektite found at the site (3). However, 55 years and 36 absolute datings later, considerable uncertainty remains regarding the potential age of Sangiran's extensive and deep fossiliferous strata. This uncertainty makes it difficult for paleoanthropologists to connect Sangiran hominids to distant Asian sites and, therefore, to unveil the relative chronology of the earliest human migrations in Southeast Asia. This uncertainty can be explained by several factors: the stratigraphic and geographic dispersal of fossils over such a large territory, decontextualized discoveries by inhabitants, and dating discrepancies.

The first discoveries of artifacts and, later, of hominid fossils in the Sangiran dome were reported by von Koenigswald in the 1930s (4).

Some pieces of a complex puzzle

Shown are first hominin migrations (red arrows) outside of the African continent and Eurasian hominin sites older than 1 Ma [circle, site with artifact discoveries; square, site with hominin fossils; triangle, site with artifacts and fossils (ages in Ma)]. The map combines relief and vegetation-cover density (made with Natural Earth II). Inset shows an enlarged version of the Java island.



The hominid fossils found led to descriptions of two new species—*Meganthropus paleojavanicus* and *Pithecanthropus dubius*—alongside *Pongo* sp. and the archaic and classic groups of *Pithecanthropus* (*Homo*) *erectus*. This hominid taxonomic richness is still under study (1) and has spurred interdisciplinary work by Indonesian-German, -Japanese, -American, and -French teams. A lithostratigraphic framework (study of strata rocks facies) consolidated by biostratigraphic observations (assigning ages to rock strata using fossils) emerged in the second half of the 20th century. Hominid fossils have been attributed, with some incertitude, to the upper part of the Sangiran black-clay formation, the upper-lying boundary Grenzbank conglomeratic layers, and Bapang fluviovolcanic formation.

For 25 years, two chronological frameworks for this sedimentary sequence have been facing off. One presents a “younger” chronology for the hominid fossil layers [from between 1.3 and 1.1 million years (Ma) to between 0.7 and 0.6 Ma] and the other an “older” chronology (from between 1.7 and 1.6 Ma to 1 Ma). The “younger” framework is based on fission-track dating (zircons, amphiboles, and tektites) (5), K/Ar dating (amphiboles and tektites), and Ar/Ar dating (amphiboles) (6), along with paleomagnetism studies on fine-textured sediments, stratigraphic positions of Australasian tektite finds, and electron spin resonance dating of quartz. The “older” framework is based on Ar/Ar dating of pumice hornblende minerals (7, 8). Unfortunately, many publications dealing with early human migrations out of Africa have brushed this dating discrepancy problem under the carpet by referring to only one (mostly the “older”) of the two conflicting chronologies.

The new study by Matsu'ura *et al.* makes a seminal contribution to the “younger” chronological framework. The three pairs of new datings show a tuff (volcanic ash from eruption) below the hominid-bearing layers to be only 1.34 Ma of age, and the fossil-rich layers of the Grenzbank and lowermost Bapang formations to be <0.97 Ma and 0.88 Ma of age, respectively. The datings of the tuff and volcanoclastic layers in the new study are based on a combination of U/Pb and fission-track dating on multiple zircon grains. Until now, the oldest hominid-bearing layers at Sangiran have been included among the rare human-bearing sites outside Africa that have been dated earlier than 1.5 Ma.

Previously, deposits from the PERNING hominid site in East Java were dated to the competitor age of 1.6 Ma. However, these deposits have been rejuvenated to an uncertain age of <1.49 Ma (9). Therefore, a “younger” chronology for Sangiran hominids implies that humans migrated from Asia to Southeast Asia

and Java ~300,000 years later than previous estimates. This means that *H. erectus*'s arrival on Javanese sites took place a step later relative to the Dmanisi (Georgia) and Lantian or Nihewan basin sites (China) (see the figure).

In the Sangiran dome area, the oldest fully terrestrial layers constrain the first potential apparition of *H. erectus* fossils. These layers were characterized by in situ pedogenetic traces and terrestrial taxon stratigraphic positions. Such traces are found in the upper part of the Sangiran black-clay formation, with the underlying tuff dated, by Matsu'ura *et al.*, to 1.3 Ma. This date can be taken as a maximal age for local hominid discoveries; however, other sites in the wider regional sedimentary basin could bear older, fully terrestrial deposits, which should be studied.

In the middle of hominid-bearing strata, the Grenzbank layers, are fossil- and artifact-rich beds, now anchored at 0.9 Ma (1.6 to 1.5 Ma in the “older” chronology). Drastic worldwide changes, such as the sea level drop of 120 m induced by the first 100,000-year global glaciation cycles, began about 0.9 to 0.86 Ma. During this period, immigration via the Asian Sunda Shelf (see the figure) of new fauna and classic *H. erectus* populations must have strongly affected the preestablished hominid species.

Researchers have yet to discover who lived with (or replaced) whom in Sangiran. For example, the hominid-rich layers of the Grenzbank zone include fossils from at least three hominid species, who might or might not have lived in the same ecosystem, depending on diachronism of this boundary layer at the dome's scale. A challenge regarding local Sangiran hominids is to correlate sedimentary sequences of remote hominid findspots through tephrostratigraphy, which uses the geochemical characteristics of tuffs (such as volcanic glass) to realize chronostratigraphic correlations. Apart from the race to the oldest hominid site, defining the chronological relations among hominid species and artifacts is an exciting field of research. ■

REFERENCES AND NOTES

1. C. Zanolli *et al.*, *Nat. Ecol. Evol.* **3**, 755 (2019).
2. S. Matsu'ura *et al.*, *Science* **367**, 210 (2020).
3. G. H. R. von Koenigswald, *Report of the I.N.Q.U.A. Congress VI* (1964).
4. G. H. R. von Koenigswald, *Ingenieur Nederlandsch-Indië* **1**, 185 (1934).
5. N. Watanabe, D. Kadar, *Quaternary Geology of the Hominid Fossil Bearing Formations in Java* (Geological Research and Development Centre, Bandung, Indonesia, 1985).
6. H. Saleki, thesis, *Muséum National d'Histoire Naturelle, Institut de Paléontologie Humaine* (1997).
7. C. C. Swisher 3rd *et al.*, *Science* **263**, 1118 (1994).
8. R. Larick *et al.*, *Proc. Natl. Acad. Sci. U.S.A.* **98**, 4866 (2001).
9. M. J. Morwood *et al.*, *Aust. Archaeol.* **57**, 1 (2003).

ACKNOWLEDGMENTS

E. Gallet-Moron provided assistance on the figure.

10.1126/science.aba3800

QUANTUM CHEMISTRY

Flipping carbon monoxide on a salt surface

Advanced mid-infrared techniques identify orientational isomers

By Shiwei Wu

The adsorption of carbon monoxide (CO) molecules on solid surfaces is a classic model system in fundamental surface science. In most previous studies, this diatomic CO molecule adsorbs normal to the surface with the carbon atom pointing downward. This configuration is referred to as the “C-down” adsorption geometry. On page 175 of this issue, Lau *et al.* (1) report an unexpected upside-down isomer of CO molecules adsorbed on a NaCl(100) surface, referred to as the “O-down” adsorption geometry. The observation of an O-down orientational isomer, interconverting with the normal C-down isomer, reveals an isomerizing double-well quantum system in the condensed phase. The distinct interactions of the two orientational isomers with the NaCl(100) surface, repulsive for the O-down and attractive for the C-down at the Na⁺ adsorption sites, enrich the scenarios for CO molecule adsorptions. These results call for new and accurate theoretical studies of condensed-phase quantum isomerization.

In Lau *et al.*'s work, the O-down orientational isomer is produced by using infrared laser excitation to flip the normal C-down CO molecules on a NaCl(100) surface at 7 K. They found that the lifetime of the O-down isomer is short for a single CO monolayer on a NaCl(100) surface exposed to vacuum. This O-isomer only takes less than 100 s to convert back to the normal C-down isomer. However, when they covered the monolayer with more CO overlayers (~100 monolayers), the O-down isomers could be stabilized and last indefinitely. Upon thermal annealing at a higher temperature (22 K), the O-down isomer could be converted back to the normal C-down isomer.

State Key Laboratory of Surface Physics, Key Laboratory of Micro and Nano Photonic Structures (MOE), and Department of Physics, Fudan University, Shanghai 200433, China. Email: swwu@fudan.edu.cn

The beauty of Lau *et al.*'s work lies particularly in a newly developed apparatus that enabled high-resolution mid-infrared fluorescence spectroscopy to resolve clearly the quantum states of both isomers in a CO monolayer (see the figure). Upon pulsed mid-infrared excitation in resonance with the vibrational fundamental transition ($v = 0 \rightarrow v = 1$) of CO molecules, the CO monolayer was vibrationally excited. Through the dipole-dipole interaction among neighboring molecules, the CO molecules were populated to higher vibrational quantum states, v , up to $v = 30$ in the work. Following this rapid vibrational energy pooling process (2), the oscillating CO molecules acted like dipole antennas that were being damped by the electromagnetic interactions with the NaCl crystal. According to earlier work (3) by the same research group, the damping mechanism could be ascribed to Sommerfeld's theory (proposed in 1909) of radio transmission along Earth's surface via ground waves (4). During the damping process, the radiative dipolar emission between vibrational quantum states led to the observed mid-infrared optical spectra.

Because the two orientational isomers experience different electrostatic potentials upon adsorption, they exhibited distinct anharmonic vibrational progressions. Lau *et al.* closely examined the laser-induced fluorescence spectra and discovered two sets of vibrational progressions. Compared to the gas-phase CO molecule, one set is blue-shifted in energy, and the other is red-shifted. Based on a simple electrostatic model, they attributed the blue-shifted one to that of the C-down isomer, and the red-shifted to the O-down isomer. They also estimated the laser-induced conversion from the C-down to the O-down isomer to be about 46% of a monolayer. In addition, Lau *et al.* were able to observe the laser-induced flipping of CO molecules from the mid-infrared absorption spectra by stabilizing the O-down isomer in the buried CO monolayer.

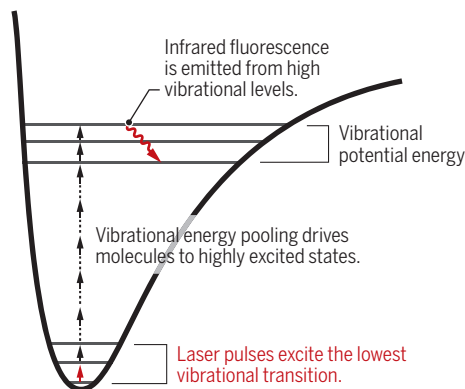
It is worth noting that the laser-induced mid-infrared fluorescence from CO overlayers on NaCl(100) was first reported by Chang and Ewing in 1990 (5). In that study, the vibrational progression of CO molecules

Up and down

Lau *et al.* used a high-resolution mid-infrared spectrometer to resolve the laser-induced fluorescence of the C-down and O-down orientational isomers in a CO monolayer on a NaCl(100) surface.

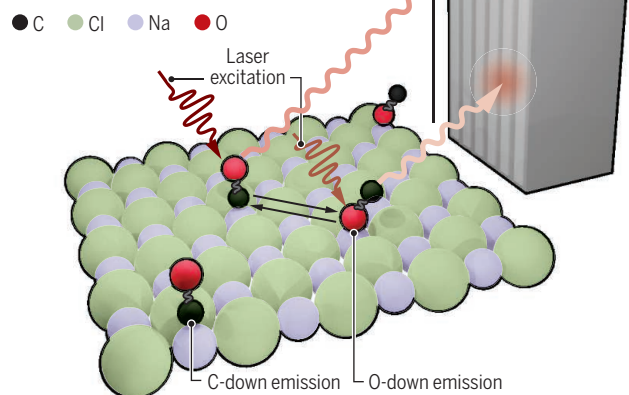
Infrared fluorescence

Excitation is driven from low vibrational levels, and emission occurs from high vibrational levels.



Sensitive detection

Excitation is driven from low vibrational levels, and emission occurs from high vibrational levels. A superconducting nanowire single-photon detector (SNSPD) is cooled to 0.3 K.



was resolved by using a liquid-nitrogen-cooled InSb photovoltaic detector. Lau *et al.* could achieve much better spectral resolution by using the latest technology based on an amorphous WSi superconducting nanowire single-photon detector (SNSPD). In comparison to the commercially available SNSPDs that work at $\sim 1.5 \mu\text{m}$, the WSi-based SNSPD operates in the mid-infrared range and is suitable for detecting vibrational fingerprints (6). The authors also managed to improve the mid-infrared signal-to-noise ratio compared to that obtained in their previous work (3). For example, the detection sensitivity was improved by using a larger ($25 \mu\text{m}$ by $100 \mu\text{m}$ versus $10 \mu\text{m}$ by $10 \mu\text{m}$) SNSPD to match the size of the light-guiding fiber. The monochromator was also cooled to a lower temperature (40 versus 77 K) to reduce the amount of blackbody radiation, the major source of background radiation. All of these instrumentation improvements have contributed

to the successful observation of infrared spectra in this study.

This observation of laser-induced isomerization in CO monolayers raises many interesting and fundamental questions. In terms of molecular mechanisms, it is not yet known how the normal C-down isomer converts to the O-down isomer, nor what the intermediate states are that form during the conversion. In addition to the vibrational energy pooling among molecules, the role of electronic excitation in the conversion needs to be explored. The state-selective lifetime of the O-down isomer can also be measured. All of these questions may be addressed by further exploiting the single-photon counting and ultrafast time response of the SNSPD.

Moreover, the role of the NaCl(100) substrate in stabilizing both orientational isomers is not clear, and it is still a question whether other substrates can host the O-down isomer. Defects or adsorbates on some surfaces may also stabilize the O-down isomer. To address these issues, other experimental techniques with high spatial resolution and spectral sensitivity, such as inelastic electron tunneling microscopy and spectroscopy (7), can be used.

The work by Lau *et al.* also provides a good example of how interdisciplinary collaboration fosters technological innovation and scientific advancement. The mid-infrared SNSPD based on an amorphous WSi superconducting nanowire is an emerging technology. Its application is by no means limited to infrared spectroscopy for molecular recognition in surface chemistry. Much wider applications to embrace this new technology, including single-photon detection for thermal imaging, infrared spectroscopy for quantum materials, and infrared telescopy for astrophysics, can be expected. ■

REFERENCES AND NOTES

1. J. A. Lau *et al.*, *Science* **367**, 175 (2020).
2. H.-C. Chang, G. E. Ewing, *Phys. Rev. Lett.* **65**, 2125 (1990).
3. L. Chen *et al.*, *Science* **363**, 158 (2019).
4. A. Sommerfeld, *Ann. Phys.* **28**, 665 (1909).
5. H.-C. Chang, G. E. Ewing, *J. Phys. Chem.* **94**, 7635 (1990).
6. L. Chen *et al.*, *Acc. Chem. Res.* **50**, 1400 (2017).
7. H. J. Lee, W. Ho, *Science* **286**, 1719 (1999).

10.1126/science.aba1100

POLICY FORUM

RESEARCH POLICY

Waiting for data: Barriers to executing data use agreements

Delays stem from institutional factors and negotiating challenges, some of which appear amenable to reform

By Michelle M. Mello^{1,2}, George Triantis¹,
Robyn Stanton², Erik Blumenkranz¹,
David M. Studdert^{1,2}

Many academic researchers who use preexisting data to conduct research describe a common experience: waiting for university officials to finalize and sign contracts necessary to transfer the data. These data use agreements (DUAs) detail the terms under which data will be disclosed, transferred, stored, and used, specifying rights and obligations for both the data supplier and the recipient (1). Faculty members often struggle to understand why DUAs for transfers of seemingly low-risk data take so long to conclude. To understand reasons for delays and explore what might be done to streamline the process, we interviewed a sample of university officials responsible for negotiating DUAs. This first empirical investigation of the DUA process found that procedural inefficiencies, incomplete information, data suppliers' lack of incentives and familiarity with academic practices, and faculty unresponsiveness may be more important contributors to delays than the lawyers being at loggerheads over their respective positions. Although researchers may view DUAs as another symptom that research has become "overlawyered," our study suggests that they may underappreciate the importance of these contracts and the complexity of negotiating them.

DUAs typically require institutional review, negotiation, and signoff because of the obligations and potential risks they impose on the university (including risks of civil liability, regulatory noncompliance, reputational damage, and compromised research principles). The review, usually conducted by attorneys or contract administrators within the university, may be intensive and prolonged. Agreements concerning data

transfers from private companies may be particularly difficult because companies may not share the university's norms concerning open science, freedom of publication, intellectual property (IP) ownership, and human-subjects protection.

Delays in executing DUAs may frustrate grant deadlines, trainees' needs, and researchers' ability to respond to current events with timely research. Combined with other regulatory requirements, these delays contribute to a climate in which those responsible for research oversight are perceived as obstructing the progress of science.

COMPLAINTS, BARRIERS, SOLUTIONS

Interviews were completed with 59 individuals representing 48 of the top-50 U.S. universities in terms of total research expenditures in 2015 [all 50 were approached; (2)] (see supplementary materials for further details on methods, data, and results). Interviews focused on contracts that governed transfers of data to university researchers from another U.S. entity and were not pure nondisclosure agreements, agreements for transfer of tangible materials, or clinical trial agreements. Two-thirds of the interviewees were based at public institutions. Nearly all respondents dealt with all types of data suppliers, or "counterparties" (academic, industry, government, nonprofit), but 9% did not negotiate industry contracts.

Complaints heard from faculty

Contract negotiators from 83% of institutions said that they had heard complaints from faculty about the DUA execution process. The gist of these complaints was that getting DUAs signed interposed an excessive and unnecessary delay in getting research started. Some faculty reportedly viewed DUAs as unnecessary, questioning why "good faith and the honor system" cannot suffice. Negotiators connected this view to a lack of understanding of why certain contractual provisions are problematic and how "the entire university community can be affected if something is not done properly," as well as faculty mem-

bers' misplaced confidence that the university can accept such terms because "nothing's going to go wrong." Negotiators reported that some faculty complained that the process involves "too much paperwork" for a "simple agreement" and wonder, "Why isn't there just one template for everything?" Some faculty reportedly lamented the "bureaucratic hot potato" involved in obtaining signoff from multiple university offices, which may include the institutional review board (IRB), privacy, information technology/security (IT), clinical trials, compliance, technology transfer, and sponsored research. Negotiators perceived that faculty had unrealistic expectations that reflected a lack of appreciation of the negotiators' workload (see table S2 in supplementary materials).

Process factors contributing to delay

Among nine process factors that may contribute to delays, contract negotiators identified their workload as the most common and serious problem (see fig. S1). Many negotiators commented that other types of contracts took priority over DUAs, and several observed that the volume of DUAs was increasing as organizations were becoming "more careful" about privacy. The next most common problem was delays on the part of faculty in responding to questions or requests, which was also characterized as difficult to overcome. Delays due to the need to comply with university policies (e.g., information security) were characterized as a serious or moderate problem when they did occur by about half the respondents, but reportedly occurred less frequently than delays due to faculty dilatory responsiveness. The problem typically arose from the time needed to consult the IT or privacy office or modify IT architecture. How responsibility for DUAs was allocated across university offices was another process factor with relatively low frequency but high seriousness. Faculty sometimes submitted requests to the wrong office, and it was often unclear which offices needed to be involved because faculty provided insufficient information. Lack of incentives on the part of the data supplier to reach agreement also did not frequently contribute to delays but was a serious problem when it did. This problem generally arose in negotiations with industry because companies did not view sharing their data with researchers as a "revenue-generating stream" or share the university's research mission.

Troublesome contractual provisions

Among seven specific DUA provisions, information privacy and security provisions (including, for example, prohibitions on reidentifying individuals and disclosing data to third parties and requirements for how data must be stored) stood out as

¹Stanford Law School, Stanford, CA 94305, USA.

²Center for Population Health Sciences, Stanford University School of Medicine, Stanford, CA 94305, USA.
Email: mmello@law.stanford.edu

both a frequently contested issue in negotiations and a serious problem in getting DUAs executed (see the figure). Negotiators described having to consult the privacy office to determine the classification of the data covered under the Health Insurance Portability and Accountability Act (HIPAA); consulting IT about whether the researcher's IT security satisfied the data supplier's terms; and where it did not, having to build a custom IT solution or renegotiate those terms. They perceived the security measures demanded by data suppliers to be excessive in many cases.

Recommendations for streamlining

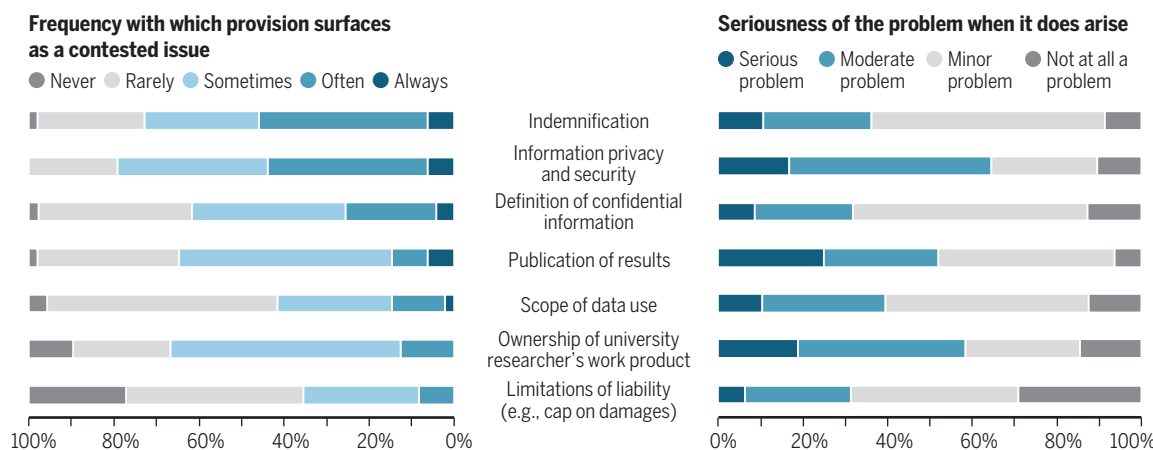
Negotiators offered several suggestions for improving the DUA execution process (see the box). Those who emphasized increasing staffing in the office with primary responsibility for DUA review reasoned that efficiency improvements alone will be inadequate, given the rapid growth in DUA volume. Among those who emphasized the value of a universal DUA template, a few mentioned that they use and like the template being pilot tested by the Federal Demonstration Partnership (FDP) with the goal of improving quality and consistency in the DUA process

need to strengthen communication with faculty at the initial intake phase. Well-designed, online submission portals could substantially reduce the amount of back-and-forth required to obtain missing information.

Even if universities can successfully mitigate these bureaucratic issues, another issue will continue to cause delays: the gap in incentives between the researchers who seek data and those from whom data are sought. Although academic researchers have strong reasons to pursue their work expeditiously, data suppliers often have weak incentives to share their data. University negotiators felt

Contractual provisions that contribute to delays

The seriousness question was not asked of respondents who answered that the provision was "Never" a problem. Denominator for proportions is the number of nonmissing responses.



Indemnification provisions, which require the university to pay liability costs incurred by the data supplier arising from the researcher's use of the data, also frequently arose as a negotiating issue but were somewhat easier to resolve. Public universities were constrained by state law in what they could accept. Some private universities acceded to the data supplier's demands; others engaged in protracted negotiations to obtain the narrowest possible language.

Negotiations over the definition of confidential information were fairly common but relatively easy to resolve; efforts focused on ensuring that it excluded research results. Negotiations over ownership of faculty members' work product were less common but relatively difficult to resolve. These disputes arose mostly with industry data suppliers and involved assertions of ownership rights over inventions and research results that were unacceptable because they conflicted with university policy. Similar issues arose with provisions restricting the researcher's right to publish.

(3, 4). FDP is a consortium of 90 research institutions and 10 federal agencies that collaborates to identify ways to improve the efficiency of research; initial efforts have focused on federal contracts.

OPTIONS FOR ACTION BY UNIVERSITIES

The contributors to delay that we identified fall into three broad categories: bureaucratic problems, incentives gaps, and lawyering issues. Although faculty complaints about delays often appear to conflate overlawyering with bureaucratic problems, the latter presents several distinct reform options.

First, given the increasing use of DUAs, staffing in the offices responsible for DUA negotiation has lagged behind the growth in demand for these services. Second, interoffice coordination problems contribute to inefficiency. Negotiators had little appetite for centralizing review in one office but perceived opportunities to coordinate better with others around the university, such as IT and the IRB; they recommended creating clear workflows from office to office and making faculty aware of them. Third, there was a strong felt

they were at the mercy of counterparties for whom completing the DUA, much less accepting compromises, was not a priority. This incentive gap sometimes slowed the negotiation process and forced universities to yield on substantive provisions.

The third set of issues relates to clashes between DUA negotiators over what is and is not acceptable in the contract. Negotiators reported that the most common and serious of these substantive issues related to provisions concerning information privacy and security, indemnification, and the definition of confidential information; provisions concerning publication rights and ownership of academic researchers' work product were less commonly in dispute but serious problems when they were. These are no mere matters of "legalese"; each implicates potentially important risks to the university and faculty member.

Some of these points of tension appear amenable to efficiency gains. For example, negotiations over privacy provisions may be streamlined by use of a robust intake system that elicits key information from faculty and negotiator "playbooks" that list essential, preferred, and acceptable contract wording and rationales. These measures can quickly determine whether particular actions (for example, designating the data as a Limited Data Set under HIPAA) are appropriate. In our sample, 85% of negotiators used playbooks or other written tools; 78% found them useful and 22% somewhat useful.

Indemnification is another actionable area. At least where low-risk data are involved, university contract negotiators may be spending more time on these provisions

than is warranted. If good privacy and security protections are in place, the risk of a data breach is low, and haggling over who pays in the unlikely event of a breach that causes harm should not obstruct timely data transfers for research. Yet, negotiators at 13 of 48 universities had walked away from a negotiation because of indemnification issues.

When it comes to provisions safeguarding publication rights and ownership of faculty members' work product, on the other hand, universities must remain resolute. These provisions implicate core values of the university and of open science. A potential strategy for minimizing haggling over non-negotiable issues is for universities as a group to more clearly signal their unified position. Existing university policies setting forth institutional commitments to academic freedom and policies concerning IP are helpful in communicating norms, but even more helpful would be a universal DUA template.

Onerous data security requests by suppliers pose a thornier challenge. A universal template could help in this area by educating counterparties about customary standards for transferring and storing data of different levels of sensitivity. Efforts by universities to centralize and standardize data protection infrastructure and procedures could also reduce DUA-by-DUA negotiation of data security arrangements.

For reasons outlined above, the ongoing FDP template project is a promising development. The first template, currently in the pilot phase, does not cover all types of data or relationships but does represent careful thinking about de-identified data (4). It consists of a basic agreement and several attachments that can be added for different types of data and situations. The initiative demonstrates the feasibility of crafting DUA language that is acceptable to a broad range of universities. Negotiators in our sample who were participating in the pilot felt that the template should be adopted by other institutions and likened it to the Uniform Biological Material Transfer Agreement (UBMTA), a successful initiative by the U.S. National Institutes of Health (NIH) to disseminate a template MTA (5–7). Other groups also have developed template agreements for data sharing that provide useful models (8, 9).

Agreeing on language concerning higher-risk data likely will be more difficult than crafting the initial FDP template, as will engaging private companies and nonfederal units of government. Moreover, the FDP is a content-focused intervention, and our findings show that clashes over DUA provisions are nested within an ar-

Recommendations

Contract Negotiators' Suggestions for Streamlining the DUA Execution Process

Improve the intake process (*n* = 16)

- Ensure that faculty provide better information on the nature of the data and research.
- Create an electronic submission system similar to those used for IRB and grant applications.
- Designate one office as the point of entry into the review process; route to others as needed.

Improve coordination across reviewing offices within the university (*n* = 12)

- Have IT office review information security provisions before DUAs are routed for general legal review.
- Create a "campus map" of all offices that must review a DUA and lay out "an end-to-end process."

Increase staffing in the office primarily responsible for DUA reviews (*n* = 11)

- Calibrate staffing to increasing volume of DUAs.
- Compare staffing and volume across university offices that review different types of contracts.
- Hire specialists in data privacy issues or more reviewers whose sole focus is DUAs.

Pursue a universal DUA template (*n* = 5)

- Move toward a common template that is broadly acceptable to both universities and counterparties.
- Include modules for different types of data.

Educate faculty about the complexity and importance of DUAs (*n* = 5).

- Elevate visibility of the issue, comparable to training on HIPAA and human subjects protection.
- Educate as to why DUA negotiation is not always straightforward.

ray of environmental and process factors, many of them internal to universities.

Our study has limitations. Our sample consisted of research-intensive U.S. universities. Universities in other countries may face different challenges owing to different privacy laws, and universities with less research may have lower demand for DUAs but also fewer resources. Our sam-

ple size was too small to permit subgroup analyses. Some interview responses may be subject to socially desirable response bias. Finally, in most cases we interviewed only one negotiator per university. Different information might have been obtained by interviewing additional negotiators or more senior officials.

DUAs protect researchers' publication and IP rights and minimize universities' risks of civil liability, fines, and reputational harm from data breaches and violations of state and federal law. There is value in crafting them carefully. Balanced against this imperative, however, is the need to ensure that they do not unduly delay research. Long waits for data are already a fact of life, and the problem will only grow with the inexorable increase in the volume and complexity of data exchanges. New data-sharing requirements for federal grantees will likely speed this increase as researchers are increasingly asked to transmit data to others (4, 10–12). To preserve key interests of universities while avoiding delays that test researchers' patience and impede scientific progress, reforms will need to address the full range of contributing factors.

REFERENCES AND NOTES

1. Federal Demonstration Partnership, "FDP data transfer and use agreement project glossary of terms" (2018); https://thefdp.org/default/assets/File/Documents/dtua_glossary.pdf.
2. National Science Foundation, "Higher Education Research and Development Survey" (2015); www.nsf.gov/statistics/srvyherd/.
3. Federal Demonstration Partnership, "Contracts" (2018); <https://thefdp.org/default/committees/research-administration/contracts/>.
4. Federal Demonstration Partnership, "FDP data transfer and use agreement (DTUA) template and pilot webinar" (2018); <https://thefdp.org/default/committees/research-compliance/data-stewardship/>.
5. T. Bubela, J. Guebert, A. Mishra, *PLOS Biol.* **13**, e1002060 (2015).
6. V. Rodriguez, *Nat. Biotechnol.* **23**, 489 (2005).
7. National Institutes of Health, *Fed. Regist.* **60**, 12771 (1995).
8. D. Mascalzoni *et al.*, *Eur. J. Hum. Genet.* **23**, 721 (2015).
9. B. M. Knoppers *et al.*, P3G International Steering Committee, *Nat. Biotechnol.* **31**, 384 (2013).
10. J. R. Polanin, M. Terzian, *J. Clin. Epidemiol.* **106**, 60 (2019).
11. K. Tucker *et al.*, *BMC Med. Res. Methodol.* **16** (S1), 77 (2016).
12. Institute of Medicine, *Sharing Clinical Trial Data: Maximizing Benefits, Minimizing Risk* (National Academies Press, Washington, DC, 2015).

ACKNOWLEDGMENTS

This work was supported by a grant from the Alfred P. Sloan Foundation (grant no. G-2016-7232). The sponsor had no role in the design or execution of the study or the interpretation of data. Data were managed using REDCap electronic data capture tools hosted at Stanford University School of Medicine and supported by Stanford Clinical and Translational Science award no. UL1 TR001085 from NIH–National Center for Research Resources.

SUPPLEMENTARY MATERIALS

science.sciencemag.org/content/367/6474/150/suppl/DC1

10.1126/science.aaz7028



PH2 b, rendered here, was discovered by the Planet Hunters citizen science project.

BOOKS *et al.*

RESEARCH METHODS

People-powered discovery

A physicist reveals how citizen science is reshaping research

By **Lea A. Shanley**

To understand how star formation varies in different galaxies, Chris Lintott and Kevin Schawinski needed to sort elliptical galaxies from spirals. But image recognition software can be costly to produce and needs training data to generate accurate results. The repository they had in mind—the Sloan Digital Sky Survey—included photometric observations of nearly one billion objects and spectra from more than four million objects. Inspired by Stardust@home, a 2006 project at the University of California–Berkeley that enlisted thousands of volunteers to search for interstellar dust particles in millions of images, the pair launched Galaxy Zoo in 2007.

During the first year, 150,000 volunteers contributed 50 million high-quality data classifications. With this training dataset in hand, the duo wrote an algorithm to identify star-forming blue ellipticals. The results were surprising: Other elliptical galaxies substantially exceeded the star formation rates of the Milky Way.

Galaxy Zoo's success led to the creation of Zooniverse, a more expansive platform—cofounded by Lintott, Lucy Fortson, Pamela Gay, Stuart Lynn, Arfon Smith, and others—that allows researchers to apply the same

approach to other scientific challenges. In *The Crowd and the Cosmos*, Lintott joins a growing cadre of authors focusing on the contributions of volunteers to the scientific enterprise (1–5), documenting the lessons learned from these projects, as well as trends in astronomy that opened the doors for new ways of doing science—from making data more open and remotely accessible to analyzing big data with machine learning. He also reflects with passion and curiosity on the detective work needed to explain the mysteries of the Universe.

Zooniverse and projects therein have enabled more than a million volunteers to contribute their skills remotely to scientific research—no specialized background or expertise required. The platform also features a community forum that allows citizen scientists' research questions to emerge. While participating in Galaxy Zoo, for example, Dutch schoolteacher Hanny van Arkel found a blue blob in galaxy IC 2497 and asked a simple question on the forum—what is it? The object, dubbed “Hanny's Voorwerp” (“Hanny's thingy”), turned out to be a rare quasar ionization echo.

Lintott uses Hanny's Voorwerp to highlight the problem of “inattentional bias,” which can occur when one is so intently looking for a specific object that one misses the unexpected. Professionals can be prone

to this bias, Lintott notes, whereas newer volunteers “are likely to be conscious of all sorts of things in the data, some interesting and novel and some not.”

Zooniverse expanded the perceived value of citizen science, shifting it from educational to a tool for making meaningful contributions to scientific research. More than 200 peer-reviewed publications have arisen from Zooniverse projects, 63 from Galaxy Zoo alone.

Citizen science projects have had to overcome a hierarchical view of science that originated in the Victorian era and persists today. This view assigns status and greater value to the contributions of those who direct or fund a scientific endeavor as compared with the contributions of those who do the work. Lintott pushes back: “Rather than...viewing...[the] Eminent Scientist as apart from the crowd—someone who assigns tasks and reserves only for themselves the right to analyze the results—it instinctively seems to me that it is impossible to draw a clear line between where the supposedly menial tasks of data gathering, classification, and exploration stop and some sort of Proper Science starts. It's all just science.”

Forty-two meta-studies explored the sociotechnical opportunities and challenges presented by Zooniverse, including the need to incorporate design thinking into projects; the need to understand computer-human interactions as well as what motivates volunteers to participate; the need to develop robust data quality assurance protocols; and the need to rethink who should be included as a publication author. By addressing these challenges, the Zooniverse helped to revolutionize the practice of citizen science.

Although convolutional neural networks can be trained to classify galaxies or to differentiate galaxies from stars, they still may overlook unusual and important objects. By paying close attention to each system individually, Lintott asserts, citizen science may help us discover something fundamentally new. ■



The Crowd and the Cosmos
Chris Lintott
Oxford University Press,
2020. 288 pp.

REFERENCES AND NOTES

1. M. Nielsen, *Reinventing Discovery* (Princeton Univ. Press, 2013).
2. C. Cooper, *Citizen Science* (Harry N. Abrams, 2016).
3. M. E. Hannibal, *Citizen Scientist* (The Experiment, 2016).
4. D. Cavalier, E. B. Kennedy, Eds., *The Rightful Place of Science* (Consortium for Science, Policy and Outcomes, 2016).
5. A. H. Kimura, A. Kinchy, *Science by the People* (Rutgers Univ. Press, 2019).

10.1126/science.aaz8636

The reviewer is at the Nelson Institute for Environmental Studies, University of Wisconsin–Madison, Madison, WI 53706, USA. Email: lshanley@wisc.edu

PHOTO: H. GIGUERE, M. GIGUERE/PLANET HUNTERS

MEDIA STUDIES

Fun and games and ecosystems

Video games—even those without explicit educational goals—can offer insights into ecology

By **Stephanie LeMenager**

When a designer decides to turn his billion-dollar video game into an exercise in sustainable downsizing in Richard Powers's novel *The Overstory*, another character asks, "How are limits and shortages and permadeath going to be fun?" People playing video games want to level up and accumulate, to monetize social status and trade it. Such hypercapitalist tendencies do not exactly encourage behaviors that will lead to the mitigation of climate change and other environmental crises.

But video games might not be enemies to planetary redemption. In *Playing Nature*, Alenda Chang, a media scholar and game designer, begins with the provocative claim that game worlds are kin to natural systems. She

Chang argues that video games can teach players the gist of key ecological concepts like scale, entropy, and collapse. "Gist" is important here; she doesn't claim that games always get the science right, just that they give players an abiding interest in, and feel for, complex processes and nonhuman viewpoints.

Games, she writes, are "evocative spaces" that can stimulate emotional intelligence and respectful curiosity about the world. Thatgamecompany's *Flower*, for example, creates a mood of reverence for plant life by placing the player in the role of a pollinating wind that travels among unopened buds. Might and Delight's *Shelter*, about a mother badger trying to protect her young, conveys some of the emotional experience associated with habitat loss. E-Line Media's *Never Alone*, which features an Arctic

Playing Nature: Ecology in Video Games

Alenda Y. Chang
University of Minnesota
Press, 2019. 320 pp.



around a "health mystery" and seeks to inform at-risk communities about asthma and air-pollution management while training individuals to help their communities.

Chang does not limit her study to games that have an explicit educational purpose. She considers the realistic locations of *Grand Theft Auto* and the blending of outdoor play with augmented reality in the mobile game *Pokémon Go* as evidence that the edges between natural and man-made places are porous. Her decision to treat all video games with seriousness implies that games of all stripes can foster knowledge and should be seen as important forms of art and cultural expression.

Chang ends *Playing Nature* with a discussion about how much video games cost the world in terms of energy and pollution. They cost a lot, it turns out, even if digital entertainment weighs much lighter in a typical household's carbon budget than heating and air conditioning.

As fellow media scholars, including Jennifer Gabrys, Toby Miller, and Nicole Starosielski, have similarly documented, here Chang dives into the material impacts of the internet, e-waste, and online data storage. She refers to the ongoing health crises at toxic digital waste dumps in places such as Guiyu, China, and Agbogbloshie, Ghana, and considers potential future harms, such as those that may accompany the placement of data centers—always in need of cooling—in the sensitive ecosystems of coastal waters. (This begs the question of why waste disposal almost never appears as a playable problem in video games, which tend to favor apocalypse scenarios over stories of structural innovation that leads to enhanced survival.)

In the end, *Playing Nature* asks more questions than it answers about what video games do to Earth and to us. But by daring to ask how video games might make the world lively and sound, Chang sparks a necessary conversation. ■



Players earn credits by documenting flora and fauna in Hello Games's 2016 game *No Man's Sky*.

calls them "mesocosms"—experiments that incorporate or replicate aspects of the natural world—and cites games such as *Colossal Cave Adventure*, which deftly maps portions of the Mammoth Cave of Kentucky, and *Firewatch*, which accurately replicates the Ute Mountain lookout tower and various U.S. National Forest sites, as examples of games at the intersection of play and real life.

fox and was cocreated with the Cook Inlet Iñupiaq, conveys a sense of indigenous knowledge systems in which humans consider nonhuman animals kin.

Games also teach. Chang touches on several games intended to contribute to environmental education. Ken Eklund's *World Without Oil*, for example, challenges players to vividly imagine and document how they might adapt to an oil shock, while *Air-Quest*, designed by University of California educators (including Chang), is framed

The reviewer is at the Department of English, University of Oregon, Eugene, OR 97403, USA. Email: slemen@uoregon.edu

10.1126/science.aaz7351



A volunteer cleans oil from rocks on a beach in northeastern Brazil.

Edited by Jennifer Sills

Retraction

After publication of the Report “Site-selective enzymatic C—H amidation for synthesis of diverse lactams” (1), efforts to reproduce the work showed that the enzymes do not catalyze the reactions with the activities and selectivities claimed. Careful examination of the first author’s lab notebook then revealed missing contemporaneous entries and raw data for key experiments. The authors are therefore retracting the paper.

Inha Cho, Zhi-Jun Jia, Frances H. Arnold*

Division of Chemistry and Chemical Engineering, California Institute of Technology, Pasadena, CA 91125, USA.

*Corresponding author.

Email: frances@chem.e.caltech.edu

REFERENCES AND NOTES

1. I. Cho, Z.-J. Jia, F. H. Arnold, *Science* **364**, 575 (2019).

10.1126/science.aba6100

Brazil oil spill response: Time for coordination

In his News In Depth story “Mystery oil spill threatens marine sanctuary in Brazil” (8 November 2019, p. 672), H. Escobar discusses a dense crude oil spill that arrived at Brazil’s northeastern tropical coast in late August 2019. Given its extent (more than 3000 km) (1) and the recorded impacts (2), this spill is considered the most severe environmental disaster ever recorded in tropical coastal regions. More than 40 marine protected areas and a unique set of poorly explored coastal ecosystems (3) that

include intertidal rocky shores, rhodolith beds, sandy beaches, mangroves, estuarine systems, seagrass beds, and coral reefs have been affected. Exacerbating the ecological, social, and economic impacts, Brazil’s government action has been inadequate.

The Brazilian federal government has shown poor coordination with the non-governmental organizations, military, civil society, states, and Brazilian municipalities to address the oil spill’s effects (4). The lack of coordination and proper transparent guidelines made a rapid response nearly impossible. The federal government disbanded the executive and support committees responsible for oil-spill accidents (Contingency Plan for Oil Pollution team) in early 2019 (4). The resulting lack of leadership delayed the governmental response to the oil spill (5). Moreover, the recent budget cuts to science (6, 7) and unraveling of environmental policies (8, 9) undermine the capacity of Brazilian institutions to understand and solve the impacts of this uncontrolled environmental disaster.

Shallow and deep oil extraction is a delicate matter. The inadequate response to this disaster highlights the importance of establishing science-based solutions to prevent extensive and long-term impacts of coastal and offshore oil extraction. Governments must execute a coordinated response so as not to aggravate the problems.

M. O. Soares^{1,2*}, C. E. P. Teixeira¹, L. E. A. Bezerra¹, S. Rossi^{2,3}, T. Tavares¹, R. M. Cavalcante¹

¹Instituto de Ciências do Mar (LABOMAR),

Universidade Federal do Ceará, Meireles,

Fortaleza, 60165-081, Brazil. ²Institut de

Ciència i Tecnologia Ambientals (ICTA),

Universitat Autònoma de Barcelona (UAB),

08193 Cerdanyola del Vallès, Barcelona, Spain.

³Dipartimento di Scienze e Tecnologie Biologiche

ed Ambientali, Università del Salento, 73100 Lecce, Italy.

*Corresponding author.

Email: marcelosoares@ufc.br

REFERENCES AND NOTES

1. The International Tanker Owners Pollution Federation, “Oil tanker spill statistics 2018” (ITOPF, 2018); www.itopf.org/knowledge-resources/data-statistics/statistics.
2. Instituto Brasileiro do Meio Ambiente e dos Recursos Naturais Renováveis, “Manchas de óleo/Litoral Brasileiro” (IBAMA, 2019); www.ibama.gov.br/manchasdeoleo/#fauna [in Portuguese].
3. Instituto Brasileiro do Meio Ambiente e dos Recursos Naturais Renováveis, “Manchas de óleo/Litoral Brasileiro” (IBAMA, 2019); www.ibama.gov.br/manchasdeoleo/#localidades [in Portuguese].
4. Government of Brazil, “Decreto no. 9.759 de 11 de abril de 2019: Extingue e estabelece diretrizes, regras e limitações para colegiados da administração pública federal” (2019); www.in.gov.br/materia/-/asset_publisher/Kujrw0TZC2Mb/content/id/71137350/dole-2019-04-11-decreto-n-9-759-de-11-de-abril-de-2019-71137335 [in Portuguese].
5. M. N. Jha, J. Levy, Y. Gao, *Sensors* **8**, 236 (2008).
6. C. Angelo, *Nature* **568**, 2 (2019).
7. C. Nobre, *Nature* **574**, 455 (2019).
8. D. Abessa, A. Famá, L. Buruaem, *Nat. Ecol. Evol.* **3**, 510 (2019).
9. M. T. C. Thomé and C. F. B. Haddad, *Science* **364**, 1144 (2019).

10.1126/science.aaz9993

Brazil oil spill response: Government inaction

In his News In Depth story “Mystery oil spill threatens marine sanctuary in Brazil” (8 November 2019, p. 672), H. Escobar describes the contamination of 2500 km of Brazil’s northeast coast caused by oil from an offshore oil spill, which is threatening marine biodiversity, livelihoods, and human health in one of the country’s most iconic and touristic places. The spill has already affected 15 marine protected areas (1) and had incalculable impacts on wildlife and

ecological services, which could last for decades (2, 3). Escobar also mentioned the Brazilian government's delayed action and disinformation campaign in response to the spill, but he does not sufficiently describe the government's malfeasance.

Brazil's federal government has been profoundly lax in the face of this environmental catastrophe. On 17 October 2019, the Federal Prosecution Service, responsible for ensuring social and individual rights in matters of public interest, denounced the government's inaction (4). The government responded that the Contingency Plan for Oil Pollution Incidents (5) had already been activated, with "necessary adaptations," but never clarified what those adaptations were (4). This Contingency Plan was improperly implemented: It should have contained a comprehensive set of guidelines to organize an integrated action plan that mitigated further contamination from the spill and alleviated its impacts (5).

While the government neglected its responsibilities, volunteers from civil society risked their lives to help remove more than 5000 tons of oiled residue from 980 areas (6), including beaches and mangroves, often without support or personal protective equipment (7). State and local governments have collaborated as best as they can, but they depend on federal agencies' direction and resources. The oil is no longer reaching the beaches (6), but environmental and human health monitoring will be necessary for several years (8).

In less than a year, Brazil has experienced multiple environmental tragedies, including a mudslide (9), uncontrolled fires in the Amazon (10), and now an oil spill. Despite these threats, the Bolsonaro government has dismantled environmental policy (10). Brazilian biodiversity is crucial for ecological services and climate regulation (11). Civil society, researchers, nongovernmental organizations, and international markets should pressure the Brazilian government to reverse its destructive environmental agenda.

H. D. Brum^{1*}, J. V. Campos-Silva^{2,3}, E. G. Oliveira⁴

¹Instituto de Desenvolvimento Sustentável e Meio Ambiente do Rio Grande do Norte (IDEMA)/FUNDEP, Natal, Rio Grande do Norte, Brazil.

²Programa de Pós-Graduação em Diversidade Biológica e Conservação nos Trópicos, Instituto de Ciências Biológicas e da Saúde, Universidade Federal de Alagoas, Maceió, Alagoas, Brazil.

³Faculty of Environmental Sciences and Natural Resource Management, Norwegian University of Life Sciences, Ås, Norway. ⁴Programa de Pós-Graduação em Ecologia, Instituto de Biociências, Universidade Federal do Rio Grande do Norte, Natal, Rio Grande do Norte, Brazil.

*Corresponding author. Email: hdbbrum@gmail.com

REFERENCES AND NOTES

- C. C. Maretti, "Óleo no litoral do Nordeste e do Brasil," *O Eco* (2019); www.oeco.org.br/colunas/claudio-maretti/oleo-no-litoral-do-nordeste-e-do-brasil/ [in Portuguese].
- P. F. Kingston, *Spill Sci. Tech. Bull.* **7**, 53 (2002).

- M. G. Barron, *Toxic. Path.* **40**, 315 (2012).
- Ministério Público Federal, Ação Civil Pública Cível 0805679-16.2019.4.05.8500 (2019); www.conjur.com.br/dl/justica-federal-manda-mpf-emendar.pdf [in Portuguese].
- Presidência da República, "Decreto no. 8.127 de 22 de outubro de 2013" (2013); www.planalto.gov.br/ccivil_03/_ato2011-2014/2013/decreto/d8127.htm [in Portuguese].
- Marinha do Brasil, "Nota à imprensa" (December 17 2019); https://www.marinha.mil.br/sites/default/files/nota_gaa_17dez_0.pdf [in Portuguese].
- D. Phillips, "Brazilians rally to clean beaches amid outrage at Bolsonaro's oil spill inaction" *The Guardian* (2019); www.theguardian.com/world/2019/oct/22/brazil-oil-spill-beaches-bolsonaro-volunteers.
- SEVS, "Intoxicações exógenas relacionadas à exposição ao petróleo no litoral de Pernambuco" (Informe 06/2019); https://12ad4c92-89c7-4218-9e11-0ee136fa4b92.filesusr.com/ugd/3293a8_c5ecdcbfcb41a4a0fb92ac3fa780e718d.pdf [in Portuguese].
- J. V. Campos-Silva, C. A. Peres, *Science* **363**, 1046 (2019).
- D. Abessa, A. Famá, L. Buruam, *Nat. Ecol. Evol.* **3**, 510 (2019).
- IPBES, "Summary for policymakers of the global assessment report on biodiversity and ecosystem services of the Intergovernmental Science-Policy Platform on Biodiversity and Ecosystem Services," S. Díaz et al., Eds. (IPBES Secretariat, Bonn, Germany, 2019).

10.1126/science.aba0369

Brazil oil spill response: Protect rhodolith beds

In his News In Depth story "Mystery oil spill threatens marine sanctuary in Brazil" (8 November 2019, p. 672), H. Escobar highlights important ecosystems that have been affected by the spill. However, he did not mention the Brazilian rhodolith beds—the most extensive, abundant, and diverse biogenic carbonate habitats in the South Atlantic (1). The oil spill severely threatens these ecosystems, which comprise a staggering 2×10^{11} tons of carbonatic bank (2), stretch from 5°N to 27°S along the Brazilian coast, and cover a seabed potential area of 229,000 km² (1).

Brazil's rhodolith beds are recognized as an oasis of diversity (3). Although they harbor species of great economic and ecological value, they remain unprotected. The oil pollution will likely cause major socio-environmental and economic losses, similar to those caused by the Deepwater Horizon incident in the Gulf of Mexico (4). The contamination will compromise the region's food security as well as biodiversity conservation and efficient management. Moreover, the ongoing oil spill could have global consequences given the potential biogeochemical role of rhodolith beds in the oceanic carbon balance (1, 5). Thus, this event must not be downplayed or concealed, as has been attempted in the case of Brazilian mining accidents (6) and Amazon deforestation and fires (7). We advocate urgent action to evaluate and mitigate the oil spill and to remediate and restore areas on the

oil slick route. Brazil must follow in the footsteps of Australia and Europe (8) and prioritize rhodolith bed conservation.

M. Nasri Sissini^{1,2}, F. Berchez³, J. Hall-Spencer⁴, N. Ghilardi-Lopes⁵, V. F. Carvalho^{1,2}, N. Schubert^{1,6}, G. Koerich^{1,2}, G. Diaz-Pulido⁷, J. Silva⁶, E. Serrão⁶, J. Assis⁶, R. Santos⁶, S. R. Floeter^{1,2}, L. Rörig¹, J. B. Barufi¹, A. F. Bernardino⁸, R. Francini-Filho⁹, A. Turra¹⁰, L. C. Hofmann¹¹, J. Aguirre¹², L. Le Gall¹³, V. Peña¹⁴, M. C. Nash¹⁵, S. Rossi^{16,17}, M. Soares¹⁷, G. Pereira-Filho¹⁸, F. Tâmega¹⁹, P. A. Horta^{1,2*}

¹Laboratório de Ficologia, Departamento de Botânica, Universidade Federal de Santa Catarina, 88040-970, Florianópolis, Santa Catarina, Brazil.

²Programa de Pós-Graduação em Ecologia, Universidade Federal de Santa Catarina, 88040-970, Florianópolis, Santa Catarina, Brazil. ³CienTec Park and Instituto de Biociências, Universidade de São Paulo, 05422-970, São Paulo, Brazil.

⁴Marine Biology and Ecology Research Centre, University of Plymouth, Plymouth PL4 8AA, UK.

⁵Center for Natural and Human Sciences, Federal University of ABC, 09210-170, Santo André, São Paulo, Brazil.

⁶Centre of Marine Sciences, University of Algarve, Campus Gambelas, 8005-139 Faro, Portugal.

⁷School of Environment and Science, and Australian Rivers Institute—Coasts & Estuaries, Griffith University, QLD 4111, Australia.

⁸Departamento de Oceanografia e Ecologia, Universidade Federal do Espírito Santo, 29075-910, Vitória, Espírito Santo, Brazil.

⁹Centro de Ciências Aplicadas e Educação, Universidade Federal da Paraíba, 58297-000, Rio Tinto, Paraíba, Brazil.

¹⁰Departamento de Oceanografia Biológica, Instituto Oceanográfico, Universidade de São Paulo, 05508-900, São Paulo, Brazil.

¹¹Alfred Wegener Institute Helmholtz Center for Polar and Marine Research, 27570 Bremerhaven, Germany.

¹²Departamento Estratigrafía y Paleontología, Universidad de Granada, 18001 Granada, Spain.

¹³Muséum National d'Histoire Naturelle—Institut de Systématique, Evolution, Biodiversité, 75231 Paris, Cedex 05, France.

¹⁴BioCost Research Group, Universidade da Coruña, 15071, Coruña, Spain.

¹⁵Research School of Earth Sciences, Australian National University, Canberra, ACT, Australia.

¹⁶Dipartimento di Scienze e Tecnologie Biologiche ed Ambientali, DiSTeBA, University of Salento, Lecce, Italy.

¹⁷Instituto de Ciências do Mar (Labomar), Universidade Federal do Ceará, 60165-081, Fortaleza, Ceará, Brazil.

¹⁸Departamento de Ciências do Mar, Universidade Federal de São Paulo, 11070-100, Santos, São Paulo, Brazil.

¹⁹Programa de Pós-Graduação em Oceanografia, Instituto de Oceanografia, Universidade Federal do Rio Grande, 96203-900, Rio Grande, Rio Grande do Sul, Brazil.

*Corresponding author. Email: paulo.horta@ufsc.br

REFERENCES AND NOTES

- V. F. Carvalho et al., *Mar. Environ. Res.*, 10.1016/j.marenvres.2019.104827 (2019).
- J. D. Milliman, C. A. B. Amaral, *Ann. Congr. Brasil Geo.* **28**, 335 (1974).
- G. M. Amado-Filho, *Ciencias Mar.* **36**, 371 (2012).
- R. Kerr, E. Kintisch, E. Stokstad, *Science* **328**, 674 (2010).
- N. Schubert et al., *Sci. Total Environ.* **676**, 455 (2019).
- H. Escobar, *Science* **350**, 1138 (2015).
- C. A. Nobre, *Nature* **574**, 455 (2019).
- J. J. Kantun et al., in *Rhodolith/Maerl Beds: A Global Perspective* (Springer International Publishing, Boca Raton, 2017), pp. 265–280.

COMPETING INTERESTS

R.S., E.S., and J.A. are funded by Foundation for Science and Technology. E.S. is also funded by a Pew Marine Fellowship. P.A.H. and M.S. are funded by Coordination for the Improvement of Higher Education Personnel. M.S. is also funded by Conselho Nacional de Desenvolvimento Científico e Tecnológico and Fundação Cearense de Apoio ao Desenvolvimento Científico e Tecnológico. N.S. is funded by the European Union's Horizon 2020 Research and Innovation Programme.

10.1126/science.aba2582

RESEARCH

IN SCIENCE JOURNALS

Edited by Michael Funk

NATURAL HAZARDS

Limiting sea-level rise sustainably

One of the most devastating effects of anthropogenic global warming will be sea-level rise. Sound climate policy depends on robust predictions of the degree of sea-level rise associated with various emission scenarios. However, over the course of centuries, sea level will respond to atmospheric radiative forcing quite differently than surface temperature, the main focus of current emissions limits.

Future sea-level rise will threaten coastal cities such as Venice, Italy, which experienced a series of severe tidal floods in November 2019.

Li *et al.* developed integrated assessment models that suggest that a more effective way forward involves formally establishing acceptable targets for sea-level rise. According to this work, climate policies designed specifically to limit sea-level rise may be more sustainable and less expensive than policies driven by temperature targets alone. —KVH
Sci. Adv. 10.1126/sciadv.aaw9490 (2019).

STEM CELL BIOLOGY

Niche relocated by muscle contraction

Regulation of adult stem cells by their microenvironment, or niche, is essential for tissue homeostasis and for regeneration after injury and during aging. Normal regression of hair follicles during the hair cycle poses a particular challenge for maintaining a functional proximity of stem cells to their niche, especially the specialized mesenchymal cells of the dermal papilla. Using mice as a model organism, Heitman *et al.* demonstrate that the follicle dermal sheath is an active

smooth muscle that drives tissue remodeling through coordinated cell contraction, enabling renewed contact between the dermal papilla and hair follicle stem cells during hair follicle regression. This biomechanical mechanism of niche relocation may be utilized in other stem cell niche systems. —BAP

Science, this issue p. 161

PALEOANTHROPOLOGY

Dating the arrival of the first hominins in Java

The World Heritage archaeological site at Sangiran on the island of Java in Indonesia

has major importance for the understanding of human arrival and evolution in Asia. However, the timing of the first appearance of *Homo erectus* at the site has been controversial. Using a combination of dating techniques for hominin-bearing sediments, Matsu'ura *et al.* resolved the arrival of *H. erectus* at ~1.3 million years ago (see the Perspective by Brasseur). This dating suggests that the earliest hominins in Sangiran are at least 200,000 years younger than has been thought and may represent an important step to the resolution of the controversy. —AMS

Science, this issue p. 210;
see also p. 147

QUANTUM SIMULATION

Spin and charge go their separate ways

Strongly interacting chains of fermions are predicted to exhibit two types of collective excitations: spinons, which carry only spin, and holons, which carry only charge. These excitations move at different velocities. Signatures of this so-called spin-charge separation have been observed in solid-state systems, but obtaining direct dynamical evidence is tricky. With this goal in mind, Vijayan *et al.* perturbed a chain of ultracold interacting fermions housed in a one-dimensional optical lattice by removing one

PHOTO: BLOOMBERG/GETTY IMAGES

of the atoms. This gave rise to two independent excitations, which the researchers identified as spinons and holons using a quantum gas microscope. —JS

Science, this issue p. 186

LIGHTNING

Gamma-ray flash from a lightning leader

Terrestrial gamma-ray flashes (TGFs) are millisecond pulses of gamma rays produced by thunderstorms. Neubert *et al.* observed a TGF from above, using instruments on the International Space Station. High-speed photometry in optical, ultraviolet, x-ray, and gamma-ray bands allowed them to determine the sequence of events that produced the TGF. Emission from an intracloud lightning leader was followed within a millisecond by the TGF. The subsequent lightning flash produced an electromagnetic pulse, which induced expanding waves of ultraviolet emission in the ionosphere above the thunderstorm, called an elve. The authors conclude that high electric fields produced within the lightning leader generated the TGF. —KTS

Science, this issue p. 183

ANTIBIOTIC RESISTANCE

Challenges of drug combinations

Combinations of antibiotics are used to treat intractable infections such as methicillin-resistant *Staphylococcus aureus*. Clinically, however, drugs tend to be used empirically, and results can be contradictory. Liu *et al.* translated observations made in vitro to patient samples to understand the role of antibiotic tolerance in promoting or suppressing resistance when drug combinations are used (see the Perspective by Berti and Hirsch). Although bacterial populations exposed to multiple antibiotics can develop

tolerance to multiple drugs, one drug in a combination may be able counter resistance to a partner drug and provide effective therapy. However, if tolerance has already emerged to one drug, the combination may end up promoting the transmission of resistance to a partner drug. —CA

Science, this issue p. 200;

see also p. 141

GPCR SIGNALING

An accessory protein skews signaling

Ghrelin is a peptide secreted by the stomach during fasting to promote food intake. The accessory protein MRAP2 interacts with the ghrelin receptor GHSR1a, a G protein-coupled receptor (GPCR), and is important for the appetite-stimulating effects of ghrelin. Rouault *et al.* found that MRAP2 promoted biased signaling downstream of ghrelin-mediated activation of GHSR1a by inhibiting β -arrestin recruitment to the receptor and potentiating $G_{\alpha_{11}}$ -dependent signaling. Accessory proteins, not just ligands, can thus bias GPCR signaling. —WW

Sci. Signal. **13**, eaax4569 (2020).

CATALYSIS

Confining peroxide to make methanol

In principle, hydrogen peroxide would be an efficient oxidant for the conversion of methane to methanol under mild conditions. In practice, however, it is currently too expensive to produce the peroxide ahead of time for this purpose. Jin *et al.* report a catalyst system that generates and concentrates hydrogen peroxide for immediate reaction with methane. A hydrophobically coated zeolite keeps the peroxide close to the gold and palladium active site, where incoming methane is then selectively oxidized to methanol. —JSY

Science, this issue p. 193

IN OTHER JOURNALS

Edited by **Caroline Ash**
and **Jesse Smith**



The aerial microbiota above Singapore show diurnal patterns of occurrence.

MICROBIOTA

Up in the clouds with the fungi

Airborne transport of microorganisms is assumed to occur over vast global scales, but we know little about it. Gusareva *et al.* undertook a year-long metagenomic study of atmospheric organisms above Singapore. Daily patterns were seen in more than 700 taxa, dominated by eukaryotes. At night, spores of basidiomycete fungi formed the greatest airborne biomass. Ascomycete fungal spores prevailed during daytime and correlated with rainfall. The richness of the bacterial groups Firmicutes and Proteobacteria peaked at noon, whereas Cyanobacteria and Actinobacteria abundances stayed uniform over 24 hours. The chief variable was the shift between temperatures at night (26°C) and day (35°C at noon), which presumably drives lift-off. —CA

Proc. Natl. Acad. Sci. U.S.A. **116**, 23299 (2019).

MOLECULAR BIOLOGY

Coincidence detection stalls ribosome

Translation of aberrant messenger RNAs that lack in-frame stop codons leads to malfunctioning proteins. To prevent this deleterious effect, cells have quality control processes to monitor translation into polyadenylated regions, including

ribosome stalling. Using a combination of biochemistry and structural biology approaches, Chandrasekaran *et al.* show how ribosomes stall selectively on polyadenylated regions. Polylysine peptide (the codon AAA is decoded as lysine) in the exit channel of a ribosome slows translation, whereas a stabilized polyadenylated RNA helix in a ribosome decoding

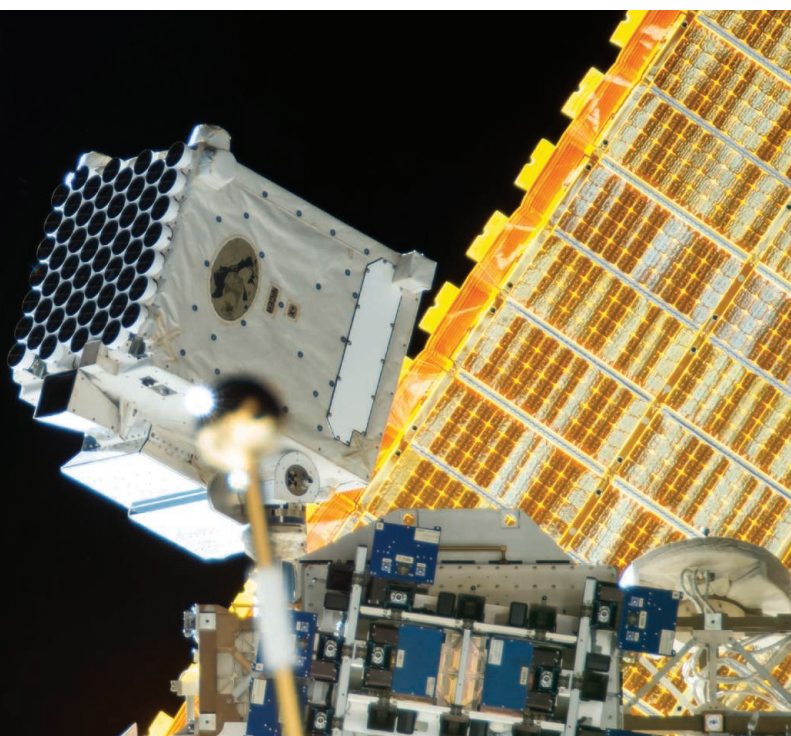
ASTROPHYSICS

Interior properties of a neutron star

Neutron star interiors are composed of exotic neutron-rich matter that cannot be produced in laboratories, and its properties are of interest to both astronomers and nuclear physicists. The Neutron Star Interior Composition Explorer (NICER) instrument performs precise timing of x-ray emission from fast-spinning neutron stars. Riley *et al.* and Miller *et al.* report independent blind analyses of the same NICER dataset for a single neutron star. The resulting models have some differences but lead to mass and radius measurements that are consistent within their uncertainties. Companion papers show how the NICER measurements constrain the properties of exotic neutron-rich matter. —KTS

Astrophys. J. Lett. **887**, L21, L24 (2019).

The NICER instrument mounted on the International Space Station



center blocks incoming transfer RNAs. Therefore, coincidence detection of both polylysine and polyadenylate allows polyadenylated regions, but not polylysine, within normal coding regions to halt translation. —SYM
Nat. Struct. Mol. Biol. **26**, 1132 (2019).

GENE EXPRESSION

Sensing amino acid starvation

Most Gram-positive bacteria have genetic switches that regulate the expression of genes involved in amino acid synthesis. These switches are sequences called T-boxes that occur before the coding sequence in the relevant messenger RNAs. They bind to specific transfer RNA (tRNA) and, if it is charged with amino acid, suppress expression of the messenger RNA. Three papers—by Li *et al.*, Battaglia *et al.*, and Suddala and Zhang, with an overview provided by Weaver and Serganov—describe the structures of different classes of T-boxes bound to tRNA. The structures show differences in anticodon recognition that

ensure specific binding. The papers differ in their interpretations of how expression is inhibited when the tRNA is charged with amino acid. —VV
Nat. Struct. Mol. Biol. **26**, 1094, 1106, 1114, 1081 (2019).

IMMUNOLOGY

Infection rewires liver metabolism

The liver serves as an important hub for metabolism and host-pathogen interactions. However, the link between these two functions is poorly understood. To study this link, Lercher *et al.* infected mice with chronic lymphocytic choriomeningitis virus (LCMV). Infection caused pronounced transcriptional changes to the liver's metabolic wiring, which in turn altered the host's systemic metabolism. These effects were driven by reprogramming of the hepatocyte urea cycle by type I interferon signaling. The resulting reduction in the ratio of arginine to ornithine in the circulation suppressed antiviral CD8⁺ T cell responses. Notably, treatment of mice with recombinant pegylated human arginase 1 (used to

inhibit hepatocellular carcinoma proliferation) lessened LCMV-induced hepatitis. Thus, the liver can control T cell-mediated tissue pathology by tweaking the metabolites it releases into the circulation. —STS
Immunity **51**, 1074 (2019).

BIOMATERIAL

A recruitment center for biorepair

Although it is possible to incorporate tissue-specific cells into a biomaterial for tissue repair, it requires cell isolation and expansion and a way to constrain the cells after implantation. An alternative option would be a biomaterial that harnesses and accelerates the body's own capabilities for repair. Adenosine is found throughout the body, but its concentration will temporarily and locally spike after a tissue injury because it acts as an extracellular signaling molecular to encourage repair. Because boronate molecules bond to and sequester adenosine, Zeng *et al.* developed a polymeric material that incorporates 3-(acrylamido) phenylboronic acid. When

implanted as a patch at the site of a bone injury, the polymer maintained an increased level of adenosine, thus promoting osteoblastogenesis and angiogenesis. —MSL
Adv. Mat. 10.1002/adma.201906022 (2019).

GENDER BIAS

A higher standard for women

Despite the absence of explicit gender bias among journal editors and reviewers, female economists were held to a higher standard in order to publish their work. Four leading economics journals shared data on nearly 30,000 manuscripts with Card *et al.*, who found that author gender did not influence key aspects of the evaluation process. However, when looking at future citations as a proxy for the quality of the research, female-authored papers received 25% more citations than similarly evaluated male-authored papers, suggesting that women needed to produce higher quality work than men in order for referees to recommend publication. —BW
Quart. J. Econ. **135**, 269 (2020).

PHOTO: NASA

METALLURGY**An anti-embrittlement roadmap**

Hydrogen is important for energy applications such as fuel cells but tends to diffuse into materials and make them more susceptible to fracture. Chen *et al.* tackled the challenge of identifying the exact location of hydrogen atoms in two common steels. The light weight and high mobility of hydrogen creates serious problems with conventional techniques. The authors used cryo-transfer atom probe tomography to show that hydrogen is pinned to various interfaces in the steels. This direct look into hydrogen trapping should help with the development of materials that are more resistant to hydrogen embrittlement. —BG

Science, this issue p. 171

QUANTUM CHEMISTRY**Upside-down molecules on a salt surface**

The quantum states of molecules are usually measured in gas-phase studies to minimize collisions that would blur the spectra. However, for carbon monoxide (CO) molecules adsorbed on a NaCl(100) surface, infrared emission from even high vibrational states can be resolved. In quantum-state resolved spectra, Lau *et al.* found that infrared-laser excitation of a monolayer of CO adsorbed on NaCl(100) forms an isomer in which CO binds to Na⁺ through its O atom in an upside-down configuration (see the Perspective by Wu). These results could be understood with a simple vibrationally adiabatic electrostatic theory, making this system convenient for studies of the isomerization chemistry. —YS

Science, this issue p. 175;
see also p. 148

CHEMICAL PHYSICS**The “hole” story of water ionization**

The direct observation of the cationic hole H₂O⁺ that is formed in liquid water after ionization has been a long-standing experimental challenge. Previous attempts using optical and ultraviolet techniques have failed to reveal its key spectroscopic signature during ultrafast transformation into a OH radical. Loh *et al.* address this gap by using intense, ultrafast x-ray pulses from an x-ray free electron laser at ~530 electron volts. They found compelling evidence for the formation H₂O⁺ and its decay to an OH radical by a proton transfer mechanism and elucidated the other fastest-time scale steps in the early-time dynamics of ionized liquid water. —YS

Science, this issue p. 179

TOPOLOGICAL MATTER**Reaching a conductance plateau**

The surface of the iron-based superconductor FeTe_{0.55}Se_{0.45} satisfies the necessary conditions to support topological superconductivity. Under the application of a magnetic field, vortices with zero-bias peaks that are consistent with Majorana bound states have been observed. Using scanning tunneling spectroscopy, Zhu *et al.* studied the conductance of these states as the tip-sample distance was reduced (see the Perspective by Sau). The researchers found that the value of the conductance increased and eventually saturated. For one of the vortices they studied, the conductance reached a quantized value that is characteristic of the Majorana bound states. —JS

Science, this issue p. 189;
see also p. 145

DEVELOPMENTAL BIOLOGY**Apoptosis prevents left-right crossing**

Animals generally display a bilateral body plan, with symmetry between the left and right sides. Maya-Ramos and Mikawa examined the mechanism that prevents the crossing of cells between sides. Using chick embryos, they show that cellular mixing between sides is prevented by a barrier at the embryonic midline that involves programmed cell death and the extracellular matrix. This work demonstrates the dependence of normal development on programmed cell death during the gastrulation stage. —BAP

Science, this issue p. 197

SIGNAL TRANSDUCTION**A tRNA synthase in metabolic control**

Leucyl-tRNA synthetase 1 (LARS1), which covalently couples leucine to its cognate transfer RNAs (tRNAs), appears to have broader roles in the control of leucine metabolism. The enzyme also serves as a leucine sensor for the mechanistic target of rapamycin complex 1 (mTORC1), which regulates protein synthesis, metabolism, autophagy, and cell growth. Yoon *et al.* show that in cells deprived of glucose, LARS1 is phosphorylated by Unc-51 like autophagy activating kinase 1 (see the Perspective by Lehman and Abraham). This phosphorylation decreases leucine binding to LARS1 and, in turn, should decrease translation, reduce activation of mTORC1, and perhaps free up leucine for use in the generation of adenosine triphosphate in glucose-starved cells. —LBR

Science, this issue p. 205;
see also p. 146

PANCREATITIS**Pancreatic stress management**

Pancreatitis results from the premature activation of digestive enzymes in the pancreas and can be life-threatening. Hernandez *et al.* found pancreatic fibroblast growth factor 21 (FGF21) deficiency in three mouse models and patient biopsies of acute and chronic pancreatitis. This deficiency resulted from the activation of the integrated stress response. Accordingly, both administration of FGF21 and pharmacologic stress-response inhibition restored FGF21 and alleviated symptoms in acute and chronic models of the disease. FGF21 treatment also prevented pancreatitis onset in a model of endoscopic retrograde cholangiopancreatography, a therapeutic procedure that carries pancreatitis risk. —CAC

Sci. Transl. Med. **12**, eaay5186 (2020).

CANCER**Improving cancer screening**

National cancer screening programs, such as mammography for breast cancer, are often variably implemented such that thresholds for positivity, frequency of testing, and the types of tests used are inconsistent. Cancer screening can result in overdiagnosis and other harms. How can the optimal strategy for cancer screening be found? In a Perspective, Kalager and Bretthauer discuss how the harms of cancer screening can be balanced against the benefits by comparing the variables of screening tests in national trials as part of public health programs. These learning screening programs could improve public health by basing screening programs on current clinical data. —GKA

Science, this issue p. 143

BIODIVERSITY

Finding new species

Thousands of species have been described, and, although most may agree that many thousand remain undiscovered, identifying new taxa of charismatic vertebrates, like birds, is rare. Rheindt *et al.* describe five new songbird species and five new subspecies found on a single small island near Sulawesi, Indonesia, over a single 6-week expedition (see the Perspective by Kennedy and Fjeldså). They targeted the area because of its geological history and complexity and the historical notes of other explorers. They argue that similar approaches in other regions could also lead to the discovery of new species. —SNV

Science, this issue p. 167;
see also p. 140

RESEARCH ARTICLE

STEM CELL BIOLOGY

Dermal sheath contraction powers stem cell niche relocation during hair cycle regression

Nicholas Heitman^{1,2,3}, Rachel Sennett^{1,2,3}, Ka-Wai Mok^{1,2}, Nivedita Saxena^{1,2,3}, Devika Srivastava^{1,2}, Pieter Martino^{1,2}, Laura Grisanti^{1,2}, Zichen Wang⁴, Avi Ma'ayan⁴, Panteleimon Rempoulas⁵, Michael Rendl^{1,2,6*}

Tissue homeostasis requires the balance of growth by cell production and regression through cell loss. In the hair cycle, during follicle regression, the niche traverses the skin through an unknown mechanism to reach the stem cell reservoir and trigger new growth. Here, we identify the dermal sheath that lines the follicle as the key driver of tissue regression and niche relocation through the smooth muscle contractile machinery that generates centripetal constriction force. We reveal that the calcium-calmodulin-myosin light chain kinase pathway controls sheath contraction. When this pathway is blocked, sheath contraction is inhibited, impeding follicle regression and niche relocation. Thus, our study identifies the dermal sheath as smooth muscle that drives follicle regression for reuniting niche and stem cells in order to regenerate tissue structure during homeostasis.

Multipotent progenitors produce new cells to replace those that have been lost by injury or by natural turnover and shedding in rapidly renewing tissues such as the bone marrow and hair follicle (1). However, progenitors have limited renewal capacity and must be replenished from the stem cell reservoir, which is coordinated with specialized niche cells (2–4). During hair growth, the specialized dermal papilla (DP) cluster at the base of follicle bulbs secretes niche signals to orchestrate matrix progenitor proliferation, migration, and differentiation (5, 6) (fig. S1A). To reboot the progenitor pool throughout life, repeated cycles of follicle regression (catagen), rest (telogen), and regrowth (anagen) (7) (fig. S1B) derive new cells from the stem cell reservoir located in the bulge and germ of the upper follicle (8–12). At the beginning of regression, matrix progenitors stop proliferating and terminally differentiate (fig. S1B). Throughout regression, then, nearly all outer root sheath (ORS) progenitors along the entire length of catagen follicles undergo

apoptotic pruning (13) (Fig. 1A and fig. S1B) that is driven by extrinsic signals (14, 15). Only the ORS progenitors located closely below the bulge stem cells survive and retain multipotency to give rise to a new bulge and germ (16, 17). This new stem cell reservoir then becomes reactivated by niche signals from the intact, surviving DP after it has relocated from the follicle base to the new bulge and germ in order to regenerate the follicle of the next growth cycle (18–20) (fig. S1B).

In relocating to the stem cell reservoir, the DP trails the regressing epithelial strand of dying ORS progenitors and travels more than 90% of the hair follicle length (fig. S2) toward the bulge and germ stem cell reservoir. Such drastic tissue remodeling poses a considerable challenge for stem cell regulation in establishing the required proximity to its niche for receiving activating signals. Indeed, detachment of the DP leads to stem cell dysfunction and hair loss (21, 22). Two hypotheses for DP movement have been proposed for many years (23): (i) an “apoptotic force” generated by dying cells in the shrinking follicle and (ii) a “contraction force” by follicle-encapsulating dermal sheath (DS) cells (Fig. 1A and fig. S1B) based on alpha smooth muscle actin (α SMA) expression identified nearly three decades ago (24).

Dermal sheath is essential for reuniting stem cells and niche

We set out to address whether the DS is important for niche relocation during follicle regression. We first established DS-specific targeting using cartilage proteoglycan *Aggrecan* (*Acan*) as a genetic driver. ACAN protein is found in skin only in the follicle basement

membrane that separates the DS from epithelium (25) (Fig. 1B). Using *Acan*^{CreER} mice crossed with the *R26*^{LSL-tdTomato} reporter (*Acan*^{tdT}) enabled inducible targeting during catagen regression, restricted within skin to the DS (fig. S3). To test its functional role, we selectively ablated the DS at early catagen using inducible diphtheria toxin driver *R26*^{LSL-DTA} (*Acan*^{DTA}) (Fig. 1C). In follicles with effective ablation, only DS cell remnants were left at the beginning of regression (Fig. 1D). By subsequent telogen rest, follicles in control skin were fully regressed (Fig. 1E) and follicles with inefficient DS ablation equally regressed (fig. S4), but many follicles with fully ablated DS (fig. S4) remained aberrantly long (Fig. 1, E and F), suggesting a threshold requirement of minimal remaining DS for regression. In stalled follicles, hair shafts extended down to the follicle base and DPs remained deep in the dermis (Fig. 1G). Stalled follicle lengths ranged from partially regressed to completely stalled deep within the dermis (Fig. 1H). This indicates that the DS is required for progression of follicle regression during catagen and for niche relocation to the stem cell reservoir in the upper follicle.

We next analyzed the stalled follicle phenotype more closely with lineage-specific markers (figs. S1A and S5A) to determine the degree of catagen dysfunction in nonregressing hair follicles lacking DS. Immunofluorescence confirmed the absence of the DS and widespread ORS cells around shafts of stalled follicles (Fig. 1I). Rounded DP cell clusters at the bulb end were no longer engulfed by proliferative matrix progenitors (Fig. 1I). Likewise, hair shaft and inner root sheath precursors were also absent (fig. S5B), because differentiation during anagen growth (fig. S5A) had ended and catagen regression was initiated. Apoptosis was also undetectable in DS-ablated follicles (Fig. 1I), suggesting that catagen did not proceed beyond the early steps and that normal catagen cell death (fig. S5C) was absent. Between hair shafts and ORS was a single differentiated layer (Fig. 1I), reminiscent of the companion layer in growing hair follicles (fig. S5A) and of inner bulge cells at telogen (fig. S5D). Together, the phenotypic analyses indicated that long, nonregressed follicles were not caused by continued matrix progenitor proliferation or erroneous differentiation but resulted from a failure of hair shaft and DP movement toward the skin surface and concomitant absence of ORS progenitor apoptosis. Thus, the DS may exert a physical force fundamental for the upward travel of hair shaft and DP niche.

Dermal sheath expresses the molecular machinery of smooth muscles

To explore if the DS expresses the contractile molecular machinery of smooth muscles that could execute follicle regression and niche

¹Black Family Stem Cell Institute, Icahn School of Medicine at Mount Sinai, New York, NY, USA. ²Department of Cell, Developmental and Regenerative Biology, Icahn School of Medicine at Mount Sinai, New York, NY, USA.

³Graduate School of Biomedical Sciences, Icahn School of Medicine at Mount Sinai, New York, NY, USA. ⁴Department of Pharmacological Sciences, Mount Sinai Center for Bioinformatics, BD2K-LINCS Data Coordination and Integration Center, Knowledge Management Center for Illuminating the Druggable Genome (KMC-IDG), Icahn School of Medicine at Mount Sinai, New York, NY, USA.

⁵Department of Dermatology, Institute for Regenerative Medicine, University of Pennsylvania Perelman School of Medicine, Philadelphia, PA, USA. ⁶Department of Dermatology, Icahn School of Medicine at Mount Sinai, New York, NY, USA.

*Corresponding author. Email: michael.rendl@mssm.edu

relocation, we isolated DS cells for transcriptome analysis, in comparison to DP and dermal fibroblasts (DFs). We flow-sorted DS, DP, and DF populations from cells that were isolated from digested back skins of *Sox2^{GFP}*; *Lefty-RFP* reporter mice (6, 26) and were also stained for mesenchymal receptor platelet-derived growth factor receptor A (PDGFRA) (Fig. 2, A and B, and fig. S6, A and B). DS cells expressed *Sox2^{GFP}* and PDGFRA, but not red fluorescent protein (RFP), and could be cleanly distinguished from DP and DFs (27) (Fig. 2, A and B). Verification of known marker expression for DS, DP, and DFs demonstrated their identity and purity (fig. S6C). Analyzing the RNA sequencing-generated transcriptomes of DS, DP, and DFs and of ORS, matrix, and melanocytes (27) by hierarchical clustering and principal components established their close lineage relationship (fig. S7, A and B). Comparative analysis of gene expression then revealed a DS molecular signature of 483 enriched genes reflecting their specialized functions (Fig. 2C, fig. S7C, and table S1). Gene ontology analysis of the DS signature expectedly yielded extracellular matrix organization categories (Fig. 2D), because the DS is closely associated with the basement membrane that separates the mesenchyme from follicle epithelium. The DS signature was also enriched for genes involved in “muscle filament sliding” and “smooth muscle contraction” (Fig. 2D). Gene set enrichment analysis for “regulation and process of smooth muscle contraction” (table S2) showed significant enrichment in the DS (Fig. 2E), suggesting smooth muscle identity and function.

Several core components of the Ca^{2+} -dependent smooth muscle contraction pathway (Fig. 2F) were highly enriched in the DS, including *Calml* (calmodulin, CaM), *Mylk* (myosin light chain kinase, MLCK), *Myh11* (myosin heavy chain 11, MYH11), *Myh9* (myosin light chain 9, MYL9), and *Acta2* (α SMA) (Fig. 2G). Several pan-smooth muscle genes (28), such as *Cald1* (caldesmon 1), *Smtn* (smoothelin), and *Tagln* (transgelin, SM22), were also part of the DS signature (Fig. 2G and fig. S7, D and E). Among these, *Cald1* and *Smtn* are not expressed in contractile myofibroblasts (29), indicating that the DS expresses genes of bona fide smooth muscles. During smooth muscle contraction, mechanical forces are generated through actomyosin cross-bridges and adenosine triphosphate (ATP)-powered myosin ratcheting action (30) (Fig. 2F). Three-dimensional (3D) immunofluorescence revealed that the DS forms a network of α SMA stress fibers that wrap the follicle in concentric rings (Fig. 2H), suggesting that the potential actomyosin forces would be directed toward the center of the longitudinal axis in centripetal fashion. Actomyosin cross-bridge formation is pro-

moted when CaM-activated MLCK phosphorylates regulatory myosin light chains (e.g., MYL9; Fig. 2, F, G, and I) that associate with myosin heavy chain molecular motors (e.g., MYH10; Fig. 2, F, G, and I). Expression of

phosphorylated MYL9 (pMYL9) confirms the active state of myosin in the entire length of DS (Fig. 2I), which we observed throughout catagen (fig. S8), and supports DS functional contractile activity. Finally, several smooth

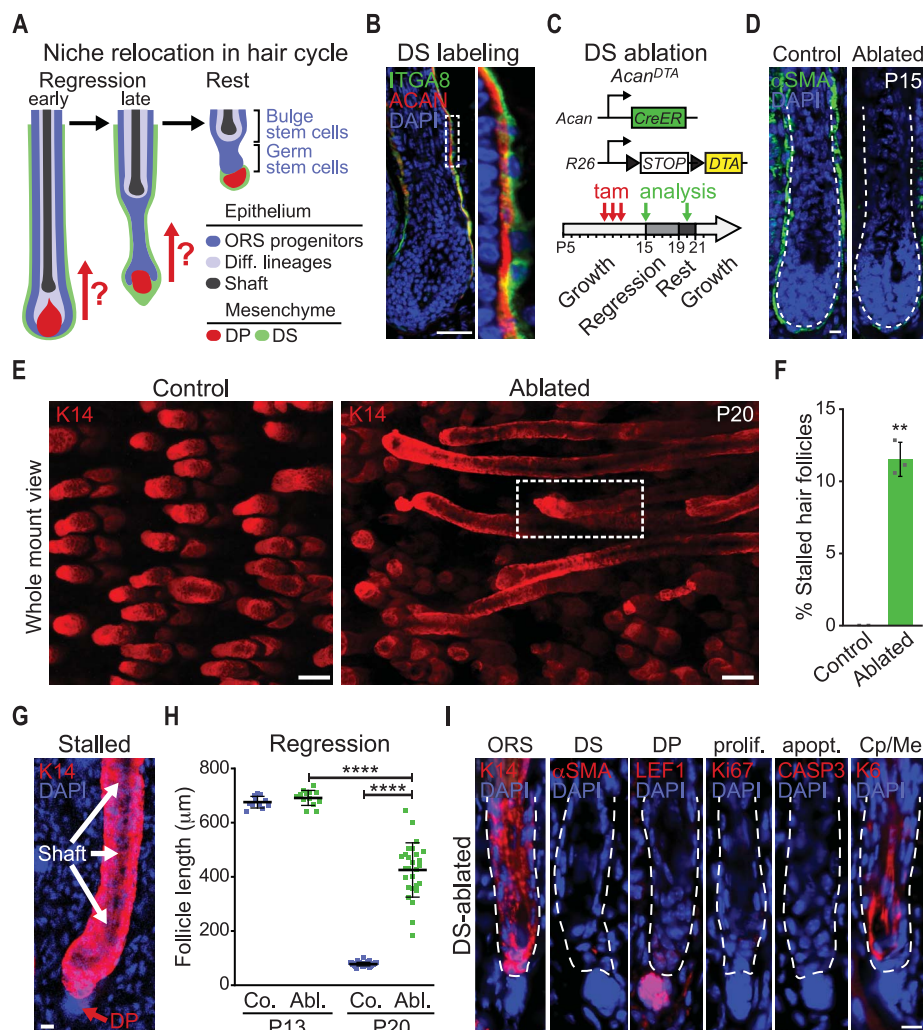


Fig. 1. The dermal sheath is required for hair follicle regression. (A) Schematic of catagen regression during the hair cycle. Hair shaft, inner root sheath, and matrix progenitors are eliminated by terminal differentiation and extrusion from the skin. The majority of ORS progenitors (blue) are eliminated by apoptosis. It is unknown how the surviving DP niche relocates to the bulge and germ stem cell reservoir to activate new hair growth after a period of rest. (B) Immunofluorescence (IF) for ACAN, secreted by ITGA8⁺ DS cells. The right image is a magnification of the region enclosed by the white dashed line in the left image. DAPI, 4',6-diamidino-2-phenylindole. (C) Schematic of cytotoxic DS ablation during regression. tam, tamoxifen; P, postnatal day. (D) IF for α SMA in control (*R26^{LSL-DTA}*) and DS-ablated (*Acan^{CreER}; R26^{LSL-DTA}*) back skin. The white dashed lines indicate the location of the basement membrane between ORS and DS. (E) Whole-mount IF for ORS marker K14 in P20 back skins (viewed from the dermis side, anterior is to the left). Control follicles are in telogen resting phase. Note the elongated follicles after DS ablation that are stalled in the regression phase. The white dashed box indicates the region shown in (G). (F) Quantification of the percentage of stalled follicles at P20 ($n = 698$ follicles in control and 895 follicles in DS-ablated skin in five mice). $^{**}P = 0.003$, by unpaired two-tailed Student's *t* test. (G) Magnification of the region enclosed by the white dashed line in (D) also stained with DAPI showing that the hair shaft and DP remain at the bulb tip of stalled follicles. (H) Quantification of follicle lengths [$n = 11$ for P13 control (Co.), $n = 14$ for P13 ablated (Abl.), $n = 80$ for P20 control, and $n = 27$ for P20 stalled; 11 mice]. $^{****}P < 10^{-4}$, by unpaired two-tailed Student's *t* test. (I) Stalled follicles have no DS (α SMA⁻) but retain intact DP (LEF1⁺). K14⁺ ORS progenitor and K6⁺ companion (Cp) and medulla (Me) layers are present and lack apoptosis (activated CASP3) or proliferation (Ki67) markers. The white dashed lines indicate the location of the basement membrane. Scale bars are 50 μ m [(B) and (E)] and 10 μ m [(D) and (I)].

muscle proteins were expressed in human scalp hair follicles, suggesting conservation of smooth muscle components in the DS between mice and humans (fig. S9). Overall, these results demonstrate that the DS harbors the contractile apparatus and its regulatory elements, long hypothesized by the presence of α SMA (24).

Dermal sheath contraction is required for follicle regression

We next explored whether DS cells can functionally contract in a smooth muscle-like fashion through Ca^{2+} -dependent MLCK activation. Isolated, short-term cultured DS cells were membrane depolarized by an extracellular K^+ spike to activate voltage-gated Ca^{2+} channels in the presence of Fluo8 fluorescent Ca^{2+} indicator (fig. S10A). The switch from Na^+ to high- K^+ media led to effective Ca^{2+} influx within 1.5 min. Tracing the cell surface area of *Acan^{tdT}*-marked DS cells cultured on a soft substrate demonstrated functional contraction in high- K^+ conditions in vitro (fig. S10B).

Next, we tested whether the DS can functionally contract and compress microdissected intact hair follicles (Fig. 3A). Live imaging of freshly isolated follicles showed significant reduction of follicle widths after 3 min in high K^+ , consistent with contraction of concentric α SMA-myosin rings (Fig. 3, B and D, and movie S1), which was effectively blocked by preincubation with the MLCK-specific inhibitor ML7 (Fig. 3, C and D, and movie S2). These data demonstrate that the DS can functionally contract by activation of voltage-gated Ca^{2+} channels in the $CaM \rightarrow MLCK \rightarrow MYL-MYH-\alpha$ SMA pathway.

To determine whether smooth muscle-like contraction is a main function of the DS to propagate hair follicle regression *in vivo*, we blocked the MLCK pathway by topical ML7 application on the back skin of mice throughout catagen regression (Fig. 3E). In the back skins of mice receiving vehicle control, follicles regressed normally into telogen with the DP relocated next to the stem cell reservoir (Fig. 3F and fig. S10C). Blocking smooth muscle

contraction with ML7, however, resulted in a notable failure of regression with long stalled follicles stranded deep in the dermis in the center of the treated skin (Fig. 3, F and G), reminiscent of the DS-ablated phenotype (Fig. 1E). The DP here also remains at the tip of stalled follicles (Fig. 3H), but in contrast to ablated follicles, the intact DS surrounds follicles including DP. Taken together, these data demonstrate that DS contraction is functionally required for follicle regression and DP niche relocation to the stem cells.

Visualizing regression movements by intravital imaging

By utilizing intravital two-photon microscopy of unperturbed skin in live mice (15, 18) (fig. S11A), we investigated where the DS contracts and by which force mechanism the DS drives niche relocation. For this, we first established triple-color fluorescent reporters to visualize both the DS and neighboring progenitors (Fig. 4A). *Acan*^{tdT} labels the flat DS cell cytoplasm in red, and *Tbx18*^{H2BGFP} (31)

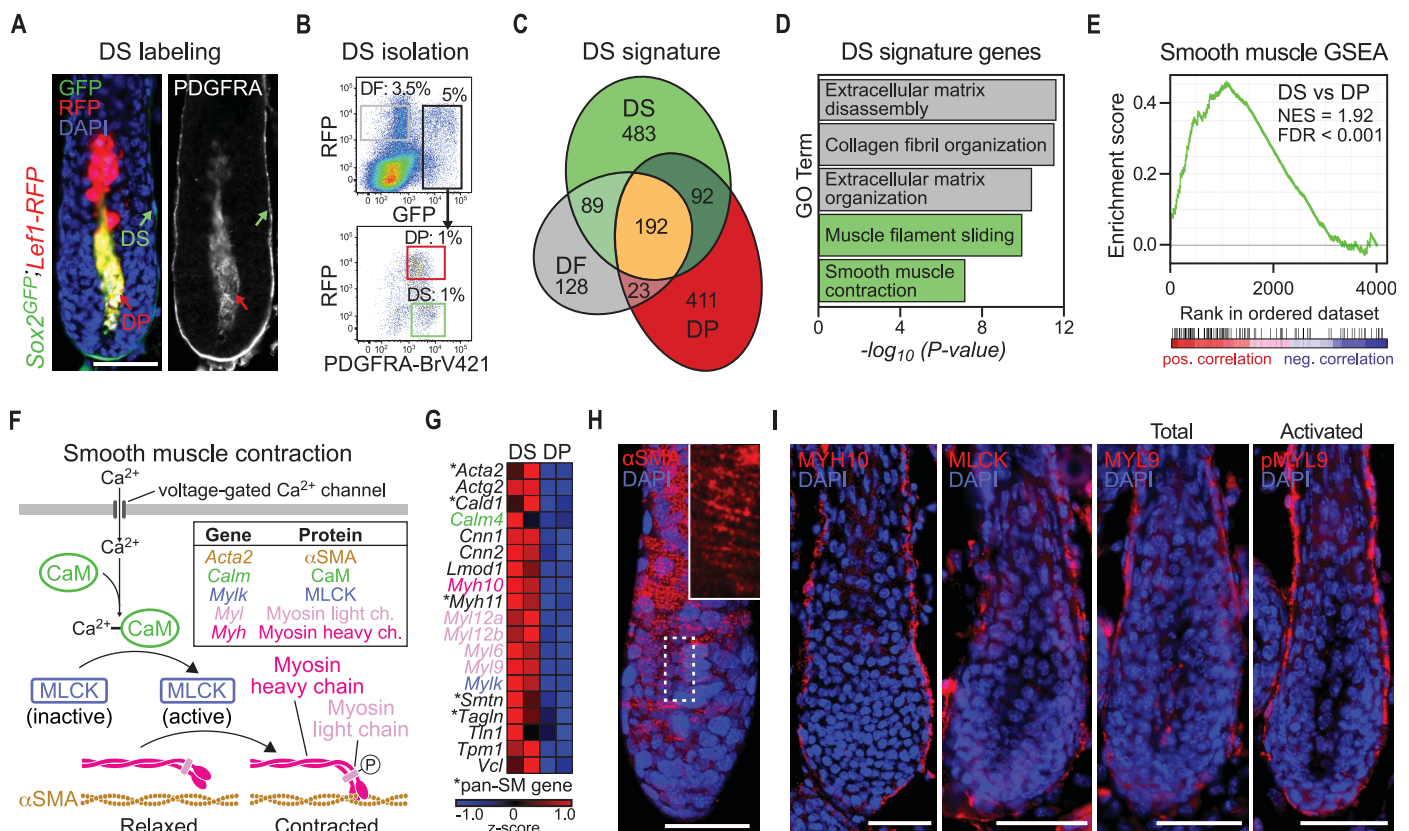


Fig. 2. The dermal sheath expresses the molecular machinery of smooth muscles. (A and B) Labeling of DS and DP (A) and flow cell sorting (B) from *Sox2^{GFP};Lef1-RFP* P5 back skin after IF for PDGFRA. DFs were sorted for comparison. (C) Venn diagram of gene signatures. (D) Gene ontology analysis of DS signature. (E) Gene set enrichment analysis (GSEA) for genes involved in “smooth muscle contraction and regulation” are highly enriched in DS. NES, normalized enrichment score; FDR, false discovery rate. (F) Schematic of

Ca²⁺-dependent smooth muscle contraction pathway. **(G)** Heatmap of smooth muscle contraction gene expression. Ca²⁺ contraction pathway and pan-smooth muscle genes (asterisks) are highly enriched in DS. **(H)** 3D IF for α SMA fibers arranged in a concentric ring-like network wrapping around the follicle. The inset is a magnification of the area enclosed by the white dashed line. **(I)** IF of smooth muscle contraction components in DS. Scale bars are 50 μ m.

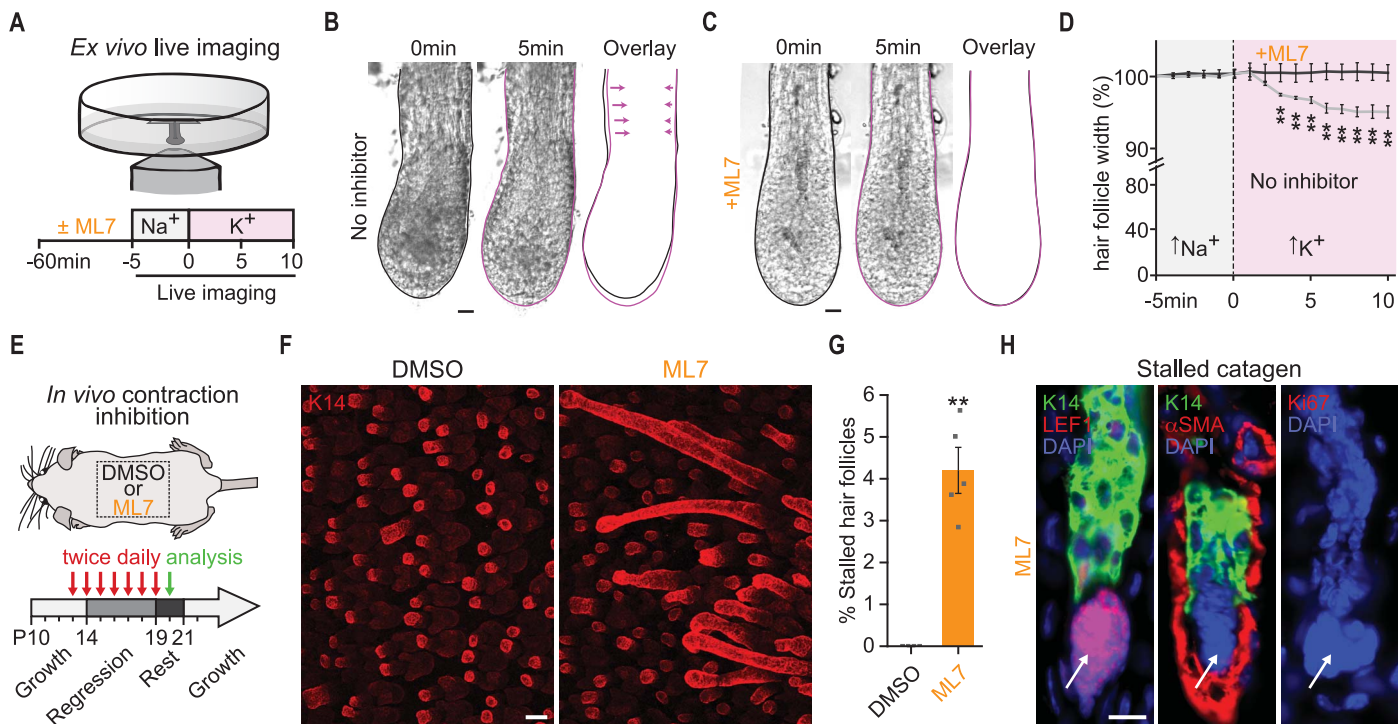


Fig. 3. The dermal sheath functionally contracts and is required for regression in vivo. (A) Schematic of live-imaging microdissected follicles preincubated with or without MLCK inhibitor ML7 and after high K⁺ depolarization. (B and C) Still images from bright-field movie at start (black) and end (pink) of high K⁺ incubation in the absence of inhibitor (B) and in the presence of ML7 (C). Overlays highlight reduction of follicle width, blocked by ML7. (D) Quantification of follicle widths during live imaging. n = 7 follicles for ML7 and no inhibitor preincubation. Data points are mean ± SD. **P < 0.01, by unpaired two-tailed Student's t test. (E to G) Topical inhibition of MLCK by ML7 blocks hair follicle regression

in vivo. Schematic of ML7 or vehicle (DMSO, dimethyl sulfoxide) application during catagen (E). Whole-mount IF of P20 back skins shows normal regression of follicles into telogen rest in control but stalled follicles in contraction-inhibited ML7-treated regions (F). Quantification of the percentage of stalled follicles (n = 1071 control, and n = 1019 ML7-treated; 10 mice) (G). Data bars are mean ± SD. **P = 0.001, by unpaired two-tailed Student's t test. (H) IF for LEF1, Ki67, αSMA, and K14. Stalled follicles have intact DS (αSMA) and DP (LEF1) that are no longer engulfed. Epithelial cells (K14) of stalled follicles are not proliferative (Ki67). Scale bars are 50 μm [(B), (C), and (F)] and 10 μm (H).

labels DS and DP nuclei in bright and dim green. To additionally label all nuclei of neighboring progenitors bright blue, we generated a *K14-H2BCer* transgenic line (Fig. 4A and fig. S12, A and B). The triple-color fluorescent reporter combination (fig. S12C) enabled simultaneous live imaging of DS, DP, and follicle epithelium at a single excitation wavelength (fig. S11, B and C) and thus fine-mapping of their absolute and relative movement over time.

Cell tracking during a 5-hour span of catagen regression demonstrated upward movement of the hair shaft and DP, as expected (Fig. 4B, fig. S13A, and movie S3). By contrast, the DS and ORS showed minimal movement in the long axis (Fig. 4C and fig. S13, B and C), indicating that hair shaft upward movement occurs at the interface between ORS progenitors and shaft, as previously observed (15). The lack of relative movement between DS and ORS suggested strong connections through the separating basement membrane. We next visualized hair shaft regression movements directly after contraction blocking in vivo (Fig. 4D). Live imaging the same follicle before and

after topical ML7 application demonstrated that blocking smooth muscle contraction effectively abrogated upward movement of hair shafts. Together, our labeling setup and live-imaging time frame effectively captured the movements of key components during catagen regression and confirmed the requirement of smooth muscle contraction.

We then asked by which mechanism the niche becomes relocated during regression to reach its final position next to the stem cell reservoir and tested two long-standing hypotheses (24) (Fig. 4E): (i) an apoptotic force from the epithelial strand pulls the DP (23) and (ii) the DS contracts to push the DP and/or hair shaft upward. To investigate the first hypothesis, we measured the length of the epithelial strand during the 5-hour imaging window. If shrinking due to dying cells would generate force for pulling the DP, we would expect shortening of the strand correlating to DP movement (Fig. 4E). However, we observed that individual epithelial strand lengths remained constant throughout (Fig. 4, F and G) despite steady upward DP movement,

consistent with similar rates of shaft and DP upward movement (Fig. 4C). Although forces from individual migrating epithelial strand cells could contribute to upward DP movement, our findings suggest that apoptotic force is not a major driver of regression.

To test the hypothesis that a DS-generated contractile force pushes the DP from underneath, we next investigated potential DS contraction movement below the DP. Coinciding with DP upward movement, we would expect DS centripetal movement underneath the DP. Therefore, we measured the cross-sectional diameter of the DS over time, which, however, remained unchanged (Fig. 4, H and I), suggesting that direct DS contraction under the DP likely does not account for its relocation.

Contraction at the follicle bottleneck pulls the niche via the epithelial strand

We then considered a variation of the contraction hypothesis, in which DS contraction generates constriction forces that push the shaft upward, which in turn would pull both the epithelial strand and the DP upward (Fig. 5A).

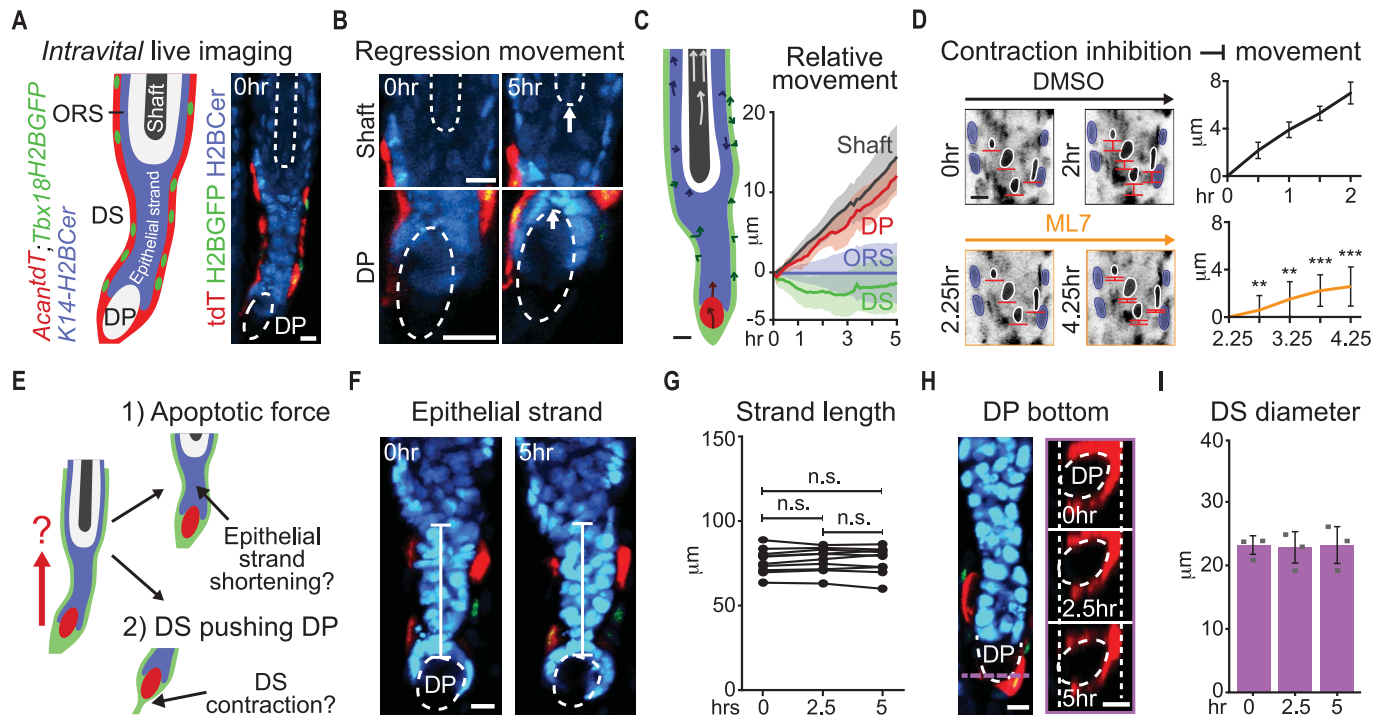


Fig. 4. Dermal sheath contraction is required for hair shaft and niche relocation. (A) Triple-fluorescent reporter follicles for intravital 3D time-lapse imaging of catagen regression in live mice (5 hours). *Acan^{tdT}* and *Tbx18^{H2BGFP}* mark DS cytoplasm and nuclei, respectively. *K14-H2BCer* highlights all epithelial nuclei. The DP was recognized by low-level *Tbx18^{H2BGFP}* expression and surrounding epithelial and DS cells. (B) Upward movement of hair shaft and DP during regression. Tracking of individual ORS, shaft, and DS cells and of upper and lower bounds of DP during 5-hour imaging. The white arrows indicate distance traveled of shaft and DP. (C) Quantification of live cell tracking relative to ORS movement (7.5-min intervals). Shaft and DP move upward relative to ORS and DS. Solid lines are averages; shaded areas are SD. $n = 13$ hair shaft, $n = 8$ DP, $n = 26$ ORS, and $n = 17$ DS measurements (seven follicles, three imaging sessions). (D) In vivo contraction blocking during intravital imaging in

K14-H2BCer mice. Inverted grayscale still images at beginning and end of vehicle control followed by ML7 application. Quantification of live tracking of shaft cells (black) relative to ORS (blue). $n = 9$ follicles from two independent imaging sessions. $**P < 0.01$, and $***P < 0.001$, by paired two-tailed Student's *t* test. (E) Schematic of two historically hypothesized mechanisms for DP niche relocation during regression. (F and G) Fluorescence images from time-lapse movie (F) and quantification (G) of the length of regressing epithelial strand. Strand lengths remain unchanged and stable ($n = 10$ follicles). $P = 0.572$, by unpaired two-tailed Student's *t* test (0 versus 5 hours). (H) DS cross-sectional diameter at DP bottom ($n = 4$ follicles). $P = 0.994$, by unpaired two-tailed Student's *t* test (0 versus 5 hours). (I) Quantification of DS diameter that remains unchanged over time. Data bars are mean \pm SD. Scale bars are 10 μ m.

The observation of a constant epithelial strand length over time (Fig. 4, F and G) supports this alternative hypothesis in which the strand acts as a stable tether between the shaft and DP (Fig. 4F). Indeed, centripetal contraction movement of DS cells right at the border that forms a “bottleneck” between the shaft-containing club hair and the narrower epithelial strand (Fig. 5, B and C) indicates that DS contraction pushes the shaft upward (Fig. 5B and movie S3). After measuring the cross-sectional diameter of the follicle-wrapping DS cell ring at this bottleneck, we found a significant decrease over time coinciding with shaft upward movement (Fig. 5, D and E). These data reveal that the DS moves centripetally at the bottleneck toward the center, suggesting that it contracts to generate the constriction force necessary for pushing the hair shaft upward—akin to the squeezing motion of a toothpaste tube—which then pulls the DP by its connec-

tion to the hair shaft via the epithelial strand (Fig. 5F).

Concluding remarks

Here, we answer the long-standing question of how the niche is relocated nearly the entire length of the follicle to reach its essential stem cell-adjacent position. Through intravital imaging, contraction assays in isolated cells and intact follicles ex vivo, and in vivo inhibition of contraction, we demonstrate that DS is a smooth muscle that contracts to power the key follicle regression movements during the catagen phase of the hair cycle. We directly tested the hypotheses that proposed apoptotic or contraction forces propel catagen progression, based on observations possible at the time, and consolidated them into a model in which the niche relocates to the stem cells through a series of force relays (Fig. 5F). As an adaptation of the original contraction hypothe-

sis, the DS contracts throughout catagen at the club hair–epithelial strand bottleneck, where, because of its angle, the centripetal constricting force gets redirected to an upward pushing force on the shaft. This force is then relayed through the tether-like epithelial strand pulling the DP. At the end stage of regression, when the hair shaft has reached its final position and the DS trails below the DP as a hollow sleeve, it is possible that forces generated by the space reduction of apoptosing cells then pull in the niche next to the stem cell reservoir before launching regrowth in the next cycle that regenerates the follicle for new hair shaft production.

Intimate cross-talk between stem cells and their niches is vital for proper stem cell maintenance and cell fate decisions. Therefore, it is not surprising that niches are found in anatomically distinct locations for hematopoietic stem cells in the bone marrow and intestinal

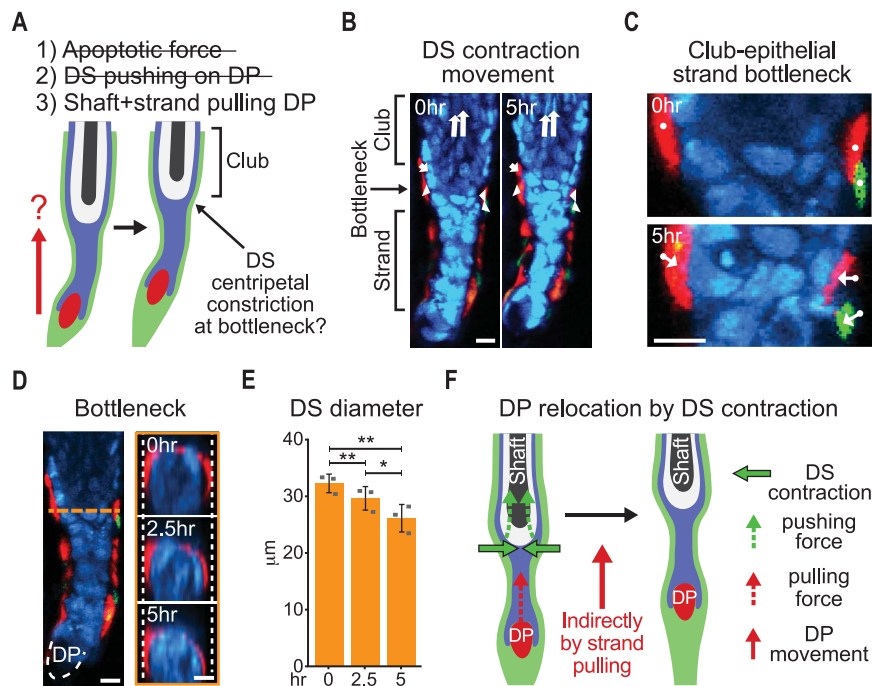


Fig. 5. Dermal sheath contraction pushes the hair shaft and indirectly pulls the niche.

(A) Schematic of a third, alternative hypothesis for DP niche relocation by DS contraction at the bottleneck between the shaft-containing club hair and narrower regressing epithelial strand. (B) Live cell tracking of DS centripetal constriction movement at club hair-epithelial strand bottleneck and of hair shaft upward movement. White arrows are starting and ending positions of 5-hour tracking (seven follicles, three imaging sessions). (C) High magnification of fluorescence time-lapse images at club hair-epithelial strand bottleneck. (D) DS cross-sectional diameter at club hair-epithelial strand bottleneck. The diameter of the follicle-wrapping DS cell ring decreased over time. (E) Quantification of DS diameter at bottleneck decreases over time ($n = 3$ follicles). $*P = 0.021$, $**P = 0.009$, and $P = 0.010$, by unpaired two-tailed Student's t test (0 versus 5 hours). Data bars are mean \pm SD. (F) Model for DP niche relocation during regression. DS contraction forces centripetally constrict the follicle at the bottleneck to move the hair shaft upward, which pulls the DP upward via the epithelial strand. Scale bars are 10 μ m.

stem cells at the crypt base. Providing close proximities for paracrine signaling and insulation from outside influences, most stem cell niche systems under homeostasis remain structurally stable, but after injury to the niche, reestablishment is vital for the restoration of long-term function (32, 33). Although hematopoietic stem cells can mobilize and home to their niche, such as during transplantation (34), the more restricted freedom of movement of epithelial stem cells may limit their homing potential. Here, we discovered another smooth muscle function—relocating a niche to its stem cell reservoir—to add to the vast array of diverse roles of smooth muscles throughout the body. This example highlights the evolutionary advantage of repurposing pre-existing functionality rather than inventing new systems in the wake of new adaptive challenges. Further study may identify more instances of the function of smooth muscle contraction in regulating stem cell-niche sig-

naling range in homeostasis, which could be lost or exploited in disease.

REFERENCES AND NOTES

- Y. Ge, E. Fuchs, *Nat. Rev. Genet.* **19**, 311–325 (2018).
- P. Rompolas, K. R. Mesa, V. Greco, *Nature* **502**, 513–518 (2013).
- Y.-C. Hsu, L. Li, E. Fuchs, *Cell* **157**, 935–949 (2014).
- E. Laurenti, B. Göttgens, *Nature* **553**, 418–426 (2018).
- E. Legué, J.-F. Nicolas, *Development* **132**, 4143–4154 (2005).
- C. Clavel *et al.*, *Dev. Cell* **23**, 981–994 (2012).
- S. Müller-Röver *et al.*, *J. Invest. Dermatol.* **117**, 3–15 (2001).
- G. Cotsarelis, T. T. Sun, R. M. Lavker, *Cell* **61**, 1329–1337 (1990).
- H. Oshima, A. Rochat, C. Kedzia, K. Kobayashi, Y. Barrandon, *Cell* **104**, 233–245 (2001).
- R. J. Morris *et al.*, *Nat. Biotechnol.* **22**, 411–417 (2004).
- C. Blanpain, W. E. Lowry, A. Geoghegan, L. Polak, E. Fuchs, *Cell* **118**, 635–648 (2004).
- T. Tumber *et al.*, *Science* **303**, 359–363 (2004).
- G. Lindner *et al.*, *Am. J. Pathol.* **151**, 1601–1617 (1997).
- K. Foitzik *et al.*, *FASEB J.* **14**, 752–760 (2000).
- K. R. Mesa *et al.*, *Nature* **522**, 94–97 (2015).
- M. Ito, G. Cotsarelis, K. Kizawa, K. Hamada, *Differentiation* **72**, 548–557 (2004).

- Y.-C. Hsu, H. A. Pasolli, E. Fuchs, *Cell* **144**, 92–105 (2011).
- P. Rompolas *et al.*, *Nature* **487**, 496–499 (2012).
- V. Greco *et al.*, *Cell Stem Cell* **4**, 155–169 (2009).
- N. Oshimori, E. Fuchs, *Cell Stem Cell* **10**, 63–75 (2012).
- S. J. Mann, *Anat. Rec.* **170**, 485–499 (1971).
- W. Ahmad *et al.*, *Science* **279**, 720–724 (1998).
- K. S. Stenn, R. Paus, *Physiol. Rev.* **81**, 449–494 (2001).
- C. A. Jahoda, A. J. Reynolds, C. Chaponnier, J. C. Forester, G. Gabbiani, *J. Cell Sci.* **99**, 627–636 (1991).
- S. Malgoures, S. Thibaut, B. A. Bernard, *Br. J. Dermatol.* **158**, 234–242 (2008).
- M. Rendl, L. Lewis, E. Fuchs, *PLOS Biol.* **3**, e331 (2005).
- A. Rezza *et al.*, *Cell Rep.* **14**, 3001–3018 (2016).
- J. A. Beamish, P. He, K. Kottke-Marchant, R. E. Marchant, *Tissue Eng. Part B Rev.* **16**, 467–491 (2010).
- M.-L. Bochaton-Piallat, G. Gabbiani, B. Hinz, *FASEB J.* **25**, 752 (2016).
- R. A. Murphy, J. S. Walker, J. D. Strauss, *Comp. Biochem. Physiol. B Biochem. Mol. Biol.* **117**, 51–60 (1997).
- L. Grisanti *et al.*, *J. Invest. Dermatol.* **133**, 344–353 (2013).
- M. Dominici *et al.*, *Blood* **114**, 2333–2343 (2009).
- H. Bonig, T. Papayannopoulou, *Leukemia* **27**, 24–31 (2013).
- T. Lapidot, A. Dar, O. Kollet, *Blood* **106**, 1901–1910 (2005).

ACKNOWLEDGMENTS

We thank V. Horsley, T. Tumber, R. Paus, M. Rangl, and R. Krauss for invaluable discussions and comments on the manuscript. We are especially grateful to C. Jahoda for helpful discussions and launching dermal sheath research decades ago. Many thanks to D. Dubin and H. Khorasani for providing human scalp skin samples and to the personnel at ISMMS Flow Cytometry, Microscopy, Genomics, and Mouse Genetics CoREs for technical assistance. **Funding:** The ISMMS Microscopy CoRE was supported by NIH Shared Instrumentation grant IS10R0026639. N.H. and R.S. were supported by training grant T32GM007280 from NIH/NIGMS. N.H. was also supported by T32HD075735 from NIH/NIDCR and F30AR070639 from NIH/NIAMS. D.S. and N.S. were supported by a fellowship of the Training Program in Stem Cell Research from the New York State Department of Health (NYSTEM-C32561GG). K.-W.M. was supported by The Science Appearance Career Development Award fellowship from the Dermatology Foundation. A.M. was supported by grants from NIH/OD (U54HL127624 and U24CA224260). P.R. was supported by an NIH/NEI grant (R01EY030599). M.R. was supported by grants from NIH/NIAMS (R01AR071047 and R01AR063151) and the New York State Department of Health (NYSTEM-C029574 and NYSTEM-C32561GG) and by a fellowship from the Irma T. Hirsch Trust. **Author contributions:** N.H., R.S., and M.R. designed the experiments and overall study. N.H. and M.R. wrote the manuscript. N.H., D.S., R.S., K.-W.M., N.S., P.M., and L.G. performed the experiments. Z.W. and A.M. assisted with transcriptome analysis. P.R. assisted with two-photon imaging. All authors discussed the results and participated in the manuscript preparation and editing. M.R. supervised the study. **Competing interests:** N.H., R.S., and M.R. are inventors on a confidential provisional patent application that covers the subject matter of this article. The authors declare no other competing interests. **Data and materials availability:** All data presented in this study are available in the main text or the supplementary materials. Raw and analyzed RNA-sequencing data generated during this study are available in the Gene Expression Omnibus (GEO) repository under accession GSE136996.

SUPPLEMENTARY MATERIALS

science.sciencemag.org/content/367/6474/161/suppl/DC1
Materials and Methods
Figs. S1 to S13
Tables S1 to S3
References (35–44)
Movies S1 to S3

[View/request a protocol for this paper from Bio-protocol.](#)

9 May 2019; accepted 11 December 2019
Published online 19 December 2019
10.1126/science.aax9131

BIODIVERSITY

A lost world in Wallacea: Description of a montane archipelagic avifauna

Frank E. Rheindt^{1*}, Dewi M. Prawiradilaga², Hidayat Ashari², Suparno², Chyi Yin Gwee¹, Geraldine W. X. Lee¹, Meng Yue Wu¹, Nathaniel S. R. Ng^{1,3†}

Birds are the best-known animal class, with only about five or six new species descriptions per year since 1999. Integrating genomic and phenotypic research with arduous fieldwork in remote regions, we describe five new songbird species and five new subspecies from a small area near Sulawesi, Indonesia, all collected in a single 6-week expedition. Two factors contributed to the description of this large number of species from such a small geographic area: (i) Knowledge of Quaternary Period land connections helped pinpoint isolated islands likely to harbor substantial endemism and (ii) studying accounts of historic collectors such as Alfred Wallace facilitated the identification of undercollected islands. Our findings suggest that humans' understanding of biogeographically complex regions such as Wallacea remains incomplete.

Birds (Aves) have long been a model organism across many biological disciplines because of our relatively detailed knowledge of their ecology, distribution, relationships, and global diversity (1). Their model status has become further entrenched with our planet's deepening man-made biodiversity crisis (2–4), which can often be evaluated most easily through the study of organismic groups that were already comprehensively known before being affected by modern anthropogenic processes such as habitat loss, the wildlife trade, and climate change.

The known global diversity of birds currently stands at ~11,000 species (5–7). In 1946, the late Ernst Mayr famously announced that “...the period of new discoveries is practically at its end. I doubt that in the entire world even as many as 100 new [bird] species remain to be discovered...” (8). Mayr's prediction was right until the 1990s: the 20th century saw a limited number of genuinely new species descriptions (8–15) even though taxonomic reassessments and so-called “species splits” have continued to contribute to an unhalting increase in the global species tally (16). Meanwhile, ornithology has entered a minor renaissance of species discovery in the 21st century, with average rates of bird descriptions slightly rebounding to ~5.6 species per year (a total of 95 descriptions from 2000 through 2016; table S1).

Most of these new discoveries have come from South America (~61%), particularly the Andes and the Amazon, and refer to serendipitous finds blending into a slow trickle of single new species descriptions [e.g., tapaculos of the genus *Scytalopus* (17)]. Expeditions such as those of Johann Natterer in Brazil (1817 to 1835), which led to the description of ~40 bird species new to science (18), are not known to have occurred after the 19th century.

Description of five new species and five new subspecies of birds from a small area off Sulawesi

From November 2013 through January 2014, we conducted a bird-collecting expedition to three small, little-explored island groups off the northeastern coast of Sulawesi in present-day central Indonesia (19) (Fig. 1). Here, we formally describe five bird species and five subspecies from this expedition that are new to science and provide details of a long-overlooked local avifauna that has only come to light through recent exploration.

The three islands targeted by our collecting activity are situated in Indonesia's Wallacean region, an archipelago at the interface between the Oriental and Australian biogeographical realms (Fig. 1) named after Alfred R. Wallace, who was the most famous historical collector exploring this area. Six of our 10 new forms (three new species and three subspecies; Fig. 1) were found at higher elevations on Taliabu (~2950 km²), the largest member of the Sula Islands, rising to over 1400 m. Three of the forms (two new species and one subspecies) were detected in the hills of Peleng (~2400 km²), the largest island in the Banggai group, rising to just over 1000 m. One new subspecies comes from Batudaka (~250 km²), the larger of the two main constituents of the Togian group, an agglomeration of low-lying islands barely reaching above ~350 m.

The description of this many bird species from such a geographically limited area is a rarity. Past examples include a series of consecutive collecting expeditions to multiple sites in northern Peru organized by Louisiana State University and collaborating teams >40 years ago (1970 to 1978), which produced type material for at least eight new bird species (20–27), three new species from the Kontum mountain range in central Vietnam collected by Jonathan Eames and coworkers during two expeditions (1996, 1999) (28–30), three new species in the African Rubeho mountains collected by Jacob Kiure during extended fieldwork across nearly 3 years (2000, 2002) (31–34), four new species in an unexplored type of Amazonian forest substrate (“white sand forest”) near Iquitos (Peru) collected by José Álvarez Alonso between 1995 and 1999 (35–38), and four new species in a small Amazonian interfluvium between the Madeira and Aripuanã rivers collected by members of a mostly Brazilian group of collaborators during fieldwork between 2004 and 2011 (39–42). These latter cases raise the possibility that unexplored areas of bird endemism may await discovery.

Earth-historic insights guided our exploratory activity

On a global scale, our findings indicate that modern exploration to find undescribed species diversity can be targeted to areas of high promise. The more important of the two main reasons that we concentrated our field efforts on the islands of Taliabu and Peleng is a modern body of bathymetric data indicating the presence of deep sea between the latter two islands and Sulawesi (Fig. 1) (43). Sea depth is an important and long-neglected factor in determining the distinctness of an island's terrestrial communities. As the Earth has undergone a succession of 20 to 30 glacial periods over the past ~2 million years, global sea levels have repeatedly dropped by up to ~120 m during the peaks of ice ages, most recently at ~18,000 years before present (44, 45), leading to land expansion especially in regions such as Australasia that are dominated by shallow shelf. Consequently, islands surrounded by sea greater than 120 m in depth would have remained isolated throughout the Quaternary Period (Fig. 1), increasing both rates of extinction and rates of endemism by severing gene flow between island populations. By contrast, islands that are linked to greater landmasses by areas of shallow sea (<120 m) would have merged with them through cyclical land-bridge formation, leading to gene flow between populations. Even small amounts of gene flow are powerful in counteracting biotic differentiation, reducing the potential for endemism on such islands (46).

Unaware of the exact earth-historic processes at the time, Wallace himself was likely

¹National University of Singapore, Department of Biological Sciences, 14 Science Drive 4, Singapore 117543. ²Division of Zoology, Research Center for Biology, Indonesian Institute of Sciences (LIPI), Jalan Raya Jakarta Bogor KM 46, Cibinong Science Center, Cibinong 16911, Indonesia. ³Department of Conservation and Research, Wildlife Reserves Singapore, 80 Mandai Lake Road, Singapore 729826.

*Corresponding author. Email: dbrsfe@nus.edu.sg †Present address: Wildlife Reserves Singapore, 80 Mandai Lake Road, Singapore 729826.

the first to point out the uncanny faunal resemblance among shelf islands such as Borneo and Sumatra with mainland Asia while puzzling over the high levels of endemism on other, smaller landmasses such as Sulawesi and

Halmahera that would appear no more isolated if one is oblivious that they are surrounded by deeper sea (47). Although only separated by <15 km of sea water, Peleng has never been connected to

Sulawesi (~180,000 km²) owing to a deep sea channel separating the two (Fig. 1). Instead, the two smaller islands of Peleng and Taliabu have had Quaternary land connections with each other, forming one paleoisland (Fig. 1),

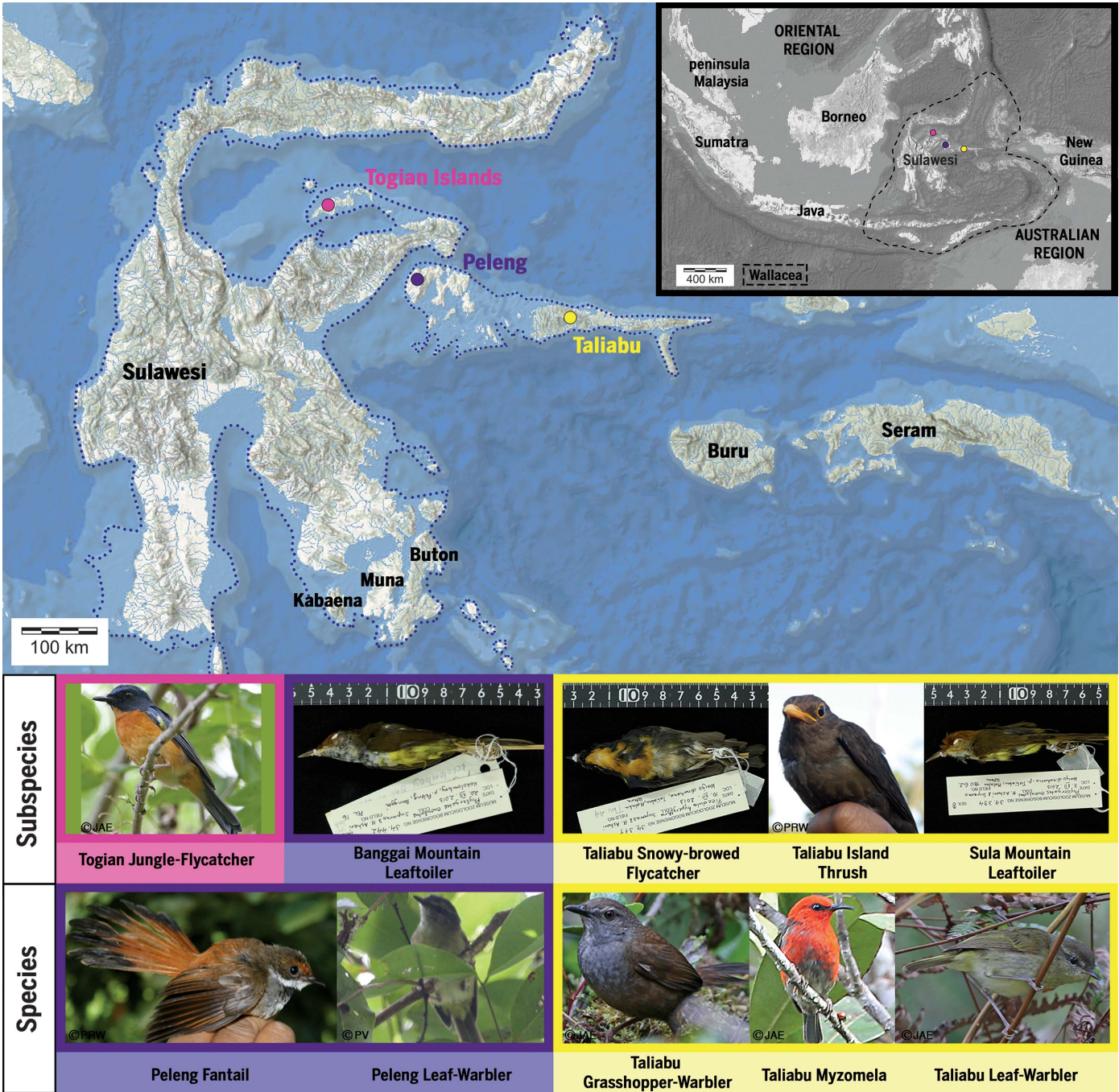


Fig. 1. Map of Sulawesi and satellite islands, with the fieldwork localities on Togian, Peleng, and Taliabu depicted by pink, purple, and yellow circles, respectively. The blue dotted line on the main map reflects the ~120-m isobath, roughly indicating land extent during glacial maxima. The map inset shows the Indonesian Archipelago, with the Wallacean region demarcated by a black dashed line. Photos representing each newly described

taxon (labeled by their proposed English names), including three type specimens (aligned against rulers), are color coded with their respective island distribution. The seven live bird photos do not depict type specimens and were taken by photographers on independent visits to the islands. [Photos courtesy of James A. Eaton (JAE), Peter R. Wilton (PRW), and Philippe Verbelen (PV)]

which explains some of their faunal sharing (48, 49). This bathymetric constellation was our strongest incentive to concentrate on these islands to search for new species diversity (19, 48, 49). Our approach has been further vindicated by the upgrade of five previously recognized avian subspecies from Peleng and Taliabu to species level after new bioacoustic and genomic data established an understanding of true levels of divergence (50–53).

The disproportionate importance of Quaternary land connections in defining how many individual species a landmass harbors can be gauged by contrasting Taliabu and Peleng with other satellite islands off Sulawesi. The southeastern arm of Sulawesi is surrounded by three comparably sized islands that provide a point of reference (Fig. 1): (i) Kabaena (~19 km from Sulawesi and ~900 km² in size); (ii) Buton (~6 km from Sulawesi and ~4400 km² in size); and (iii) Muna (~11 km from Sulawesi and ~2890 km² in size). Sea depth separating these three islands from Sulawesi is generally only 40 to 80 m at its deepest, indicating that all three have been repeatedly connected with Sulawesi by land bridges during glacial periods, including the Last Glacial Maximum only ~18,000 years before present (44, 45). Not a single avian endemic species is known from these three islands despite exploratory activity over the past ~10 years equaling ours in methodology and effort [e.g., (54–56)]. This lack of endemism is notable compared with the 23 bird species recognized as being endemic to Taliabu, Peleng, and smaller surrounding islands (57) when including the five species newly described here and others upgraded in recent research (50–53).

Compared with other islands of a similar or greater size, Taliabu and Peleng are perhaps the last candidates in the Indonesian Archipelago that are both surrounded by deep sea and ornithologically undercollected. However, for other organismic groups, many such islands of high promise remain to be explored. Going forward, we recommend the use of bathymetry beyond birds and beyond the Indonesian Archipelago to predict how promising an island may be in terms of undiscovered diversity of a wide range of terrestrial organisms. Birds are generally volant and relatively large in body size, a combination that suggests they may, on average, be better dispersers than frogs, reptiles, and many invertebrates, which would render the presence or absence of land bridges an even more crucial determinant of endemism in the latter groups. In addition to sea depth, the elevational range and age of an island would also serve as an indicator to gauge potential for endemism. Previous work on Wallacean fauna has demonstrated the importance of topographic relief and high elevations for generating species endemism (58). On the contrary, the age of continuously

emergent land is an unknown property for most Wallacean islands and is poorly characterized for others (59, 60).

Knowledge of historic collection gaps was crucial in finding new birds

Alfred Wallace, aided by a number of helpers in addition to >100 contemporaneous, mostly European, explorers operating roughly until the world wars (after which collecting activity largely ceased), procured a comprehensive collection of Wallacea's birds that forms the basis of our understanding of the regional avifauna (47, 61). Most islands larger than a few square kilometers have therefore been ornithologically explored to some extent. Beyond bathymetric considerations guiding our exploratory plans, we sought to focus on parts of Wallacea that had received the least coverage by historic collectors, which would therefore hold the highest promise of harboring undescribed avian diversity. Studying the routes and operations of historic collecting expeditions and identifying gaps has been a fruitful approach to pinpoint focal areas in our case, just as it was instrumental in generating some of the high new species totals during exploratory fieldwork in northern Peru almost half a century ago (20–27).

The three islands we targeted were characterized by a particularly incomplete historic coverage (Fig. 1): (i) Taliabu and its neighbors, together forming the Sula group, were only briefly visited by eight historic collecting expeditions, all of which remained in coastal areas and failed to penetrate the highlands of the interior because of poor accessibility (61); (ii) Peleng and the remaining islands of the Banggai group were visited along their coastline by only three historic collectors who never ventured far uphill into the interior (61); and (iii) the Togian Islands (including Batudaka) were frequented by only two historic bird collectors (61) but have been targeted by modern Indonesian collecting expeditions (62, 63).

Against this background of historic collecting activity, it is perhaps not surprising that nine of the 10 new forms we here describe come from the higher elevations of Taliabu and Peleng (roughly >800 m). When we first penetrated these areas (48, 49), we found a highly distinct montane local avifauna comprising an unusual number of birds that had remained undiscovered by historic collectors. The only modern ornithologists frequenting the taller mountains of Taliabu before our first visit (48) were probably P. J. Davidson and co-workers, who in 1991 undertook an exploratory survey up to ~800 m, where they made the first observations of four of the six new forms that we describe here (64) but obtained no biological material for formal descriptions. Peleng remained equally

unexplored to modern ornithology: before our own first observations (19, 49), we are only aware of Mochamad Indrawan and colleagues' occasional exploratory forays in the 1990s and early 2000s (49).

New taxon descriptions

To confer nomenclatural availability on the 10 new bird forms, the supplementary materials (sections SM1 to SM11) provide full species and subspecies descriptions, including detailed information on the description of each holotype, diagnosis, etymology, variation within the taxon, history of discovery, distribution, status, taxonomic rationale, and a list of specimens examined. Our baseline taxonomy follows Eaton, van Balen, Brickley, and Rheindt (57), and ZooBank Life Science Identifiers (LSIDs) are given for each newly described taxon to comply with article 8.5.3 of the code of the International Commission on Zoological Nomenclature (65).

Species delimitation is a perennially contentious scientific topic that has variably divided the biological community into different factions, each following its own "species concept" (66). Even when strict standards and criteria are followed, there is a large gray zone within which decisions to confer species versus subspecies rank can be seen as subjective. We adopt the "multidimensional biological species concept" (67), an updated version of modern biology's first species concept (68, 69), which continues to be the most widely applied such concept in ornithology and probably in all of biology. Although the criteria of the original biological species concept hinged strongly on the interpretation of "reproductive isolation," more modern versions are careful to note that reproductive isolation is not absolute and can be inferred through numerous proxies, e.g., a lack of gene flow as suggested by character discreteness or genomic divergence.

We used an integrative approach that relies on a combination of characters, variously including morphology, bioacoustics, ecology, genetic, and genomic data depending on taxon. In our application of the multidimensional biological species concept, we frequently resort to the "yardstick approach" (70), which compares the magnitude of differences among our island populations with differences between members of closely related, well-studied species pairs in which species-level divergence is firmly established. We have tried to remain conservative in our taxonomic decisions, conferring species rank only where our evidence base is strong and retaining subspecies rank in one or two cases where some colleagues may have opted for species rank. Although all five of our new species can by various definitions be assigned to larger radiations within genera that combine sets of species that geographically replace one another (68), they often

belong to the bioacoustically most unusual members within their respective radiation, and their status as distinct species long overlooked by modern ornithology is not in doubt.

Conservation implications

Both Taliabu and Peleng have suffered from rampant forest destruction. On both islands, virtually no primary lowland forest remains, and most highland forests have been affected by some form of logging and/or forest fires, the latter presumably caused by recent climate change (48, 49). Although most of the new forms here described seem to tolerate some form of habitat degradation and were readily detected in secondary forest and edge, some may be threatened, and one of them, the Taliabu grasshopper warbler, is of particular concern as its habitat on the mountain tops of Taliabu may have shrunk to a few square kilometers, some of which was burned in the 1980s and logged in the 1990s (see supplementary materials, section SM3). Urgent, long-lasting conservation action is needed for some of the new forms to survive longer than a couple of decades beyond their date of description.

REFERENCES AND NOTES

1. T. Birkhead, J. Wimpenny, B. Montgomerie, *Ten Thousand Birds: Ornithology Since Darwin*. (Princeton Univ. Press, 2014).
2. A. D. Barnosky et al., *Nature* **471**, 51–57 (2011).
3. M. L. McCallum, *Biodivers. Conserv.* **24**, 2497–2519 (2015).
4. G. Ceballos et al., *Sci. Adv.* **1**, e1400253 (2015).
5. E. C. Dickinson, J. V. Remsen, *The Howard & Moore Complete Checklist of the Birds of the World* (Aves Press, ed. 4, 2013), vol. 1.
6. E. C. Dickinson, L. Christidis, *The Howard & Moore Complete Checklist of the Birds of the World* (Aves Press, ed. 4, 2014), vol. 2.
7. F. Gill, D. Donsker, *IOC World Bird List* (version 8.1; 2018); <https://doi.org/10.14344/IOC.ML.8.1>.
8. E. Mayr, *Auk* **63**, 64–69 (1946).
9. E. Mayr, *Proceedings of the Linnean Society of New York* **45**, 19–23 (1935).
10. E. Mayr, *J. Ornithol.* **98**, 22–35 (1957).
11. E. Mayr, *J. Ornithol.* **112**, 302–316 (1971).
12. E. Mayr, F. Vuilleumier, *J. Ornithol.* **124**, 217–232 (1983).
13. F. Vuilleumier, M. LeCroy, E. Mayr, *Bull. Br. Ornithol. Club* **112**, 267–309 (1992).
14. F. Vuilleumier, E. Mayr, *J. Ornithol.* **128**, 137–150 (1987).
15. J. T. Zimmer, E. Mayr, *Auk* **60**, 249–262 (1943).
16. G. Sangster, *Proc. Biol. Sci.* **276**, 3185–3191 (2009).
17. N. K. Krabbe, T. S. Schulenberg, J. Fjeldsà, in *Illustrated Checklist of the Birds of the World*, J. del Hoyo, N. J. Collar, Eds. (Lynx Edicions, 2016), Volume 2: Passerines, pp. 76–81.
18. A. von Pelzel, *Zur Ornithologie Brasiliens: Resultate von Johann Nattersers Reisen in den Jahren 1817 bis 1835* (Pichler, 1871).
19. F. E. Rheindt, D. M. Prawiradilaga, S. Suparno, H. Ashari, P. R. Wilton, *Treubia* **41**, 61–90 (2014).
20. J. P. O'Neill, G. R. Graves, *Auk* **94**, 409–416 (1977).
21. J. W. Fitzpatrick, J. P. O'Neill, *Auk* **96**, 443–447 (1979).
22. J. W. Fitzpatrick, J. P. O'Neill, *Wilson Bull.* **98**, 1–14 (1986).
23. J. W. Fitzpatrick, J. W. Terborgh, D. E. Willard, *Auk* **94**, 195–201 (1977).
24. J. W. Fitzpatrick, D. E. Willard, J. W. Terborgh, *Wilson Bull.* **91**, 177–186 (1979).
25. T. S. Schulenberg, M. D. Williams, *Wilson Bull.* **94**, 105–113 (1982).
26. G. R. Graves, J. P. O'Neill, T. A. Parker III, *Wilson Bull.* **95**, 1–168 (1983).
27. N. K. Johnson, R. E. Jones, *Auk* **118**, 334–341 (2001).
28. J. C. Eames, C. Eames, *Bull. Br. Ornithol. Club* **121**, 10–22 (2001).
29. J. C. Eames, L. T. Trai, N. Cu, R. Eve, *IBIS* **141**, 1–10 (1999).
30. J. C. Eames, L. T. Trai, C. Nguyen, *Bull. Br. Ornithol. Club* **119**, 4–15 (1999).
31. R. C. Bowie, J. Fjeldsà, J. Kiure, *IBIS* **151**, 709–719 (2009).
32. P. Beresford, J. Fjeldsà, J. Kiure, *Auk* **121**, 23–34 (2004).
33. R. C. Bowie, J. Fjeldsà, *J. East Afr. Nat. Hist.* **94**, 191–202 (2005).
34. J. Fjeldsà, J. Kiure, *Bull. Br. Ornithol. Club* **123**, 52–56 (2003).
35. M. L. Isler, J. A. Alonso, P. R. Isler, B. M. Whitney, *Wilson J. Ornithol.* **113**, 164–177 (2001).
36. B. M. Whitney, J. A. Alonso, *Wilson J. Ornithol.* **117**, 113–128 (2005).
37. B. M. Whitney, J. A. Alonso, *Auk* **115**, 559–576 (1998).
38. J. A. Alonso, B. M. Whitney, *Wilson J. Ornithol.* **113**, 1–10 (2001).
39. B. Whitney et al., in *Handbook of the Birds of the World*, J. del Hoyo, A. Elliott, J. Sargatal, D. A. Christie, Eds. (Lynx Edicions, 2013), Special Volume: New Species and Global Index, pp. 282–285.
40. B. Whitney et al., in *Handbook of the Birds of the World*, J. del Hoyo, A. Elliott, J. Sargatal, D. A. Christie, Eds. (Lynx Edicions, 2013), Special Volume: New Species and Global Index, pp. 263–267.
41. B. M. Whitney, F. Schunck, M. A. Rêgo, L. F. Silveira, in *Handbook of the Birds of the World*, J. del Hoyo, A. Elliott, J. Sargatal, D. A. Christie, Eds. (Lynx Edicions, 2013), Special Volume: New Species and Global Index, pp. 286–291.
42. B. Whitney, M. Cohn-Haft, G. Bravo, F. Schunck, L. Silveira, in *Handbook of the Birds of the World*, J. del Hoyo, A. Elliott, J. Sargatal, D. A. Christie, Eds. (Lynx Edicions, 2013), Special Volume: New Species and Global Index, pp. 277–281.
43. J. J. Becker et al., *Mar. Geol.* **32**, 355–371 (2009).
44. H. K. Voris, *J. Biogeogr.* **27**, 1153–1167 (2000).
45. R. Bintanja, R. S. van de Wal, J. Oerlemans, *Nature* **437**, 125–128 (2005).
46. P. Weigelt, M. J. Steinbauer, J. S. Cabral, H. Kreft, *Nature* **532**, 99–102 (2016).
47. A. R. Wallace, *The Malay Archipelago: The Land of the Orang-Utan and the Bird of Paradise; A Narrative of Travel, with Studies of Man and Nature* (Macmillan, 1869).
48. F. E. Rheindt, *Bull. Br. Ornithol. Club* **130**, 33–51 (2010).
49. F. E. Rheindt, F. Verbelen, D. D. Putra, A. Rahman, M. Indrawan, *Bull. Br. Ornithol. Club* **130**, 181–207 (2010).
50. F. E. Rheindt, J. A. Eaton, F. Verbelen, *Wilson J. Ornithol.* **123**, 429–440 (2011).
51. N. J. Collar, J. Eaton, R. Hutchinson, *Forktail* **29**, 19–24 (2013).
52. N. S. R. Ng, F. E. Rheindt, *Avian Res.* **7**, 2 (2016).
53. K. M. Garg, B. Chattopadhyay, P. R. Wilton, D. Malia Prawiradilaga, F. E. Rheindt, *Mol. Phylogenet. Evol.* **125**, 196–203 (2018).
54. D. P. O'Connell et al., *Forktail*, **33**, 14–19 (2017).
55. D. P. O'Connell et al., *IBIS* **161**, 806–823 (2018).
56. D. P. O'Connell et al., *Zool. J. Linn. Soc.* **186**, 701–724 (2019).
57. J. A. Eaton, S. van Balen, N. W. Brickle, F. E. Rheindt, *Birds of the Indonesian Archipelago: Greater Sundas and Wallacea* (Lynx Edicions, 2016).
58. C. Y. Gwee et al., *Mol. Phylogenet. Evol.* **109**, 246–258 (2017).
59. R. Hall, *J. Asian Earth Sci.* **20**, 353–431 (2002).
60. A. M. S. Nugraha, R. Hall, *Palaeogeogr. Palaeoclimatol. Palaeoecol.* **490**, 191–209 (2018).
61. C. M. N. White, M. D. Bruce, *The Birds of Wallacea (Sulawesi, the Moluccas and Lesser Sunda Islands, Indonesia): An Annotated Check-list* (British Ornithologists' Union, 1986).
62. M. Indrawan, P. C. Rasmussen, Sunarto, *Wilson J. Ornithol.* **120**, 1–10 (2008).
63. M. Indrawan, S. Somadikarta, *Bull. Br. Ornithol. Club* **124**, 160–170 (2004).
64. P. J. Davidson, T. Stones, R. S. Lucking, *Bird Conserv. Int.* **5**, 1–20 (1995).
65. International Commission on Zoological Nomenclature, *International Code of Zoological Nomenclature* (International Trust for Zoological Nomenclature, ed. 4, 1999).
66. Q. D. Wheeler, R. Meier, *Species Concepts and Phylogenetic Theory: A Debate* (Columbia Univ. Press, 2000).
67. E. Mayr, *Philos. Sci.* **63**, 262–277 (1996).
68. E. Mayr, *Principles of Systematic Zoology* (McGraw-Hill, 1969).
69. E. Mayr, *Systematics and the Origin of Species, from the Viewpoint of a Zoologist* (Harvard Univ. Press, 1942).
70. E. Mayr, P. Ashlock, *Principles of Systematic Zoology*. (McGraw-Hill, ed. 2, 1991).

ACKNOWLEDGMENTS

We thank the numerous people who have helped with mist-netting and fieldwork: on Taliabu, we are indebted to P. Obrin and his villager friends from *kampung* Wahe; on Peleng, we would like to extend our gratitude to L. Moopok, A. Maleso, and his son, as well as their villager friends from *kampung* Kokolomboi; and on Batudaka, we thank our team of helpers and porters from the village of Wakai. We would also like to express our thanks to P. R. Wilton for help in the field, photographic material, and sound recordings. We are indebted to P. Ng, J. A. Eaton, F. Verbelen, R. Hutchinson, R. Gallardy, P. Rasmussen, M. Indrawan, and B. van Balen for helpful comments, sound recordings, and/or photographic material. K. Sadanandan is acknowledged for help with laboratory work. P. Rasmussen, P. Ng, and J. Ascher provided comments or contributions to early drafts. P. Ng provided various types of logistic and organizational support. Finally, although all the new bird forms described herein are new to science and were collected as museum material by us for the first time, some of them were first observed by researchers before us. In this context, we acknowledge Mo. Indrawan's activities on Peleng and exploratory activities by the University of East Anglia on Taliabu led by P. J. Davidson. We are indebted to the Research Centre for Biology–LIPI for helping facilitate the permits necessary to carry out this research. The Ministry of Research & Technology of Indonesia issued a research permit (no. 10/TKPKIPA/FRP/SM/X/2013) dated 23 October 2013 to F.E.R. **Funding:** This research was funded by grants from the Faculty of Science of the National University of Singapore (WBS R-154-000-570-133), the Department of Biological Sciences (WBS R-154-000-583-651), and the Singapore Ministry of Education (Tier 2; WBS R-154-000-A59-112). We acknowledge museums contributing samples to this research, in particular the Museum Zoologicum Bogoriense in Cibinong (West Java) and the American Museum of Natural History in New York. **Author contributions:** F.E.R. conceived of this research; D.M.P. provided crucial contributions for facilitating permits and logistics for this research; F.E.R., D.M.P., H.A., and Suparno conducted the field research; Suparno prepared the type material of the new taxa for museum deposition; F.E.R. performed specimen inspection with input from D.M.P. and H.A.; F.E.R. wrote the manuscript with input from D.M.P., C.Y.G. and G.W.X.L. performed bioacoustic and genetic analyses for *Locustella*. M.Y.W. performed genetic analysis for *Myzomela*. N.S.R.N. performed genome-wide analysis for *Phylloscopus* and *Phyllergates*. C.Y.G., G.W.X.L., M.Y.W., and N.S.R.N. created the figures in both the manuscript and the supplementary materials. **Competing interests:** The authors declare no competing interests. **Data and materials availability:** All sequences generated in this study are available on GenBank under the following accession numbers: *Myzomela*: MN431646 and MN431648 to MN431655; *Locustella*: MN597052 to MN597062; *Phylloscopus* and *Phyllergates*: PRJNA566263 (genomic data), MN518850 to MN518857 (*Phyllergates* mitochondrial data) and MN518858 to MN518862 (*Phylloscopus* mitochondrial data). All other data and materials used are available in the supplementary materials.

SUPPLEMENTARY MATERIALS

science.sciencemag.org/content/367/6474/167/suppl/DC1
Figs. S1 to S15
Tables S1 to S6
References (71–137)

4 March 2019; accepted 21 November 2019
10.1126/science.aax2146

REPORT

METALLURGY

Observation of hydrogen trapping at dislocations, grain boundaries, and precipitates

Yi-Sheng Chen^{1,2}, Hongzhou Lu^{3*}, Jiangtao Liang⁴, Alexander Rosenthal⁵, Hongwei Liu⁶, Glenn Sneddon^{1,2}, Ingrid McCarroll¹, Zhengzhi Zhao⁴, Wei Li⁷, Aimin Guo³, Julie M. Cairney^{1,2*}

Hydrogen embrittlement of high-strength steel is an obstacle for using these steels in sustainable energy production. Hydrogen embrittlement involves hydrogen-defect interactions at multiple-length scales. However, the challenge of measuring the precise location of hydrogen atoms limits our understanding. Thermal desorption spectroscopy can identify hydrogen retention or trapping, but data cannot be easily linked to the relative contributions of different microstructural features. We used cryo-transfer atom probe tomography to observe hydrogen at specific microstructural features in steels. Direct observation of hydrogen at carbon-rich dislocations and grain boundaries provides validation for embrittlement models. Hydrogen observed at an incoherent interface between niobium carbides and the surrounding steel provides direct evidence that these incoherent boundaries can act as trapping sites. This information is vital for designing embrittlement-resistant steels.

Although the phenomenon was first identified a century ago (1), hydrogen embrittlement (HE) remains an extremely important unsolved industrial challenge. High-strength steels are particularly prone to early fracture and reduced toughness in the presence of hydrogen (2), which limits their possible manufacturing routes and industrial applications. An example is in the automotive industry, which is looking to use high-strength steels to increase fuel efficiency by reducing weight while still meeting strength requirements (3). Another example is the use of steel for the hydrogen-pressurized pipes and storage containers that would be required to underpin hydrogen fuel as a form of energy (4). These barriers are examples of the challenges for using steel in the decarbonizing technologies that are likely required to meet the global commitments of the 2016 Paris Agreement (5). The development of steels that are resistant to HE requires a solid understanding of the interaction between hydrogen and steels.

The specific origin of HE has long been a topic of debate, and no precise proposed mechanism exists that is consistent with all the observed HE consequences. HE phenomena are

specific to material and microstructure (6). For high-strength steels that display intergranular failure, HE has been attributed to decohesion caused by hydrogen segregation at grain boundaries (GBs) (7), whereas for others that display transgranular failure with a dimple-like fracture surface, embrittlement has been associated with a weakening effect in the presence of hydrogen (6). To describe this effect, Beachem proposed a model in which hydrogen enhances dislocation activity, facilitating the formation of voids, and their subsequent coalescence allows crack propagation, leading to the observed dimples (8). Beachem's model is known as hydrogen-enhanced local plasticity and was later supported by in situ transmission electron microscopy (TEM) observations of enhanced dislocation activity in the presence of gaseous hydrogen (9). The missing piece of evidence to fully validate both models (that is, hydrogen-facilitated decohesion and hydrogen-enhanced dislocation mobility) is direct evidence of the presence of hydrogen at these critical microstructural features.

In addition to hydrogen at GBs and dislocations, the interaction between hydrogen and second phases, such as carbides, is important. These features have the potential to provide HE resistance by serving as hydrogen traps preventing the availability of hydrogen for embrittlement (10).

To understand both embrittlement and trapping, we require information about the position of hydrogen atoms in relation to microstructural features at the nanometer-length scale. However, the combination of the low level of interaction between an electron and hydrogen and the extremely fast diffusion of hydrogen in steels renders it extremely difficult to experimentally determine the location

of hydrogen by electron microscopy (11). Thermal desorption spectroscopy (TDS) provides macroscale information about hydrogen desorption, but this hydrogen originates from all of the possible trapping sites, making it difficult to distinguish the contributions from the different types of hydrogen-containing features (12). This problem obscures our understanding of the specific roles of, for example, GBs, dislocations, and precipitates. Solving this problem removes the impediment to better microstructural design of HE-resistant materials.

Mass spectroscopy techniques are suited to identifying the location of hydrogen because it can be identified by its ratio of mass to charge state (11). The high spatial and mass resolution of atom probe tomography (APT) makes it useful for mapping hydrogen in nanoscale features in three dimensions (13–16). APT is regularly used for both precipitate analyses and identification of microstructural defects such as GBs and dislocations through associated elemental segregation (17–19). Deuterium has almost the same chemical properties as hydrogen but a slightly lower diffusion coefficient in steel due to its larger mass (20). The use of deuterium circumvents several potential hydrogen artefacts and, combined with cryogenic sample transfer, allows us to obtain precise observations of the distribution of hydrogen around nanoscale features. Here, we provide direct evidence of hydrogen localization to achieve a mechanistic understanding of hydrogen-materials interactions and facilitate the development of hydrogen-resistant steels.

We subjected a niobium-bearing low-carbon steel to two different heat treatments to produce ferritic and martensitic states (21). The ferritic state was well annealed and contained few dislocations, allowing uncomplicated analysis of carbide precipitates. By contrast, the fine-grained martensitic state had a high density of dislocations and GBs (both high and low angle). We examined the microstructures of both materials by using transmission Kikuchi diffraction (TKD) (22) and TEM (Fig. 1). We confirmed that the martensitic sample consisted of much finer grains and that these grains also contain low-angle lath boundaries (Fig. 1, A and D). We made a high-resolution image of the niobium carbide (NbC) precipitate (Fig. 1C) indicated with white arrows in the bright-field TEM image (Fig. 1B). We took both images under the $[1-10]_{\text{ferrite}}$ incident beam condition (Fig. 1C, inset). We did not observe an orientation relationship between the precipitates and the matrix, indicating that they were incoherent, as suggested by their round shape. We observed an extremely high density of dislocations in the martensitic sample (Fig. 1, E and F). We took the dark-field image with the use of the $(220)_{\text{ferrite}}$ diffracted vector (23) (Fig. 1F, arrow). We examined atom

¹Australian Centre for Microscopy and Microanalysis, The University of Sydney, Sydney, Australia. ²School of Aerospace, Mechanical and Mechatronic Engineering, The University of Sydney, Sydney, Australia. ³CITIC Metal Co., Beijing, China. ⁴Collaborative Innovation Center of Steel Technology, University of Science and Technology Beijing, Beijing, China. ⁵Microscopy Solutions Pty., Caulfield North, Australia. ⁶Sydney Microscopy and Microanalysis, The University of Sydney, Sydney, Australia. ⁷Institute of Advanced Steels and Materials, School of Materials Science and Engineering, Shanghai Jiao Tong University, Shanghai, China.
*Corresponding author. Email: julie.cairney@sydney.edu.au (J.M.C.); luhz@citic.com (H.L.)

probe needles prepared from the martensitic sample (fig. S3) and found that they also contained GBs and a high density of dislocations.

We confirmed with thermal desorption experiments that hydrogen was present in samples that had been electrolytically precharged with hydrogen (Fig. 2). For the martensitic sample, we found a substantial hydrogen desorption peak when the sample reached between 100° and 300°C (Fig. 2A). We believe this peak corresponds to hydrogen that was absorbed at the abundant dislocations in the martensite, consistent with other studies that used the same technique (12, 24, 25). On magnifying the scale of Fig. 2A, we found that the data from the ferritic sample contain two peaks in Fig. 2B, one at ~100° to 200°C and the other at ~300° to 350°C. We attribute these peaks to hydrogen at the ferrite GBs (26) and at NbC precipitates (27), respectively. Of course, the martensitic sample might also be expected to contain hydrogen at GBs. However, any signal from the GB hydrogen in the martensitic sample was likely buried in the large peak associated with dislocations. Resolving the exact hydrogen-trapping behavior would require peak deconvolution, which is challenging because we do not have enough information to get a statistically robust deconvolution (28).

We performed APT on both samples. We charged needle-shaped samples with deuterium and transferred them via a complete cold chain into the atom probe chamber (21). Because the needle-shaped sample is small, and hydrogen-deuterium is prone to recombination and desorption if it reaches the specimen surface (29), it is crucial that diffusion is minimized by maintaining the cold chain. We collected data from a deuterium-charged ferritic sample (Fig. 3) and a deuterium-free reference sample, confirming that the deuterium signal, at a mass-to-charge ratio of 2, is only present for the deuterium-charged sample (fig. S5, A and B). The charged sample contains three NbC precipitates in a ferritic matrix (Fig. 3A). Slices that were 5 nm thick and taken through the center of the precipitates (Fig. 3B, left) allow us to visualize the deuterium (Fig. 3, C and D, red spheres) in the vicinity of the carbide precipitates. We found that the deuterium atoms are mostly located at the interfaces between NbC and ferrite.

We then quantitatively analyzed the NbC precipitates from top to bottom in the *z* direction (Fig. 3B, right), which is the direction that provides the highest spatial resolution (30). We obtained data from cylindrical regions of interest through the precipitate centers (Fig. 3, E and F). Peaks in deuterium concentration were aligned with the edges of the NbC profile, confirming that the deuterium was mostly located at the precipitate-matrix interface. Proximity histograms based on a 1% niobium

isoconcentration surface (isosurface) (31) also showed the localization of the deuterium at the interface (fig. S6).

Carbides are well known to trap hydrogen and reduce embrittlement, but the mechanism is not clear. Conflicting arguments have emerged about whether the trapping is in the carbide bulk, at the interface, or both. Previous atom probe studies showed that deuterium was present in the vicinity of carbides for a peak-aged vanadium carbide (14), including along the direction of the coherent (001) surface, but were unable to resolve details of whether it is located at the interface or the carbide bulk. For much smaller, coherent vanadium carbides, deuterium was found in the bulk (13), presumably because of strain in the

precipitates and a high resulting fraction of carbon vacancies (32, 33).

In this study, we show deuterium trapping at carbide interfaces in larger, incoherent precipitates. Our results are consistent with the earlier findings that carbide interfaces can effectively trap hydrogen (28, 34) and that, for equivalent volume fractions of vanadium carbide, alloys with smaller precipitates, and hence a higher effective carbide-matrix interface area, trap more hydrogen (35).

Our martensitic sample contains a much higher volume-fraction of dislocations and GBs than our ferritic sample. Two atom probe datasets from this sample (Fig. 4) both contained a high density of dislocations that were enriched with carbon, identifiable by their

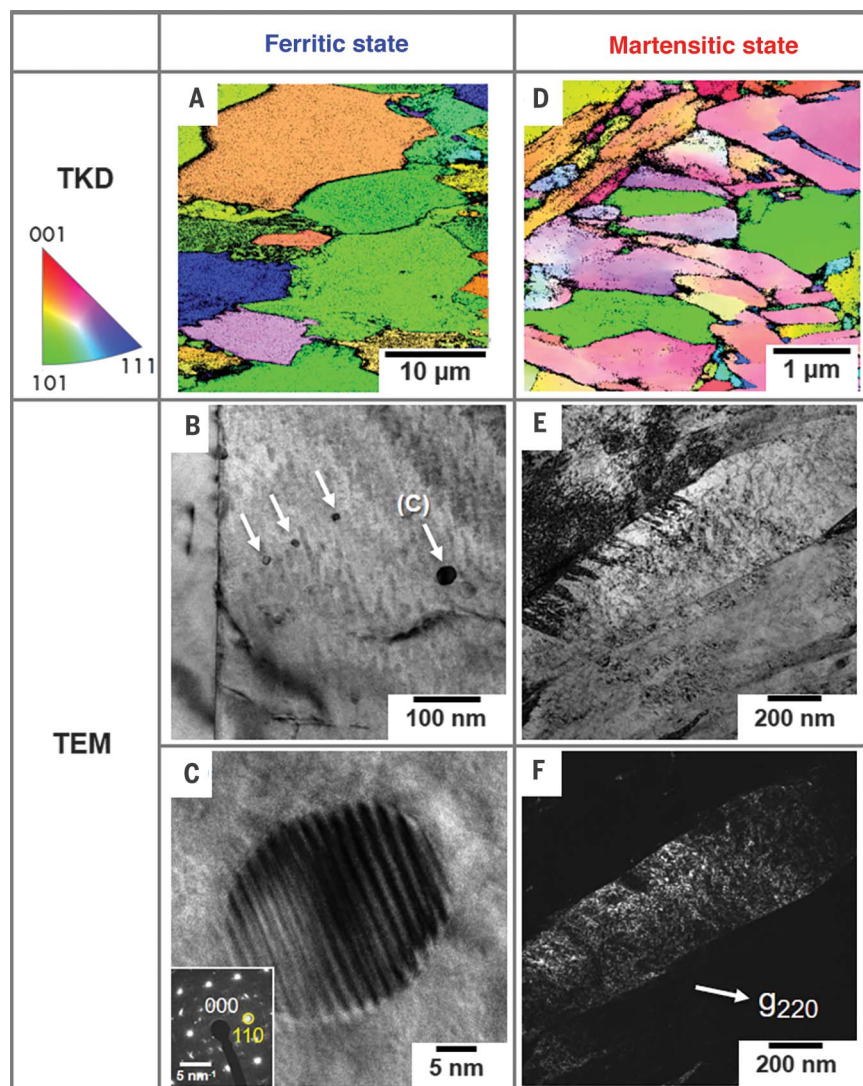


Fig. 1. Microstructure of the ferritic and martensitic steels. (A and D) TKD inverse pole figure maps of the ferritic and martensitic samples, respectively, showing the grain size and orientation. (Scales differ for these two panels.) (B and C) Low- and high-magnification bright-field images of the NbC precipitates in the ferritic sample. The precipitate shown in (C) is marked in (B). (E and F) Bright- and dark-field images of the same area showing the high density of dislocations in the martensitic sample.

linear morphology. The first dataset contains only dislocations (Fig. 4, A and B, and movies S2 and S3), and the second dataset also contains three carbon-enriched GBs connected by a triple line, which are most likely low-angle martensitic lath boundaries (Fig. 4, E and F, and movie S4). Solute carbon is known to segregate at the lattice defects of iron (19),

so we were able to highlight the GB and dislocations by 2% carbon isosurfaces. The dislocations are highlighted by transparent blue isosurfaces, whereas the GBs are highlighted by transparent red isosurfaces. We confirmed the presence of deuterium by comparing the mass spectrum from this sample (fig. S5C) with that of a martensitic

sample that had also been deuterium-charged and cryogenically transferred but then left to desorb in the buffer chamber at room temperature overnight (fig. S5D).

A slice taken from the center of the dataset shown in Fig. 4B shows the spatial correlation between the carbon and deuterium (Fig. 4C) in the vicinity of the dislocations (movie S3). We conducted a proxigram analysis based on the 2% carbon isosurface (Fig. 4D), which provides the average composition as a function of the distance from the isosurface (31). We found that deuterium was concentrated at the core of the dislocations. Very little niobium was present in these regions, distinguishing them from the carbides we observed in the ferritic sample (Fig. 3, E and F).

For the GB region, we found that the amount of carbon segregation to the GBs varied across the boundary plane. For this reason, the transparent red isosurface in Fig. 4, E and F, does not capture the full area of the boundary. To show the continuous nature of the boundary, *z* axis slice views (Fig. 4G) were taken from the positions indicated in Fig. 4F. We found that three GBs were connected by a triple line. Deuterium atoms in the martensitic sample are also concentrated in the GB region, demonstrating that the GBs also act as trapping sites. We created a composition line profile across the GB area (Fig. 4H, taken from the area shown in Fig. 4E, bottom right corner). We found carbon and deuterium at the GB but very little niobium segregation.

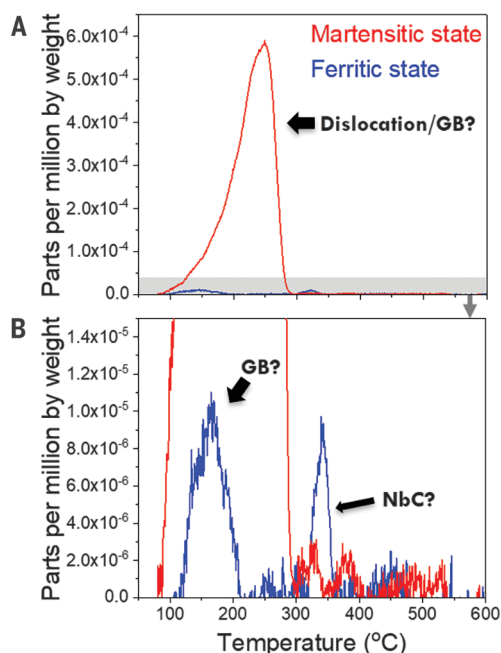


Fig. 2. TDS data showing the temperature at which trapped hydrogen is released for the two types of steel. (A) Full dataset.

The large peak in the data for the martensitic steel is thought to be the result of trapping at dislocations. (B) Details of the region shaded in gray in (A). The peak at 100° to 200°C is thought to correspond to trapping at the GBs, and the peaks at higher temperatures are thought to be due to trapping at carbides.

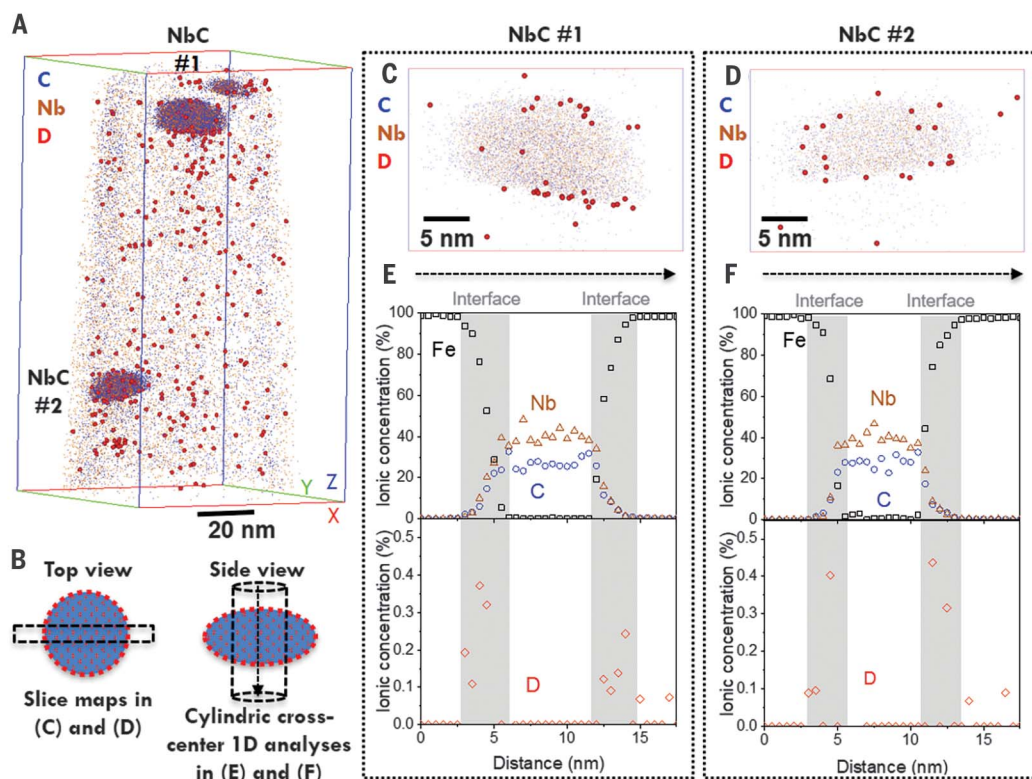
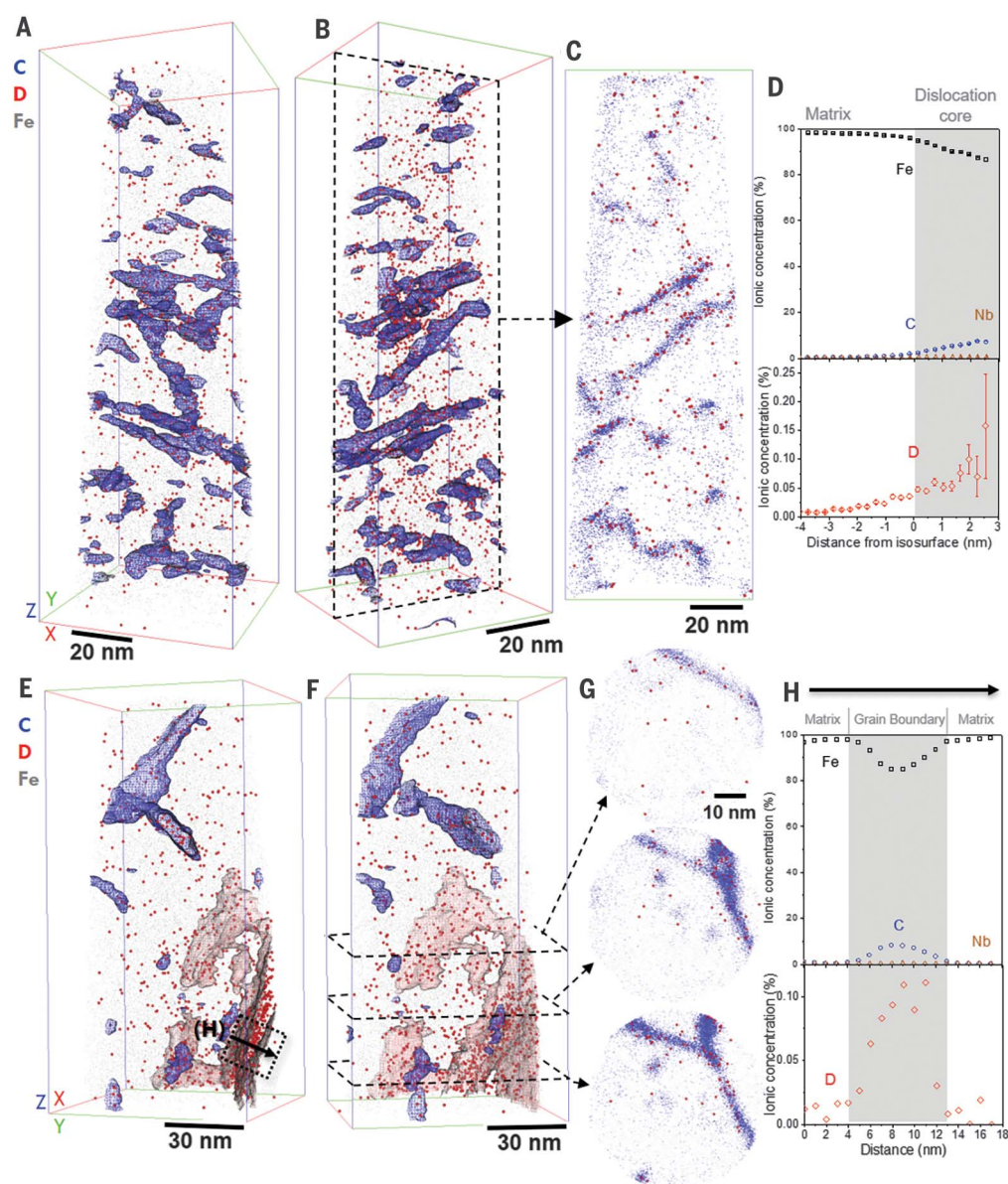


Fig. 3. APT analysis of a deuterium-charged ferritic steel sample containing NbC.

(A) Full reconstructed atom map showing atoms with mass-to-charge ratios that match deuterium (large red spheres), carbon (small blue spheres), and niobium (small brown spheres). (B) Schematic describing the data in (C) to (F). (C and D) *y* Axis slices 5 nm thick through the center of the top (NbC#1) and bottom (NbC#2) precipitates, respectively, showing carbon, niobium, and deuterium atoms. (E and F) One-dimensional (1D) *z* axis composition profiles through the centers of NbC#1 and NbC#2, respectively, extracted from a 7-nm-diameter cylindrical region of interest with a bin width of 0.5 nm and no overlapping of bins.

Fig. 4. APT analyses of deuterium-charged martensitic steel samples containing GBs and dislocations.

(A and B) Views at two different angles of a reconstructed atom map showing deuterium (red), iron (gray), and 2% carbon isosurfaces in blue. This sample contains a high density of linear, carbon-decorated dislocations (movie S2). (C) Slice, 5 nm thick, from the center of the dataset shown in (B) (indicated with the black dashed rectangle) with carbon atoms (blue) and deuterium atoms (red) showing the spatial correlation between the two elements. Movie S3 shows this 5-nm slice moving across the full dataset. (D) Collective proxigram analysis of the 70 dislocations and carbon isosurfaces contained in (A), showing that the dislocations have carbon and deuterium at their cores but little niobium. (E and F) Two views of a different dataset from the same sample. Again, features are highlighted by 2% carbon isosurfaces, with one of these surfaces that encompasses a GB region highlighted by a transparent red isosurface. (G) z Axis, 5-nm-thick slices from the GB region, indicated in (F) (movie S4). (H) 1D composition profile with a 1-nm step size from a volume of 20 nm by 20 nm by 18 nm across the GB marked in (E).



All the features we analyzed contain carbon. This observation is consistent with experimental evidence by TDS showing the hydrogen trapping in a specimen that is known to contain carbon-decorated lattice defects in a martensitic steel (36). A reasonable speculation is that an affinity between carbon and hydrogen might lead to the hydrogen trapping. However, a theoretical study showed that the carbon atoms in lattice defects have only a weak influence on the hydrogen trapping (37), and other modeling has successfully predicted the presence of trapped hydrogen at dislocations in a body-centered cubic lattice (38). Therefore, we believe that the observed hydrogen is directly related to the presence of lattice defects, rather than the result of attraction by segregated carbon atoms.

In this study, cryogenic APT has enabled the measurement of the distribution of hydrogen at dislocations, GBs, and precipitates. We anticipate that this method will continue to be used in the future as a complement to detailed TEM analysis (including in situ tests), mechanical testing in the presence of hydrogen, and first-principles calculations to provide further insights into mechanisms of embrittlement and its prevention.

Our observation of hydrogen atoms at dislocations and GBs confirms the existence of excess hydrogen at defects, an assumption that underpins critical theories of HE. Knowledge of hydrogen trapping at incoherent interfaces provides a pathway for the design of alloys in which embrittlement is prevented or delayed.

REFERENCES AND NOTES

- W. H. Johnson, *Nature* **11**, 393 (1875).
- S. Lynch, *Corros. Rev.* **30**, 105–123 (2012).
- J. Venezuela, Q. L. Liu, M. X. Zhang, Q. J. Zhou, A. Atrous, *Corros. Rev.* **34**, 153–186 (2016).
- Hydrogen Strategy Group, Hydrogen for Australia's Future, COAG Energy Council, (Australian Government, 2018).
- United Nations Framework Convention on Climate Change, *The Paris Agreement* (UNFCCC, 2015).
- I. M. Robertson et al., *Metall. Mater. Trans. A Phys. Metall. Mater. Sci.* **46**, 2323–2341 (2015).
- H. W. Liu, *Eng. Fract. Mech.* **78**, 2563–2571 (2011).
- C. D. Beachem, *Metall. Trans.* **3**, 437 (1972).
- I. M. Robertson, *Eng. Fract. Mech.* **68**, 671–692 (2001).
- H. K. D. H. Bhadeshia, *ISIJ Int.* **56**, 24–36 (2016).
- M. Koyama et al., *Mater. Sci. Technol.* **33**, 1481–1496 (2017).
- W. Y. Choo, J. Y. Lee, *Metall. Trans., A, Phys. Metall. Mater. Sci.* **13**, 135–140 (1982).
- Y.-S. Chen et al., *Science* **355**, 1196–1199 (2017).
- J. Takahashi, K. Kawakami, Y. Kobayashi, *Acta Mater.* **153**, 193–204 (2018).
- J. Takahashi, K. Kawakami, Y. Kobayashi, T. Tarui, *Scr. Mater.* **63**, 261–264 (2010).

16. J. Takahashi, K. Kawakami, T. Tarui, *Scr. Mater.* **67**, 213–216 (2012).
17. M. Kuzmina, M. Herbig, D. Ponge, S. Sandlöbes, D. Raabe, *Science* **349**, 1080–1083 (2015).
18. M. K. Miller, *J. Mater. Sci.* **41**, 7808–7813 (2006).
19. J. Wilde, A. Cerezo, G. D. W. Smith, *Scr. Mater.* **43**, 39–48 (2000).
20. A. T. Paxton, I. H. Katzarov, *Acta Mater.* **103**, 71–76 (2016).
21. Materials and methods are available as supplementary materials.
22. P. W. Trimby *et al.*, *Acta Mater.* **62**, 69–80 (2014).
23. D. B. Williams, C. B. Carter, *Transmission Electron Microscopy: A Textbook for Materials Science* (Springer, ed. 2, 2009), pp. 277.
24. M. Nagumo, *Mater. Sci. Technol.* **20**, 940–950 (2004).
25. K. Takai, H. Shoda, H. Suzuki, M. Nagumo, *Acta Mater.* **56**, 5158–5167 (2008).
26. I. J. Park, S. M. Lee, H. H. Jeon, Y. K. Lee, *Corros. Sci.* **93**, 63–69 (2015).
27. E. Wallaert, T. Depover, M. Arafim, K. Verbeken, *Metall. Mater. Trans., A Phys. Metall. Mater. Sci.* **45**, 2412–2420 (2014).
28. F. G. Wei, K. Tsuzaki, *Metall. Mater. Trans., A Phys. Metall. Mater. Sci.* **37**, 331–353 (2006).
29. H. Suzuki, K. Takai, *ISIJ Int.* **52**, 174–180 (2012).
30. B. Gault, M. P. Moody, J. Cairney, S. P. Ringer, *Atom Probe Microscopy* (Springer, 2012).
31. O. C. Hellman, J. B. du Rivage, D. N. Seidman, *Ultramicroscopy* **95**, 199–205 (2003).
32. X. X. Yu, C. R. Weinberger, G. B. Thompson, *Comput. Mater. Sci.* **112**, 318–326 (2016).
33. D. Di Stefano *et al.*, *Phys. Rev. B* **93**, 184108 (2016).
34. M. Ohnuma, J. I. Suzuki, F. G. Wei, K. Tsuzaki, *Scr. Mater.* **58**, 142–145 (2008).
35. A. Turk, D. San Martin, P. E. J. Rivera-Diaz-del-Castillo, E. I. Galindo-Nava, *Scr. Mater.* **152**, 112–116 (2018).
36. M. Enomoto, D. Hirakami, T. Tarui, *Metall. Mater. Trans. A Phys. Metall. Mater. Sci.* **43**, 572–581 (2012).
37. A. P. A. Subramanyam, A. Azócar Guzmán, S. Vincent, A. Hartmaier, R. Janisch, *Metals* **9**, 291 (2019).
38. A. De Backer *et al.*, *Nucl. Fusion* **58**, 016006 (2018).

ACKNOWLEDGMENTS

The authors thank T. Paxton (King's College London), P.-C. Hsu (Duke University), H.-W. Yen (National Taiwan University), Y.-C. Lo (National Chiao Tung University), D. Xie (Xi'an Jiaotong University), H. Jiang (University of Western Australia), B. Gault (Max Planck Institute for Iron and Steel Research), T. Sato, G. Derrick, X. Cui, B. Pace, and M. He (all University of Sydney) for useful discussions. Y.-S.C. thanks his family members for support. **Funding:** The authors acknowledge funding from Australian Research Council Linkage Project (LP180100431), Future Fellowship (FT180100232), CITIC-CBMM Nb Steel Award Fund Program (2018FWNB30064), the 2019 University of Sydney Postdoctoral Fellowship, and USYD-SJTU Partnership Award, as well as the research facilities supported by Microscopy Australia and the University of Sydney. **Author**

contributions: Y.-S.C. drafted the manuscript, supported the development of the cryo-transfer protocol, conducted the APT experiment, and analyzed all the data. H.Lu conceptualized the study, designed the samples, and acquired research funds. J.L. produced the samples and conducted the TDS experiment. A.R. designed and produced the cryo-transfer system and developed the cryo-transfer protocol. H.Liu and G.S. conducted the TEM imaging and the TKD mapping, respectively. I.M. developed the cryo-transfer protocol. Z.Z. provided the facilities for sample production and processing. W.L. provided the TDS facility. A.G. provided the research funds. J.M.C. provided the microscope facilities and cryo-transfer analyses, supervised the project, and finalized the manuscript. **Competing interests:** The authors declare no competing interests. **Data and materials availability:** All data are available in the main text or the supplementary materials and can be accessed online via <https://cloudstor.aarnet.edu.au/plus/s/zvgZQzSQhledy6V>.

SUPPLEMENTARY MATERIALS

science.sciencemag.org/content/367/6474/171/suppl/DC1
Materials and Methods
Figs. S1 to S7
Table S1
References (39, 40)
Movies S1 to S4

13 August 2019; accepted 14 November 2019
10.1126/science.aaz0122

QUANTUM CHEMISTRY

Observation of an isomerizing double-well quantum system in the condensed phase

Jascha A. Lau^{1,2}, Arnab Choudhury^{1,2}, Li Chen^{2*}, Dirk Schwarzer², Varun B. Verma³, Alec M. Wodtke^{1,2,4,†}

Molecular isomerization fundamentally involves quantum states bound within a potential energy function with multiple minima. For isolated gas-phase molecules, eigenstates well above the isomerization saddle points have been characterized. However, to observe the quantum nature of isomerization, systems in which transitions between the eigenstates occur—such as condensed-phase systems—must be studied. Efforts to resolve quantum states with spectroscopic tools are typically unsuccessful for such systems. An exception is CO adsorbed on NaCl(100), which is bound with the well-known OC–Na⁺ structure. We observe an unexpected upside-down isomer (CO–Na⁺) produced by infrared laser excitation and obtain well-resolved infrared fluorescence spectra from highly energetic vibrational states of both orientational isomers. This distinctive condensed-phase system is ideally suited to spectroscopic investigations of the quantum nature of isomerization.

Direct conversion of molecules between their isomeric forms requires methods to reorganize bonds between constituent atoms. Such methods include thermal activation, laser-stimulated excitation (1–4), and electron-stimulated excitation (5–7). Understanding the quantum nature of isomerization is still a missing cornerstone in chemical science, as transitions between the quantum states involved in isomerization have never been detected. Stimulated emission pumping spectroscopy (8, 9) has been used to examine the eigenstates of gas-phase systems capable of undergoing 1,2-hydrogen transfer reactions: e.g., HCN \rightleftharpoons CNH (10–12), HC \equiv CH \rightleftharpoons :C=CH₂ (13, 14), and HCP \rightleftharpoons CPH (15). Yet even for these systems, it is challenging to detect quantum states from both isomers. Up to now, the most detailed quantum-state-resolved study employed high-resolution photoelectron spectroscopy to probe the HC \equiv CH \rightleftharpoons :C=CH₂ isomerization reaction and showed that the eigenstates of the in-plane rocking mode of vinylidene have appreciable acetylenic character (16). For symmetric systems that resemble chemical isomerization, such as the geared tunneling motion of the hydrogen-bonded HF dimer, HF \cdots HF \rightleftharpoons FH \cdots FH, delocalized states can be unambiguously identified from tunneling splitting (17).

Despite advances in understanding the vibrational character of these double-well sys-

tems (18, 19), isomerization requires interactions with the environment that induce transitions between states. Hence, it would be desirable to extend quantum-state-resolved spectroscopy to temporally evolving systems in condensed phases. Unfortunately, the quantum states of condensed-phase systems generally cannot be spectroscopically resolved, and the theory needed for comparisons to experiment is much more demanding than that for small isolated molecules. We recently reported infrared emission spectra from monolayers of CO adsorbed at a NaCl(100) surface (20, 21) using a spectrometer based on a superconducting nanowire single-photon detector (SNSPD) (22). Infrared laser excitation produced vibrationally excited CO by vibrational energy pooling (23), which

could be accurately described by a kinetic Monte Carlo simulation (21). The interactions of the CO molecule with the NaCl lattice were described by a Sommerfeld ground-wave limit in which energy flow to the surface is dominated by electrodynamic interactions instead of the anharmonic interatomic forces that are normally much more important (21). These findings reflect the importance of electrostatic interactions in this system.

Here we present quantum-state-resolved infrared spectroscopy of two orientational isomers of a monolayer of CO on NaCl(100) observed in both absorption and emission. The ground-state orientation exhibits a short C–Na distance with the CO bond axis close to the surface normal; a less stable orientational isomer has a short O–Na bond with the bond axis tilted farther from the surface normal. Hereafter, we refer to these species as C-down and O-down, respectively. Vibrational energy pooling produces CO adsorbates with energies up to 6 eV, leading to infrared emission from well-resolved quantum states of both isomers. In fact, infrared laser excitation converts a substantial fraction of C-down to O-down. The lifetime of back-conversion to the C-down structure is short ($\lesssim 10^2$ s) at a surface temperature of 7 K. If we bury this monolayer under a weakly interacting CO overlayer, the lifetime of the O-down isomer becomes indefinite. From these data, we derived vibrational constants for both isomers in the monolayer and the buried monolayer. The shifts in the vibrational constants of the two orientational isomers referenced to the isolated gas-phase CO molecule obey a simple electrostatic model

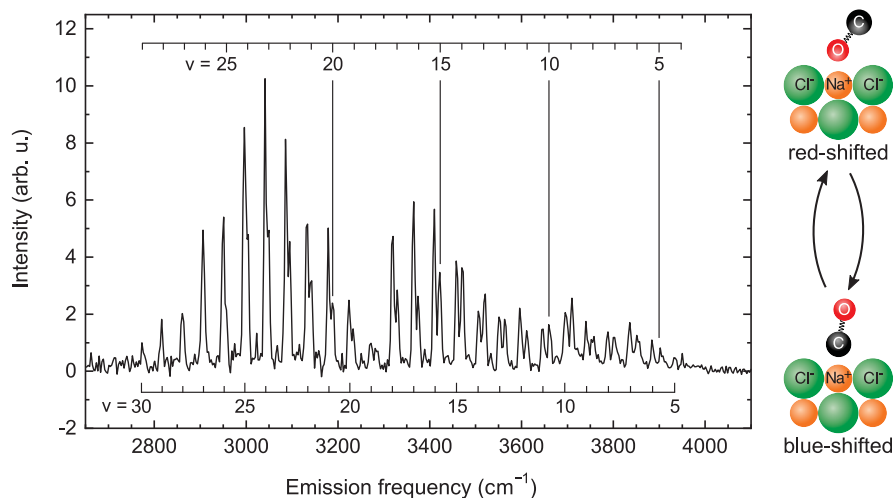


Fig. 1. Dispersed fluorescence spectrum from a monolayer of CO undergoing energy pooling.

Two vibrational progressions shown by combs obey the simple anharmonic oscillator formula of Eq. 4, allowing derivation of precise vibrational constants for both progressions. One progression represents an anharmonic oscillator with blue-shifted frequencies compared with those of gas-phase CO; the second progression appears with red-shifted frequencies. The blue- and red-shifted oscillators are assigned to orientational isomers of CO at the NaCl interface, atomic scale representations of which are shown. Only overtone emission ($\Delta v = -2$) is shown, and the emission signal is integrated during the initial 200 μ s after laser excitation. arb. u., arbitrary units.

¹Institute for Physical Chemistry, University of Göttingen, Tammannstr. 6, 37077 Göttingen, Germany. ²Department of Dynamics at Surfaces, Max-Planck Institute for Biophysical Chemistry, Am Faßberg 11, 37077 Göttingen, Germany.

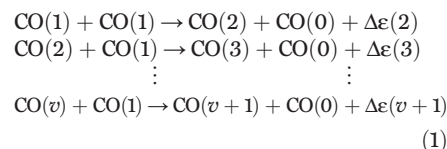
³National Institute of Standards and Technology, Boulder, CO 80305, USA. ⁴International Center for Advanced Studies of Energy Conversion, Georg-August University of Göttingen, Tammannstraße 6, 37077 Göttingen, Germany.

*Present address: State Key Laboratory of Molecular Reaction Dynamics, Dalian Institute of Chemical Physics, Chinese Academy of Sciences, Dalian, Liaoning 116023, People's Republic of China.

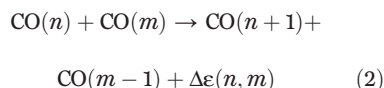
†Corresponding author. Email: awodtke@mpibpc.mpg.de

that also describes the stable structures of the two isomers.

Figure 1 shows a section of the dispersed infrared fluorescence spectrum in the region of the first overtone obtained after pulsed IR excitation of the $^{13}\text{C}^{18}\text{O}(v=0 \rightarrow 1)$ transition in a $^{13}\text{C}^{18}\text{O}$ monolayer sample. A process of rapid vibrational energy pooling leads to infrared emission from a manifold of vibrationally excited states of CO between $v=4$ and 30. Populating vibrationally excited states results first from a sequence of energy transfer processes shown in Eq. 1.



Here the integers represent CO's vibrational quantum number, v . These processes collect or "pool" vibrational energy into a fraction of the CO sample, eventually depleting the laser-prepared $\text{CO}(v=1)$ population. The highest value of v reached by these processes occurs when $\Delta\epsilon(v)$ —the energy release, which increases monotonically with v —exceeds the energy of the highest-frequency transverse phonon of NaCl (2*T*). This occurs above $v=7$. Slower but still important processes allow pooling to even higher vibrational states.



Again, only those processes in which $\Delta\epsilon(n, m)$ is less than the highest transverse phonon energy are important; m and n are between about 7 and 25. The larger average distance between these molecules reduces the rate of pooling.

With the use of an improved SNSPD-based spectrometer (24), two spectral progressions were resolved and assigned according to the combs of Fig. 1. We fit these two vibrational progressions using an energy expression for a harmonic oscillator with two anharmonic corrections

$$\begin{aligned} E(v) = & \hbar c \omega_e(v + 1/2) - \\ & \hbar c \omega_e x_e(v + 1/2)^2 + \hbar c \omega_e y_e(v + 1/2)^3 \end{aligned} \quad (3)$$

where h is Planck's constant, c is the speed of light, ω_e is the harmonic frequency, and $\omega_e x_e$ and $\omega_e y_e$ are anharmonic constants. The anharmonic nature of the C–O bond leads to an increasing shift of the overtone emission wave number, $\tilde{\nu}$, to lower values with increasing vibrational quantum number as can be seen from Eq. 4

$$\begin{aligned} \tilde{\nu} = \frac{1}{\lambda} = & \frac{E(v) - E(v-2)}{\hbar c} = 2\omega_e + \\ & (-4v+2)\omega_e x_e + (6v^2 - 6v + 7/2)\omega_e y_e \end{aligned} \quad (4)$$

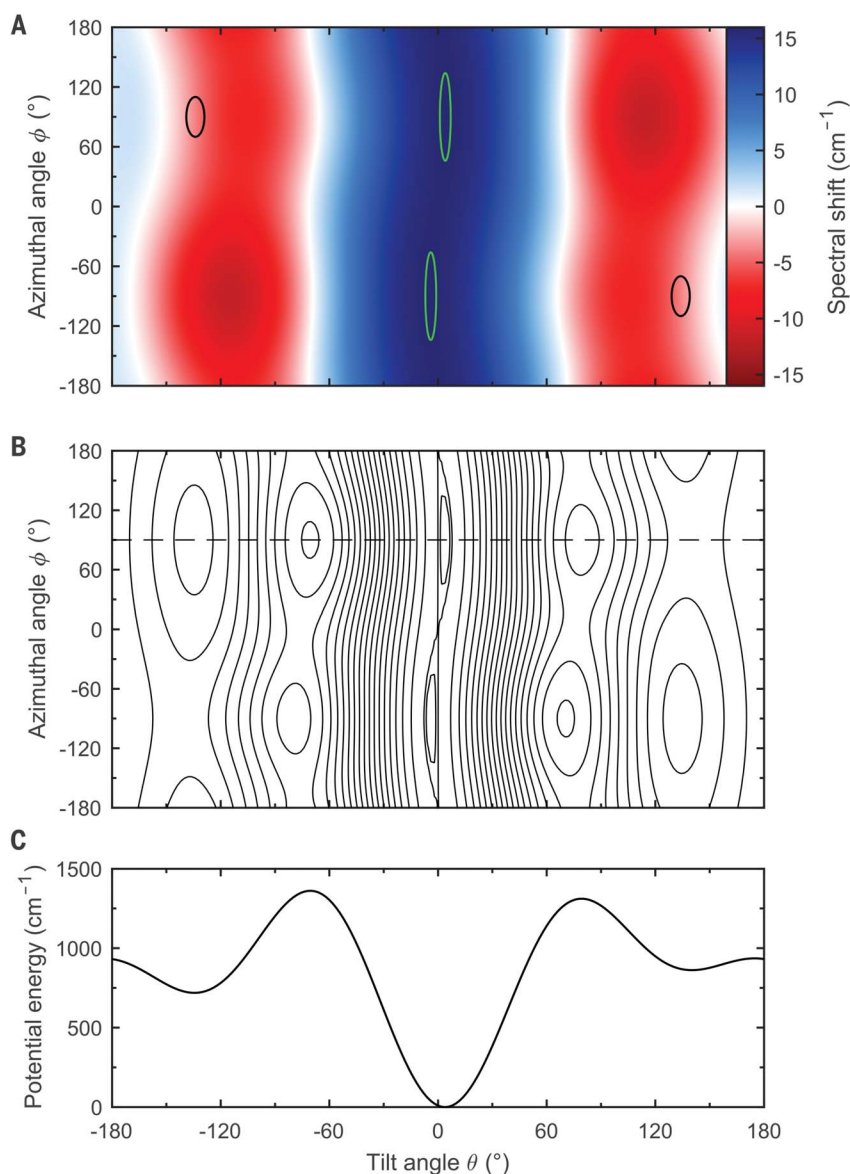


Fig. 2. Calculated dependence of the spectral frequency shift on the molecular orientation. (A) Changing the orientation of CO at NaCl results in frequency shifts due to electrostatic interactions with its surroundings. This spectral shift is calculated explicitly for the $v=0 \rightarrow 1$ transition. Green ovals indicate global minima on the electrostatic potential for $\text{CO}(v=0)$ with a C-down orientation. Black ovals indicate local minima for the O-down structure separated by a barrier much larger than $k_B T$ (k_B , Boltzmann constant; T , temperature). Minima indicated by the same color correspond to identical orientations. The model predicts a blue shift for the C-down structure (+15.9 cm⁻¹) and a red shift for the O-down structure (−3.9 cm⁻¹). All shifts in wave number are relative to the isolated gas-phase molecule. (B) Vibrationally adiabatic electrostatic potential surface for the rotation of a single $\text{CO}(v=0)$ molecule in the monolayer structure. The contour lines show multiples of 75 cm⁻¹. Contour lines for 5 and 10 cm⁻¹ have been added around $\theta = 0^\circ$ to illustrate the shallow global minimum. (C) Cut through the potential surface at $\phi = 90^\circ$, as indicated by the dashed line in (B).

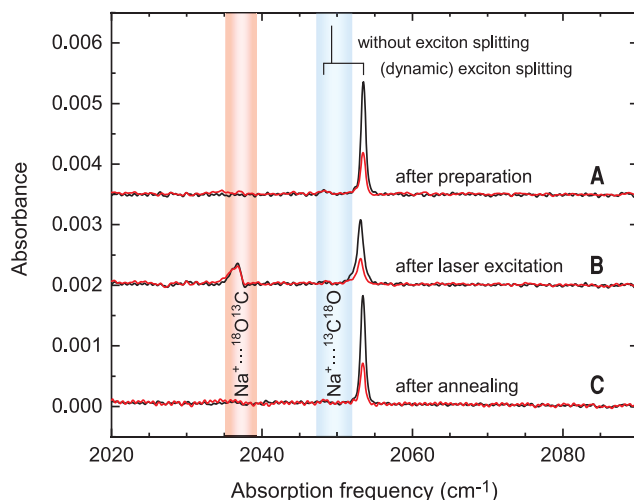
where λ is the emission wavelength. The fitting procedure leads to precise values of ω_e , $\omega_e x_e$, and $\omega_e y_e$ for both spectral progressions. Table S1 displays these vibrational constants and extrapolated fundamental frequencies, along with reported values for gas-phase $^{13}\text{C}^{18}\text{O}$. The fundamental frequencies of the two emitters are shifted from that of the gas-phase molecule,

but in opposite directions (+7.6 and −9.3 cm⁻¹). The harmonic frequencies ω_e show similar shifts, and $\omega_e x_e$ and $\omega_e y_e$ are slightly increased for both emitters.

The changes in the spectroscopic constants can be understood as a perturbation of the gas-phase molecule due to electrostatic interactions with its environment. A CO molecule

Fig. 3. Polarization-dependent FTIR spectrum of the two emitters in a buried monolayer. (A) The $^{13}\text{C}^{18}\text{O}$ monolayer was

prepared on NaCl(100) and covered with ~100 monolayers of $^{12}\text{C}^{16}\text{O}$. Similar to the bare monolayer, the C-down structure shows a doublet with frequencies at 2048.2 and 2053.5 cm^{-1} due to vibrational exciton splitting. The splitting and the estimated frequency without splitting, as it would appear in emission, are indicated above the peaks (24). (B) The same sample has been irradiated with an infrared laser, inducing vibrational energy pooling in the buried $^{13}\text{C}^{18}\text{O}$ monolayer. The C-down absorption is reduced in intensity and a new absorption appears red-shifted by ~15 cm^{-1} , consistent with the prediction of the electrostatic model presented in Fig. 2. The red and blue bands indicate the positions of the $^{13}\text{C}^{18}\text{O}(v=0 \rightarrow 1)$ transition, as predicted from the vibrational constants of table S1 derived from the infrared emission spectrum in fig. S3. The vertical line labeled “without exciton splitting” should be compared to the blue band. (C) FTIR spectrum obtained after annealing the sample to 22 K for 20 min. The O-down isomer has been converted back to the C-down structure. For all three curves, black and red spectra were recorded with a p- and s-polarized light source, respectively, and the effective resolution is ~0.7 cm^{-1} . Small absorption features due to impurities in the overlayer have been subtracted from all three spectra.



in vibrational state v will exhibit first-order energy corrections described by

$$E^{(1)} = f(\vartheta, \phi) F \mu_{vv} + g(\vartheta, \phi) \frac{\partial F}{\partial z} \Theta_{vv} + h(\vartheta, \phi) \frac{\partial^2 F}{\partial z^2} \Omega_{vv} + \dots \quad (5)$$

when interacting with the local electric field, F , at a distance z from the NaCl(100) surface. Here, μ_{vv} , Θ_{vv} , and Ω_{vv} are the expectation values of the dipole, quadrupole, and octopole moments of CO in the vibrational state v . $f(\vartheta, \phi)$, $g(\vartheta, \phi)$, and $h(\vartheta, \phi)$ describe the orientation dependence of the interactions. As in Eq. 3, the expectation values of the multipole moments can be represented as a power series in $(v+1/2)$. For a given orientation, linear terms in $(v+1/2)$ give rise to a shift in ω_e , whereas quadratic and cubic terms lead to shifts in $\omega_e x_e$ and $\omega_e y_e$, respectively. Therefore, the emission frequencies of vibrational states below $v=5$, for which the multipole moments are well described by a linear function (table S3), should show the same shift relative to the gas-phase frequencies. In fact, the experimental frequency shifts for $v \leq 10$ are identical within the uncertainty of the measured peak positions. For higher vibrational states, electrostatically induced changes in the anharmonic constants, $\omega_e x_e$ and $\omega_e y_e$, produce additional contributions to the frequency shifts. Unfortunately, accurate values of μ_{vv} , Θ_{vv} , and Ω_{vv} are not available for such high states, and this pre-

vents a meaningful comparison of the experimentally observed frequencies with the predictions from an electrostatic model. Therefore, in the following analysis we restrict such comparisons to the observed fundamental frequency shift, where anharmonic contributions can be neglected.

The blue and red shifts of the fundamental frequencies from the gas-phase value are a direct result of the two emitters exhibiting different orientations on the NaCl surface. To envision this, consider the dipolar contribution to the interaction with the local electric field of the surface for the C-down molecule. In this case, the interaction is attractive, but because $|\mu_{00}|$ is greater than $|\mu_{11}|$, the $v=0$ state is more stabilized by the interaction than is the $v=1$ state—this gives rise to a blue-shifted transition. For the O-down molecule, the interaction is repulsive and, for the same reason, the $v=1$ level is less destabilized than the $v=0$ level—this gives rise to a red shift.

All multipole interactions with the surface and the neighboring CO molecules must be considered to correctly obtain the frequency shift. We have constructed an electrostatic model of the frequency shift including dipole, quadrupole, and octopole contributions (24). The calculated fundamental frequency shifts depend on two orientational angles (Fig. 2A). In this model, the CO bond of the C-down molecule is nearly normal to the surface with a tilt angle $\theta = 4^\circ$ (Fig. 2, B and C). The O-down molecule is found at $\theta = 134^\circ$ (i.e., the CO

bond is tilted by 46° from the surface normal). The calculated frequency shifts of +15.9 and -3.9 cm^{-1} for the C-down and O-down isomer, respectively, as well as the total frequency splitting are in good qualitative agreement with the experimental shifts of +7.6 and -9.3 cm^{-1} . A similar positive offset is observed for the frequency shift of an isolated CO molecule adsorbed on NaCl (24). This analysis shows that both emitters are perturbed gas-phase CO molecules, altered by their electrostatic interactions with the NaCl surface and nearby CO molecules, and that they result from different orientational isomers.

Although only the C-down species is excited to $v=1$ initially, the vibrational levels of both orientational isomers are close in energy and, thus, energy transfer processes as in Eqs. 1 and 2 are also possible between molecules in different orientations. Assuming that the total vibrational energy is evenly distributed between C-down and O-down, a crude estimate of the steady-state fraction of O-down molecules (46%) can be derived from the average intensity ratio between equal vibrational states in Fig. 1. The O-down isomer in the monolayer does not convert back to the C-down structure during the ~10 ms in which infrared fluorescence is observed. But its lifetime is sufficiently short that an absorption or laser-induced fluorescence (LIF) excitation spectrum for the O-down species could not be obtained (we require minutes to move the sample into position for an absorption experiment or to attempt to record a LIF spectrum of the O-down isomer).

The O-down isomer can, however, be stabilized indefinitely if we perform the vibrational energy pooling experiment on a buried monolayer. Using pulsed molecular beam dosing (fig. S1B), a $^{13}\text{C}^{18}\text{O}$ monolayer sample was prepared on NaCl(100), and a $^{12}\text{C}^{16}\text{O}$ overlayer was deposited on top of it. Just as for the uncovered monolayer, we observe vibrational energy pooling and infrared emission spectra that show two emitters (C-down and O-down) when the infrared laser is used to selectively excite $^{13}\text{C}^{18}\text{O}(v=0 \rightarrow 1)$ in the buried monolayer (fig. S3).

The long lifetime of O-down CO in the buried monolayer allows us to obtain its infrared absorption spectrum. Figure 3 shows three Fourier transform infrared (FTIR) absorption spectra obtained with various treatments of the buried monolayer. Initially after sample preparation, only the C-down species is present with absorption features at 2048.2 and 2053.5 cm^{-1} , blue-shifted from the CO gas-phase absorption at 2043.7 cm^{-1} . The strong polarization dependence of the absorption results from the geometry of the experiment and the near-normal orientation of the CO bond in the adsorbed species (25, 26). After ~6000 pulses of IR light have irradiated the sample and induced vibrational energy pooling, the absorption of C-down

is reduced and a new absorption is seen at 2037 cm^{-1} , red-shifted from the gas-phase value. The red and blue bands of Fig. 3 indicate the predicted positions of the $^{13}\text{C}^{18}\text{O}(v = 0 \rightarrow 1)$ transition, as determined from the vibrational constants of table S1 derived from the infrared emission spectrum in fig. S3. The lack of a polarization dependence for the O-down absorption indicates a tilt angle, θ , consistent with the predictions of the electrostatic model of Fig. 2. Finally, Fig. 3C shows the full recovery of the C-down isomer and loss of the O-down isomer when the sample has been annealed to 22 K for ~ 20 min.

In this work, we observed infrared emission and absorption spectra of two orientational isomers of CO adsorbed to NaCl(100) and discovered how the C-down isomer can be converted to the less stable O-down isomer through infrared laser excitation. Our findings emphasize that, in contrast to most previously studied systems that exhibit a single orientation necessary to form a chemical bond between the molecule and the surface, adsorbates bound by electrostatic interactions exhibit more diverse adsorption geometries that are more easily interconverted, owing to the vibrational dependence of the electrostatic interactions. Ground-state CO has a dipole oriented as $\text{C}^{\delta-}\text{O}^{\delta+}$ (table S3), which leads to an electrostatic bond with the C atom adjacent to a Na^+ ion. In the high vibrational states observed in this work, the dipole moment reverses sign ($\text{C}^{\delta+}\text{O}^{\delta-}$), contributing a force that can rotate the molecule to the O-down configuration. Yet this simplified picture, although intuitively appealing, neglects a number of potentially important effects. If a full-dimensional potential energy surface can be calculated, as has been accomplished for other condensed-phase systems (27), quantum dynamics of isomerization can be studied with theory and compared to experimental results, leading to a deeper understanding of this phenomenon.

Many future experiments are now possible. Relevant to better understanding the quantum nature of isomerization, the lifetime of the O-down interconversion to C-down can be directly measured, and state-to-state pathways from one isomer to another can be mapped using time-resolved pump-probe methods. Beyond this, other examples of switchable adsorbates are also likely to be found in the future, because systems dominated by weak electrostatic interactions are common. Candidates for future study include CO on other salt crystals and CO on insulating solids such as hydrogen-terminated diamond, hydrogen-terminated silicon, and metal oxides. Because substrate variation can strongly influence both the vibrational energy pooling and the relative stability of the two isomers, controlled switching between the isomers may also be achievable. Electronic excitation of CO to the $\text{a}^3\Pi$ state also results in sudden changes in both the sign and magnitude of the dipole moment (28) that likely lead to reorientation and intersystem crossing to the ground state. The use of electronic excitation to induce isomerization in such condensed-phase systems promises another experimental approach to quantum-state-resolved isomerization. Such detailed experimental studies provide a fruitful breeding ground for new and accurate theoretical studies of condensed-phase quantum isomerization.

REFERENCES AND NOTES

1. P. Nogly *et al.*, *Science* **361**, eaat0094 (2018).
2. V. I. Prokhorenko *et al.*, *Science* **313**, 1257–1261 (2006).
3. T. Kobayashi, T. Saito, H. Ohtani, *Nature* **414**, 531–534 (2001).
4. M. Tsuda, M. Giaccum, B. Nelson, T. G. Ebrey, *Nature* **287**, 351–353 (1980).
5. T. Kudernac *et al.*, *Nature* **479**, 208–211 (2011).
6. A. Safiei, J. Henzl, K. Morgenstern, *Phys. Rev. Lett.* **104**, 216102 (2010).
7. B. Y. Choi *et al.*, *Phys. Rev. Lett.* **96**, 156106 (2006).
8. C. E. Hamilton, J. L. Kinsey, R. W. Field, *Annu. Rev. Phys. Chem.* **37**, 493–524 (1986).
9. C. Kittrell *et al.*, *J. Chem. Phys.* **75**, 2056–2059 (1981).

10. X. M. Yang, C. A. Rogaski, A. M. Wodtke, *J. Opt. Soc. Am. B* **7**, 1835 (1990).
11. D. M. Jonas, X. M. Yang, A. M. Wodtke, *J. Chem. Phys.* **97**, 2284–2298 (1992).
12. M. Silva, R. Jongma, R. W. Field, A. M. Wodtke, *Annu. Rev. Phys. Chem.* **52**, 811–852 (2001).
13. M. P. Jacobson, R. W. Field, *J. Phys. Chem. A* **104**, 3073–3086 (2000).
14. Y. Q. Chen, D. M. Jonas, J. L. Kinsey, R. W. Field, *J. Chem. Phys.* **91**, 3976–3987 (1989).
15. H. Ishikawa *et al.*, *Annu. Rev. Phys. Chem.* **50**, 443–484 (1999).
16. J. A. DeVine *et al.*, *Science* **358**, 336–339 (2017).
17. T. R. Dyke, B. J. Howard, W. Klemperer, *J. Chem. Phys.* **56**, 2442–2454 (1972).
18. J. M. Bowman, B. Gazdy, J. A. Bentley, T. J. Lee, C. E. Dateo, *J. Chem. Phys.* **99**, 308–323 (1993).
19. M. Joyeux, S. C. Farantos, R. Schinke, *J. Phys. Chem. A* **106**, 5407–5421 (2002).
20. L. Chen *et al.*, *Opt. Express* **26**, 14859–14868 (2018).
21. L. Chen *et al.*, *Science* **363**, 158–161 (2019).
22. L. Chen *et al.*, *Acc. Chem. Res.* **50**, 1400–1409 (2017).
23. H. C. Chang, G. E. Ewing, *Phys. Rev. Lett.* **65**, 2125–2128 (1990).
24. See supplementary materials.
25. D. Schmicker, J. P. Toennies, R. Vollmer, H. Weiss, *J. Chem. Phys.* **95**, 9412–9415 (1991).
26. J. Heidberg, E. Kampshoff, M. Suhren, *J. Chem. Phys.* **95**, 9408–9411 (1991).
27. Y. Wang, B. C. Shepler, B. J. Braams, J. M. Bowman, *J. Chem. Phys.* **131**, 054511 (2009).
28. B. G. Wicke, R. W. Field, W. Klemperer, *J. Chem. Phys.* **56**, 5758–5770 (1972).

ACKNOWLEDGMENTS

Funding: We acknowledge support from the MPS-EPFL joint international Center in Molecular Nanoscience and Technology.

Author contributions: J.A.L. performed infrared emission spectroscopy experiments, analyzed data, and constructed the electrostatic model. A.C. performed infrared emission spectroscopy experiments and analyzed data. L.C. and D.S. built and commissioned the instrument. V.B.V. developed the SNSPDs used in this work. A.M.W. conceived the experiment and wrote the first draft of the paper. A.M.W., V.B.V., D.S., J.A.L., and A.C. also participated in writing and revising the paper. **Competing interests:** None declared. **Data and materials availability:** All data needed to evaluate the conclusions in the paper are present in the paper or the supplementary materials.

SUPPLEMENTARY MATERIALS

science.sciencemag.org/content/367/6474/175/suppl/DC1
Materials and Methods
Supplementary Text
Figs. S1 to S4
Tables S1 to S3
References (29–40)

1 September 2019; accepted 13 November 2019
10.1126/science.aaz3407

CHEMICAL PHYSICS

Observation of the fastest chemical processes in the radiolysis of water

Z.-H. Loh^{1*}, G. Doumy², C. Arnold^{3,4,5}, L. Kjellsson^{6,7}, S. H. Southworth², A. Al Haddad², Y. Kumagai², M.-F. Tu², P. J. Ho², A. M. March², R. D. Schaller^{8,9}, M. S. Bin Mohd Yusof¹, T. Debnath¹, M. Simon¹⁰, R. Welsch^{3,5}, L. Inhester³, K. Khalili¹¹, K. Nanda¹², A. I. Krylov^{3,12}, S. Moeller¹³, G. Coslovich¹³, J. Koralek¹³, M. P. Minitti¹³, W. F. Schlotter¹³, J.-E. Rubensson⁶, R. Santra^{3,4,5*}, L. Young^{2,14*}

Elementary processes associated with ionization of liquid water provide a framework for understanding radiation-matter interactions in chemistry and biology. Although numerous studies have been conducted on the dynamics of the hydrated electron, its partner arising from ionization of liquid water, H_2O^+ , remains elusive. We used tunable femtosecond soft x-ray pulses from an x-ray free electron laser to reveal the dynamics of the valence hole created by strong-field ionization and to track the primary proton transfer reaction giving rise to the formation of OH. The isolated resonance associated with the valence hole ($\text{H}_2\text{O}^+/\text{OH}$) enabled straightforward detection. Molecular dynamics simulations revealed that the x-ray spectra are sensitive to structural dynamics at the ionization site. We found signatures of hydrated-electron dynamics in the x-ray spectrum.

Radiolysis of liquid water is a universal phenomenon that accompanies the interaction of high-energy radiation with matter in aqueous environments. It is of fundamental importance in many domains (1), including water-cooled nuclear reactors where radiolysis products cause corrosion (2). Living organisms consist of 80% water by weight (3); hence, the detection of radiation-induced genomic damage via radiolysis of water is foundational to medical treatment, diagnosis, and even extended human space flight (4).

Although ionizing radiation is delivered via various vehicles (x-rays, γ -rays, charged particles), its interaction with matter can be understood conceptually as individual absorption events along the particle path accompanied by a cascade of electrons, ions, and radicals (5). Consider the most elementary process: ionization of pure liquid water, which leads to the formation of a hydrated-electron precursor and a cationic hole (H_2O^+). Both spe-

cies are very reactive. The dynamics of the hydrated electron, e_{aq}^- , has been the subject of numerous studies (6–11) since the discovery of its visible spectrum (12), which peaks at 718 nm and spans 500 to 1000 nm, a range convenient for ultrafast laser spectroscopies. In stark contrast, its ionization partner, H_2O^+ , has not been experimentally detected. The H_2O^+ is predicted to undergo rapid sub-100-fs proton transfer to a neighboring water molecule to yield the hydronium cation (H_3O^+) and the hydroxyl radical (OH) (1, 13, 14). Attempts to directly observe the H_2O^+ cation using ultrafast visible or ultraviolet probes have been inconclusive because of its ultrashort lifetime and masked spectral signature (6, 14, 15). Thus, basic questions regarding the ionization of water remain. What is the lifetime of H_2O^+ ? What are the absorption spectra of H_2O^+ and OH? What is the extent of hole delocalization in H_2O^+ and its time scale for localization relative to proton transfer?

Here, we introduce an ultrafast x-ray probe that enables us to track the primary chemical reaction following ionization of liquid water, namely $\text{H}_2\text{O}^+ + \text{H}_2\text{O} \rightarrow \text{OH} + \text{H}_3\text{O}^+$. Combined experiment and theory yield insight for this newly accessible spectral regime. X-rays are well suited for probing the short-lived H_2O^+ cation and OH radical, as their absorption lines fall cleanly in the water window. Removal of an electron from the outermost valence orbital ($1b_1$) of H_2O produces a new transition for H_2O^+ that is red-shifted from the $1a_1 \rightarrow 4a_1$ pre-edge transition at 535 eV (16) roughly by the highest occupied molecular orbital–lowest unoccupied molecular orbital (HOMO–LUMO) gap ΔE (17), as shown in Fig. 1A. The OH radical, isoelectronic to H_2O^+ , possesses a nearby x-ray absorption resonance, whereas the other product of proton transfer, H_3O^+ , has resonances that fall in a region of strong water

absorption (Fig. 1B). Figure 1C shows the experimental configuration, consisting of a 60-fs, 800-nm strong-field ionization pump (10), a tunable ~ 30 -fs ultrafast x-ray probe from the Linac Coherent Light Source (LCLS) x-ray free electron laser (XFEL) (18), and three photon-in/photon-out detection channels.

Signatures of the impulsively produced valence hole and excess electron appeared in all three detection channels when the incident x-ray energy was scanned. Figure 2A displays data from the dispersed fluorescence channel, whereas the transmission mode is used in Fig. 2, B to D. Figure 2A shows absorption before and after ionization ($\Delta t < 0$ ps and $\Delta t > 100$ fs, respectively). At negative time delay, the absorption is that of liquid water—that is, nonresonant ionization of the valence and inner-valence levels of water plus the pre-edge transition. (Saturation effects prevented a clear observation of the pre-edge resonance.) At positive time delay, two new features are apparent: an absorption resonance at 525.9 eV and a shift of the pre-edge absorption to lower energies. The new absorption resonance is consistent with the creation of a hole in the outermost valence level of liquid water. The corresponding H_2O^+ transition energy can be estimated to be 526.9 eV using the binding energies in liquid water of the O 1s core level (538.1 eV) (19) and the $1b_1$ HOMO (11.2 eV) (20). The isoelectronic OH exhibits a gas-phase absorption peak at 525.85 eV (21).

The H_2O^+ cation produced by the ionization of liquid water is widely expected to decay via a pseudo-first-order reaction involving proton transfer to a neighboring water molecule,



to yield the OH radical and the H_3O^+ species. In the absence of electron scavengers, the OH radical subsequently undergoes geminate recombination (22) with the ejected electron to give OH $^-$. The time-resolved differential absorption spectrum, $\Delta A = A(\Delta t) - A(\Delta t < 0)$, showed a prompt increase at time zero, followed by a narrowing of the spectral width within the first picosecond, and finally a gradual decay at longer time delays (Fig. 2B). We modeled this behavior as sequential kinetics: The species initially produced by ionization decays with lifetime τ_1 to give an intermediate species with lifetime τ_2 , with absorption spectra $S_1(E)$ and $S_2(E)$, respectively.

We assigned $S_2(E)$, obtained by averaging ΔA for time delays between 1.5 and 5.8 ps, to the OH radical (Fig. 2C). $S_2(E)$ can be fit to a sum of two Lorentzians: a main peak at 525.97 ± 0.08 eV and a sideband, weaker by a factor of ~ 7 , at 526.45 ± 0.12 eV. The 0.48-eV energy spacing between the two peaks is in reasonable agreement with the 0.53-eV spacing of the vibrational progression for core-excited

¹Division of Chemistry and Biological Chemistry, School of Physical and Mathematical Sciences, Nanyang Technological University, Singapore. ²Chemical Sciences and Engineering Division, Argonne National Laboratory, Lemont, IL, USA.

³Center for Free-Electron Laser Science, DESY, Hamburg, Germany.

⁴Department of Physics, Universität Hamburg, Hamburg, Germany.

⁵Hamburg Centre for Ultrafast Imaging, Hamburg, Germany.

⁶Department of Physics and Astronomy, Uppsala University, Uppsala, Sweden.

⁷European XFEL GmbH, Schenefeld, Germany.

⁸Center for Nanoscale Materials, Argonne National Laboratory, Lemont, IL, USA.

⁹Department of Chemistry, Northwestern University, Evanston, IL, USA.

¹⁰Sorbonne Université and CNRS, Laboratoire de Chimie Physique-Matière et Rayonnement, LCPMR, F-75005 Paris, France.

¹¹Department of Energy Conversion and Storage, Technical University of Denmark, Roskilde, Denmark.

¹²Department of Chemistry, University of Southern California, Los Angeles, CA, USA.

¹³Linac Coherent Light Source, SLAC National Accelerator Laboratory, Menlo Park, CA, USA.

¹⁴Department of Physics and James Franck Institute, University of Chicago, Chicago, IL, USA.

*Corresponding author. Email: zhiheng@ntu.edu.sg (Z.-H.L.); robin.santra@cfeel.de (R.S.); young@anl.gov (L.Y.)

gas-phase OH (21). Both peaks have a common FWHM (full width at half maximum) of 0.48 ± 0.02 eV, considerably broader than the 0.1-eV spectral bandwidth of the XFEL pulses and the 0.147-eV natural linewidth (21), which suggests inhomogeneous broadening by the solvent environment.

With the x-ray absorption line shape of the aqueous OH radical $S_2(E)$ determined, the next step is to extract the time constants τ_1 and τ_2 and the spectral line shape of the short-lived component $S_1(E)$. We used a Gaussian instrument response function of 106-fs FWHM and performed a surface fit of the experimental data shown in Fig. 2B. (We did not convolve the kinetic model with the experimental energy resolution of 0.1-eV FWHM because the experimentally observed spectral features were much broader.) The surface fit yielded $\tau_1 = 0.18 \pm 0.02$ ps, $\tau_2 = 14.2 \pm 0.4$ ps, and a Lorentzian absorption line shape $S_1(E)$ centered at 526.01 ± 0.13 eV with a FWHM of 0.98 ± 0.04 eV. The decay of the OH radical, τ_2 , most likely originates from geminate recombination of the OH radical with a hydrated electron. The recombination time constant of 14.2 ± 0.4 ps is considerably shorter than those reported in the literature (22), most likely because of the high initial ionization fraction accelerating the geminate recombination process. Geminate recombination between e_{aq}^- and OH in ionized liquid water has been extensively investigated by time-resolved optical spectroscopy (22) and is beyond the scope of the present study. Nonetheless, considering the relative diffusion coefficients of the reactants and the reaction radius, our observed time scale for geminate recombination suggests an approximate ionization fraction of 1.7%, in relatively good agreement with the ionization fraction estimated on the basis of OH x-ray absorbance (see below). The spectral line shape $S_1(E)$ and time constant τ_1 can be assigned either to the decay of H_2O^+ or to the cooling of a vibrationally hot OH radical. Both species should exhibit a larger spectral linewidth than the OH radical. The x-ray absorption linewidth of H_2O^+ may be similar to the 1.5 eV-wide $1b_1$ band in the valence photoelectron (20) and the x-ray emission spectra (23) of liquid water, whose widths have been attributed to a multitude of hydrogen-bonding configurations and intermolecular geometries. The x-ray absorption spectrum of vibrationally excited OH may be broadened if additional hot-band transitions are present.

Further insight into the early-time dynamics was obtained with time traces at three selected photon energies: 525.43, 525.93, and 526.73 eV (Fig. 2D). These time traces correspond to the isotropic signal $\Delta A_{iso} = (\Delta A_{||} + 2\Delta A_{\perp})/3$, reconstructed from measurements in which the relative polarizations of the pump and probe pulses are parallel ($\Delta A_{||}$) and perpendicular

(ΔA_{\perp}). ΔA_{iso} is independent of rotational reorientation of the transient species in solution and is therefore sensitive only to population dynamics. Upon inspection, the ΔA_{iso} time trace for 525.93 eV shows a markedly delayed rise relative to those for 525.43 and 526.73 eV. Attempts to perform a global fit with two time constants could not reproduce the early-time dynamics (see supplementary materials). The presence of this delayed rise suggests the existence of an additional ultrafast process (24) that was not captured in our analysis of the two-dimensional dataset shown in Fig. 2B. Indeed, global fitting of the ΔA_{iso} time traces revealed a new component with a time constant of 46 ± 10 fs, whereas the other two time constants extracted from the fit, 0.16 ± 0.03 ps and 9.2 ± 1.3 ps, are comparable to those obtained from the analysis of the dataset shown in Fig. 2B. This additional time constant appeared as a growth component at 525.93 eV and, to a smaller extent, at 526.73 eV

as well, hence accounting for their delayed appearances relative to the signal at 525.43 eV, which rose with the instrument response function (where prompt absorption by vertically ionized water is expected from the calculated relative positions of the OH and H_2O^+ resonances). That the 46-fs component manifested itself as a growing signal at 525.93 eV, near the peak position of the OH radical absorption maximum at 525.97 eV, strongly suggests that it reflects the time scale for the formation of the OH radical. Given that OH is formed from the decay of the H_2O^+ radical cation, this interpretation would therefore suggest a lifetime of 46 fs for the H_2O^+ radical cation. The experiments were conducted at near-ambient temperature, making them practically relevant. In this non-equilibrium situation, any local temperature rise does not affect the ultrafast proton transfer time scale.

To understand the observed ultrafast dynamics, we performed quantum mechanical

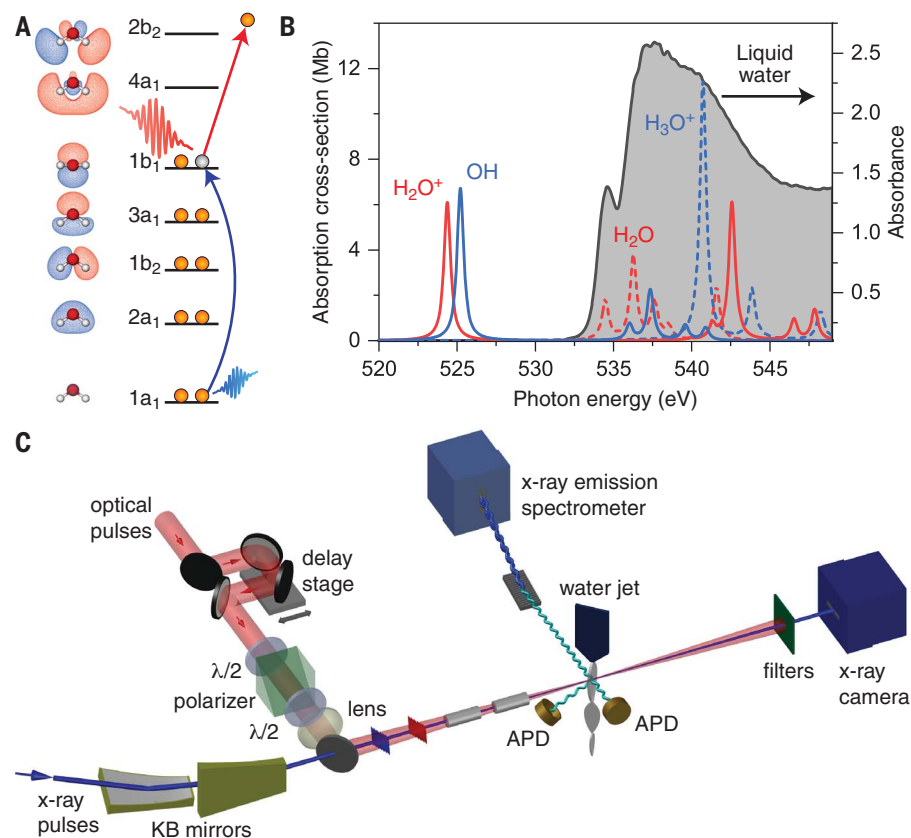


Fig. 1. Ultrafast x-ray laser probe of ionization dynamics of liquid water. (A) Ionization of H_2O produces H_2O^+ with a strong isolated soft x-ray absorption resonance ($1a_1 \rightarrow 1b_1$). (B) Absorption resonances in the gas phase for the four species associated with elementary proton transfer: $H_2O^+ + H_2O \rightarrow OH + H_3O^+$ calculated with 6-311(2+,+)G(2df,p) basis with uncontracted core (oxygen) using fc-cvs-EOM-CCSD (36). Only H_2O^+ and OH fall outside the region of strong absorption by liquid water (37) (i.e., in the water window). (C) Schematic of the experimental setup: 800-nm strong-field ionization pump and time-delayed x-ray probe. The x-ray probe is monitored simultaneously in transmission, total fluorescence and dispersed fluorescence as a function of pump-probe time delay and incident photon energy (see supplementary materials).

and classical (QM/MM) excited-state molecular dynamics simulations of liquid water following strong-field ionization. We considered initial ionization in the upper 1.5 eV of the valence band and averaged across 107 initial geometries of liquid water. Non-Born-Oppenheimer effects were taken into account by Tully's fewest-switches surface-hopping approach (25). We combined a QM description of a $(\text{H}_2\text{O})_{12}^+$ cluster with an MM description of surrounding water molecules. The electronic structure was obtained at the Hartree-Fock level of theory using Koopmans' theorem to obtain singly ionized states and using the 6-31G basis set as implemented in our software package XMOLECULE (26, 27) (see supplementary materials).

Our simulations explored to what extent transient x-ray absorption is sensitive to ultrafast structural dynamics in water. The time-resolved x-ray absorption spectrum of the valence hole is shown in Fig. 3A for the first 100 fs after the initial hole formation. Although initially electronic states down to HOMO-6 were populated, the trajectories arrived at the cationic ground state within 25 fs (Fig. 3B) and non-Born-Oppenheimer effects were no longer present. This was accompanied by hole localization on a comparable time scale.

Proton transfer can be characterized by the distance between the charge and hole center. Directly after ionization, the charge and hole are overlapped at the H_2O^+ ; as proton transfer proceeds, the hole stays on the OH moiety, while the charge is carried away by the H_3O^+ (14). Figure 3C shows that the charge-hole separation is correlated with the completion of proton transfer. Within our model using bond-order analysis (28), the proton transfer time scale was found to be 60 fs, in good agreement with (14). We further investigated the chemical environment surrounding the $\text{H}_2\text{O}^+/\text{OH}$, where the valence hole is located, to extract correlations with x-ray spectral signatures. The average distance from the $\text{H}_2\text{O}^+/\text{OH}$ oxygen to the nearest H_2O oxygen is shown in Fig. 3D along with the spectral shift (the peak position of Fig. 3A). Initially, the partially negatively charged oxygens are pulled toward the region of positive charge (H_2O^+), giving rise to the redshift of the absorption peak. This motion initiates proton transfer; thus, at the point of maximum redshift, proton transfer is only about 25% complete (Fig. 3C). As a consequence of charge-hole separation, the distance between OH and the neighboring oxygens increases, and the redshift shrinks. In this way, proton transfer is indirectly reflected in the time evolution of the x-ray absorption peak position.

The results presented here offer insight into the elementary dynamics of the highly reactive and short-lived ion and neutral radical species in ionized liquid water. Our experimental

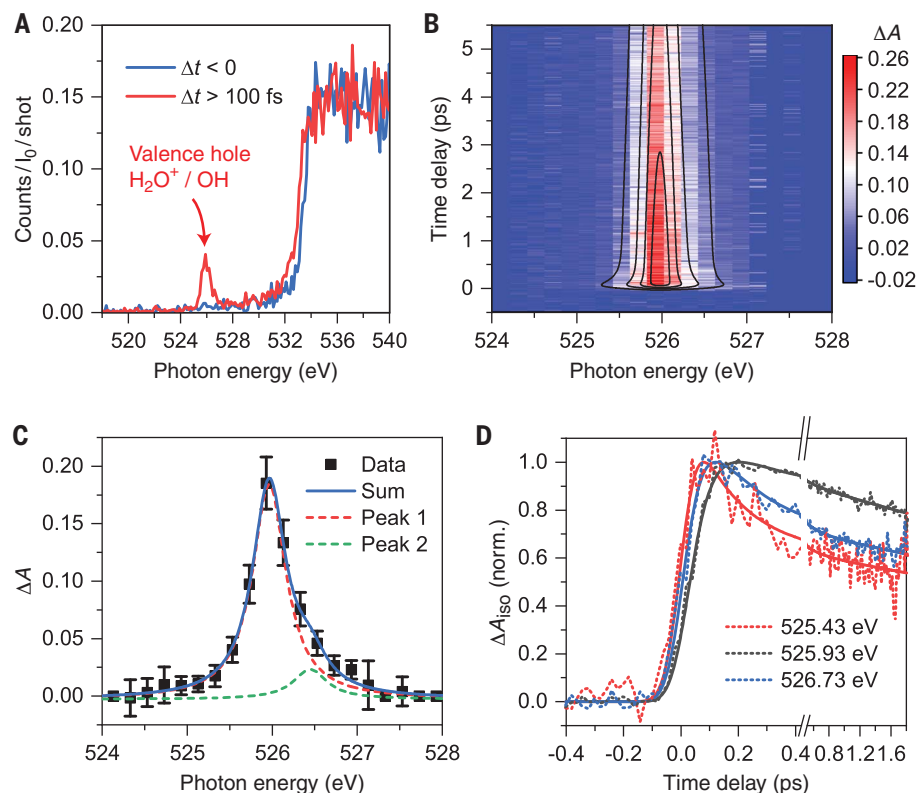


Fig. 2. Transient x-ray absorption spectroscopy for the reaction $\text{H}_2\text{O}^+ + \text{H}_2\text{O} \rightarrow \text{OH} + \text{H}_3\text{O}^+$.

(A) Absorption for $\Delta t < 0$ and $\Delta t > 100$ fs monitored through the dispersed fluorescence channel. (B) Differential absorption ΔA in the valence hole ($\text{H}_2\text{O}^+/\text{OH}$) region. Spectra collected at 216 time delays between 1.5 and 5.8 ps are averaged to produce the resonance profile, which is fit to a sum of two Lorentzians. Error bars denote SD. A total of 31 energy sweeps and 27,546 shots are collected. (C) X-ray absorption spectrum of the aqueous OH radical. (D) Polarization averaged time traces at three x-ray probe energies: 525.43, 525.93, and 526.73 eV.

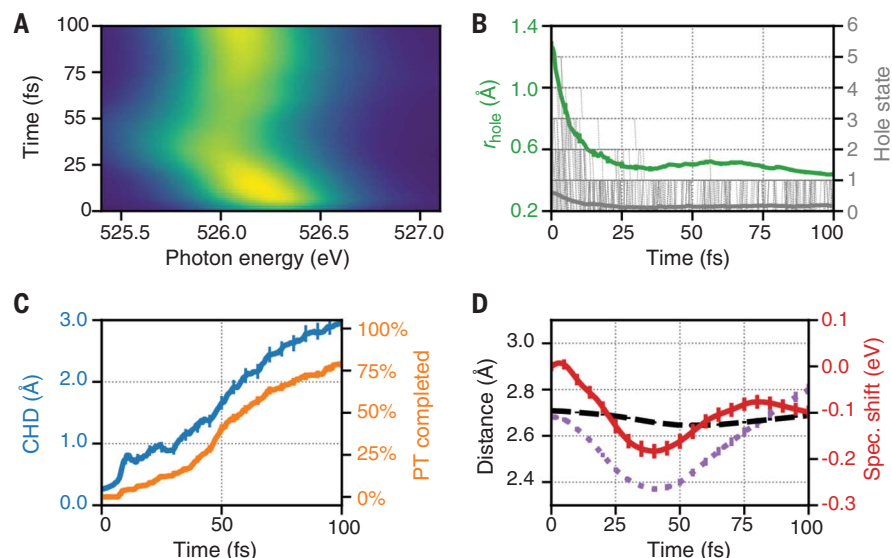


Fig. 3. Calculated x-ray absorption spectra and trajectory analysis. (A) Resonant x-ray absorption spectrum of ionized water. (B) Hole radius (green) and nonadiabatic dynamics (gray, solid line shows average). (C) Charge-hole distance (CHD) (blue) and completed proton transfer percentage (orange). (D) Average distance between oxygens in H_2O molecules (black) along with the average distance of the $\text{H}_2\text{O}^+/\text{OH}$ oxygen to the nearest oxygen (purple) and the spectral shift of the x-ray absorption resonance (red).

approach offers several advantages over previous attempts (6, 14, 15) to determine the lifetime of the elusive H_2O^+ radical cation. First, relative to traditional two-photon ultraviolet photoionization, strong-field ionization provides access to a large concentration of ionized species in solution. Assuming a cross section of ~ 7 Mbarn for the O 1s resonant absorption of the OH radical, we estimated an ionization fraction of $\sim 0.8\%$ under our experimental conditions. Second, the H_2O^+ and OH radicals exhibit strong O 1s \rightarrow 2p-like resonant transitions in the soft x-ray absorption spectra because they possess open O 2p subshells. These resonances occur in the background-free, near-edge spectral region, enabling detection down to concentrations of a few millimolar. In comparison, previous attempts using spectrally resolved visible transient absorption spectroscopy to observe the H_2O^+ radical cation via its predicted absorption signature at 2.3 eV were unsuccessful because its weak absorption was masked by the strong, broad hydrated-electron absorption feature and further complicated by cross-phase modulation artifacts (6, 14, 15).

Our study revealed three distinct time scales in the early-time dynamics of ionized liquid water: 46 ± 10 fs, 0.18 ± 0.02 ps, and 14.2 ± 0.4 ps, tentatively assigned to the decay of the H_2O^+ radical cation via proton transfer, vibrational cooling of the hot OH radical produced from H_2O^+ , and geminate recombination of OH with the hydrated-electron by-product, respectively. The first two processes, hitherto unobserved, are of particular interest. The assignment of the 46-fs component to the lifetime of the H_2O^+ cation is supported by QM/MM molecular dynamics simulations, which predict a lifetime of 60 fs. However, we note that the same simulations also showed that hole localization occurs within 30 fs. As such, with the currently available time resolution, hole localization also contributed to the observed dynamics. On the intermediate time scale, the 0.18-ps component was tentatively assigned to vibrational cooling of hot OH radicals that are produced upon ultrafast proton transfer. The formation of a vibrationally excited OH product from H_2O^+ is likely, considering the 3% change in equilibrium OH bond lengths between gas-phase H_2O^+ (0.9992 \AA) (29) and OH (0.9697 \AA) (30). The assignment of the 0.18-ps component to vibrational relaxation of the OH radical is supported by studies of the OH stretch of liquid H_2O , where numerous time-resolved infrared spectroscopic measurements show vibrational relaxation and vibrational energy transfer occurring within 0.2 to 0.3 ps (31, 32).

We expect that a future study with higher time resolution and signal-to-noise ratios could furnish a more accurate H_2O^+ lifetime and at the same time permit the observation

of ultrafast dynamics involving possible hole alignment, coherences, and nonadiabatic dynamics induced by radiolysis. With improved statistics over a wide range of probe photon energies, we also anticipate the possibility of isolating the spectral signatures of H_2O^+ and the hot OH radical. Interestingly, in addition to valence hole dynamics observed at 526 eV, the soft x-ray probe appeared to be sensitive to the dynamics of the electron that was injected into the solvent by ionization. The spectral changes observed in the vicinity of the pre-edge absorption (531.0 to 533.7 eV) fit a universal time constant of 0.26 ± 0.03 ps that matches previous studies of hydrated-electron formation (7, 8) (see supplementary materials). Future experiments focusing on the pre-edges and main edges of ionized liquid water that require a sub-micrometer-thick liquid jet could potentially yield the electronic energy level diagram of ionized liquid water (33) and shed light on its electronic relaxation dynamics, as well as possibly discern the cavity versus non-cavity model for the structure of the hydrated electron (34).

REFERENCES AND NOTES

- B. C. Garrett *et al.*, *Chem. Rev.* **105**, 355–390 (2005).
- S. Gordon, in *Early Developments in Radiation Chemistry*, J. Kroh, Ed. (Royal Society of Chemistry, 1989), pp. 163–204.
- E. Alizadeh, L. Sanche, *Chem. Rev.* **112**, 5578–5602 (2012).
- F. E. Garrett-Bakelman *et al.*, *Science* **364**, eaau8650 (2019).
- M. Inokuti, *Rev. Mod. Phys.* **43**, 297–347 (1971).
- F. H. Long, H. Lu, K. B. Eisenthal, *Phys. Rev. Lett.* **64**, 1469–1472 (1990).
- A. Migus, Y. Gauduel, J. L. Martin, A. Antonetti, *Phys. Rev. Lett.* **58**, 1559–1562 (1987).
- P. Kambhampati, D. H. Son, T. W. Kee, P. F. Barbara, *J. Phys. Chem. A* **106**, 2374–2378 (2002).
- M. H. Elkins, H. L. Williams, A. T. Shreve, D. M. Neumark, *Science* **342**, 1496–1499 (2013).
- J. Li, Z. Nie, Y. Y. Zheng, S. Dong, Z.-H. Loh, *J. Phys. Chem. Lett.* **4**, 3698–3703 (2013).
- J. M. Herbert, M. P. Coons, *Annu. Rev. Phys. Chem.* **68**, 447–472 (2017).
- E. J. Hart, J. W. Boag, *J. Am. Chem. Soc.* **84**, 4090–4095 (1962).
- E. Kamarchik, O. Kostko, J. M. Bowman, M. Ahmed, A. I. Krylov, *J. Chem. Phys.* **132**, 194311 (2010).
- O. Marsalek *et al.*, *J. Chem. Phys.* **135**, 224510 (2011).
- Y. Gauduel, S. Pommeret, A. Migus, A. Antonetti, *Chem. Phys.* **149**, 1–10 (1990).
- T. Fransson *et al.*, *Chem. Rev.* **116**, 7551–7569 (2016).
- C. G. Elles, C. A. Rivera, Y. Zhang, P. A. Pieniazek, S. E. Bradforth, *J. Chem. Phys.* **130**, 084501 (2009).
- P. Emma *et al.*, *Nat. Photonics* **4**, 641–647 (2010).
- B. Winter, E. F. Aziz, U. Hergenhan, M. Faubel, I. V. Hertel, *J. Chem. Phys.* **126**, 124504 (2007).
- K. Nishizawa *et al.*, *Phys. Chem. Chem. Phys.* **13**, 413–417 (2011).
- S. Stranges, R. Richter, M. Alagia, *J. Chem. Phys.* **116**, 3676–3680 (2002).
- R. A. Crowell, D. M. Bartels, *J. Phys. Chem.* **100**, 17940–17949 (1996).
- J. H. Guo *et al.*, *Phys. Rev. Lett.* **89**, 137402 (2002).
- M. J. Rosker, M. Dantus, A. H. Zewail, *J. Chem. Phys.* **89**, 6113–6127 (1988).
- J. C. Tully, *J. Chem. Phys.* **93**, 1061–1071 (1990).
- Y. Hao, L. Inhester, K. Hanasaki, S.-K. Son, R. Santra, *Struct. Dyn.* **2**, 041707 (2015).

- K. Khalili *et al.*, *Struct. Dyn.* **6**, 044102 (2019).
- L. Inhester *et al.*, *J. Phys. Chem. Lett.* **9**, 1156–1163 (2018).
- T. R. Huet, C. J. Pursell, W. C. Ho, B. M. Dinelli, T. Oka, *J. Chem. Phys.* **97**, 5977–5987 (1992).
- K. P. Huber, G. Herzberg, in *NIST Chemistry WebBook, NIST Standard Reference Database Number 69*, P. J. Linstrom, W. G. Mallard, Eds. (National Institute of Standards and Technology); <http://webbook.nist.gov>.
- F. Perakis *et al.*, *Chem. Rev.* **116**, 7590–7607 (2016).
- M. L. Cowan *et al.*, *Nature* **434**, 199–202 (2005).
- A. P. Gaiduk, T. A. Pham, M. Govoni, F. Paesani, G. Galli, *Nat. Commun.* **9**, 247 (2018).
- R. E. Larsen, W. J. Glover, B. J. Schwartz, *Science* **329**, 65–69 (2010).
- L. Young, Z.-H. Loh, R. Santra, C. Arnold, Data for “Observation of the fastest chemical processes in the radiolysis of water.” Zenodo repository. DOI: 10.5281/zenodo.3543680.
- M. L. Vidal, X. Feng, E. Epifanovsky, A. I. Krylov, S. Coriani, *J. Chem. Theory Comput.* **15**, 3117–3133 (2019).
- M. Nagasaka, T. Hatsui, T. Horigome, Y. Hamamura, N. Kosugi, *J. Electron Spectrosc. Relat. Phenom.* **177**, 130–134 (2010).

ACKNOWLEDGMENTS

Funding: Supported by the U.S. Department of Energy (DOE) Office of Science, Office of Basic Energy Sciences, Chemical Sciences, Geosciences, and Biosciences Division, which supports the Argonne group under contract DE-AC02-06CH11357. Use of the LCLS, SLAC National Accelerator Laboratory, and resources of the Center for Nanoscale Materials, Argonne National Laboratory, are supported by DOE Office of Science, Office of Basic Energy Sciences under contracts DE-AC02-76SF00515 and DE-AC02-06CH11357. Also supported by Laboratory Directed Research and Development funding from Argonne National Laboratory for conceptual design and proposal preparation (L.Y.); Singapore Ministry of Education grants MOE2014-T2-052 and RG105/17 (Z.-H.L., M.S.B.M.Y., and T.D.); Swedish Science Council grant 2018-04088 (L.K. and J.-E.R.); the CNRS GotoXFEL program (M.S.); the Deutsche Forschungsgemeinschaft Cluster of Excellence “Advanced Imaging of Matter” (EXC 2056, project ID 390715994) (C.A., R.W., and R.S.); DOE Office of Science, Office of Basic Energy Sciences, Chemical Sciences, Geosciences, and Biosciences Division grant DE-SC0019451 (L.I. and R.S.); the European Research Council under the European Union’s Horizon 2020 research and innovation program (grant agreement 681881) (K.K.); NSF grant CHE-1856342 (A.I.K. and K.N.); and a Simons Fellowship in Theoretical Physics and Mildred Dresselhaus Award from the Hamburg Centre for Ultrafast Imaging, which supported a sabbatical at DESY in Germany (A.I.K.). **Author contributions:** L.Y., Z.-H.L., and R.S. originated the project concept; W.F.S., G.D., M.-F.T., R.D.S., and S.H.S. designed the experimental apparatus and characterized the target; Z.-H.L., G.D., C.A., L.K., S.H.S., A.A.H., Y.K., M.-F.T., P.J.H., A.M.M., M.S.B.M.Y., T.D., M.S., S.M., G.C., J.K., M.P.M., W.F.S., J.-E.R., and L.Y. executed the experiment and collected the experimental data; Z.-H.L., Y.K., L.K., J.-E.R., and L.Y. analyzed the experimental data; R.S., C.A., R.W., L.I., K.K., K.N., and A.I.K. provided supporting theoretical calculations; L.Y., Z.-H.L., R.S., and C.A. wrote the paper with comments from all authors. L.Y. was responsible for the coordination of the project. **Competing interests:** A.I.K. is a board member and a part owner of Q-Chem Inc. **Data and materials availability:** The underlying data are available in the supplementary materials and Zenodo, the CERN repository (35).

SUPPLEMENTARY MATERIALS

science.sciencemag.org/content/367/6474/179/suppl/DC1
Materials and Methods
Supplementary Text
Figs. S1 to S11
Tables S1 to S3
References (38–51)

12 September 2019; accepted 15 November 2019
10.1126/science.aaz4740

LIGHTNING

A terrestrial gamma-ray flash and ionospheric ultraviolet emissions powered by lightning

Torsten Neubert^{1*}, Nikolai Østgaard², Victor Reglero³, Olivier Chanrion¹, Matthias Heumesser¹, Krystallia Dimitriadou¹, Freddy Christiansen¹, Carl Budtz-Jørgensen¹, Irfan Kuvvetli¹, Ib Lundgaard Rasmussen¹, Andrey Mezentsev², Martino Marisaldi^{2,4}, Kjetil Ullaland², Georgi Genov², Shiming Yang², Pavlo Kochkin², Javier Navarro-Gonzalez³, Paul H. Connell³, Chris J. Eyles³

Terrestrial gamma-ray flashes (TGFs) are transient gamma-ray emissions from thunderstorms, generated by electrons accelerated to relativistic energies in electric fields. Elves are ultraviolet and optical emissions excited in the lower ionosphere by electromagnetic waves radiated from lightning current pulses. We observed a TGF and an associated elve using the Atmosphere-Space Interactions Monitor on the International Space Station. The TGF occurred at the onset of a lightning current pulse that generated an elve, in the early stage of a lightning flash. Our measurements suggest that the current onset is fast and has a high amplitude—a prerequisite for elves—and that the TGF is generated in the electric fields associated with the lightning leader.

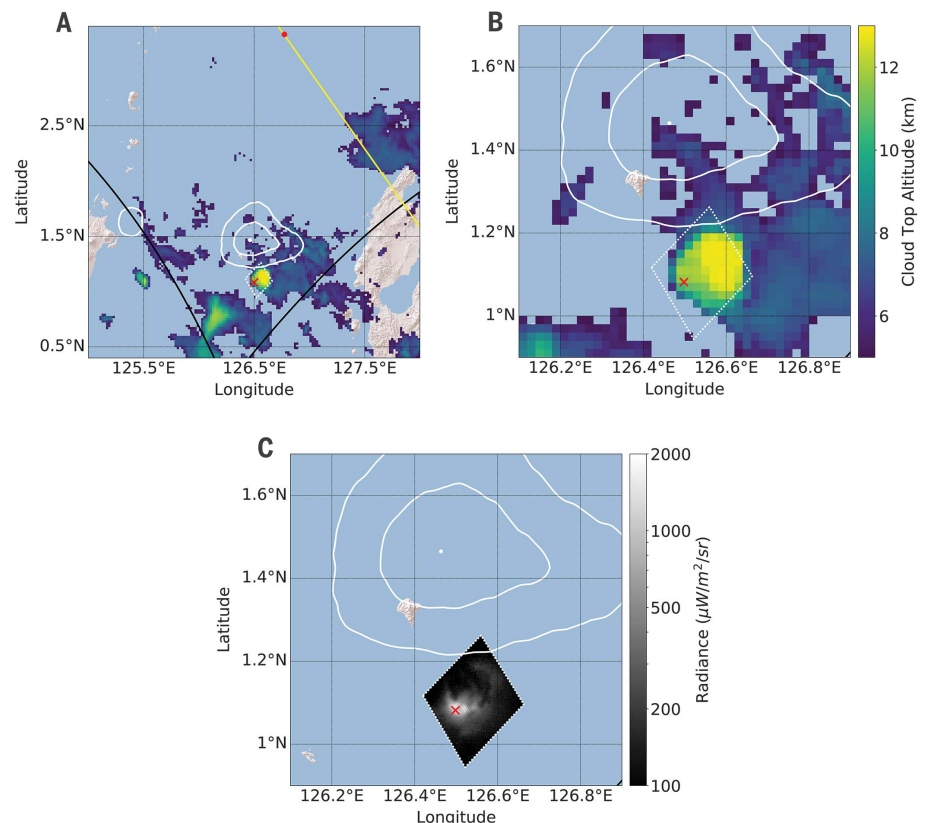
Transient luminous emissions (TLEs), such as sprites, jets, and elves, occur above thunderstorm clouds (1). Terrestrial gamma-ray flashes (TGFs) are brief (less than a few milliseconds) emissions of photons, reaching energies of tens of MeV, observed by astrophysical satellites passing over thunderstorms (2–5). TGFs were initially thought to originate from high-altitude TLEs, where low atmospheric absorption would allow the TGF photons to escape, but their source was later determined to be within the

thunderstorm clouds (6–8). It is now understood that TGFs are produced by bremsstrahlung radiation from electrons with energies in the runaway regime, where the cross sections for interactions decrease with further acceleration (9). The generation of TGFs requires seed electrons in this regime that start a runaway electron avalanche. The seeds can be electrons released by cosmic ray interactions with the atmosphere, born with high energies (10), or cold electrons in streamers that are accelerated into the runaway regime in the electric fields of

lightning leader tips (11). The relativistic electron flux must then be amplified for the bremsstrahlung to reach the measured flux levels, as in relativistic runaway electron avalanches, possibly enhanced by feedback effects from positrons created by pair production and from ionization by backscattered bremsstrahlung (9). The role of the large-scale electric field in a cloud relative to the enhanced field at a lightning leader tip, however, is still debated (9–11).

We present observations with the Atmosphere-Space Interactions Monitor (ASIM), onboard the International Space Station (ISS), of a TGF produced in the initial stage of a lightning flash. The TGF was observed east of the island of Sulawesi in Indonesia on 10 October 2018, at 13:01:33.100080 Coordinated Universal Time (UTC). ASIM has two x-ray and gamma-ray detectors, three ultraviolet (UV) and optical photometers, and two optical imaging cameras (12–14). The instruments are pointed toward the nadir (directly downward) to minimize gamma-ray flux losses due to atmospheric absorption. Figure 1, A and B, shows the location of the TGF, the surrounding cloud top

Fig. 1. Location of the TGF event observed on 10 October 2018. (A) Cloud top altitudes (15) are shown according to the color scale to the right of (B). The yellow curve shows the ISS orbit; the red dot marks its position at the onset time of the TGF at 13:01:33.100080 UTC. The white dot marks the most probable TGF location, with white contours outlining the 68% and 95.4% confidence regions. The black curves outline the southern limit of the full field of view of the optical instruments, the white dash-lined box outlines the cropped segment of the image downlinked from the ISS, and the red cross is the location of a coincident lightning event detected by WWLLN (15). (B) The same view zoomed in to the active cloud region. A single thundercloud partially overlaps with the TGF 95% confidence region. (C) The TGF position overlain with a projection of the ASIM camera image in the 337-nm filter; exposure time, 83 ms. The attitude of the ASIM instruments is calibrated to align the WWLLN lightning location with the maximum optical activity of the ASIM image.



¹National Space Institute, Technical University of Denmark (DTU Space), Kongens Lyngby, Denmark. ²Birkeland Centre for Space Science, Department of Physics and Technology, University of Bergen, Bergen, Norway. ³Image Processing Laboratory, University of Valencia, Valencia, Spain. ⁴Astrophysics and Space Science Observatory, National Institute for Astrophysics, Bologna, Italy. *Corresponding author. Email: neubert@space.dtu.dk

Fig. 2. Light curves of the event.

The gamma-flash trigger time is at $t = 0$, which corresponds to 13:01:33.100080 UTC.

(A) Photometer (left axis) and x-ray and gamma-ray (right axis) measurements around the time of the event. LED is the low-energy x-ray detector (50 to 350 keV) and HED the high-energy detector (300 keV to 30 MeV). The UV photometer measures 180 to 235 nm and is multiplied by 100 to show on the same scale as the optical photometers. All three photometers sample at 100 kHz. (B) The same data shown zoomed in further at the time of the TGF.

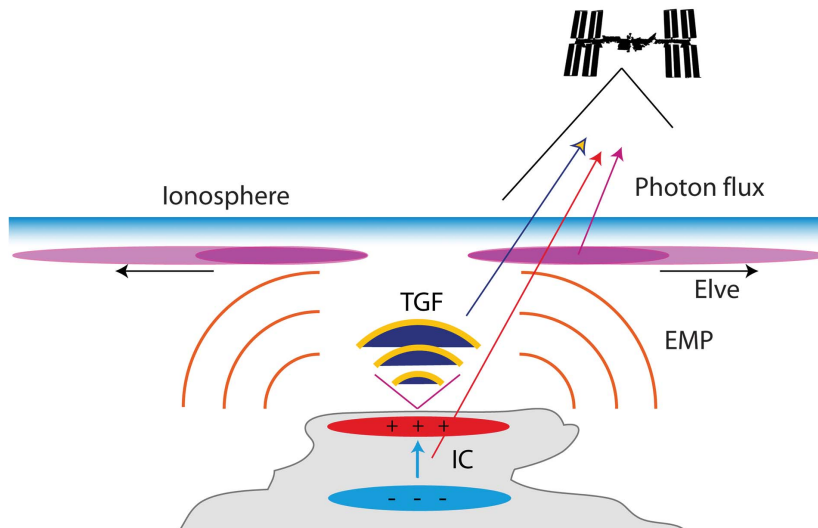
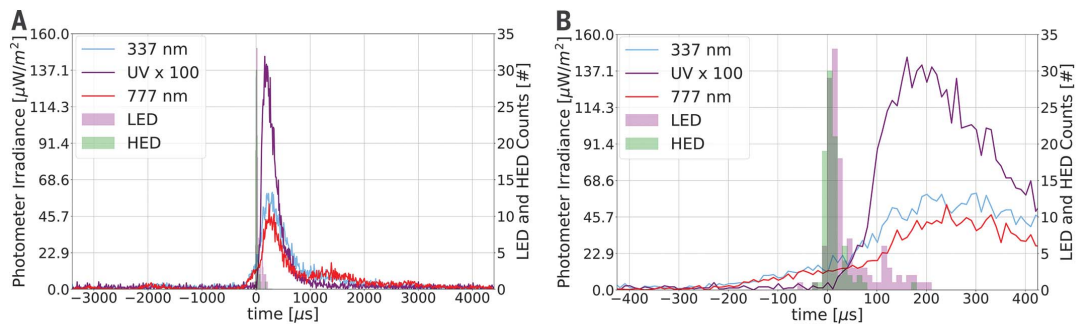


Fig. 3. Our proposed scenario. An intra-cloud (IC) lightning event generates a TGF and electromagnetic pulse (EMP). The EMP excites expanding waves of UV emission in the lower ionosphere (elve). TGF and UV emissions are observed by ASIM on the ISS (arrows).

altitudes derived from observations by the Himawari weather satellite (15), and the full and cropped field of view of the ASIM optical instruments. Figure 1C shows the projection of the ASIM camera image and the location of a coincident lightning event detected by the World Wide Lightning Location Network (WWLLN) (15).

The instrument data projections are to 12 km altitude, 1 km below the maximum altitude of the cloud top (Fig. 1C). The pointing direction of the sensors is determined from the ISS attitude and the nominal mounting of the ASIM platform. It is calibrated by assuming that the WWLLN lightning location is at the maximum optical activity of the ASIM image. This correction is $\sim 1.4^\circ$, corresponding to 11.8 km at ground level, which also aligns the ASIM image of the cloud with its position in the Himawari data. The WWLLN lightning location has an uncertainty of ~ 5 km and occurred ~ 11 ms after the time estimated by the ASIM

photometer pulses (15), which is within the ~ 20 ms uncertainty in the absolute timing signal received by ASIM from the ISS. The TGF source location is estimated from the angle of arrival of 70- to 350-keV photons to the ASIM low-energy x-ray detector (LED). This angle is determined from the shadow pattern cast by a coded mask onto the pixelated detector plane. The relative pointing direction between the LED and the optical sensors has not been calibrated, so we assume its nominal value (co-aligned). We conclude that the optical and x-ray measurements provide a consistent identification of this small (20 km^2) convective cloud as the source of the lightning associated with the TGF.

The signals of the three ASIM photometers around the time of the event are shown in Fig. 2. The photometers measure continuum emission in the UV band (180 to 235 nm) covering part of the Lyman-Birge-Hopfield system of N_2 , as well as line emissions from N_2 2P at

337 nm (filter width 5 nm) and O I at 777.4 nm (filter width 3 nm), all at sample frequencies of 100,000 Hz. Also shown in Fig. 2 are the observations of the TGF, in photon counts measured by the LED (50 to 350 keV) and the high-energy detector (HED, 300 keV to 30 MeV). The time resolution is 1 μs for the LED and 27 ns for the HED, and the relative timing accuracy between the optical sensors and LED/HED is $\pm 5 \mu\text{s}$.

The optical activity began several milliseconds before the main optical pulses and intensified at a time $t = -200 \mu\text{s}$, measured with respect to the onset of the HED pulse, signifying an increase of the lightning current. The onset of the TGF coincided with the onset of the UV emissions (to within 10 μs), and an accelerated increase in the 337-nm and 777.4-nm signals appeared as a change in their slope 0 to 60 μs after the TGF trigger (15). The TGF lasted about 30 to 40 μs and had a weaker tail extending to $\sim 80 \mu\text{s}$ for the high-energy photons and $\sim 200 \mu\text{s}$ for the low-energy photons (detected by the HED and LED, respectively), consistent with delays expected from Compton scattering of x-rays and gamma rays in the atmosphere (16).

The emissions at 777.4 nm are from atomic oxygen and therefore from the current in a lightning leader channel, and the 337-nm emissions are mostly from the lightning discharge in the cloud (leader and streamers) (17) with negligible contributions from the ionosphere (i.e., an elve) (18). UV emissions, although strongly damped in the atmosphere, are seen here with an amplitude that rises more rapidly than the optical signals, which is the signature of an elve (18). Elves are quite common emissions (19), ~ 1 ms in duration, excited by the electromagnetic pulse (EMP) from the large current impulse of cloud-to-ground lightning (20) or intra-cloud lightning (21). The EMP energizes free electrons at the lower edge of the ionosphere at 80 to 90 km altitude, which excite the atmospheric constituents. The radiation pattern from the lightning current onset excites rings of elve emission centered above

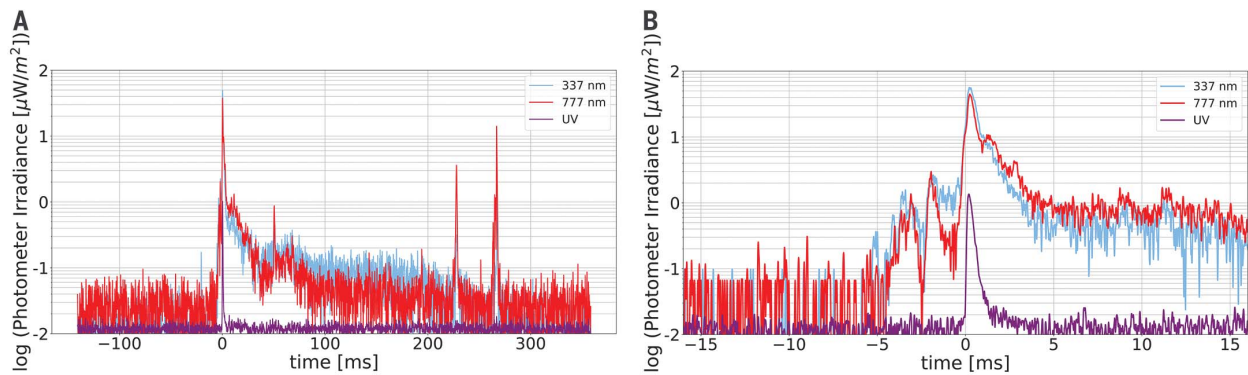


Fig. 4. Analysis of the lightning flash. (A) The same data as Fig. 2 but on a logarithmic scale and smoothed by a Gaussian filter with width $\sigma = 10$ samples. Two additional optical pulses occur 200 to 300 ms after the initial flash. (B) The same data zoomed in to the start of the flash smoothed with $\sigma = 2$ samples. Optical emission begins 5 ms prior to UV emission and the TGF.

the lightning (for vertical lightning), which rapidly expand horizontally with detectable radii from ~ 50 to 400 km (22). The ASIM imaging cameras are not sufficiently sensitive to measure elves because of their short duration and large spatial extent when observed toward the nadir, so we only analyze data from the photometers.

The UV elve was detected with a delay corresponding to the travel times of the EMP to the ionosphere and of UV photons from the ionosphere to the instruments. The shortest combined path is approximately the direct path, considering the geometry of the observations (Fig. 3). We therefore consider the initiation of the UV pulse as coinciding with the initiation of the current pulse, which starts $\lesssim 10 \mu\text{s}$ after the onset of the TGF. The equivalent optical photons are scattered in the cloud, causing the optical pulse to broaden and the peak to be delayed by several hundred microseconds or more, depending on the optical depth of the source and on the cloud properties (23). This is consistent with the UV and optical pulses we observe (Fig. 2B). The characteristics of the optical pulses also resemble those of lightning emissions observed by the Fast On-orbit Rapid Recording of Transient Events (FORTE) satellite (24). This suggests that the current source lifetime is much shorter than the optical pulses, although we cannot further characterize the pulse current from optical measurements alone. The first optical photons to arrive at the sensors are those that have undergone the least scattering in the cloud. A pulse is first detected by ASIM when the flux levels are above the sensor sensitivity thresholds, and the onset of a pulse may therefore appear with a delay. For this event, the optical pulses are bright and rising out of pre-activity; this suggests that a delay from the limits of the sensor sensitivities and of cloud scattering are minor, and therefore that the optical pulses should start at approximately the same time as the UV pulse, as observed.

The photometer measurements are shown on a logarithmic scale in Fig. 4. The TGF and the associated high-amplitude pulses occur ~ 5 ms after the beginning of the lightning flash (Fig. 4B), consistent with studies of radio emissions from TGF-producing flashes (25). The flash fades over ~ 280 ms, terminating with two smaller optical pulses (Fig. 4A). The onset of the emission at $t = -5$ ms could reflect the time when an upward-propagating lightning leader first becomes detectable in the cloud, or it may reflect the onset of the formation of the leader. The start of the leader emission is modulated by two larger oscillations (Fig. 4B), possibly related to the leader propagation, and the continuation after the TGF could reflect the continued propagation of the leader upward/horizontally into a positive-charge layer, as was previously proposed (26). However, cloud scattering is too strong to identify the spatial propagation of the leader from the camera images.

Although TGF-type emissions have been observed from leaders propagating to the ground (27), we reject that scenario as an explanation of this event because of the strong photon absorption that would occur in the lower atmosphere (9). Instead, we interpret this event as an intra-cloud lightning flash of positive polarity (Fig. 3) where the electric field ahead of the leader plays a role in producing the TGF.

The elve requires a high-amplitude lightning current pulse with a fast rise time, which suggests the formation of, or access to, a large charge reservoir within the cloud that is rapidly drained. The reservoir could be formed by the ionizing avalanche of the relativistic electrons or by the formation of an extended streamer corona, as suggested by radio signal studies of TGFs (28–30). It is likely that further current amplification is required to produce an elve. Pulses with high currents have been identified in radio observations and have been associated with TGFs (31). They are termed positive energetic in-cloud pulses (+EIPs);

they last $\sim 50 \mu\text{s}$ and may reach hundreds of thousands of amperes (31). +EIPs occur typically in the upper regions of clouds after a few milliseconds of ascending negative leader activity, and it has been suggested that they can generate TGFs and elves simultaneously (31). The TGF in this event is relatively short in duration relative to past observations (2–5). A short duration was predicted for TGFs accompanied by elves, because elves require lightning source currents that vary more rapidly (31). The optical pulses we observe may then be the counterpart of radio +EIPs.

Our observations illustrate the temporal sequence of emissions in optical, UV, x-ray, and gamma-ray bands with a time resolution of 10 μs and simultaneous imaging of a TGF in hard x-rays and optical images. The observations provide evidence that there is a connection between TLEs and TGFs after all.

REFERENCES AND NOTES

- V. P. Pasko, Y. Yair, C. L. Kuo, *Space Sci. Rev.* **168**, 475–516 (2012).
- G. J. Fishman *et al.*, *Science* **264**, 1313–1316 (1994).
- D. M. Smith, L. I. Lopez, R. P. Lin, C. P. Barrington-Leigh, *Science* **307**, 1085–1088 (2005).
- M. Marisaldi *et al.*, *J. Geophys. Res.* **115**, A00E13 (2010).
- O. J. Roberts *et al.*, *J. Geophys. Res. Space Phys.* **123**, 4381–4401 (2018).
- S. A. Cummer *et al.*, *Geophys. Res. Lett.* **32**, L08811 (2005).
- M. A. Stanley *et al.*, *Geophys. Res. Lett.* **33**, L06803 (2006).
- J. R. Dwyer, D. M. Smith, *Geophys. Res. Lett.* **32**, L22804 (2005).
- J. R. Dwyer, D. M. Smith, S. A. Cummer, *Space Sci. Rev.* **173**, 133–196 (2012).
- A. V. Gurevich, G. M. Milikh, R. A. Roussel-Dupré, *Phys. Lett. A* **165**, 463–468 (1992).
- L. P. Babich, E. I. Bochkov, I. M. Kutsyk, T. Neubert, O. Channion, *J. Geophys. Res.* **122**, 8974–8984 (2017).
- T. Neubert *et al.*, *Space Sci. Rev.* **215**, 26 (2019).
- N. Østgaard *et al.*, *Space Sci. Rev.* **215**, 23 (2019).
- O. Channion *et al.*, *Space Sci. Rev.* **215**, 28 (2019).
- See supplementary materials.
- S. Celestin, V. P. Pasko, *Geophys. Res. Lett.* **39**, L02802 (2012).
- R. A. Armstrong *et al.*, *J. Atmos. Sol. Terr. Phys.* **60**, 787–799 (1998).
- F. J. Pérez-Invernón, A. Luque, F. J. Gordillo-Vázquez, *J. Geophys. Res.* **123**, 7615–7641 (2018).
- A. B. Chen *et al.*, *J. Geophys. Res.* **113**, A08306 (2008).
- U. S. Inan, W. A. Sampson, Y. N. Taranenko, *Geophys. Res. Lett.* **23**, 133–136 (1996).
- R. A. Marshall, C. L. da Silva, V. P. Pasko, *Geophys. Res. Lett.* **42**, 6112–6119 (2015).

22. C. L. Kuo *et al.*, *J. Geophys. Res.* **117**, A07320 (2012).
23. T. E. Light, D. M. Suszcynsky, M. W. Kirkland, A. R. Jacobson, *J. Geophys. Res.* **106**, 17103–17114 (2001).
24. T. E. Light, D. M. Suszcynsky, A. R. Jacobson, *J. Geophys. Res.* **106**, 28223–28231 (2001).
25. S. A. Cummer *et al.*, *Geophys. Res. Lett.* **42**, 7792–7798 (2015).
26. R. U. Abbasi *et al.*, *J. Geophys. Res.* **123**, 6864–6879 (2018).
27. X.-M. Shao, T. Hamlin, D. M. Smith, *J. Geophys. Res.* **115**, A00E30 (2010).
28. B. G. Mailyan *et al.*, *J. Geophys. Res.* **123**, 5933–5948 (2018).
29. F. Lyu *et al.*, *Geophys. Res. Lett.* **45**, 2097–2105 (2018).
30. F. Lyu *et al.*, *Geophys. Res. Lett.* **43**, 8728–8734 (2016).
31. N. Y. Liu, J. R. Dwyer, S. A. Cummer, *J. Geophys. Res. Space Phys.* **122**, 10563–10576 (2017).

ACKNOWLEDGMENTS

We thank M. Stolzenburg and M. Rycroft for valuable comments, and the World Wide Lightning Location Network for the lightning

location data used in this paper. **Funding:** ASIM is a mission of the European Space Agency (ESA), funded by ESA and national grants of Denmark, Norway, and Spain. ESA PRODEX contracts C 4000115884 (DTU) and 4000123438 support the ASIM Science Data Centre (Bergen). The science analysis is supported by ESA Topical Team contract 4200019920/06/NL/VJ; the European Commission, Innovative Training Network SAINT, project grant 722337-SAINT; European Research Council grant AdG-FP7/2007-2013: n 320839; Research Council of Norway contracts 223252/F50 and 208028/F50 (CoE/BCSS); and Ministerio Ciencia, Innovacion y Universidades grant ESP 2017-86263-C4. **Author contributions:** T.N. leads the ASIM project; N.Ø. leads the LED and HED instrument consortia, supported by C.B.-J. and I.K.; V.R. leads the LED imaging analysis, supported by J.N.-G. and P.H.C.; O.C. leads the optical instrument consortium, supported by M.H. and K.D.; F.C. performed in-orbit LED health analysis; I.L.R. performed in-flight calibration of the photometers; K.U., G.G., S.Y., P.K., and C.J.E. conducted LED and HED in-orbit commissioning;

and M.M. and A.M. performed LED and HED data analysis.

Competing interests: The authors declare no competing interests.

Data and materials availability: The ASIM data for this event are provided in data S1 to S5. The WWLLN lightning data, cloud data, and ISS attitude data are provided in the supplementary materials.

SUPPLEMENTARY MATERIALS

science.sciencemag.org/content/367/6474/183/suppl/DC1

Materials and Methods

Supplementary Text

Fig. S1

Data S1 to S5

References (32–35)

2 April 2019; accepted 31 October 2019

Published online 12 December 2019

10.1126/science.aax3872

QUANTUM SIMULATION

Time-resolved observation of spin-charge deconfinement in fermionic Hubbard chains

Jayadev Vijayan^{1,2,*}, Pimonpan Sompert^{1,2,*}, Guillaume Salomon^{1,2}, Joannis Koepsell^{1,2}, Sarah Hirthe^{1,2}, Annabelle Bohrdt^{2,3}, Fabian Grusdt^{2,3,4}, Immanuel Bloch^{1,2,5}, Christian Gross^{1,2}

Elementary particles carry several quantum numbers, such as charge and spin. However, in an ensemble of strongly interacting particles, the emerging degrees of freedom can fundamentally differ from those of the individual constituents. For example, one-dimensional systems are described by independent quasiparticles carrying either spin (spinon) or charge (holon). Here, we report on the dynamical deconfinement of spin and charge excitations in real space after the removal of a particle in Fermi-Hubbard chains of ultracold atoms. Using space- and time-resolved quantum gas microscopy, we tracked the evolution of the excitations through their signatures in spin and charge correlations. By evaluating multipoint correlators, we quantified the spatial separation of the excitations in the context of fractionalization into single spinons and holons at finite temperatures.

Strongly correlated quantum many-body systems often exhibit behaviors that cannot be attributed to the properties of the individual particles. Instead, the collective nature of the excitations can lead to the emergence of quasiparticles that are fundamentally distinct from free electrons. For example, in one-dimensional (1D) quantum systems, electron-like excitations do not exist but are replaced by decoupled collective spin and charge modes (1). These two independent excitation branches feature different propagation velocities (2) and have previously been studied in the Luttinger liquid regime (3) of quasi-1D solids using spectroscopic techniques, such as angle-resolved photoemission spectroscopy (4–6) and conductance measurements in metallic quantum wires (7–9). Cold-atom experiments have been used extensively to study attractive 1D bosonic and fermionic gases (10–15), but the investigation of repulsive 1D fermionic gases has been more recent (16–18). Trapping fermionic spin mixtures in optical lattices has enabled a clean and well-controlled realization of the 1D Fermi-Hubbard model. Being an exactly solvable paradigmatic model (19–21) for strongly correlated electrons, this has allowed for quantitative comparisons between theory and experiments. Such experiments can probe the regime that lies in between the low-energy Luttinger liquid and the spin-incoherent Luttinger liquid; for the latter, the temperature is on the order of or exceeds

the magnetic energy (22). Recent equilibrium signatures of spin-charge separation have been observed in ultracold lattice gases using quantum gas microscopy (23, 24). However, real-space tracking of the dynamics of the individual excitations signaling their deconfinement has been more challenging to accomplish.

Here, we demonstrate dynamical spin-charge separation directly by performing a local quench in a 1D gas of ultracold fermionic atoms and subsequently monitoring the evolution of the system with spin- and density-resolved quantum gas microscopy (18) (see Fig. 1). The local quench is realized by the high-fidelity removal of one atom from a single site of a 1D optical lattice; the lattice is initially filled with nearly one atom per site, and the system exhibits short-range antiferromagnetic spin correlations (18, 25–27). In the subsequent dynamics, we observed the emergence of two apparently independent excitations propagating at different velocities (28–30), which we assigned to spinons and holons on the basis of their characteristic signatures in the spin and charge (density) sectors.

Our experiment (24) began by loading a 2D balanced spin mixture of ⁶Li atoms in the lowest two hyperfine states into several 1D tubes using an optical lattice of spacing $a_y = 2.3 \mu\text{m}$ along the y direction. Next, a lattice of spacing $a_x = 1.15 \mu\text{m}$ was ramped up along the x direction. By varying the hopping strength along the x direction from $t/h = 190 \text{ Hz}$ to $t/h = 410 \text{ Hz}$, we realized Fermi-Hubbard chains with $U/t \sim 8$ to 20, where U is the onsite interaction energy, t is the tunneling energy, and h is Planck's constant. We fixed the total atom number in the gas to around 75 through the choice of the evaporative cooling parameters, such that the resulting Hubbard chains were prepared close to half-filling in the center of the harmonically confined cloud. This produced at least three 1D chains of mean length 13 atoms, each with a unity-filled region of

about nine sites. To perform a local quench in which a single atom is simultaneously removed from each chain, we used an elliptically shaped near-resonant laser beam at 671 nm focused to a waist of $\sim 0.5 \mu\text{m}$ along its narrow direction. This pushout beam was pulsed on for 20 μs , addressing the central sites. The power and alignment of the pushout beam was adjusted such that the probability of spin-independent removal of an atom from the addressed site was $\sim 78\%$, with $\sim 14\%$ chance of affecting the nearest neighboring sites (31). After the quench, we let the system evolve for a variable hold-time before imaging the spin and density distributions. To collect statistics, the experiment was repeated several thousand times for a given evolution time.

We first investigated the difference in the dynamics of holons and spinons by preparing 1D Hubbard chains with $t = h \times 250 \text{ Hz}$ and $U/t = 15$, corresponding to an exchange interaction of $J = h \times 65 \text{ Hz}$, where J is the spin-exchange energy, and then performing the local quench. A natural observable to characterize the subsequent dynamics of holons is the spatially resolved hole density distribution $\langle \hat{n}_i^h \rangle$ in each chain, where i labels the lattice sites. The observed distribution broadens as a function of time with a light-cone-like ballistic propagation of the wavefront (see Fig. 2A). It starts from the addressed site and reaches the edge of the unity-filled region of the chain in $5 \tau_t$, where $\tau_t = h \times (4\pi t)^{-1} = 0.32 \text{ ms}$ is the time it takes for a hole propagating at the theoretically expected maximum group velocity $v_{\text{max}}^t = a_x/\tau_t$ to move by one site. The coherent evolution of the hole can be seen in the evolving interference pattern of $\langle \hat{n}_i^h \rangle$ over time. This dynamic is found to be in excellent agreement with a single-particle quantum walk (see Fig. 2B), as expected for a spin-charge separated system.

To study the time evolution of the spin excitation, we measured nearest-neighbor spin correlations $C_i(\bar{x} = 1) = 4(\langle \hat{S}_i^z \hat{S}_{i+1}^z \rangle - \langle \hat{S}_i^z \rangle \langle \hat{S}_{i+1}^z \rangle)$ in squeezed space (denoted by \sim), obtained by removing holes and doublons from the chain in the analysis (23, 24). For strong interactions $U/t \gtrsim 8$, the spin dynamics in squeezed space is expected to be well captured by an antiferromagnetic Heisenberg model (32–34) to which we compared our results. We observed a strong reduction of the antiferromagnetic correlations in the direct vicinity of the quenched site immediately after the quench, demonstrating an enhanced probability of finding parallel spins on neighboring sites. Such a suppression was expected from the creation of spinons by the local quench (see Fig. 1A). The region with reduced antiferromagnetic correlations spread with time, with a light-cone-like propagation of the wavefront (see Fig. 2C). It reached the edge of the unity-filled region in $4 \tau_J$, where $\tau_J = h \times (\pi^2 J)^{-1} =$

¹Max-Planck-Institut für Quantenoptik, 85748 Garching, Germany. ²Munich Center for Quantum Science and Technology (MCQST), Schellingstraße 4, 80799 München, Germany. ³Department of Physics and Institute for Advanced Study, Technical University of Munich, 85748 Garching, Germany. ⁴Department of Physics and Arnold Sommerfeld Center for Theoretical Physics (ASC), Ludwig-Maximilians-Universität, Theresienstraße 37, 80333 München, Germany. ⁵Fakultät für Physik, Ludwig-Maximilians-Universität, Schellingstraße 4, 80799 München, Germany. *These authors contributed equally to this work. †Corresponding author. Email: jayadev.vijayan@mpq.mpg.de

1.56 ms is the time it takes for a spinon propagating at the theoretically expected maximum group velocity $v_{\max}^J = a_x/\tau_J$ to move by one site. In contrast to the highly coherent evolution of the hole, the finite temperature $k_B T/J \sim 0.75$, where k_B is the Boltzmann constant and T is temperature, in our system prevented us from observing any interference effects in the spin dynamics. However, the observed ballistic wavefront was still expected from the Heisenberg model at our temperatures (31, 35, 36).

Next, we extracted the velocities of the spin and charge excitations emerging from the quench. We monitored the spatial width of the squeezed space correlator $C_i(\bar{x} = 1)$ and hole distributions as a function of time (Fig. 3A, inset). We then used a linear fit to determine their respective velocities (Fig. 3A). For the data shown in Fig. 3A, taken at $U/t = 15$, we found a ratio of 5.31 ± 0.43 between the two propagation velocities, indicating a large difference in the velocities of the two excitation channels. Despite the finite nonzero temperature in our system, the extracted velocities are in excellent agreement with both exact diagonalization results of an extended $t - J$ model (31) as well as a single-particle quantum walk for a hole and a Heisenberg model prediction at our temperature for the spin excitations.

To investigate the scaling of the velocities with the tunneling and spin-exchange energies t and J , we repeated the experiment for different U/t by tuning the lattice depth. Within our experimental uncertainties, we found the extracted velocities to be in good agreement with the maximum expected group velocities v_{\max}^t and v_{\max}^J for the two excitation channels (see Fig. 3, B and C). These correspond to the velocities of a free holon and spinon at the maximum group velocity allowed by their dispersion. Unlike the Luttinger liquid regime, which only describes low-energy excitations, our local quench excited all momentum modes, the fastest of which is tracked here.

An essential feature of spin-charge deconfinement is the existence of unbound states of spin and charge excitations, allowing them to spatially separate over arbitrary large distances. To quantify the dynamical deconfinement, we studied the spin correlations across the propagating hole as a function of time, through the spin-hole-spin (SHS) correlator $C_{\text{SHS}}(2) = 4 \langle \hat{S}_i^z \hat{n}_{i+1}^h \hat{S}_{i+2}^z \rangle$, a spin correlator conditioned on having a hole at site $i + 1$ (23, 24) (Fig. 4A). Immediately after the quench, the hole is likely to be surrounded by parallel spins, and C_{SHS} retains a positive value. The measured spin correlations are consistent with the next-nearest-neighbor correlations $C(2) = 4(\langle \hat{S}_i^z \hat{S}_{i+2}^z \rangle - \langle \hat{S}_i^z \rangle \langle \hat{S}_{i+2}^z \rangle)$ in the absence of the quench. As the hole propagates, the sign of C_{SHS} becomes negative and, by $4 \tau_t$, approaches the nearest-neighbor correlations $C(1) = 4(\langle \hat{S}_i^z \hat{S}_{i+1}^z \rangle - \langle \hat{S}_i^z \rangle \langle \hat{S}_{i+1}^z \rangle)$ without the quench.

These observations indicate the decoupling of the two excitations. At longer evolution times, the antiferromagnetic correlations across the hole are reduced. We attribute this to the holon oscillating in the chain, owing to the harmonic confinement present in our system and hence to the changing overlap of the spin and charge distributions (31). The absence of binding

between the spin and charge excitations beyond the immediate vicinity of the hole is shown by calculating the normalized deviation from the mean nearest-neighbor correlations $\delta C_1(d) = \left\langle \frac{\hat{S}_i^z \hat{S}_{i+1}^z}{\langle \hat{S}_i^z \hat{S}_{i+1}^z \rangle} - 1 \right\rangle_{|i-i+1| \leq d \vee i-d}$ (see Fig. 4A, inset), where d is the distance of the hole from the closest of sites i and $i + 1$.

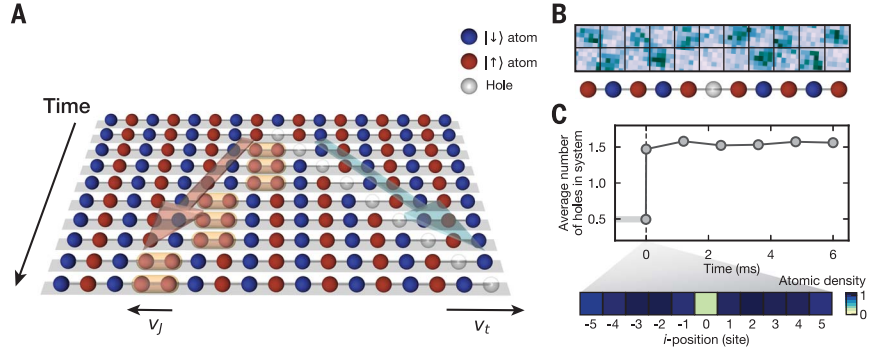


Fig. 1. Probing spin-charge deconfinement with cold atoms. (A) Cartoon depicting the fractionalization of a fermionic excitation into quasiparticles. The dynamics are initiated by removing a fermion from the Hubbard chain. This quench creates a spin (spinon) and a charge (holon) excitation, which propagate along the chain at different velocities v_J and v_t . (B) Using quantum gas microscopy, we simultaneously detected the spin and density on every site of the chain after a variable time after the quench. (C) Average number of holes in the system as a function of time (top). Error bars of 1 SEM are smaller than the symbol size. The quench, performed at 0 ms creates a hole with a probability of ~78% in the central site of the chain (bottom).

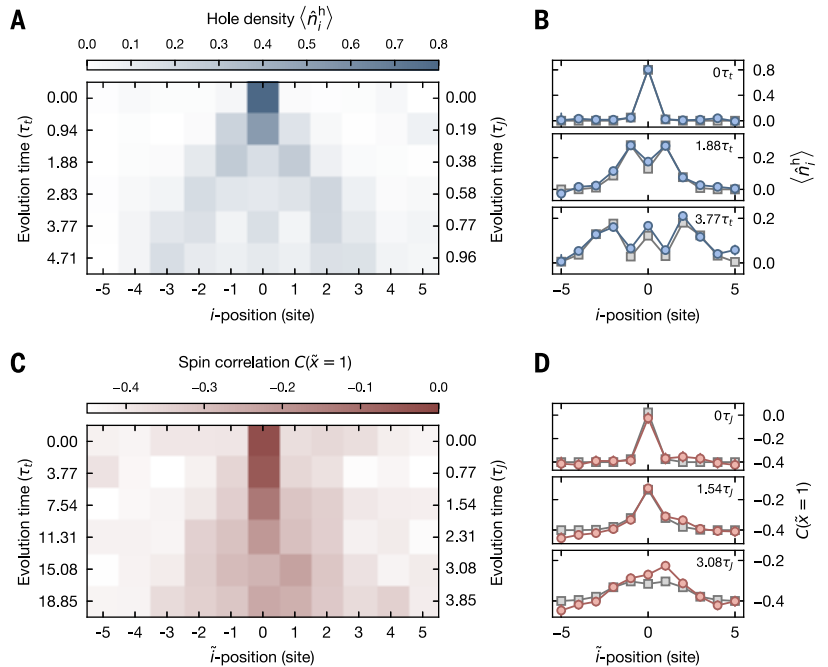


Fig. 2. Time evolution of spin and charge excitations. (A) Hole density distribution $\langle \hat{n}_i^h \rangle$ as a function of time after the quench. The wavefront of the distribution starts at the center of the chain and expands outward linearly with time. Interference peaks and dips are visible throughout the dynamics, indicating the coherent evolution of the charge excitation. (B) 1D cuts of the experimental hole density distributions at times 0, $1.88 \tau_t$, and $3.77 \tau_t$ (blue circles) are compared with simulations of a single-particle quantum walk (gray squares). (C) Nearest-neighbor squeezed-space spin correlation $C(\bar{x} = 1)$ distribution as a function of time after the quench. (D) 1D cuts of the experimental $C(\bar{x} = 1)$ distributions at times 0, $1.54 \tau_J$, and $3.08 \tau_J$ (red circles) along with exact diagonalization simulations of the Heisenberg model (gray squares) (31). Error bars denote 1 SEM.

indicates occupied sites, and \circ indicates the position of the hole. δC_1 shows no dependence on d , indicating the lack of influence of the holon on the spin excitation.

To locate the excess spin excitation in a fluctuating spinon background, we introduced an operator quantifying the local spin fluctua-

tions in squeezed space $\hat{\Sigma}_j^2 = \left(\sum_i \hat{S}_i^z f_j^\sigma(i) \right)^2$, where $f_j^\sigma(i) = \exp\left[-\frac{(i-j)^2}{2\sigma^2}\right]$ is a smooth window function centered at lattice site j with a characteristic size of σ . At zero temperature, this operator is expected to capture local fractional quantum numbers (37). A single spinon

located at site j , carrying a spin 1/2, would increase $\langle \hat{\Sigma}_j^2 \rangle$ by 1/4, provided that the mean distance between thermal spin fluctuations is larger than σ .

To study the spatial separation of the spin and charge excitations, we considered the chains at time $3.77 \tau_t$, where the highest probability of detecting the hole is at sites ± 2 . We postselected on chains with a single hole outside the central three sites of the unity-filled region and computed $\langle \hat{\Sigma}_j^2 \rangle$ for a window size $\sigma = 1.5$ (see Fig. 4B). Comparing $\langle \hat{\Sigma}_j^2 \rangle$ with the quench to its value $\langle \hat{\Sigma}_j^2 \rangle_{\text{BG}}$ without the quench, where BG indicates the background value in the absence of the quench, we observed a well-localized signal extending over the central three sites, distinct from the position of the holon. The maximum deviation $\langle \hat{\Sigma}_j^2 \rangle - \langle \hat{\Sigma}_j^2 \rangle_{\text{BG}}$ reached 0.13 ± 0.01 , about half the value expected at zero temperature. We attribute this difference mainly to the finite temperature of our system leading to a background density of thermal spin excitations. In this case, even an ideal quench would not create an initially localized spinon with unity probability, and the fractionalization scenario, where a single removed particle breaks up into precisely one holon and one spinon, holds only asymptotically at zero temperature (see Fig. 4C). A reduction in the deviation $\langle \hat{\Sigma}_j^2 \rangle - \langle \hat{\Sigma}_j^2 \rangle_{\text{BG}}$ from 1/4 is thus expected in our system, and the measured value is in good agreement with exact diagonalization calculations of the Heisenberg model at $k_B T = 0.75J$, taking into account our quench efficiency (31).

An interesting extension of this work would be to study spin-charge confinement dynamics in the dimensional crossover from 1D to 2D,

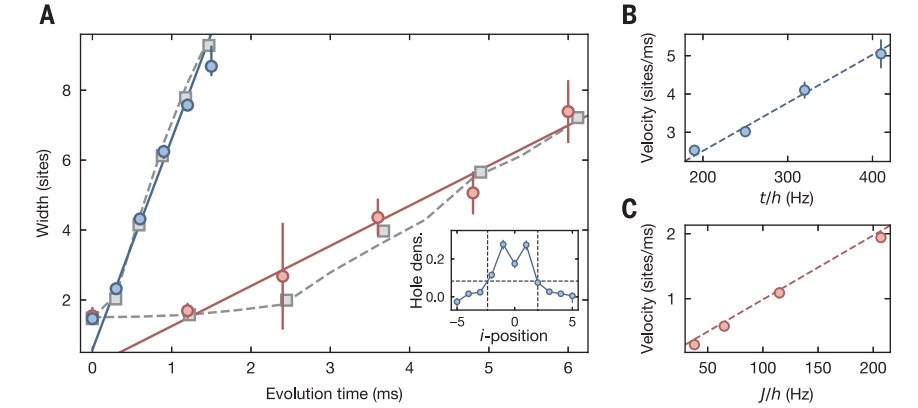
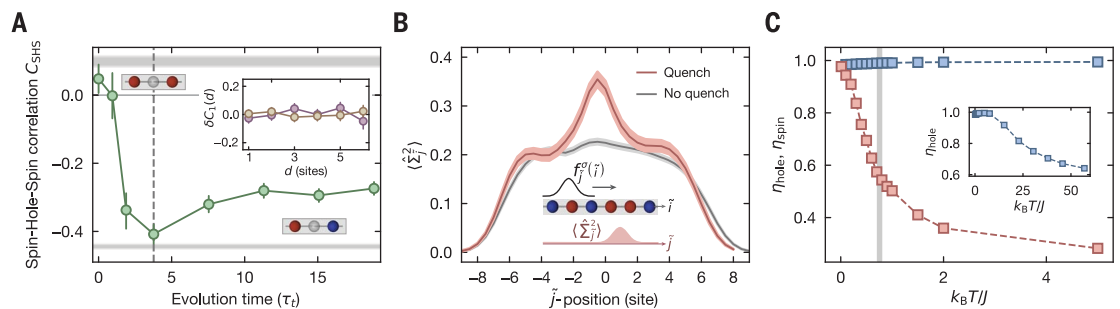


Fig. 3. Quasiparticle velocities of spinons and holons. (A) Time evolution of the widths of the hole density distributions (blue circles) and nearest-neighbor spin correlation distributions (red circles) after the quench. The measured widths are defined as the full width at 30% of maxima of the distributions (see inset). Density and spin excitations reach the edge of the unity-filled region of the chain (central nine sites) after different evolution times. Their dynamics are in quantitative agreement with both a single-particle quantum walk for the hole and exact diagonalization calculations of the Heisenberg model for the spin (gray squares). They are also found to reproduce the predictions of the extended $t-J$ model at our temperature (gray dashed lines) (31). The velocities of the spin (0.58 ± 0.04 sites/ms) and the charge (3.08 ± 0.09 sites/ms) excitations are obtained as half the slope of a linear fit to the data (solid blue and red lines), ignoring the width immediately after the quench. (B) Holon velocities as a function of t/h . The velocities of the holon (blue circles) increase linearly with the tunneling rate in the chain, consistent with $v_{\text{max}}^h = 4\pi t a_x / h$ sites/ms (blue dashed line). (C) Spin-excitation velocities as a function of J/h . The velocities of the spin excitation (red circles) increase linearly with the spin-exchange coupling in the chain, consistent with $v_{\text{max}}^s = \pi^2 J a_x / h$ sites/ms (red dashed line). Error bars denote 1 SEM.

Fig. 4. Spatial deconfinement of spin and charge excitations. (A) Spin-hole-spin correlations (C_{SHS}) averaged over the entire chain as a function of time after the quench.

The correlator starts with a positive value consistent with the next-nearest-neighbor spin correlations $C(2)$ in the absence of the quench (top gray-shaded region) and turns negative, approaching the nearest-neighbor spin correlations $C(1)$ without the quench (bottom gray-shaded region) by $4 \tau_t$. At longer evolution times, the correlator shows reduced antiferromagnetic correlations, owing to the oscillating dynamics of the hole in our finite size system. The inset shows the lack of dependence of the normalized deviation from the mean nearest-neighbor correlations δC_1 on the distance d from the hole at times $\sim 4 \tau_t$ (purple) and $\sim 19 \tau_t$ (yellow). Error bars denote 1 SEM. (B) Spatially resolved magnetization fluctuations ($\langle \hat{\Sigma}_j^2 \rangle$) in subregions of the chain with (red) and without (gray) the quench at $3.77 \tau_t$. The background fluctuations ($\langle \hat{\Sigma}_j^2 \rangle_{\text{BG}}$) are caused by quantum and thermal fluctuations in our system. The peak in the difference signal $\langle \hat{\Sigma}_j^2 \rangle - \langle \hat{\Sigma}_j^2 \rangle_{\text{BG}}$ indicates the location of the spin excitation. Gray- and



red-shaded areas denote 1 SEM without and after the quench, respectively.

(C) Efficiency of initially creating, at the central site, a single local spinon $\eta_{\text{spin}} = 4(\langle \hat{\Sigma}_{j=0}^2 \rangle - \langle \hat{\Sigma}_{j=0}^2 \rangle_{\text{BG}})$ with $\sigma = 1.5$ sites (orange) and holon $\eta_{\text{hole}} = 1 - \langle (\hat{n}_{i=0} - 1)^2 \rangle$ (blue) after an ideal quench as a function of temperature, as predicted from exact diagonalization of the Heisenberg model (for the spinon) and the Hubbard model (for the holon). With increasing temperature, η_{spin} (η_{hole} , inset) decreases because of the increase of thermal spin (density) excitations, preventing the creation of a localized spinon (holon) by the quench. Taking into account our quench efficiency, the measured amplitude is consistent with the prediction at a temperature of $k_B T/J = 0.75$ (gray-shaded region).

where polaronic signatures were recently observed (24, 38). The protocol used here could be directly implemented to extract the effective mass of a polaron. Our work opens avenues to dynamically probe the doped Fermi-Hubbard model in higher dimensions and explore fractionalization in topological phases of matter.

REFERENCES AND NOTES

1. T. Giamarchi, *Quantum Physics in One Dimension* (Clarendon, 2004).
2. J. Voit, *Rep. Prog. Phys.* **58**, 977–1116 (1995).
3. F. D. M. Haldane, *J. Phys. Chem.* **14**, 2585–2609 (1981).
4. C. Kim *et al.*, *Phys. Rev. Lett.* **77**, 4054–4057 (1996).
5. P. Segovia, D. Purdie, M. Hengsberger, Y. Baer, *Nature* **402**, 504–507 (1999).
6. B. J. Kim *et al.*, *Nat. Phys.* **2**, 397–401 (2006).
7. O. M. Auslaender *et al.*, *Science* **308**, 88–92 (2005).
8. Y. Jompol *et al.*, *Science* **325**, 597–601 (2009).
9. Y. Tserkovnyak, B. I. Halperin, O. M. Auslaender, A. Yacoby, *Phys. Rev. B Condens. Matter Mater. Phys.* **68**, 125312 (2003).
10. T. Kinoshita, T. Wenger, D. S. Weiss, *Science* **305**, 1125–1128 (2004).
11. B. Paredes *et al.*, *Nature* **429**, 277–281 (2004).
12. E. Haller *et al.*, *Science* **325**, 1224–1227 (2009).
13. T. Jacqmin, J. Armijo, T. Berrada, K. V. Kheruntsyan, I. Bouchoule, *Phys. Rev. Lett.* **106**, 230405 (2011).
14. N. Fabbri *et al.*, *Phys. Rev. A* **91**, 043617 (2015).
15. Y. A. Liao *et al.*, *Nature* **467**, 567–569 (2010).
16. T. L. Yang *et al.*, *Phys. Rev. Lett.* **121**, 103001 (2018).
17. G. Pagano *et al.*, *Nat. Phys.* **10**, 198–201 (2014).
18. M. Boll *et al.*, *Science* **353**, 1257–1260 (2016).
19. H. Bethe, *Z. Phys.* **71**, 205–226 (1931).
20. E. H. Lieb, F. Y. Wu, *Phys. Rev. Lett.* **20**, 1445–1448 (1968).
21. F. H. L. Essler, H. Frahm, F. Göhmann, A. Klümper, V. E. Korepin, *The One-Dimensional Hubbard Model* (Cambridge Univ. Press, 2005).
22. G. A. Fiete, *Rev. Mod. Phys.* **79**, 801–820 (2007).
23. T. A. Hilker *et al.*, *Science* **357**, 484–487 (2017).
24. G. Salomon *et al.*, *Nature* **565**, 56–60 (2019).
25. L. W. Cheuk *et al.*, *Science* **353**, 1260–1264 (2016).
26. M. F. Parsons *et al.*, *Science* **353**, 1253–1256 (2016).
27. P. T. Brown *et al.*, *Science* **357**, 1385–1388 (2017).
28. A. Recati, P. O. Fedichev, W. Zwerger, P. Zoller, *Phys. Rev. Lett.* **90**, 020401 (2003).
29. C. Kollath, U. Schollwöck, W. Zwerger, *Phys. Rev. Lett.* **95**, 176401 (2005).
30. C. Kollath, U. Schollwöck, *New J. Phys.* **8**, 220 (2006).
31. See supplementary materials.
32. F. Woynarovich, *J. Phys. C Solid State Phys.* **15**, 85–96 (1982).
33. M. Ogata, H. Shiba, *Phys. Rev. B Condens. Matter* **41**, 2326–2338 (1990).
34. J. Zaanen *et al.*, *Philos. Mag. B* **81**, 1485–1531 (2001).
35. H. Castella *et al.*, *Phys. Rev. Lett.* **74**, 972–975 (1995).
36. X. Zotos, F. Naef, P. Prelovsek, *Phys. Rev. B Condens. Matter* **55**, 11029–11032 (1997).
37. S. Kivelson, J. R. Schrieffer, *Phys. Rev. B Condens. Matter* **25**, 6447–6451 (1982).
38. J. Koepsell *et al.*, *Nature* **572**, 358–362 (2019).
39. C. Gross, Time-resolved observation of spin-charge deconfinement in fermionic Hubbard chains. Edmond (2019); doi: 10.17617/3.31.

ACKNOWLEDGMENTS

We thank G. Baskaran, E. Demler, T. Giamarchi, R. Moessner, and R. Shankar for useful discussions. P.S. acknowledges support from

the Development and Promotion of Science and Technology Talents Project (DPST) of Thailand. **Funding:** We acknowledge funding by the Max Planck Society (MPG), the European Union (UQUAM grant no. 319278 and PASQuanS grant no. 817482), and the Deutsche Forschungsgemeinschaft (DFG, German Research Foundation) under Germany's Excellence Strategy (EXC-2111-390814868). J.K. acknowledges funding from the Hector Fellow Academy, and G.S. acknowledges funding from the Max Planck Harvard Research Center for Quantum Optics. F.G. and A.B. acknowledge support from the Technical University of Munich–Institute for Advanced Study, funded by the German Excellence Initiative and the European Union FP7 under grant agreement 291763, from DFG grant no. KN 1254/1-1 and DFG TRR80 (Project F8). A.B. also acknowledges support from the Studienstiftung des deutschen Volkes. **Author contributions:** J.V. and P.S. acquired the data underlying this study and, together with G.S., analyzed them. J.V., P.S., G.S., J.K., and S.H. maintained and improved the experimental setup. A.B. and F.G. did the theoretical studies. I.B. and C.G. supervised the study. All authors worked on the interpretation of the data and contributed to the final manuscript. **Competing interests:** The authors declare no competing interests. **Data and materials availability:** The data that support the plots presented in this paper are publicly available from the Open Access Data Repository of the Max Planck Society (39).

SUPPLEMENTARY MATERIALS

science.sciencemag.org/content/367/6474/186/suppl/DC1
Supplementary Text
Figs. S1 to S8
Reference (40)

31 May 2019; accepted 14 November 2019
10.1126/science.aay2354

TOPOLOGICAL MATTER

Nearly quantized conductance plateau of vortex zero mode in an iron-based superconductor

Shiyu Zhu^{1,2*}, Lingyuan Kong^{1,2*}, Lu Cao^{1,2*}, Hui Chen^{1,2*}, Michal Papaj³, Shixuan Du^{1,2,4,5},
Yuqing Xing^{1,2}, Wenyao Liu^{1,2}, Dongfei Wang^{1,2}, Chengmin Shen^{1,4}, Fazhi Yang^{1,2}, John Schneeloch⁶,
Ruidan Zhong⁶, Genda Gu⁶, Liang Fu³, Yu-Yang Zhang^{2,1,4,†}, Hong Ding^{1,2,4,5,†}, Hong-Jun Gao^{1,2,4,5,†}

Majorana zero modes (MZMs) are spatially localized, zero-energy fractional quasiparticles with non-Abelian braiding statistics that hold promise for topological quantum computing. Owing to the particle-antiparticle equivalence, MZMs exhibit quantized conductance at low temperature. By using variable-tunnel-coupled scanning tunneling spectroscopy, we studied tunneling conductance of vortex bound states on FeTe_{0.55}Se_{0.45} superconductors. We report observations of conductance plateaus as a function of tunnel coupling for zero-energy vortex bound states with values close to or even reaching the $2e^2/h$ quantum conductance (where e is the electron charge and h is Planck's constant). By contrast, no plateaus were observed on either finite energy vortex bound states or in the continuum of electronic states outside the superconducting gap. This behavior of the zero-mode conductance supports the existence of MZMs in FeTe_{0.55}Se_{0.45}.

Majorana zero modes (MZMs) obey non-Abelian statistics and have potential applications in topological quantum computation (1, 2). In the past two decades, MZMs have been predicted in p-wave superconductors (3, 4) and spin-orbit-coupled materials proximitized by s-wave superconductors (5–8). Experimental evidence for MZMs has been observed in various systems, including semiconductor-superconductor nanowires (9, 10), topological insulator-superconductor heterostructures (11), and atomic chains on superconducting substrate (12, 13). Recently, fully gapped bulk iron-based superconductors have emerged as a single-material platform for MZMs (14, 15). Evidence for MZMs in topological vortices on the surface of FeTe_{0.55}Se_{0.45} has been found with scanning tunneling microscopy/spectroscopy (STM/S) (16–18).

At sufficiently low temperatures, the conductance of an MZM exhibits a quantized plateau at the value of $2e^2/h$, where e is the electron charge and h is Planck's constant (19, 20). This quantized Majorana conductance results from perfect resonant Andreev reflection guaranteed by the inherent particle-hole symmetric nature of MZM (2). A quantized conductance plateau has been observed in an InSb–Al nanowire system, which is con-

sistent with the existence of MZMs (21). However, some alternative explanations have not been ruled out; for example, the partially separated Andreev bound state (ps-ABS) can also lead to a quantized conductance plateau that is topologically trivial (22–24). Iron-based superconductors, in which STM/S experiments observed zero-bias conductance peaks (ZBCPs) (16–18, 25), have large topological gaps [estimated at ~0.7 meV for Fe(Te,Se) in (16)] and offer the possibility of observing Majorana quantized conductance without contamination from low-lying Caroli–de Gennes–Matricon bound states (CBSs) (16, 18). Results suggesting quantized conductance have been reported for (Li_{0.84}Fe_{0.16})OHFeSe (26).

Motivated by the above prospects, we used a variable-tunnel-coupling STM/S method to study the Majorana conductance over a large range of tip-sample distance in vortex cores of FeTe_{0.55}Se_{0.45} (Fig. 1A). The effective electron temperature (T_{eff}) of our STM is 377 mK, as calibrated by tunneling into aluminum (fig. S1). In STM/S, the tunnel coupling can be continuously tuned by changing the tip-sample distance (d), which correlates with the tunnel-barrier conductance ($G_N \equiv I_t/V_s$, where I_t is the tunneling current and V_s is the setpoint voltage) (16). With a 2-T magnetic field applied perpendicular to the sample surface, we observed a sharp ZBCP at a vortex core (Fig. 1B). This ZBCP neither disperses nor splits across the vortex core, as expected for an isolated MZM in a quantum-limited vortex (16–18, 25). We performed tunnel-coupling-dependent measurement on the observed ZBCP. By putting the STM tip at the center of a topological vortex (18), we recorded a set of differential conductance (dI/dV) spectra with different tip-sample distances (Fig. 1C). The ZBCP remained a well-defined peak located at zero energy [voltage offset calibration under different tunnel couplings is discussed

in (27)]. We observed a distinct behavior of ZBCP under different G_N (Fig. 1C): The ZBCP peak height saturates at a relatively high tunnel coupling (Fig. 1F), whereas the high-bias conductance outside the superconducting gap increases monotonically as a function of G_N . This behavior can be better visualized in a three-dimensional plot (Fig. 1D) and a color-scale plot (Fig. 1E) that introduce an additional axis for G_N . The zero-bias conductance reaches a plateau when G_N is around $0.3 G_0$ ($G_0 \equiv 2e^2/h$). Two plots of conductance curves as a function of G_N were extracted from Fig. 1, C to E. The zero-bias conductance barely changes over a wide range of G_N ($0.3 G_0 \sim 0.9 G_0$); the average plateau conductance (G_P) is equal to $0.64 G_0$ (Fig. 1F). By contrast, the high-bias conductance at ± 1.5 and -4.5 meV (Fig. 1G) changes by a factor of more than three as the tip-sample distance varies.

To examine the particle-hole-symmetric nature of the MZMs, we compared and contrasted conductance behavior of zero-energy MZMs and finite-energy CBSs. As demonstrated previously, there are two distinct types of vortices: topological vortices with MZM and ordinary vortices without MZM, differing by a half-integer level shift of vortex bound states (18). First, we performed a tunnel-coupling-dependent measurement on a topological vortex (Fig. 2, A and B), which showed an MZM and the first CBS level located at 0 and ± 0.31 meV, respectively. In contrast to MZM, we found that the conductance of finite-energy CBS keeps increasing with G_N and shows no plateau. We also carried out measurements on an ordinary vortex. A dI/dV spectrum showed a CBS with half-odd-integer quantization (Fig. 2C), in which the first three levels of CBSs were located at ± 0.13 , ± 0.39 , and ± 0.65 meV, respectively. Again, the conductance values of all the CBSs kept increasing and had no plateau feature in the tunnel-coupling-dependent measurement (Fig. 2D). As another check, we repeated the measurement for the same location at zero magnetic field (Fig. 2, E and F) and observed a hard superconducting gap. The zero-bias conductance and the high-bias conductance were plotted as functions of G_N (Fig. 2F, middle and bottom, respectively). It is evident that both curves keep increasing as the tunnel coupling increases. This observation can be confirmed in a z -offset plot, with a larger z -offset corresponding to a smaller tip-sample distance (fig. S3). Therefore, the conductance plateau feature has only been observed in ZBCP, which indicates behavior specific to Majorana modes.

The plateau behavior of the zero-bias conductance provides evidence for the Majorana-induced resonant Andreev reflection (19, 20). It has been well understood that a perfect transmission of electrons can occur in a symmetric double-barrier system by means of

¹Beijing National Laboratory for Condensed Matter Physics and Institute of Physics, Chinese Academy of Sciences, Beijing 100190, China. ²School of Physical Sciences, University of Chinese Academy of Sciences, Beijing 100190, China. ³Department of Physics, Massachusetts Institute of Technology, Cambridge, MA 02139, USA. ⁴CAS Center for Excellence in Topological Quantum Computation, University of Chinese Academy of Sciences, Beijing 100190, China. ⁵Songshan Lake Materials Laboratory, Dongguan, Guangdong 523808, China. ⁶Condensed Matter Physics and Materials Science Department, Brookhaven National Laboratory, Upton, NY 11973, USA.

*These authors contributed equally to this work.

†Corresponding author. Email: hlgao@iphy.ac.cn (H.-J.G.); dingh@iphy.ac.cn (H.D.); zhangyuyang@ucas.ac.cn (Y.-Y.Z.)

Fig. 1. Zero-bias conductance plateau observed on

FeTe_{0.55}Se_{0.45}. (A) A schematic of variable-tunnel-coupling STM/S method. A zero-bias conductance map under 2.0 T is shown on a sample surface. A dI/dV spectrum measured at the center of the vortex core ($V_s = -5$ mV, $I_t = 500$ pA, $V_{\text{mod}} = 0.02$ mV) is shown in the top right inset; a sharp ZBCP is observed. When the tunneling current (I_t) is adjusted by the STM regulation loop, the tunnel coupling between the STM tip and the MZM can be tuned continuously with the tip-sample distance (d). Larger tunnel coupling corresponds to smaller d and larger tunneling-barrier conductance ($G_N = I_t/V_s$, where V_s is the setpoint voltage). z -offset can be read out simultaneously, which indicates the absolute z direction motion of the STM tip. (B) A line-cut intensity plot along the dashed white arrow in the inset, measured from the same vortex shown in (A), showing a stable MZM across the vortex core. (C) An overlapping plot of dI/dV spectra under different tunnel coupling values parameterized in G_N . The blue curve is measured under the smallest G_N , whereas the green curve is measured with the largest G_N . (D) A three-dimensional plot of tunnel coupling-dependent measurement, $dI/dV(E, G_N)$. For clarity, only the data points in the energy range of $[-5.0, 0.2]$ meV are shown. (E) A color-scale plot of (C) within the energy range of $[-1.5, 1.5]$ meV that shows the spectra as a function of G_N . The z -offset information, which was taken simultaneously by STM, is provided on the top axis. The maximum distance the tip approached is 3.4 Å. This plot shares the same color bar with (D). (F) A horizontal line-cut at the zero-bias from (E). The conductance curve shows a plateau behavior with the plateau conductance (G_p) equal to $(0.64 \pm 0.04) G_0$. (G) Horizontal line-cuts at high-bias values from (E). The absence of a conductance plateau on these curves indicates conventional tunneling behavior at the energy of continuous states. All the data were measured at $T_{\text{eff}} = 377$ mK.

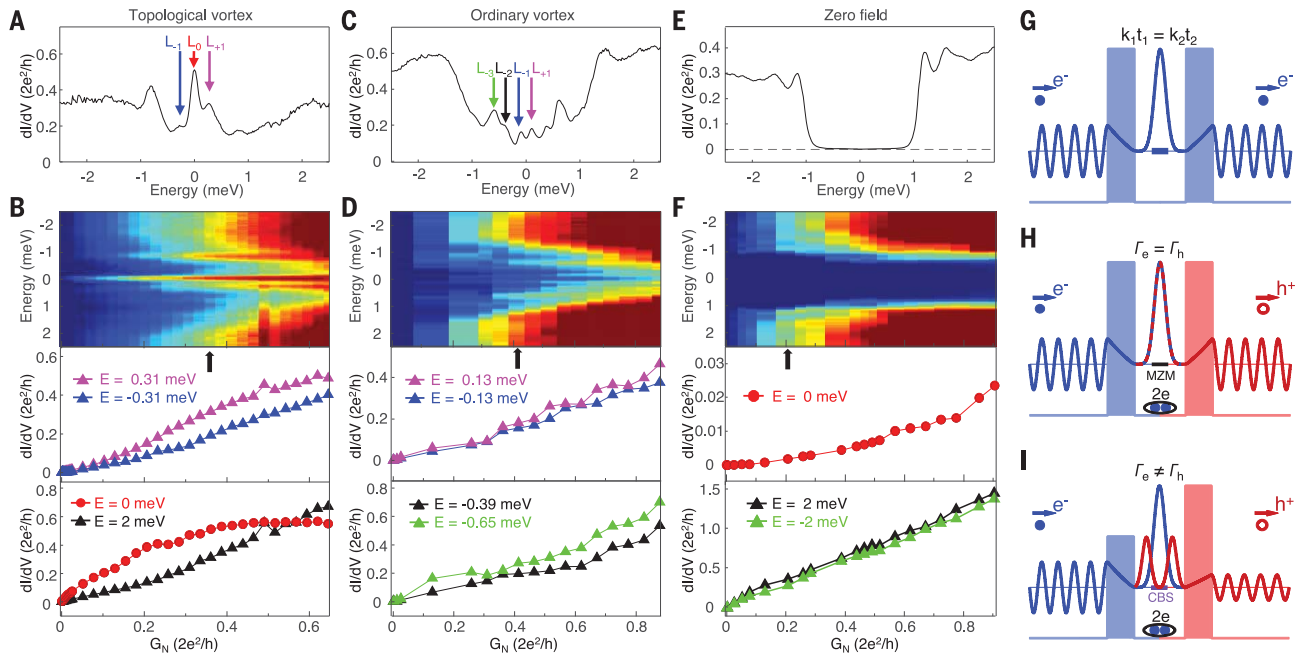


Fig. 2. Majorana-induced resonant Andreev reflection. (A) A dI/dV spectrum measured at the center of a topological vortex ($V_s = -5$ mV, $I_t = 140$ nA, $V_{\text{mod}} = 0.02$ mV), which shows a MZM (red arrow) coexisting with CBSs located at ± 0.31 meV (indicated with magenta and blue arrows). (B) A tunnel-coupling-dependent measurement on the vortex shown in (A) at 2 T. (Top) A color-scale plot, $dI/dV(E, G_N)$. The G_N position of (A) is indicated with a black arrow. (Middle) Tunnel coupling evolution of CBS conductance, which shows no plateau behavior. (Bottom) Tunnel coupling evolution of conductance at the energies of 0 meV (red circles, exhibiting a plateau) and 2 meV (black triangles, monotonically increasing). (C) A dI/dV spectrum measured at the center of an ordinary vortex ($V_s = -5$ mV, $I_t = 160$ nA, $V_{\text{mod}} = 0.02$ mV), which clearly shows three levels of CBS at ± 0.13 meV (magenta and blue arrows), ± 0.39 meV (black arrow), and ± 0.65 meV (green arrow). (D) Similar to (B), but measured on the vortex shown in (C). (Middle and bottom) Tunnel coupling evolution of CBS conductance, showing no plateau feature. (E) A dI/dV

spectrum measured at 0 T ($V_s = -5$ mV, $I_t = 80$ nA, $V_{\text{mod}} = 0.02$ mV). A hard superconducting gap can be seen. (F) Similar to (B) and (D), but measured under 0 T. (Middle) Tunnel-coupling evolution of zero-bias conductance (normal metal-superconductor junction case). (Bottom) Tunnel coupling evolution of conductance at the above gap energy (normal metal-normal metal junction case). There is no plateau behavior at 0 T. (G) A schematic of resonant tunneling through a symmetric double-barrier system. The wave function evolution of a tunneled electron is shown. kt is penetration constant. (H) The double-barrier view of the MZM-induced resonant Andreev reflection. The blue and red colors indicate the electron and hole process, respectively. The equivalence of particle and hole components in MZM ensures the same tunnel coupling on electron and hole barrier ($\Gamma_e = \Gamma_h$). (I) The double-barrier view of Andreev reflection mediated by a CBS. The arbitrary mixing of particle-hole components in CBS breaks the resonance condition. All the data were measured at $T_{\text{eff}} = 377$ mK.

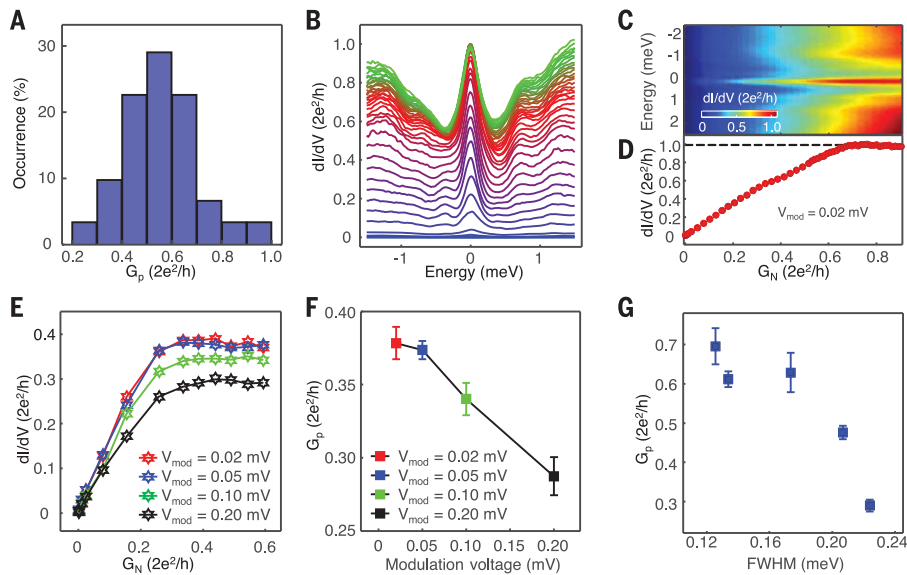


Fig. 3. The conductance variation of Majorana plateau. (A) A histogram of the G_P from 31 sets of data, which were measured with the same instrument. Sorting of the plateau conductance (G_P) in the order of increasing magnitude can be found in fig. S9 ($V_s = -5$ mV, $V_{\text{mod}} = 0.02$ mV). (B) The overlapping plot of 38 dI/dV spectra selected from a topological vortex that reaches a quantized conductance plateau ($V_s = -5$ mV, $V_{\text{mod}} = 0.02$ mV). (C) A color-scale plot of (B) within the energy range of $[-2.5, 2.5]$ meV that shows the spectra as a function of G_N . (D) A horizontal line-cut at the zero-bias from (C). The conductance curve shows that the conductance plateau reaches G_0 . (E) A series of tunnel-coupling-dependent measurements on the same MZM, with four modulation voltages of 0.02, 0.05, 0.10, and 0.20 mV. (F) The plot of G_P as a function of modulation voltage of the data shown in (E). (G) Relationship between FWHM of ZBCP and G_P , obtained from five different MZMs measured at the same experimental conditions, suggesting that the quasiparticle poisoning effect affects the plateau value. The FWHM were extracted from the spectrum measured at a large tip-sample distance with the same experimental parameters ($V_s = -5$ mV, $I_t = 500$ pA, $V_{\text{mod}} = 0.02$ mV). All the data were measured at $T_{\text{eff}} = 377$ mK.

resonant tunneling through a single quasistationary bound state (Fig. 2G). The transmission on resonance is e^2/h independent of tunnel coupling, as long as it is identical for the two barriers (28, 29). In the case of electron tunneling from a normal electrode through a barrier into a superconductor, the Andreev reflection process (30) converts the incident electron into an outgoing hole in the same electrode, resulting in a double-barrier system in the particle-hole Hilbert space. Moreover, in the case of Andreev reflection by means of a single MZM, the equal amplitude of particle-hole components, caused by the particle-antiparticle equivalence of MZM, ensures an identical tunnel coupling with electron and hole in the same electrode ($\Gamma_e = \Gamma_h$) (Fig. 2H). Thus, the resonant Andreev reflection mediated by an MZM leads to a $2e^2/h$ -quantized zero-bias conductance plateau, independent of the strength of tunnel coupling at zero temperature (19, 20, 31, 32). By contrast, low-energy CBSs (33, 34) and other trivial subgap states (22) do not have the Majorana symmetry, resulting in unequal weights for electron-hole components. The relationship of $\Gamma_e = \Gamma_h$ is broken in a CBS-mediated Andreev reflection (Fig. 2I), which leads to an absence of a conductance plateau (Fig. 2B, middle).

Moreover, the observed zero-bias conductance plateau in the vortex core disappears after the magnetic field is removed (Fig. 3, E and F) and hence cannot be attributed to quantum ballistic transport (35–40).

We observed the plateau behavior of ZBCPs repeatedly in many topological vortices [31 plateau features out of 60 measurements (41)]. We performed a statistical analysis of the observed plateau values G_P and found that most values of G_P are located around 40 to 70% of $G_0 = 2e^2/h$ (Fig. 3A). In one case, the plateau conductance reaches G_0 (Fig. 3, B to D). Both instrumental broadening and quasiparticle poisoning in our system can potentially induce deviation of G_P from the theoretical quantized value $2e^2/h$. To examine the possible effect of instrumental broadening on Majorana conductance plateau, we deliberately increased the instrumental broadening by varying the modulation voltage (V_{mod}), which is defined by the zero-to-peak amplitude of lock-in excitation. This allowed us to study the V_{mod} -evolution of the Majorana conductance plateau on a given topological vortex (Fig. 3, E and F). We found that larger V_{mod} leads to stronger suppression of G_P of MZM. In addition, we noticed that the values of conductance plateaus are correlated with the full width of half maximum (FWHM)

of the ZBCP measured under a large tip-sample distance limit. We found that G_P decreases with increasing FWHM (Fig. 3G) (detailed data are shown in fig. S5). This indicates that the quasiparticle poisoning effect (42, 43) might also play a role in reducing the conductance plateau value; the poisoning rate is expected to be spatially nonuniform in $\text{FeTe}_{0.55}\text{Se}_{0.45}$, which has intrinsic inhomogeneities.

We also checked the reversibility of the process of varying tunneling coupling in STM and found that both the topography and the conductance plateau can be reproduced during two repeated sequences of varying tunneling coupling (fig. S8), indicating the absence of irreversible damage of the tip and the sample during measurements. Other mechanisms related to zero-bias conductance plateau, such as inhomogeneity-induced ps-ABS (22–24) and class-D weak antilocalization (44), cannot be definitively excluded; complete understanding of our experiments requires further theoretical efforts. Our observation of a zero-bias conductance plateau in the two-dimensional vortex case, which approaches the quantized conductance of $2e^2/h$, provides spatially resolved spectroscopic evidence for Majorana-induced resonant electron transmission into a bulk superconductor, moving one step further toward the braiding operation applicable to topological quantum computation.

REFERENCES AND NOTES

1. A. Y. Kitaev, *Ann. Phys.* **303**, 2–30 (2003).
2. C. Nayak, S. H. Simon, A. Stern, M. Freedman, S. Das Sarma, *Rev. Mod. Phys.* **80**, 1083–1159 (2008).
3. A. Y. Kitaev, *Phys. Uspekhi* **44** (10S), 131–136 (2001).
4. N. Read, D. Green, *Phys. Rev. B Condens. Matter Mater. Phys.* **61**, 10267–10297 (2000).
5. L. Fu, C. L. Kane, *Phys. Rev. Lett.* **100**, 096407 (2008).
6. J. D. Sau, R. M. Lutchyn, S. Tewari, S. Das Sarma, *Phys. Rev. Lett.* **104**, 040502 (2010).
7. R. M. Lutchyn, J. D. Sau, S. Das Sarma, *Phys. Rev. Lett.* **105**, 077001 (2010).
8. Y. Oreg, G. Refael, F. von Oppen, *Phys. Rev. Lett.* **105**, 177002 (2010).
9. V. Mourik *et al.*, *Science* **336**, 1003–1007 (2012).
10. R. M. Lutchyn *et al.*, *Nat. Rev. Mater.* **3**, 52–68 (2018).
11. H. H. Sun *et al.*, *Phys. Rev. Lett.* **116**, 257003 (2016).
12. S. Nadj-Perge, I. K. Drozdov, B. A. Bernevig, A. Yazdani, *Phys. Rev. B Condens. Matter Mater. Phys.* **88**, 020407 (2013).
13. S. Nadj-Perge *et al.*, *Science* **346**, 602–607 (2014).
14. Z. Wang *et al.*, *Phys. Rev. B Condens. Matter Mater. Phys.* **92**, 115119 (2015).
15. P. Zhang *et al.*, *Science* **360**, 182–186 (2018).
16. D. Wang *et al.*, *Science* **362**, 333–335 (2018).
17. T. Machida *et al.*, *Nat. Mater.* **18**, 811–815 (2019).
18. L. Kong *et al.*, *Nat. Phys.* **15**, 1181–1187 (2019).
19. K. T. Law, P. A. Lee, T. K. Ng, *Phys. Rev. Lett.* **103**, 237001 (2009).
20. M. Wimmer, A. R. Akhmerov, J. P. Dahlhaus, C. W. J. Beenakker, *New J. Phys.* **13**, 053016 (2011).
21. H. Zhang *et al.*, *Nature* **556**, 74–79 (2018).
22. C. X. Liu, J. D. Sau, T. D. Stanescu, S. Das Sarma, *Phys. Rev. B* **96**, 075161 (2017).
23. C. Moore, T. D. Stanescu, S. Tewari, *Phys. Rev. B* **97**, 165302 (2018).
24. C. Moore, C. C. Zeng, T. D. Stanescu, S. Tewari, *Phys. Rev. B* **98**, 155314 (2018).
25. Q. Liu *et al.*, *Phys. Rev. X* **8**, 041056 (2018).
26. C. Chen *et al.*, *Chin. Phys. Lett.* **36**, 057403 (2019).
27. Materials and methods are available as supplementary materials.

28. R. Tsu, L. Esaki, *Appl. Phys. Lett.* **22**, 562–564 (1973).
29. L. L. Chang, L. Esaki, R. Tsu, *Appl. Phys. Lett.* **24**, 593–595 (1974).
30. G. E. Blonder, M. Tinkham, T. M. Klapwijk, *Phys. Rev. B Condens. Matter* **25**, 4515–4532 (1982).
31. K. Flensberg, *Phys. Rev. B Condens. Matter Mater. Phys.* **82**, 180516 (2010).
32. F. Setiawan, C. X. Liu, J. D. Sau, S. Das Sarma, *Phys. Rev. B* **96**, 184520 (2017).
33. C. Caroli, P. G. De Gennes, J. Matricon, *Phys. Lett.* **9**, 307–309 (1964).
34. H. F. Hess, R. B. Robinson, J. V. Waszczak, *Phys. Rev. Lett.* **64**, 2711–2714 (1990).
35. C. W. Beenakker, J. G. Williamson, L. P. Kouwenhoven, C. T. Foxon, *Phys. Rev. Lett.* **60**, 848–850 (1988).
36. J. Kammhuber *et al.*, *Nano Lett.* **16**, 3482–3486 (2016).
37. C. W. Beenakker, *Phys. Rev. B Condens. Matter* **46**, 12841–12844 (1992).
38. M. Kjaergaard *et al.*, *Nat. Commun.* **7**, 12841 (2016).
39. H. Zhang *et al.*, *Nat. Commun.* **8**, 16025 (2017).
40. Ö. Gül *et al.*, *Nat. Nanotechnol.* **13**, 192–197 (2018).
41. That we did not observe a plateau feature in the other 29 cases is because of the instability of the vortices during the tip-approaching process [(27), section 5].
42. J. R. Colbert, P. A. Lee, *Phys. Rev. B Condens. Matter Mater. Phys.* **89**, 140505 (2014).
43. I. Martin, D. Mozyrsky, *Phys. Rev. B Condens. Matter Mater. Phys.* **90**, 100508 (2014).
44. H. Pan, W. S. Cole, D. Jay, Sau and S. Das Sarma, Generic quantized zero-bias conductance peaks in superconductor-semiconductor hybrid structures. arXiv:1906.08193 [cond-mat.mes-hall] (2019).
45. S. Zhu *et al.*, Nearly quantized conductance plateau of vortex zero mode in an iron-based superconductor. Zenodo (2019); doi:10.5281/zenodo.3514211

ACKNOWLEDGMENTS

We thank P. A. Lee, C.-X. Liu, and G. Su for helpful discussions and A.-W. Wang, J.-H. Yan, and Q. Huan for technical assistance.

Funding: The work at IOP is supported by grants from the Ministry of Science and Technology of China (2019YFA0308500, 2015CB921000, 2015CB921300, and 2016YFA0202300), the National Natural Science Foundation of China (61888102 and 11888101), and the Chinese Academy of Sciences (XDB28000000, XDB30000000, and 112111KYSB20160061). L.F. and G.G. are supported by the U.S. Department of Energy (DOE) (DE-SC0019275 and DE-SC0012704, respectively). J.S. and R.Z.

are supported by the Center for Emergent Superconductivity, an Energy Frontier Research Center funded by the DOE. **Author contributions:** H.-J. G. and H.D. designed STM experiments. S.Z., L.C., H.C., Y.X., and Y.-Y.Z. performed STM experiments with assistance of W.L., F.Y., and C.S.; J.S., R.Z., and G.G. provided samples. L.F. provided theoretical explanations. Y.-Y.Z., S.D., S.Z., and L.K. processed experimental data and wrote the manuscript. All the authors participated in analyzing experimental data, plotting figures, and writing the manuscript. H.D. and H.-J.G. supervised the project. **Competing interests:** The authors declare that they have no competing interests. **Data and materials availability:** The data presented in this paper can be found in (45).

SUPPLEMENTARY MATERIALS

science.sciencemag.org/content/367/6474/189/suppl/DC1
Materials and Methods
Supplementary Text
Figs. S1 to S9
References (46–48)

15 February 2019; resubmitted 29 July 2019
Accepted 7 November 2019
10.1126/science.aax0274

CATALYSIS

Hydrophobic zeolite modification for in situ peroxide formation in methane oxidation to methanol

Zhu Jin^{1,2}, Liang Wang^{1*}, Erik Zuidema³, Kartick Mondal⁴, Ming Zhang⁵, Jian Zhang^{2†}, Chengtao Wang², Xiangju Meng², Hengquan Yang⁵, Carl Mesters⁶, Feng-Shou Xiao^{1,2*}

Selective partial oxidation of methane to methanol suffers from low efficiency. Here, we report a heterogeneous catalyst system for enhanced methanol productivity in methane oxidation by in situ generated hydrogen peroxide at mild temperature (70°C). The catalyst was synthesized by fixation of AuPd alloy nanoparticles within aluminosilicate zeolite crystals, followed by modification of the external surface of the zeolite with organosilanes. The silanes appear to allow diffusion of hydrogen, oxygen, and methane to the catalyst active sites, while confining the generated peroxide there to enhance its reaction probability. At 17.3% conversion of methane, methanol selectivity reached 92%, corresponding to methanol productivity up to 91.6 millimoles per gram of AuPd per hour.

Methanol (1–5) is an important platform molecule for producing olefins, aromatics, and other building blocks for fine chemicals (6–10). The energy-intensive conventional route to its industrial synthesis entails reforming of methane to syngas, followed by further conversion to methanol at high pressure (11–13). The direct partial oxidation of methane into methanol would be more attractive but is challenging because of methane's high C–H bond strength (104 kcal/mol), negligible electron affinity, and low polarizability (14–16). Furthermore, the methanol product is more susceptible to oxidation than methane, usually resulting in methanol oxidation under the reaction conditions (17). Expensive or toxic oxidants have been explored to surmount this challenge, but they have not been amenable to commercial application (1, 18–20). The use of low-cost O₂ as an oxidant, on the other hand, still suffers from unsatisfactory selectivity because of the favorable formation of CO₂ (21, 22). Cyclic gas-phase oxidation of methane on Cu- or Fe-containing zeolite catalysts with O₂ or H₂O might inhibit overoxidation (23–28), but requires intermittent steps to activate the oxidant and desorb the methanol product at relatively high temperatures (200° to 500°C).

Compared with gas-phase methane conversion, methane oxidation in liquid solvent at mild temperatures is less energy intensive (29–35). A Hg and Pt catalyst system was reported for methane oxidation in strongly acidic oleum to obtain methyl bisulfate, but the subsequent hydrolysis to methanol results in the formation of stoichiometric amounts of SO₂ (29). Similarly, cationic Au, Pd, and Pt catalysts are active for methane oxidation, but the use of strong oxidizing agents, such as selenic acid, still yield environmentally unfriendly by-products (29, 30). To overcome this issue, the environmentally benign oxidant hydrogen peroxide (H₂O₂) has been used for the methane oxidation in the absence of any toxic salts or strong acids (31–35). However, H₂O₂ is expensive relative to gaseous oxygen.

Recently, several groups reported successful partial oxidation of methane using H₂O₂ synthesized in situ from hydrogen and oxygen over metal nanoparticles (2, 34–39). The reported transformation proceeded with lower productivity than that observed in studies using H₂O₂ directly (1–4, 9). This phenomenon might be explained by a relatively low H₂O₂ concentration in the vicinity of the catalytically active nanoparticles (40). The key intermediate H₂O₂ is generated relatively slowly from H₂ and O₂ and can readily diffuse away from the active sites. In line with this hypothesis, preventing H₂O₂ dilution, and thereby keeping a high local concentration of H₂O₂ around metal nanoparticles, should promote methane conversion. However, this strategy has proven challenging and has not yet been demonstrated.

In this study, we addressed this challenge by finely controlling H₂O₂ diffusion in the partial oxidation of methane, using the concept of a molecular fence. AuPd alloy nanoparticles were embedded in aluminosilicate zeolite crystals, followed by hydrophobization that rendered the external surface of the zeolite

hydrophobic by appending organosilanes. We call this catalyst AuPd@zeolite-R, where the @ symbol denotes encapsulation of the nanoparticles within the zeolite and R indicates the organic substituent of the silane sheath. Our investigation demonstrates that once the hydrophilic H₂O₂ forms from H₂ and O₂, the hydrophobic sheath hinders its diffusion from the encapsulated AuPd nanoparticles, enhancing its concentration in the zeolite crystals. At the same time, the hydrophobic methane molecules can efficiently pass through the hydrophobic sheath to access the AuPd nanoparticles.

To prepare the catalyst, AuPd colloids were treated with tetraethyl orthosilicate under hydrolysis conditions to produce AuPd nanoparticles coated with amorphous silica (AuPd@SiO₂). Then, the amorphous silica sheath of AuPd@SiO₂ was crystallized into an MFI zeolite framework under solvent-free conditions, using tetrapropylammonium hydroxide as the structure-directing agent and boehmite as the alumina source, at a molar composition of 1.67 SiO₂/0.028 Al₂O₃/0.16 TPAOH/0.017 Au/0.017 Pd. The solvent-free route is crucial for the fixation of AuPd nanoparticles within the zeolite crystals. The conventional hydrothermal synthesis of zeolites caused leaching and aggregation of metal nanoparticles in the strong alkaline liquor at the high temperature (180°C) needed to form the zeolite framework (41). The organic groups (R) that form the hydrophobic fence were introduced onto the zeolite crystals via postsilylation [AuPd@zeolite-R; Au/Pd molar ratio at 1; Au and Pd weight loading at 3.24 and 1.76 weight % (wt %), respectively]. The synthesis procedures are shown in fig. S1.

Figure 1A schematically represents the catalyst in which the AuPd nanoparticles are fixed within C₁₆-modified Zeolite Socony Mobil 5 (ZSM-5) zeolite crystals (AuPd@ZSM-5-C₁₆). Characterizations by scanning electron microscopy (SEM) (fig. S2), x-ray crystallography (fig. S3), and N₂ sorption isotherms (fig. S4) confirmed the high crystallinity. Transmission electron microscopy (TEM) was consistent with AuPd nanoparticle diameters between 3 and 9 nm (Fig. 1B). High-resolution TEM imaging of the AuPd nanoparticles gave a lattice spacing of 0.25 nm, which is notably different than the typical values for metallic Au and Pd (3). This analysis confirmed the formation of alloyed particles rather than separated Au or Pd phases. The formation of the alloy was further verified by energy dispersive spectroscopic (EDS) analysis (fig. S5). Because TEM characterization represents a two-dimensional observation of three-dimensional materials, section tomography was performed (fig. S6) to determine the location of the nanoparticles either within or on the external surface of the zeolite crystals. Using this method, we could

¹Key Lab of Biomass Chemical Engineering of Ministry of Education, College of Chemical and Biological Engineering, Zhejiang University, Hangzhou 310027, China. ²Key Lab of Applied Chemistry of Zhejiang Province, Department of Chemistry, Zhejiang University, Hangzhou 310028, China.

³Shell Global Solutions International B.V., 1031HW

Amsterdam, Netherlands. ⁴Shell India Markets Pvt. Ltd., Shell Technology Centre, Plot 7, Bangalore Hardware Park, Devanahalli Industrial Area, Bangalore 562149, India. ⁵School of Chemistry and Chemical Engineering, Shanxi University, Taiyuan 030006, China. ⁶Shell International Exploration and Production, Houston, TX 77082, USA.

*Corresponding author. Email: liangwang@zju.edu.cn (L.W.); fsxiao@zju.edu.cn (F.-S.X.) †Present address: Beijing Advanced Innovation Center for Soft Matter Science and Engineering, Beijing University of Chemical Technology, Beijing 100029, China.

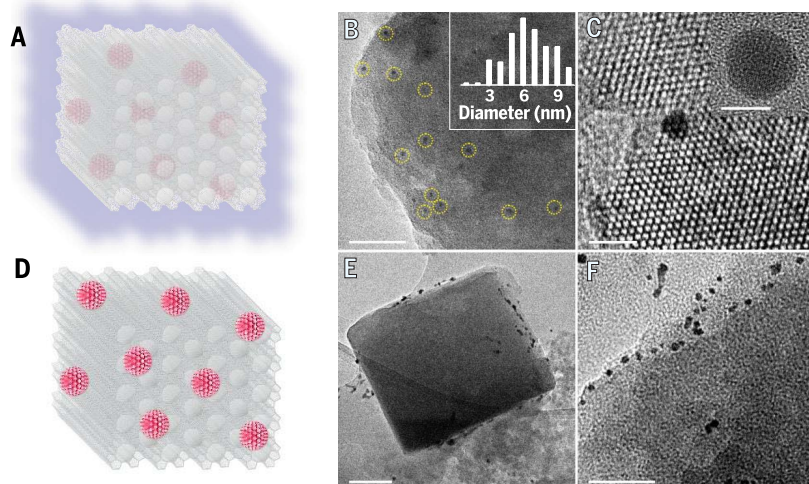


Fig. 1. Models and TEM images of the AuPd@ZSM-5-R and AuPd/ZSM-5 catalysts. Models and tomographic section TEM images of (A to C) AuPd@ZSM-5- C_{16} and (D to F) AuPd/ZSM-5. Scale bars: (B) 100 nm; (C) 10 nm (5 nm in inset); (E) 200 nm; (F) 50 nm.

confirm that for AuPd@ZSM-5- C_{16} the nanoparticles were encapsulated by the zeolite crystals (Fig. 1C) (42, 43).

The successful appending of hexadecyl groups onto the zeolite crystals was confirmed by ^{29}Si and ^{13}C nuclear magnetic resonance, fourier transform infrared spectroscopy, and thermogravimetric and differential thermal analysis (figs. S7 to S10). In addition, EDS analysis detected the organic groups on the external surface of the zeolite crystals (figs. S11 and S12). This synthesis strategy could be extended to prepare catalyst variations, including Au@ZSM-5 (fig. S13), Pd@ZSM-5 (fig. S14), AuPd@ZSM-5-Me (figs. S15 and S16), AuPd@ZSM-5- C_3 (figs. S17 to S20), and AuPd@ZSM-5- C_6 (figs. S21 to S24).

For comparison, a conventional ZSM-5 zeolite-supported AuPd nanoparticle catalyst was prepared by impregnating preformed PdAu nanoparticles on top of preformed ZSM-5 at the same Au/Pd loading (denoted AuPd/ZSM-5) (figs. S25 to S27). As expected, the AuPd nanoparticles were only detected on the external surface of the zeolite crystals (Fig. 1, E and F).

The catalysts were evaluated in the oxidation of methane using molecular H_2 and O_2 in the feed gas containing methane and inert balance gas (1/2/4/55 molar ratio of $\text{CH}_4/\text{H}_2/\text{O}_2/\text{inert gas}$, out of the explosion risks of methane at 11.5 to 20.0% and hydrogen at 4.3 to 32.2%; each reaction was tested for eight times to obtain the error bars) at 70°C (Fig. 2A, figs. S28 and S29, and tables S1 and S2). The blank run using ZSM-5 zeolite without Au or Pd failed to catalyze the reaction (fig. S30). The alloyed AuPd catalysts were active for the reaction, giving a methane conversion of 6.3% over the AuPd@ZSM-5 catalyst. When the

organic sheath was introduced, the methane conversions were enhanced by at least 2.5-fold, showing raised turnover numbers and frequencies (fig. S31). The AuPd@ZSM-5- C_3 catalyst gave a methane conversion of 16.4% with methanol selectivity of 90% (Fig. 2A). Even higher conversions of 17.1 and 17.3% were realized over AuPd@ZSM-5- C_6 and AuPd@ZSM-5- C_{16} catalysts that contained longer organic chains modified on the zeolite crystals (figs. S32 and S33). Notably, the methanol selectivity was maintained at 89 and 92% in these reactions, respectively. In these cases, formic acid appeared as the major by-product, while further overoxidation was prevented, as evidenced by the nearly undetectable CO_2 levels in the reactor (fig. S32). Formaldehyde and CO, which often appear in methane oxidation reactions, were also undetectable (figs. S32 and S33). In contrast, conventionally supported catalysts, such as AuPd/ZSM-5, exhibited very poor methane conversion at 2.2% with obviously detectable CO_2 from overoxidation (fig. S32C).

Methanol productivity of up to 84.6 to 91.6 $\text{mmol g}_{\text{AuPd}}^{-1} \text{hour}^{-1}$ could be observed for the AuPd@ZSM-5- C_3 , - C_6 , and - C_{16} catalysts (Fig. 2A and table S3). The methanol concentration was ~6.2 mmol/L in the resultant liquor, which could be concentrated into 68 wt % methanol aqueous solution by distillation at -95°C. These data outperform methanol productivities from methane oxidation over the state-of-the-art AuPd catalysts reported under similar reaction conditions in the literature (table S4), including the AuPd/TiO₂ catalyst mixed organic reductant and O_2 (methanol productivity: 35.9 $\text{mmol g}_{\text{AuPd}}^{-1} \text{hour}^{-1}$) or mixed H_2 and O_2 (methanol productivity: 10.5 $\text{mmol g}_{\text{AuPd}}^{-1} \text{hour}^{-1}$), and AuPd

nanoparticle colloidal suspensions for oxidation with H_2O_2 as initiator (methanol productivity: 11.8 $\text{mmol g}_{\text{AuPd}}^{-1} \text{hour}^{-1}$).

To shed more light on the reactions that play a role in this process, we analyzed the intermediates in the liquor during the reaction under the standard conditions (70°C, the condition in Fig. 2B). In the reactions over AuPd@ZSM-5- C_{16} and AuPd@ZSM-5 catalysts, methane conversion increased with time, and methanol, methyl peroxide, formic acid, and H_2O_2 were detectable in the reaction liquor (Fig. 2B and fig. S33). The detectable amounts of these products in the liquor are low at the beginning of the reaction, because most of the methanol product is trapped in the zeolite crystals (fig. S34) (24). For example, on the basis of the methanol detectable in the liquor after separating the solid catalysts, the methanol selectivity was low in the first 20 min (cumulative ratio of detected methanol in the liquor to the transformed methane over the full 20 min, methanol selectivity = [detected methanol in solution]/[transformed methane] $\times 100\%$). The centralized methanol and formic acid products in zeolite could be extracted by washing the zeolite catalyst with tetrahydrofuran, giving a higher carbon balance for the reaction process (table S5). In this case, methanol is the predominant extracted product, with a small amount of formic acid, confirming the hindered overoxidation, which might be due to the low methanol concentration at the beginning of the reaction. At longer reaction time (<30 min), more methane diffused into the zeolite crystals to occupy the zeolite micropores, displacing methanol from the zeolite crystals via methane-methanol competitive sorption (fig. S35). This feature shifts abundant methanol product to the liquor from within the zeolite crystals, because the methanol can easily diffuse through the hydrophobic sheath (bidirectional diffusion) (fig. S35C), which effectively hinders the methanol overoxidation and benefits the selective oxidation of methane. The methane conversion over AuPd@ZSM-5- C_{16} reached 17.3% in 30 min, where the highest methanol productivity and selectivity were obtained according to the detected methanol in the aqueous liquor (carbon balance >99%) (Fig. 2B). When AuPd@ZSM-5 was used as the catalyst, methane conversion was 6.3% at 30 min. Clearly, the presence of organic groups not only enhances methane conversion but also hinders the overoxidation of the methanol product.

Prolonging the reaction time at 70°C led to a slightly increased methane conversion but decreased methanol productivity, because the methane-methanol competitive sorption could not efficiently release the methanol at a sufficiently high methanol concentration (e.g., after reaction for 30 min) (table S6 and fig.

S36) and decreased methane partial pressure in the reactor, causing methanol overoxidation. After a reaction time of 80 min, the average methanol productivity over the full time was $61.9 \text{ mmol g}_{\text{AuPd}}^{-1} \text{ hour}^{-1}$, where ~32% of methanol was overoxidized compared with the data at 30 min ($91.6 \text{ mmol g}_{\text{AuPd}}^{-1} \text{ hour}^{-1}$). Similar reaction trends were also observed in the reactions over the AuPd@ZSM-5-C₃ catalyst under equivalent conditions (fig. S37). Further reaction for a longer period (e.g., >140 min) gave the methanol selectivity at ultralow values because of the continuous overoxidation to form abundant CO₂ (table S5 and fig. S38). For the reactions on AuPd@ZSM-5-C₁₆ at other temperatures (50°, 90°, and 110°C), similar trends were also observed (fig. S38), but the reaction for 30 min at 70°C was used as an optimized reaction because of its superior catalytic performance. These results suggest that the optimal reaction conditions are important for obtaining the high methanol yield.

Considering that the AuPd@ZSM-5 and AuPd@ZSM-5-R catalysts consist of the same AuPd nanoparticles and ZSM-5 zeolite crystals, the distinct catalytic performances of the AuPd@ZSM-5-R catalysts can be reasonably attributed to the organic sheath. The hydrophobicity of the sheathed surfaces was confirmed by water-droplet contact angle tests (32.5° on AuPd@ZSM-5, and 99°, 112°, and 115° on AuPd@ZSM-5-C₃, -C₆, and -C₁₆, respectively) (fig. S39) and water-adsorption measurements (figs. S40 to S44) (44).

The H₂O₂ was always present at a concentration >1.5 mmol/L in the solvent after the first 10 min of the methane oxidation process using the AuPd@ZSM-5 catalyst (Fig. 2C), which is in good agreement with the general consensus that methane oxidation with H₂ and O₂ proceeds via the tandem steps of (i) H₂O₂ (or peroxide species) production from H₂ and O₂ and (ii) methane oxidation using the generated H₂O₂ (or peroxide species) (3). In contrast, the measured H₂O₂ concentrations were <0.2 mmol/L in the solution when the AuPd@ZSM-5-C₁₆ and AuPd@ZSM-5-C₃ catalysts were used (Fig. 2B and fig. S37).

To understand this difference, we investigated the formation of H₂O₂ from H₂ and O₂ over these catalysts (Fig. 3A and fig. S45). The AuPd/ZSM-5 (AuPd nanoparticles on the external ZSM-5) catalyst was active, producing $46.6 \text{ } \mu\text{mol H}_2\text{O}_2$ (H₂ conversion at 6.8%, O₂ conversion at 2.7%) in the reaction liquor after 30 min (after removal of the catalyst). In contrast, the H₂O₂ quantity in the water solution reached $97.9 \text{ } \mu\text{mol}$ when the AuPd@ZSM-5 catalyst was used. We attribute this result to the high Brønsted-acid concentration in the zeolite crystals and close to the AuPd nanoparticles (45). It is widely recognized that acidity effectively hinders H₂O₂ decomposition (fig. S46). Under equivalent conditions, the

AuPd@ZSM-5-C₃ and -C₁₆ catalysts gave 18.7 and 12.8 μmol of H₂O₂ in the liquor, respectively, which is much lower than that observed with the unmodified AuPd@ZSM-5 catalyst. Washing the solid catalysts using cold methanol and tetrahydrofuran (~0°C) liberated the H₂O₂ within the zeolite crystals. A further 8.1, 78.3, and 68.4 μmol of H₂O₂ was thus obtained for AuPd@ZSM-5, AuPd@ZSM-5-C₁₆, and AuPd@ZSM-5-C₃, respectively (H₂ conversions at 9.2 to 10.8%) (fig. S45). These results indicate that ~92% of the produced H₂O₂ was dissolved into the aqueous phase over AuPd@ZSM-5, whereas 78 to 86% of H₂O₂ was confined within the zeolite crystals of AuPd@ZSM-5-C₁₆ and -C₃.

We also quantified the H₂O₂ formed in the methane oxidation system with H₂ and O₂. After a 30-min reaction time, the autoclave reactor was rapidly cooled in an ice bath to quench reactivity, and the amount of H₂O₂ was measured by titration. As shown in Fig. 3A and table S7, results were obtained that are similar to those in the H₂O₂ synthesis tests: 76 to 82% of the H₂O₂ was captured within the zeolite crystals over AuPd@ZSM-5-C₁₆ and AuPd@ZSM-5-C₃, and ~86% of the H₂O₂ easily diffused into the solution over AuPd@ZSM-5. We attribute this phenomenon to the molecular-fence effect, which enriched the H₂O₂ within the zeolite crystals. This effect

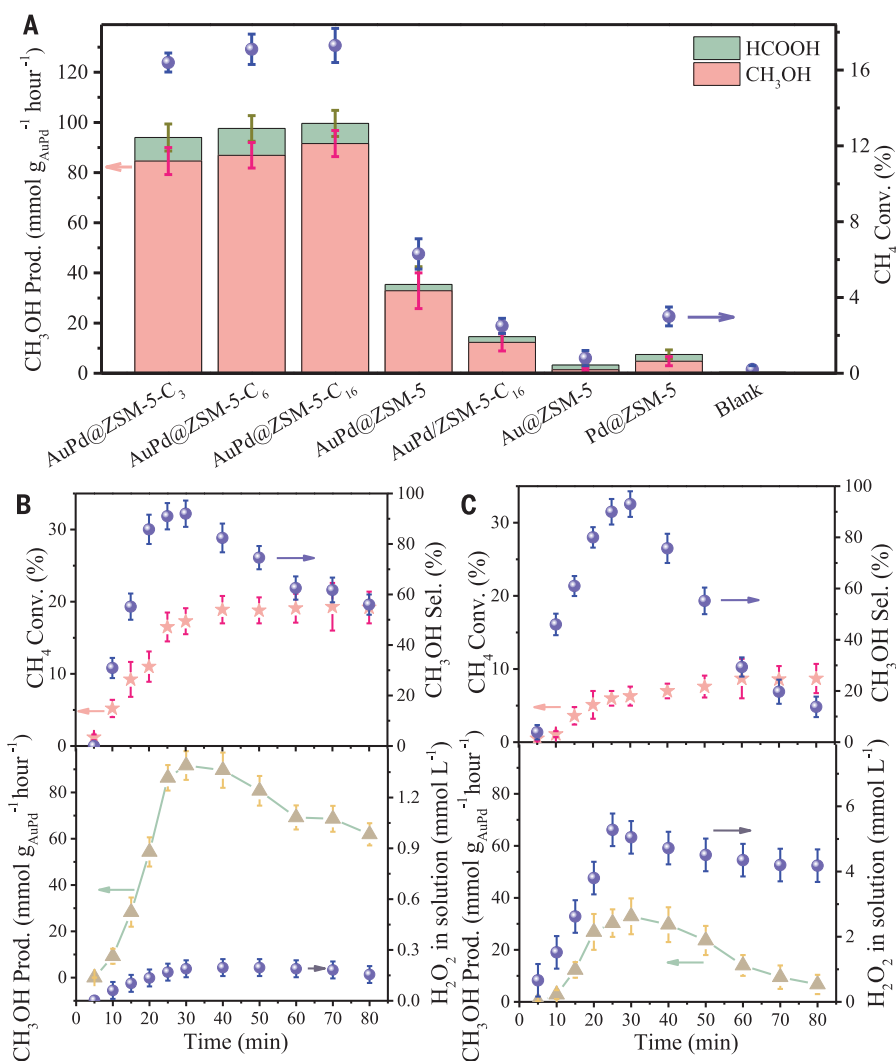


Fig. 2. Catalytic data. (A) Data characterizing the oxidation of methane with H₂ and O₂ over various catalysts. Reaction conditions: 10 mL of water, 30 min, 70°C, 27 mg of catalyst, feed gas at 3.0 MPa with 3.3% H₂/6.6% O₂/1.6% CH₄/61.7% Ar/26.8% He, and 1200 revolutions per minute (rpm). (B and C) Dependences of the methane conversion (Conv.), methanol selectivity (Sel.), methanol productivity (Prod.), and H₂O₂ concentration in water solution on reaction time over (B) AuPd@ZSM-5-C₁₆ and (C) AuPd@ZSM-5 catalysts. Reaction conditions: 10 mL of water, 70°C, 27 mg of catalyst, feed gas at 3.0 MPa with 3.3% H₂/6.6% O₂/1.6% CH₄/61.7% Ar/26.8% He, and 1200 rpm. Each reaction was tested eight times to obtain the error bars.

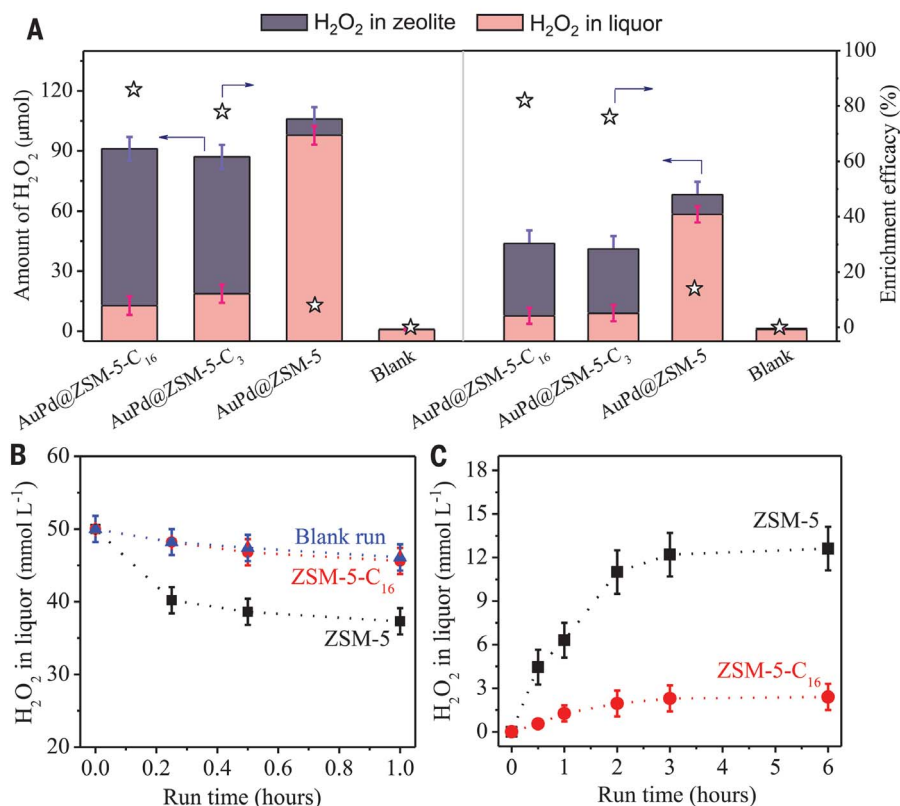


Fig. 3. Molecular-fence effect investigation. (A) Data showing the amount of H₂O₂ in the (left) H₂O₂ synthesis and (right) methane oxidation process. The enrichment efficacy is the percentage of H₂O₂ in zeolite crystals to the total amount of H₂O₂ in the reactor. Reaction conditions for H₂O₂ synthesis: 5.6 g of MeOH, 4.4 g of H₂O₂, 30 min, 0°C, 10 mg of catalyst, 4.0 MPa of feed gas with 5% H₂/10% O₂/45% Ar/40% He, and 1200 rpm. Reaction conditions for methane oxidation: 10 mL of water, 30 min, 70°C, 27 mg of catalyst, 3.0 MPa of feed gas with 3.3% H₂/6.6% O₂/1.6% CH₄/61.7% Ar/26.8% He, 15 min, and 1200 rpm. Each reaction was tested eight times to obtain the error bars. The dependences of H₂O₂ concentration in the liquor on time with (B) as-synthesized zeolites added in the H₂O₂ solution and (C) zeolites containing adsorbed H₂O₂ added into pure water. In the tests in (B), the ZSM-5 and ZSM-5-C₁₆ catalysts are pretreated in H₂O₂ solution to perfuse H₂O₂ molecules into the zeolite crystals, the H₂O₂ amounts in both samples are similar before the escape measurements. Each concentration was measured five times to obtain the error bars.

was further confirmed by Fenton reaction tests (fig. S47) (46).

To further elucidate the molecular-fence effect, H₂O₂ adsorption and desorption were probed on the ZSM-5 and ZSM-5-C₁₆ catalysts. The H₂O₂ adsorption tests were performed by dispersing the as-synthesized zeolite materials into an H₂O₂ solution (Fig. 3B). H₂O₂ concentration was reduced substantially over time in the presence of unmodified ZSM-5 but changed only slightly with ZSM-5-C₁₆. These data show that H₂O₂ is adsorbed by the unmodified ZSM-5 crystals, but not by hydrophobic ZSM-5-C₁₆. In H₂O₂ desorption tests (Fig. 3C), the zeolite-based materials were pretreated in 30 wt % H₂O₂ solution for an extended period (48 hours) to obtain H₂O₂-saturated zeolite crystals. These crystals were then added to pure water, and the resulting H₂O₂ concentration in water was measured. For unmodified ZSM-5, the concentration increased to 12.7 mmol/L over 6 hours,

demonstrating an efficient desorption of H₂O₂ from the zeolite crystals into the water process. Under the equivalent conditions, ZSM-5-C₁₆ yielded an aqueous H₂O₂ concentration of only 2.3 mmol/L in the liquor (if all the pre-adsorbed H₂O₂ in ZSM-5-C₁₆ were released, the concentration would be 10.6 mmol/L), confirming the hampered desorption of H₂O₂ from the zeolite crystals. Nonpolar molecules, such as methane, do not suffer from diffusion barriers caused by this hydrophobic sheath, as confirmed by methane adsorption tests (fig. S48). The AuPd@ZSM-5-R catalysts therefore appear to provide the ideal combination of a high local peroxide concentration and rapid methane adsorption to facilitate methanol production (fig. S49).

To support this view, we performed methane oxidation using preformed H₂O₂ as an oxidant over the various AuPd catalysts (fig. S50). AuPd/ZSM-5-C₁₆ (non-encapsulated AuPd) and

AuPd@ZSM-5 were both active for the methane oxidation to form methanol with productivities of 16.1 and 57.0 mmol g_{AuPd}⁻¹ hour⁻¹, respectively. In contrast, AuPd@ZSM-5-C₃, -C₆, and -C₁₆ catalysts exhibited extremely low methane productivities of 4.8, 4.0, and 5.5 mmol g_{AuPd}⁻¹ hour⁻¹, respectively, much lower than productivities in the systems where AuPd nanoparticles were not separated from the reaction medium by an organosilane sheath. This result clearly contrasts with the relative performances of these systems in methane oxidation using H₂ and O₂, where the AuPd@ZSM-5-R catalysts are most active. The results are again in line with a molecular-fence effect for H₂O₂, where the hydrophilic H₂O₂ fails to diffuse through the organosilane layer on the external surface of zeolite crystals to access the AuPd nanoparticles. Similarly, when H₂ and O₂ are used to generate H₂O₂ within the zeolite crystals, the peroxide cannot diffuse out readily, resulting in a high local concentration.

The molecular-fence catalyst was reusable. After a reaction, the catalyst could be separated from the reaction liquor by filtration, dried, and reused in a subsequent run. In the second run, AuPd@ZSM-5-C₁₆ exhibited methanol productivity of 91.8 mmol g_{AuPd}⁻¹ hour⁻¹ at 17.3% methane conversion, which is very similar to that of the as-synthesized catalyst (fig. S51). Even in continuous recycle tests for nine runs, the catalyst exhibited methanol productivity of 87.6 mmol g_{AuPd}⁻¹ hour⁻¹ (average productivity during the first 30 min of the ninth run) at 16.9% conversion. These data confirm the high activity, excellent selectivity, and good recyclability of these catalysts.

We have demonstrated the encapsulation of active AuPd nanoparticles inside zeolites and further modification of the resulting zeolite crystals by a hydrophobic sheath. This results in a zeolite nanoreactor with high local concentration of H₂O₂, which considerably enhances efficient oxidation of methane. We believe that zeolites with hydrophobic surfaces act as powerful supports for metal nanoparticles, and the molecular-fence concept should open a productive route to more-efficient catalysts for partial methane oxidation. This work represents a large step toward the application of direct activation of methane to produce valuable products. As yet, the productivity of the system still needs further improvement, and the batchwise operation is hampering commercial application. Future work should therefore focus on further improving methane conversion, as well as shifting to a continuous-flow mode of operation.

REFERENCES AND NOTES

1. R. A. Periana *et al.*, *Science* **280**, 560–564 (1998).
2. N. Agarwal *et al.*, *Science* **358**, 223–227 (2017).
3. M. H. Ab Rahim *et al.*, *Angew. Chem. Int. Ed.* **52**, 1280–1284 (2013).

4. R. Palkovits, M. Antonietti, P. Kuhn, A. Thomas, F. Schüth, *Angew. Chem. Int. Ed.* **48**, 6909–6912 (2009).
5. D. Saha, H. A. Grappe, A. Chakraborty, G. Orkoulas, *Chem. Rev.* **116**, 11436–11499 (2016).
6. P. Schwach, X. Pan, X. Bao, *Chem. Rev.* **117**, 8497–8520 (2017).
7. U. Olsbye *et al.*, *Angew. Chem. Int. Ed.* **51**, 5810–5831 (2012).
8. X. Guo *et al.*, *Science* **344**, 616–619 (2014).
9. C. Copéret, *Chem. Rev.* **110**, 656–680 (2010).
10. Z.-M. Cui, Q. Liu, W. G. Song, L. J. Wan, *Angew. Chem. Int. Ed.* **45**, 6512–6515 (2006).
11. H. T. Luk, C. Mondelli, D. C. Ferré, J. A. Stewart, J. Pérez-Ramírez, *Chem. Soc. Rev.* **46**, 1358–1426 (2017).
12. O. Martin *et al.*, *Angew. Chem. Int. Ed.* **55**, 6261–6265 (2016).
13. G. Centi, S. Perathoner, *Catal. Today* **148**, 191–205 (2009).
14. R. Balasubramanian *et al.*, *Nature* **465**, 115–119 (2010).
15. M. Ahlquist, R. J. Nielsen, R. A. Periana, W. A. Goddard 3rd, *J. Am. Chem. Soc.* **131**, 17110–17115 (2009).
16. J. H. Lunsford, *Catal. Today* **63**, 165–174 (2000).
17. F. Roudesly, J. Oble, G. Poli, *J. Mol. Catal. Chem.* **426**, 275–296 (2017).
18. S. H. Morejudo *et al.*, *Science* **353**, 563–566 (2016).
19. R. L. Lieberman, A. C. Rosenzweig, *Nature* **434**, 177–182 (2005).
20. R. A. Periana, O. Mironov, D. Taube, G. Bhalla, C. J. Jones, *Science* **301**, 814–818 (2003).
21. K. Natte, H. Neumann, M. Beller, R. V. Jagadeesh, *Angew. Chem. Int. Ed.* **56**, 6384–6394 (2017).
22. D. Schröder, H. Schwarz, *Proc. Natl. Acad. Sci. U.S.A.* **105**, 18114–18119 (2008).
23. D. Schroeder, A. Fiedler, J. Hrusak, H. Schwarz, *J. Am. Chem. Soc.* **114**, 1215–1222 (1992).
24. V. L. Sushkevich, D. Palagin, M. Ranocchiari, J. A. van Bokhoven, *Science* **356**, 523–527 (2017).
25. M. H. Groothaert, P. J. Smeets, B. F. Sels, P. A. Jacobs, R. A. Schoonheydt, *J. Am. Chem. Soc.* **127**, 1394–1395 (2005).
26. P. J. Smeets, M. H. Groothaert, R. A. Schoonheydt, *Catal. Today* **110**, 303–309 (2005).
27. J. S. Woertink *et al.*, *Proc. Natl. Acad. Sci. U.S.A.* **106**, 18908–18913 (2009).
28. E. M. Alayon, M. Nachtegaal, M. Ranocchiari, J. A. van Bokhoven, *Chem. Commun.* **48**, 404–406 (2012).
29. R. A. Periana, E. R. Evitt, H. Taube, Process for converting lower alkanes to esters, U.S. Patent 5,233,113 (1993).
30. R. A. Periana, D. J. Taube, H. Taube, E. R. Evitt, Catalytic process for converting lower alkanes to esters, alcohols, and to hydrocarbons, U.S. Patent 5,306,855 (1994).
31. P. Tomkins, M. Ranocchiari, J. A. van Bokhoven, *Acc. Chem. Res.* **50**, 418–425 (2017).
32. X. Cui *et al.*, *Chem* **4**, 1902–1910 (2018).
33. W. Huang *et al.*, *Angew. Chem. Int. Ed.* **55**, 13441–13445 (2016).
34. C. Hammond *et al.*, *Angew. Chem. Int. Ed.* **124**, 5219–5223 (2012).
35. S. Grundner *et al.*, *Nat. Commun.* **6**, 7546–7554 (2015).
36. R. A. Periana *et al.*, *Science* **259**, 340–343 (1993).
37. G. J. Hutchings, M. S. Scurrell, J. R. Woodhouse, *Chem. Soc. Rev.* **18**, 251–283 (1989).
38. J.-S. Min, H. Ishige, M. Misono, N. Mizuno, *J. Catal.* **198**, 116–121 (2001).
39. C. Williams *et al.*, *ACS Catal.* **8**, 2567–2576 (2018).
40. J. Xie *et al.*, *Nat. Catal.* **1**, 889–896 (2018).
41. K. Morgan, A. Goguet, C. Hardacre, *ACS Catal.* **5**, 3430–3445 (2015).
42. J. Zhang *et al.*, *Nat. Catal.* **1**, 540–546 (2018).
43. J. Zhang *et al.*, *Angew. Chem. Int. Ed.* **56**, 9747–9751 (2017).
44. M. Zhang *et al.*, *J. Am. Chem. Soc.* **138**, 10173–10183 (2016).
45. G. Noh, Z. Shi, S. I. Zones, E. Iglesia, *J. Catal.* **368**, 389–410 (2018).
46. H. Zhao, Y. Chen, Q. Peng, Q. Wang, G. Zhao, *Appl. Catal. B* **203**, 127–137 (2017).

ACKNOWLEDGMENTS

Funding: This work was supported by the National Key Research and Development Program of China (2018YFB0604801), National Natural Science Foundation of China (91634201, 21822203, and 91645105), Natural Science Foundation of Zhejiang Province (LR18B030002), Shell Global Solutions International B.V., and the Fundamental Research Funds for the Central Universities.

Author contributions: Z.J. performed the catalyst preparation, characterization, and catalytic tests. E.Z., K.M., X.M., and C.M. provided helpful discussion. J.Z. and C.W. participated in the catalyst synthesis and characterization. M.Z. and H.Y. participated in the characterization. L.W. and F.-S.X. designed the study, analyzed the data, and wrote the paper. **Competing interests:** The authors declare that there are no conflicts of interest and that they have no commercial relationships apart from the affiliations with Shell. **Data and materials availability:** Experiment details, x-ray diffraction, N₂ sorption, SEM, TEM, IR, NMR, and more catalytic data are available in the supplementary materials.

SUPPLEMENTARY MATERIALS

science.sciencemag.org/content/367/6474/193/suppl/DC1
Materials and Methods
Figs. S1 to S51
Tables S1 to S7
References (47–52)

19 November 2018; resubmitted 18 April 2019
Accepted 21 November 2019
10.1126/science.aaw1108

DEVELOPMENTAL BIOLOGY

Programmed cell death along the midline axis patterns ipsilaterality in gastrulation

Lisandro Maya-Ramos and Takashi Mikawa*

Bilateral symmetry is the predominant body plan in the animal kingdom. Cells on the left and right sides remain compartmentalized on their ipsilateral side throughout life, but with occasional variation, as evidenced by gynandromorphs and human disorders. How this evolutionarily conserved body plan is programmed remains a fundamental yet unanswered question. Here, we show that germ-layer patterning in avian gastrulation is ipsilateral despite cells undergoing highly invasive mesenchymal transformation and cell migration. Contralateral invasion is suppressed by extracellular matrix (ECM) and programmed cell death (PCD) along the embryonic midline. Ipsilateral gastrulation was lost by midline ECM and PCD inhibition but restored with exogenously induced PCD. Our data support ipsilaterality as an integral component of bilaterality and highlight a positive functional role of PCD in development.

Bilaterians have two symmetrical sides and constitute 99% of all animal species (1). Human disorders and naturally occurring bilateral gynandromorphs reveal that progenitor cells on the left and right sides give rise to cells that will primarily remain on the same (ipsilateral) side of the organism (2, 3). Although this topological cell-fate restriction is evolutionarily conserved across many animal species, ipsilaterality is not well understood (4). It is particularly intriguing how left-right cellular mixing is prevented in birds and mammals considering that in these species, gastrulating cells undergo an epithelial-mesenchymal transition (EMT), resulting in highly migratory and invasive mesenchymal cells (5).

Using the chick as a model system, we analyzed gastrulation cell-movement patterns using whole-embryo live imaging. The chick allows for high-precision control of spatiotemporal transfection parameters. The primitive streak (PS) is the conduit for germ-layer formation and defines left-right compartments in the embryo. Fluorescently tagged left and right epiblast cells moved toward the PS and underwent EMT (Fig. 1, A and B; fig. S1, A to C; and movie S1), with most ingressed cells migrating away from the PS to the ipsilateral side of transfection (left $96.1 \pm 1.2\%$, right $96.1 \pm 0.3\%$, $p = 0.9123$, $n = 14$) (Fig. 1C) (6). There is minimal mixing between left and right mesenchymal populations, effectively creating two compartments and patterning the ipsilateral sides.

To assess whether ipsilateral gastrulation is governed by inherent epiblast cell information or by non-cell-autonomous forces, an epiblast segment from green fluorescent protein (GFP)-transgenic chick embryo was grafted to the contralateral side of a stage-matched

wild-type (WT) embryo (fig. S1, D and F). In a cell-autonomous process, donor cells grafted isochronously at a contralateral side would be expected to move back to their originating side. However, grafted implants displayed ipsilateral gastrulation, identical to control grafts (heterotopic $91.3 \pm 4.7\%$, homotopic $91 \pm 2.4\%$, $p = 0.9893$, $n \geq 3$) (fig. S1, E, G, and H). These data point to an environmentally regulated process.

In both GFP-tagged and grafted embryos, labeled epiblast cells migrated without detectable obstruction until reaching the PS midline, where a sharp boundary was formed by their distribution along the PS, as if a midline barrier was preventing their movement (Fig. 1B and fig. S1, B, E, and G). This precise movement restriction hinted at a midline-specific program deterring cell crossing.

To examine the midline in depth, epiblast cells were tagged with membrane-tethered GFP for multiphoton live imaging. Results showed increased apoptotic cellular membrane blebbing as cells approached the midline (Fig. 1H, fig. S2Q, and movie S2), which is consistent with our previous report (7). TUNEL assay and cleaved caspase 3 immunofluorescent (IF) staining revealed broad epiblast programmed cell death (PCD) distribution in early gastrulation that became enriched at the midline in later stages (Fig. 1D and fig. S2).

Midline PCD did not follow classical scavenger cell-mediated cellular corpse clearance (8, 9) as continued presence of PCD at the midline was morphologically evident (Fig. 1, E to G, and figs. S2 and S3). These data indicate that PCD is enriched and persistent at the midline. Thus, we suspected that midline PCD could act as a barrier directing ipsilateral gastrulation.

To test this hypothesis, the ontogeny of midline PCD was traced with the early apoptosis reporter Annexin V (10). Yellow fluorescent protein-tagged secreted Annexin V was preferentially detected at the midline in cells under-

going blebbing compared with lateral epiblast cells (figs. S2R and S2S and movie S4). Additionally, Alexa Fluor 488-conjugated Annexin V labeling of epiblast cells revealed that PS midline cells undergoing PCD originated in the PS posterior region (Fig. 2, A to C, and movie S4). Therefore, to suppress midline PCD, the molecular pan-caspase inhibitor P35 was introduced posteriorly (Fig. 2D) (11). In embryos electroporated with P35:2A:H2B-GFP at the posterior region and H2B:RFP at lateral epiblast, many red fluorescent protein-positive (RFP⁺) cells invaded the contralateral side ($36.0 \pm 1.0\%$, $p < 0.0001$, $n = 4$) (Fig. 2, E to G; fig. S4; and movies S5 and S6). In comparison, lateral epiblast expressing P35 ingressed identically to WT cells (fig. S5). These results strongly suggest that midline PCD is required for ipsilateral gastrulation.

We surveyed several factors that could be involved in directing ipsilateral gastrulation (fig. S6). FGF and Eph signals are prominent in other midline systems, yet FGFR1-FGF8 and Eph3-EphrinB1 did not mimic the PCD midline barrier function (fig. S7) (12, 13). Therefore, we examined the ECM, which can suppress cellular movement and be involved in PCD (14, 15). Although the ECM was highly fenestrated in the lateral PS, it was uniquely enriched along the PS midline (Fig. 3, A, C, and D). Inversely, the membrane-bound matrix metalloproteinase 15 (MMP-15) had more expression in the lateral PS than in the midline PS (Fig. 3B and fig. S8). This complementary expression pattern suggested ECM regulation by MMP-15.

To test the role of ECM in ipsilateral gastrulation, laminin was depleted with the laminin subunit alpha-1 (LAMA1) morpholino (Fig. 3I and fig. S9). The resulting embryos exhibited higher contralateral invasion than scrambled morpholino controls (21.8% versus 4.3%, $p = 0.0029$, $n = 6$, $n = 3$) (Fig. 3, J and L, and movie S7). As there was more contralateral invasion after caspase 3 inhibition, we suspected that additional ECM proteins were involved in preventing contralateral invasion (Fig. 3, E and F). Indeed, introduction of MMP-15:2A:mCherry largely diminished midline ECM (Fig. 3, I, G, and H, and fig. S4), leading to robust contralateral invasion of GFP⁺ lateral cells ($39.3 \pm 1.5\%$ $p < 0.0001$, $n = 3$) (Fig. 3, K and L, and movie S8). These data point to a spatial regulation of ECM enrichment along the midline that is necessary for ipsilateral gastrulation.

Because the above data suggested that both PCD and ECM are required for ipsilateral gastrulation patterning, we suspected a potential interplay between these signaling axes (Fig. 4A). Midline ECM was apparent before PCD (fig. S10, A to K). Furthermore, P35-mediated PCD inhibition did not diminish midline ECM expression (fig. S10, L to O). By contrast, LAMA1 morpholino-mediated midline laminin knockdown decreased the amount of cleaved caspase 3

Cardiovascular Research Institute, University of California, San Francisco, San Francisco, CA 94158, USA.

*Corresponding author. Email: takashi.mikawa@ucsf.edu

signal at the midline (Fig. 4B). Given that PCD occurs throughout the embryonic disc and that midline PCD originates in cells from the posterior PS, ECM may be required for the alignment of PCD along the midline, although we cannot rule out ECM as a direct PCD inducer through anoikis (14, 16). In both scenarios, we

expect that the resulting atypically persisting midline PCD functions as a barrier to prevent contralateral invasion of gastrulating cells.

To test this possibility directly, we introduced PCD using two independent methods in midline laminin-depleted embryos (Fig. 4C) (17, 18). Induced PCD was sufficient to sup-

press contralateral invasion locally, thereby restoring ipsilateral ingress in a midline ECM-depleted background (Fig. 4, D to F; figs. S11 and S12; and movies S9 and S10). Thus, both ECM and PCD are required to pattern ipsilateral gastrulation, but only PCD is sufficient to restore ipsilaterality. In this scenario,

Fig. 1. Gastrulation is ipsilateral with PS midline PCD persistence.

(A) Experimental flow diagram. Left and right side epiblast cells were electroporated with Flag:2A:H2B-RFP (red) and Flag:2A:H2B-GFP (blue), respectively, at the early PS stage; tagged cells were traced during gastrulation. L, left; A, anterior; R, right; P, posterior; NS, nonsignificant. (B) Dorsal views of embryos at stages Hamburger–Hamilton (HH) 3 (25) (left) and HH 4⁺ (right). Arrowheads indicate the PS midline. (C) Ipsilateral versus contralateral distribution of tagged cells at end point. (D) Cleaved caspase 3⁺ cells (red) at the PS midline. Cyan is DAPI staining. (E) Dorsal view of propidium iodide-stained gastrulating embryo. Note the array of stained cells along the PS midline. (F and G) SEM images of persisting cellular debris along the PS midline (arrowheads). (H) Quantification of blebbing cells along the mediolateral axis ($n = 4$).

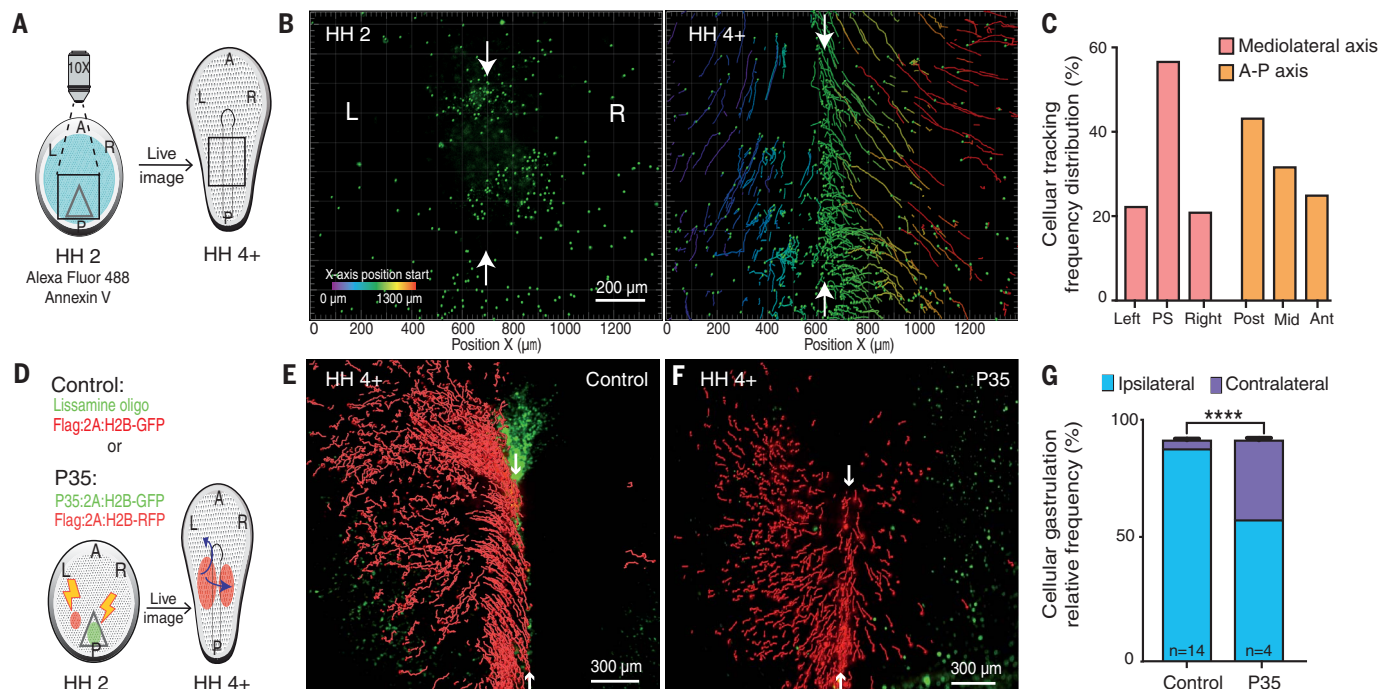
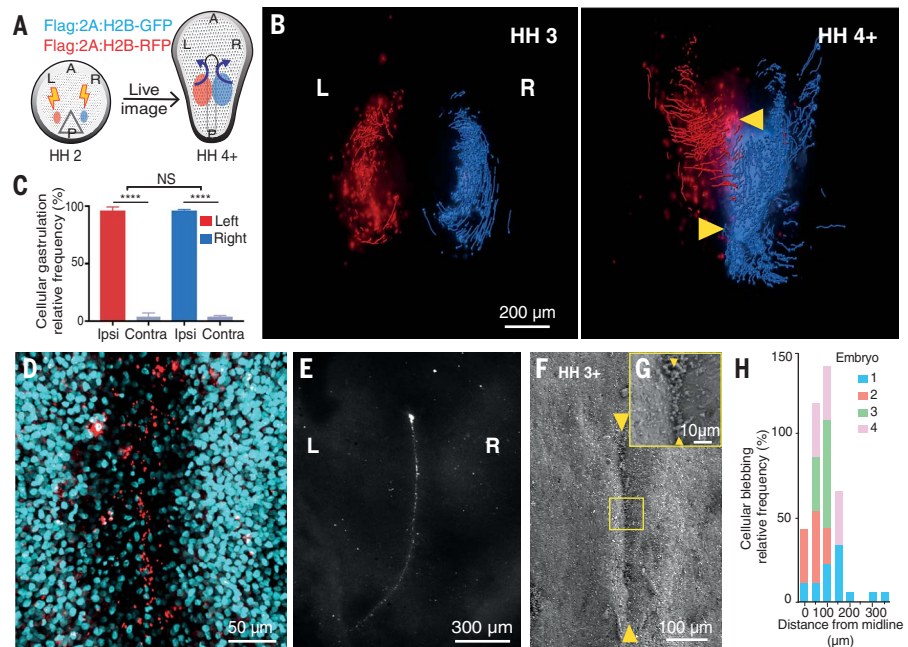


Fig. 2. PS midline PCD is necessary for ipsilateral gastrulation. (A) Diagram of Annexin V epiblast cell labeling at stage HH 2 and tracking to stage HH 4⁺. (B) Time-lapse images of labeled cell trajectories. Color code, original x-axis position; arrows, PS midline. (C) Distribution of Annexin V⁺ cells along the embryonic axes at HH 4⁺. (D) Diagram of control and P35 (green)-mediated

midline PCD suppression with tracking of lateral epiblast cells (red). (E) Control ipsilateral gastrulation of H2B-GFP⁺-tagged cells (red) with Lissamine oligo (green) along the PS. (F) Induced contralateral invasion of H2B-RFP⁺-tagged cells (red) with P35-expressing cells (green) along the PS. (G) Quantification of P35-induced contralateral invasion.

we propose that ECM aligns PCD along the midline, which prevents the contralateral invasion of mesenchymal cells, thereby patterning two ipsilateral body compartments (Fig. 4G).

We have uncovered a functional and developmental role for PCD. Although developmental PCD is classically considered a process

required for unnecessary cell removal and tissue morphogenesis (19), our data establish a positive role for PCD: the patterning of ipsilateral gastrulation. Ipsilaterality could ensure a symmetrical balance by preventing large disparities between left and right sides, resulting in proper laterality development (7), viability,

and fitness in bilaterians (20). These findings in the avian model will stimulate comparative work in mammals, amphibians, and other bilaterian species as new live-imaging technologies become widely available (21). PCD is also a mechanism to curtail pathological EMT in certain malignancies (22). Our work adds

Fig. 3. PS midline ECM is necessary for ipsilateral gastrulation.

(A) Whole-mount laminin IF staining. (B) Whole-mount MMP-15 in situ hybridization. (C, E, and G) Transverse sections of HH4 WT (C), LAMA1 morpholino (E), and hMMP15-treated (G) embryos. Shown is IF staining for laminin (Lm), fibronectin (Fn), and collagen IV (Col IV). Arrows indicate the PS midline. (D, F, and H) Measurement of IF staining intensity of ECM proteins (indicated) at various distances from the PS midline in (C), (E), and (G), respectively. AU, arbitrary units. (I) Diagram of ECM-targeted proteins and subsequent gastrulation pattern analysis. (J and K) Induced contralateral gastrulation by LAMA1 morpholino (J) and hMMP15 (K). (L) Quantification of contralateral invasion. Shown are the LAMA1 control morpholino ($n = 3$), the LAMA1 morpholino ($p = 0.0029$, $n = 6$), and the hMMP-15-treated embryo ($p < 0.0001$, $n = 3$).

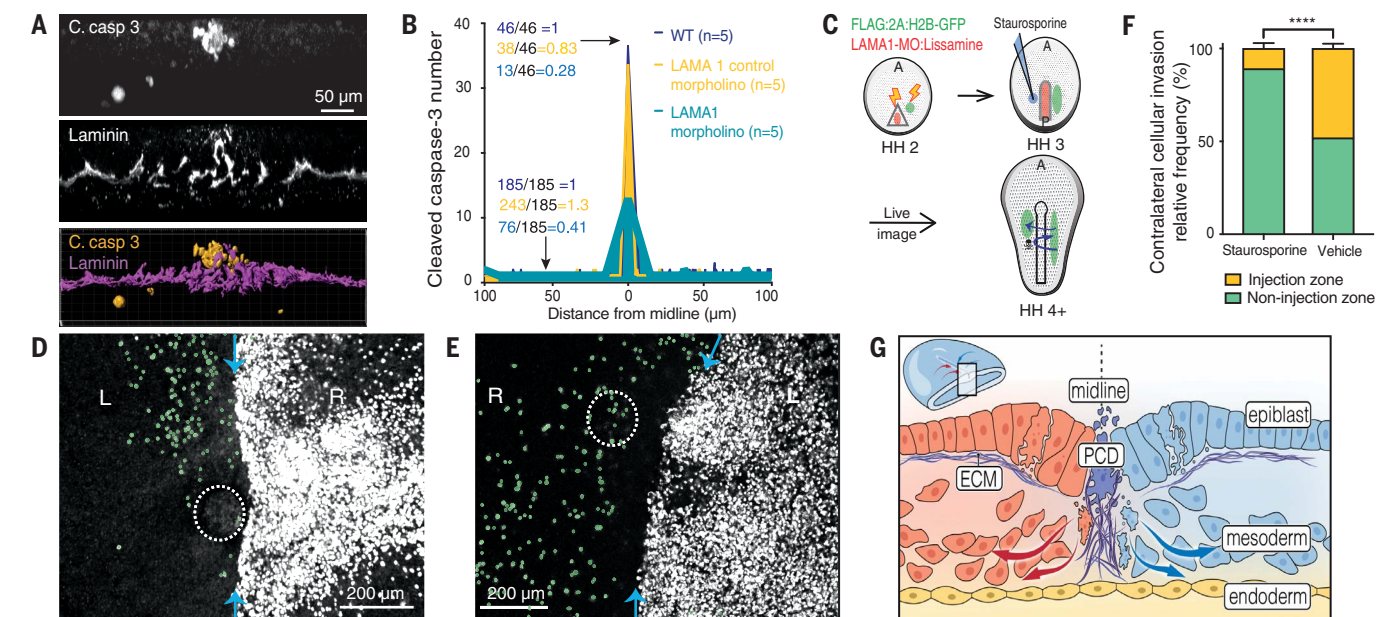
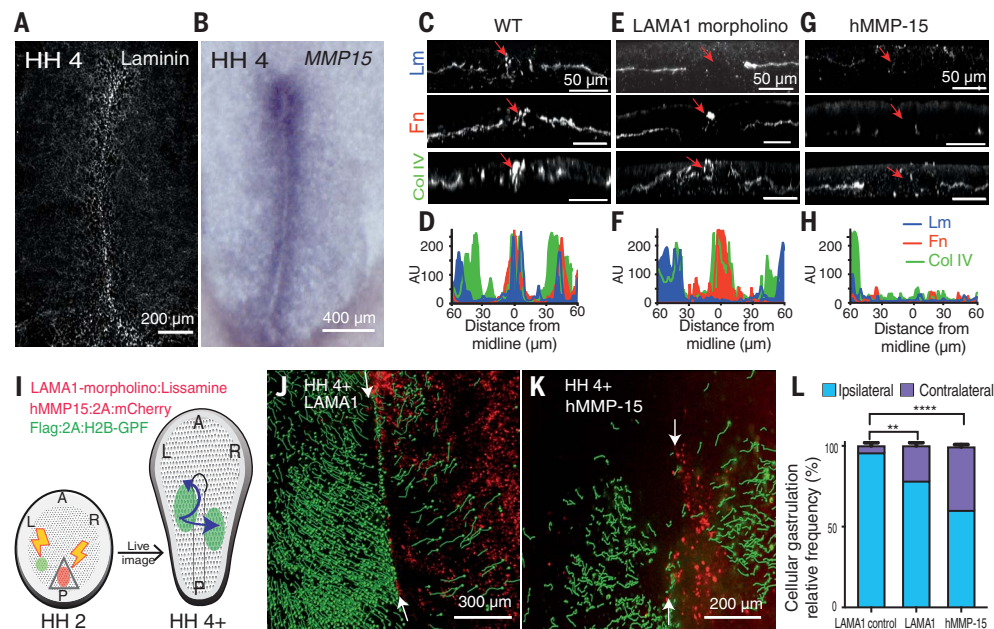


Fig. 4. Induced PCD restores ipsilateral gastrulation in ECM-depleted embryos.

(A) Transverse optical section, 10- μ m thickness, double stained for cleaved caspase 3 (top) and laminin (middle). Bottom is a 3D reconstruction. C. casp 3, cleaved caspase 3. (B) Quantification of cleaved caspase 3⁺ clusters at various distances from the PS midline in WT embryos (yellow), control morpholino (blue), and LAMA1 morpholino (aqua). Ratios represent the total number of clusters at the midline and non-midline-lateral regions. (C) Diagram of ipsilateral gastrulation

rescue by staurosporine-induced PCD. (D) Electroporated LAMA1 morpholino and staurosporine-injected embryo. Gastrulation pattern is traced by Flag:2A:H2B-GFP (white). Contralateral invading cells are pseudocolored in green. Blue arrows indicate the PS midline. (E) As in (D) but with microinjected vehicle only (dotted circle). (F) Quantification of contralateral invasion suppressed by induced PCD. Shown is the injection zone versus the noninjection zone ($p < 0.0001$, $n = 3$). (G) Model of PCD-mediated regulation for ipsilateral gastrulation.

another layer to this concept by showing that cellular mesenchymal migration directionality can be instructed by PCD in a physiological process.

REFERENCES AND NOTES

1. M. Q. Martindale, J. R. Finnerty, J. Q. Henry, *Mol. Phylogenet. Evol.* **24**, 358–365 (2002).
2. R. Happle, *Arch. Dermatol.* **129**, 1460–1470 (1993).
3. S. Aw, M. Levin, *Dev. Dyn.* **237**, 3453–3463 (2008).
4. V. Levy, O. Khaner, *Dev. Genet.* **23**, 175–184 (1998).
5. J. P. Thiery, H. Acloque, R. Y. Huang, M. A. Nieto, *Cell* **139**, 871–890 (2009).
6. T. Mikawa, A. M. Poh, K. A. Kelly, Y. Ishii, D. E. Reese, *Dev. Dyn.* **229**, 422–432 (2004).
7. K. A. Kelly, Y. Wei, T. Mikawa, *Dev. Dyn.* **224**, 238–244 (2002).
8. J. E. Sulston, H. R. Horvitz, *Dev. Biol.* **56**, 110–156 (1977).
9. K. Lauber, S. G. Blumenthal, M. Waibel, S. Wesselborg, *Mol. Cell* **14**, 277–287 (2004).
10. T. J. van Ham, J. Mapes, D. Kokel, R. T. Peterson, *FASEB J.* **24**, 4336–4342 (2010).
11. A. Sugimoto, P. D. Friesen, J. H. Rothman, *EMBO J.* **13**, 2023–2028 (1994).
12. M. Tessier-Lavigne, C. S. Goodman, *Science* **274**, 1123–1133 (1996).
13. X. Yang, D. Dormann, A. E. Münsterberg, C. J. Weijer, *Dev. Cell* **3**, 425–437 (2002).
14. S. M. Frisch, H. Francis, *J. Cell Biol.* **124**, 619–626 (1994).
15. K. Wolf *et al.*, *J. Cell Biol.* **201**, 1069–1084 (2013).
16. D. Shook, R. Keller, *Mech. Dev.* **120**, 1351–1383 (2003).
17. C. A. Belmokhtar, J. Hillion, E. Ségat-Bendirdjian, *Oncogene* **20**, 3354–3362 (2001).
18. R. A. Hill, E. C. Darnisah, F. Chen, A. C. Kwan, J. Grutzendler, *Nat. Commun.* **8**, 15837 (2017).
19. P. Meier, A. Finch, G. Evan, *Nature* **407**, 796–801 (2000).
20. C. C. Li, B. N. Chodirker, A. J. Dawson, A. E. Chudley, *Clin. Dysmorphol.* **13**, 95–98 (2004).
21. K. McDole *et al.*, *Cell* **175**, 859–876.e33 (2018).
22. I. P. Michael *et al.*, *Dev. Cell* **49**, 409–424.e6 (2019).

ACKNOWLEDGMENTS

We thank E. G. Baylon, J. Hyer, and T. Kornberg for their comments and assistance with statistical analysis and past and present Mikawa lab members for their suggestions regarding this work.

Funding: This work was supported by NIH grants R01 HL122375, R37 HL078921, R01 HL132832, and R01 HL148125. L.M.-R. was awarded a Howard Hughes Medical Institute Gilliam Fellowship.

Author contributions: T.M. and L.M.-R. conceptualized the project and wrote the manuscript. L.M.-R. performed all experiments.

Competing interests: The authors declare no competing interests.

Data and materials availability: All data are available in the main text, supplementary materials, or auxiliary files.

SUPPLEMENTARY MATERIALS

science.sciencemag.org/content/367/6474/197/suppl/DC1

Materials and Methods

Figs. S1 to S12

References (23–25)

Movies S1 to S10

[View/request a protocol for this paper from Bio-protocol.](#)

4 December 2018; resubmitted 7 August 2019

Accepted 27 November 2019

10.1126/science.aaw2731

ANTIBIOTIC RESISTANCE

Effect of tolerance on the evolution of antibiotic resistance under drug combinations

Jiafeng Liu¹, Orit Gefen¹, Irine Ronin¹, Maskit Bar-Meir^{2,3*}, Nathalie Q. Balaban^{1*}

Drug combinations are widely used in clinical practice to prevent the evolution of resistance. However, little is known about the effect of tolerance, a different mode of survival, on the efficacy of drug combinations for preventing the evolution of resistance. In this work, we monitored *Staphylococcus aureus* strains evolving in patients under treatment. We detected the rapid emergence of tolerance mutations, followed by the emergence of resistance, despite the combination treatment. Evolution experiments on the clinical strains in vitro revealed a new way by which tolerance promotes the evolution of resistance under combination treatments. Further experiments under different antibiotic classes reveal the generality of the effect. We conclude that tolerance is an important factor to consider in designing combination treatments that prevent the evolution of resistance.

Evolution experiments have shown that tolerance evolves quickly under cyclic antibiotic treatments (1–3) and subsequently promotes the evolution of antibiotic resistance (4). In contrast to resistance mutations that decrease the effectiveness of the antibiotic and elevate the minimum inhibitory concentration (MIC) (5), tolerance mutations increase the minimum time to kill the population without changing the MIC (6–10). To understand whether the evolutionary trajectory of evolving tolerance—and thereafter resistance—occurs in patients, we followed sequential isolates of life-threatening methicillin-resistant *Staphylococcus aureus* (MRSA) blood infections in which the bacterial infection persisted for at least 2 weeks despite antibiotic treatment (fig. S1).

Between May 2017 and May 2018, 2 of 48 adult patients (>18 years old) admitted to Shaare Zedek Hospital with MRSA bacteremia fitted our inclusion criteria (see materials and methods). Frozen stocks of streaks obtained from the blood cultures were prepared. The single-cell distribution of growth phenotype of the bacterial population was measured by plating serial dilutions of the frozen stock on agar plates and following the appearance of each colony with the Scanlag setup (see materials and methods).

In patients 1 and 2, we observed that colonies, arising from the bacterial population isolated 1 week after the start of treatment, occurred much later than those from the population isolated on day 1 (Fig. 1A and fig. S2). In some samples, early- and late-appearing phenotypes coexisted (Fig. 1A; see day 5), but

eventually only the late-appearing phenotype remained in both patients. From each subpopulation, single colonies were selected randomly for further analyses. MIC assays, tolerance detection tests (TDtests), and killing assays performed on these clones revealed that the late-appearing phenotype—observed on day 5 and associated with tolerance to vancomycin (VAN) (Fig. 1, B and C) (11–15)—was characterized by a reduced killing rate but showed no change to the MIC (Fig. 1D and fig. S3). The VAN-tolerant phenotype was always associated with impaired bacterial growth (Fig. 1, E and F, and fig. S4) (16–18). Whole-genome reconstruction of the ancestral strains isolated before antibiotic treatment (day 1), and comparison with whole-genome sequencing (WGS) of isolates from later days, identified a few single-point mutations—single-nucleotide polymorphisms (SNPs)—attributed to tolerance in several genes [e.g., RNA polymerase subunit (*rpoC*), transcriptional repressor of purine biosynthesis (*purR*) (in patient 1), and Clp protease subunit (*clpX*) (in patient 2) (table S1 and table S2)]. Identical SNPs were detected in isolates from different days, indicating clonal evolution, which enabled phylogenetic reconstruction (Fig. 2A).

In vitro experiments tend to use a single drug, but—as is frequently the case for patients with severe infections, such as patient 1—treatment in these cases involved several drugs. Thus, our bacterial isolates were exposed to three antibiotics: VAN, rifampicin (RIF), and daptomycin (DAP) (Fig. 2). First, only VAN was administered, which selected for strains tolerant to VAN within 5 days (Fig. 2B). RIF was combined with the VAN treatment on day 4. Because bacteremia persisted, VAN was replaced by DAP, so that from day 8 to 14, patient 1 was under treatment with RIF and DAP. Despite the combination treatment, mutations in the polymerase gene *rpoB*, which are known to generate RIF resistance (19), em-

erged after the tolerance mutations (Fig. 2C and figs. S5 to S7). The evolution of antibiotic resistance in patient 1 is notably similar to the rapid evolution of antibiotic resistance observed in vitro after a tolerant phenotype has been established in experimental evolution (4).

To understand whether the rapid evolution of RIF resistance in the patient was facilitated by the tolerance phenotype, we quantified in vitro survival to each drug—separately and in combination—at drug concentrations close to those occurring in vivo (see supplementary materials). All isolates tolerant to VAN were also highly tolerant to DAP (hereafter called VAN/DAP-tolerant) (Fig. 1C and fig. S5) (20). A representative VAN/DAP-tolerant strain showed a survival advantage of three orders of magnitude in the DAP killing assay after 1 hour (Fig. 3A; blue bars). We discovered that the RIF treatment was as effective at killing the VAN/DAP-tolerant strains as it was at killing the ancestral day 1 strain (Fig. 3A; red bars). Similarly, the combination of DAP and RIF (Fig. 3A; purple bars) did not kill the ancestral strain significantly more effectively than the VAN/DAP-tolerant strains.

To understand whether the evolution of RIF resistance in the VAN/DAP-tolerant strains can be reproduced in vitro, we performed evolution experiments with the ancestral isolate and its in-host-evolved, VAN/DAP-tolerant mutant, using the DAP and RIF combination treatment under which RIF resistance emerged. Within a few treatment cycles, in four out of five experiments, we observed selection for RIF resistance mutations in the VAN/DAP-tolerant background, reproducing the evolutionary trajectory observed in the patient. None of the five experiments led to selection of RIF resistance in the ancestral isolate (Fig. 3B; $P = 0.048$). This result led to two questions: (i) If the combination treatment leads to RIF resistance so quickly, why is DAP and RIF used in combination in the clinic? (ii) Why did RIF resistance mutations become established only in the VAN/DAP-tolerant background, despite the similar survival capacities of ancestral and VAN/DAP-tolerant strains under the combination treatment?

Paradoxically, we observed a significant decrease in survival of RIF-resistant bacteria compared with the ancestral wild-type strain (wt) under the DAP and RIF combination (Fig. 3A). DAP alone kills the wt very effectively (decrease in survival by approximately five orders of magnitude after 1 hour), whereas the combination of DAP and RIF is less effective by a factor of 100. Such a drug combination, which is less effective than a single drug, is called suppressive (fig. S8) (21). A well-known example of such an interaction is the suppressive effect of chloramphenicol—which slows growth—on beta-lactam killing, which requires

¹Racah Institute of Physics, Edmond J. Safra Campus, The Hebrew University of Jerusalem, Jerusalem, Israel.

²Pediatrics and Infectious Diseases Division, Shaare Zedek Medical Center, Jerusalem, Israel. ³Faculty of Medicine, The Hebrew University, Jerusalem, Israel.

*Corresponding author. Email: nathalie.balaban@mail.huji.ac.il (N.Q.B.); mbarmeir@gmail.com (M.B.-M.)

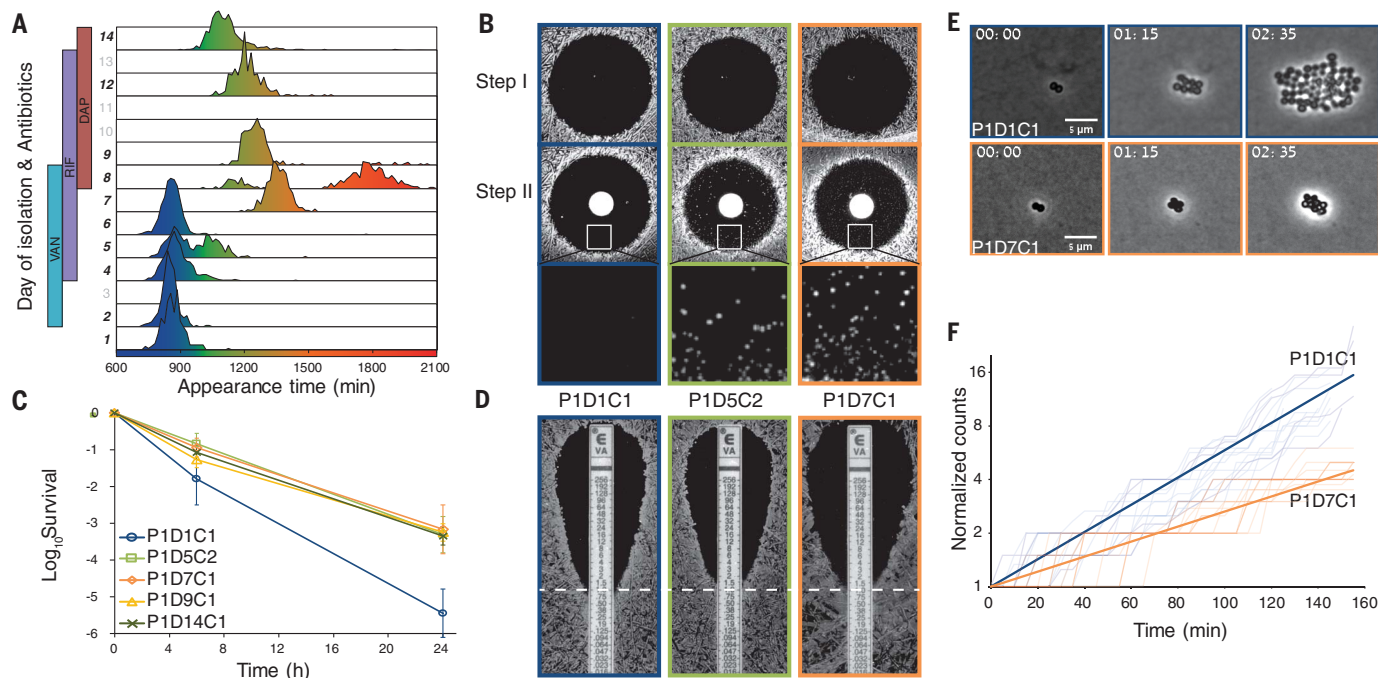


Fig. 1. Evolution of tolerance in patient 1. (A) Distribution of the time of appearance of colonies on solid medium from subsequent samples was measured by ScanLag. The y axis represents the normalized proportion of colony-forming units (CFUs) detected at each sampling time. Sample sizes $N = 244, 310, 660, 456, 932, 411, 498, 244, 240$, and 759 , respectively. (B) Tolerance detection using the TDtest (11). Step I: Single colonies isolated on day 1, 5, and 7 are exposed to a VAN disk ($10\text{ }\mu\text{g}$), which results in a zone of inhibition with similar radius in all strains (i.e., no resistance increase). Step II: Addition of a nutrient disk after the antibiotic concentration has decreased below MIC allows detection of increased survival of the tolerant strains. (Bottom) Enlargement of a region within the inhibition zone shows numerous colonies that regrew at step II for the strains isolated on day 5 and 7.

Strain names are based on patient (P#), day of isolation (D#), and clone isolated (C#). (C) Killing assay in liquid medium of clones isolated on different days from patient 1 under VAN ($30\text{ }\mu\text{g/ml}$). Data are presented as the means \pm SD from at least three biological replicates. (D) MIC measurement of VAN with Etest (epsilometer test) (micrograms per milliliters). The white dashed line denotes the value of the MIC on day 1. (E and F) Growth impairment detected in the clinical samples in the absence of antibiotics. (E) Representative time-lapse phase-contrast microscopy images of clones isolated on day 1 (upper row) and day 7 (lower row). Scale bars, $5\text{ }\mu\text{m}$. (F) Decreased growth rate in the tolerant strain (orange). Data extracted from the experiments shown in (E) display bacteria numbers over time, normalized by initial number at the beginning of observation.

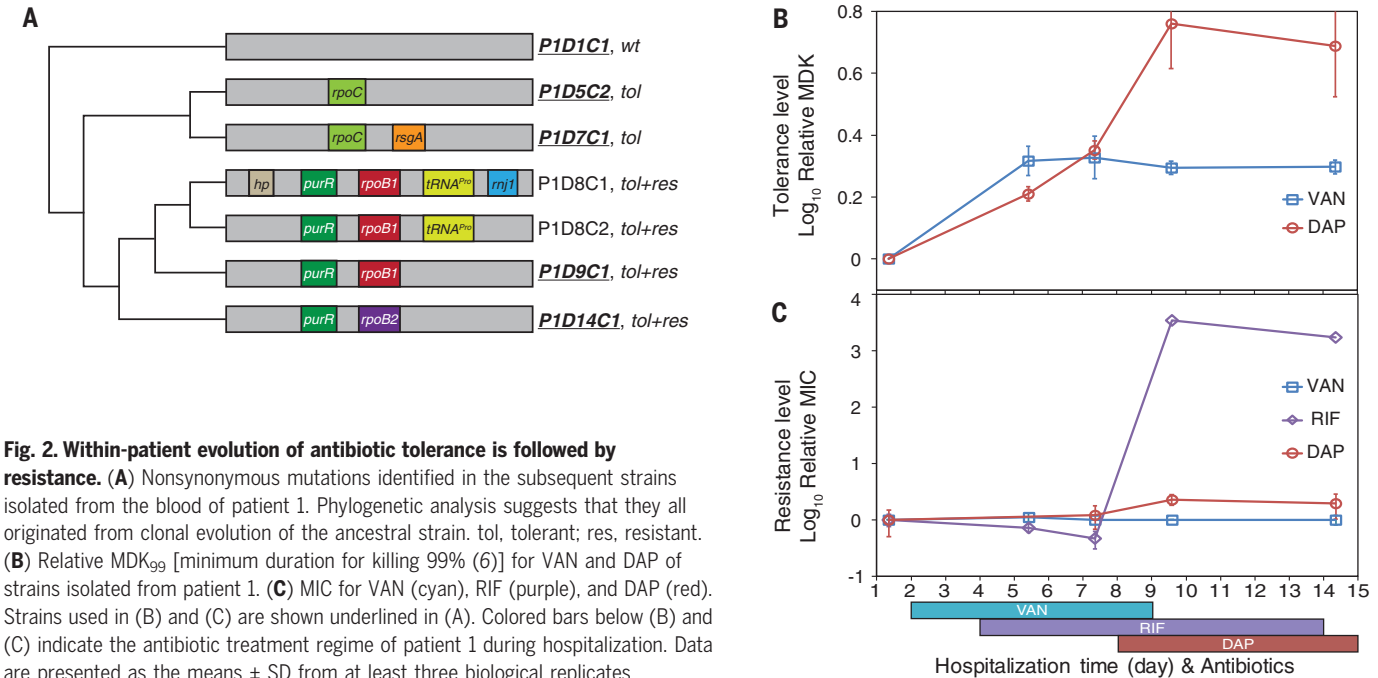
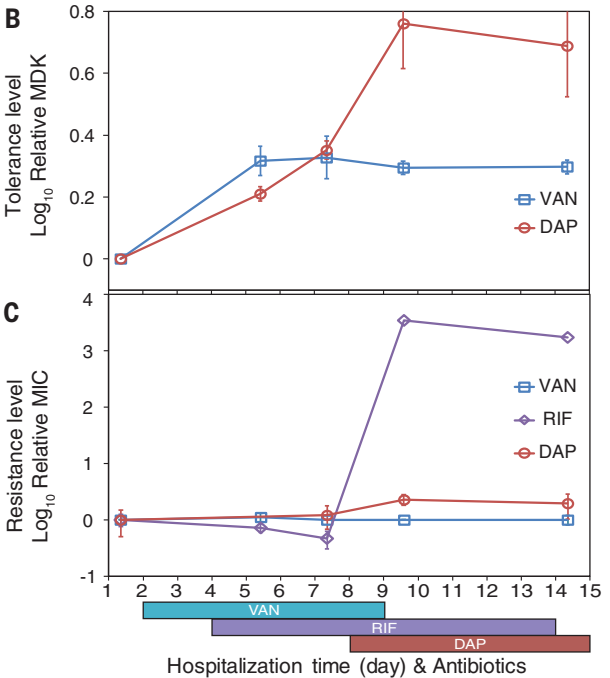


Fig. 2. Within-patient evolution of antibiotic tolerance is followed by resistance. (A) Nonsynonymous mutations identified in the subsequent strains isolated from the blood of patient 1. Phylogenetic analysis suggests that they all originated from clonal evolution of the ancestral strain. tol, tolerant; res, resistant. (B) Relative MDK₉₉ [minimum duration for killing 99% (6)] for VAN and DAP of strains isolated from patient 1. (C) MIC for VAN (cyan), RIF (purple), and DAP (red). Strains used in (B) and (C) are shown underlined in (A). Colored bars below (B) and (C) indicate the antibiotic treatment regime of patient 1 during hospitalization. Data are presented as the means \pm SD from at least three biological replicates.



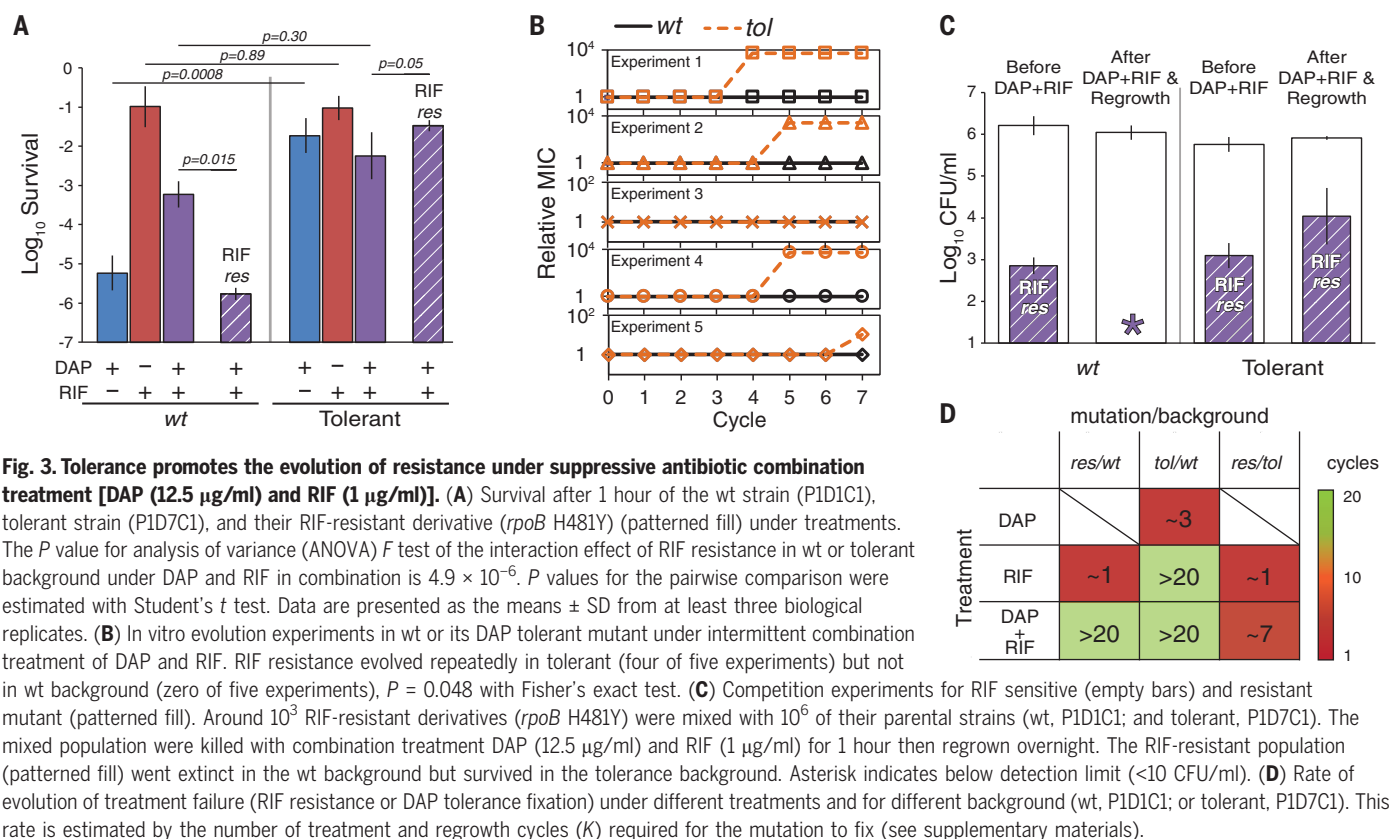


Fig. 3. Tolerance promotes the evolution of resistance under suppressive antibiotic combination treatment [DAP (12.5 μ g/ml) and RIF (1 μ g/ml)]. (A) Survival after 1 hour of the wt strain (PID1C1), tolerant strain (PID7C1), and their RIF-resistant derivative (*rpoB* H481Y) (patterned fill) under treatments. The *P* value for analysis of variance (ANOVA) *F* test of the interaction effect of RIF resistance in wt or tolerant background under DAP and RIF in combination is 4.9×10^{-6} . *P* values for the pairwise comparison were estimated with Student's *t* test. Data are presented as the means \pm SD from at least three biological replicates. (B) In vitro evolution experiments in wt or its DAP tolerant mutant under intermittent combination treatment of DAP and RIF. RIF resistance evolved repeatedly in tolerant (four of five experiments) but not in wt background (zero of five experiments), *P* = 0.048 with Fisher's exact test. (C) Competition experiments for RIF sensitive (empty bars) and resistant mutant (patterned fill). Around 10^3 RIF-resistant derivatives (*rpoB* H481Y) were mixed with 10^6 of their parental strains (wt, PID1C1; and tolerant, PID7C1). The mixed population were killed with combination treatment DAP (12.5 μ g/ml) and RIF (1 μ g/ml) for 1 hour then regrown overnight. The RIF-resistant population (patterned fill) went extinct in the wt background but survived in the tolerance background. Asterisk indicates below detection limit (<10 CFU/ml). (D) Rate of evolution of treatment failure (RIF resistance or DAP tolerance fixation) under different treatments and for different background (wt, PID1C1; or tolerant, PID7C1). This rate is estimated by the number of treatment and regrowth cycles (*K*) required for the mutation to fix (see supplementary materials).

growth to be effective (22). Correspondingly, RIF suppresses killing by DAP, such that a mutant that is fully RIF resistant—i.e., is unaffected by the presence of RIF—will experience full unsuppressed killing by DAP. It will therefore be killed more efficiently under DAP and RIF in combination than a RIF-susceptible strain. Thus, RIF resistance will not be established in the wt background under the DAP and RIF combination. This phenomenon may answer our first question: explaining the empirical use of DAP and RIF combination in the clinic (23), in alignment with the strategy of using suppressive drug combinations for the prevention of resistance in vitro (24).

We now turn to the effect of VAN/DAP tolerance on survival under the DAP and RIF combination treatment. In contrast to the reduction in survival of RIF resistance mutation in the wt strain when exposed to combination treatment, we observed that the RIF resistance mutation increased survival in the VAN/DAP-tolerant strain (Fig. 3A). RIF-resistant, VAN/DAP-tolerant mutants survive DAP exposure because of the protective effect of VAN/DAP tolerance. Thus, VAN/DAP tolerance allows RIF resistance to evolve under the DAP and RIF combination (Fig. 3B).

To verify that the rescue of resistance mutations by VAN/DAP tolerance occurs under combination with DAP and RIF, we performed competition experiments in which a small

number (~1000 bacteria) of RIF-resistant mutants were mixed with their wt ancestral strain (~ 10^6 bacteria) and exposed to DAP and RIF. Strong suppression of resistance to RIF by DAP and RIF combination treatment caused the extinction of the RIF-resistant mutants in the wt background (Fig. 3C; wt). In contrast, RIF-resistant mutants survived in the VAN/DAP-tolerant background during DAP and RIF combination treatment (Fig. 3C; tolerant, *P* = 0.0003).

The survival measurements (Fig. 3A) can be used to quantitatively determine how quickly treatment would fail because of the rapid fixation of a mutation (see “Calculation of the number of treatment cycles for the fixation of a mutation” in the supplementary materials). Because of the high probability of RIF resistance mutations (19), fixation to resistance occurred rapidly (after approximately one cycle) under RIF monotherapy (shown schematically in Fig. 3D). By contrast, evolution of RIF resistance in the wt background was delayed by more than 20 cycles of treatment with the DAP and RIF combination (Fig. 3D). However, for a VAN/DAP-tolerant strain, RIF resistance occurs much faster than for the wt (7 cycles versus >20 cycles) (Fig. 3D). This analysis answers our second question, explaining why VAN/DAP-tolerant strains have evolved RIF resistance rapidly in the host and in vitro. Thus, the DAP and RIF combination

treatment is effective at delaying both the evolution of DAP tolerance and RIF resistance, and the treatment might have been effective in patient 1 if administered before DAP tolerance had been established.

To understand whether prior evolution of tolerance is required for the evolution of resistance under other suppressive combination treatments, we measured bacterial survival under drug combinations from four different antibiotic classes. We evaluated all six possible combinations in *Escherichia coli* strain KLY and its ampicillin (AMP)- and norfloxacin (NOR)-tolerant mutant KLY *metG^T* (Fig. 4, A to D) (4). We found that four of the six combinations were suppressive in the wt strain (Fig. 4, A and C), but only two were suppressive in the tolerant strains (Fig. 4, B and D). This result indicates that some of the combinations may act similarly to the DAP and RIF combination on the evolution of RIF resistance. Thus, resistance was suppressed in the wild type but protected in a tolerant background.

We tested these predictions for the AMP and NOR combination by constructing a known NOR resistance mutation (*gyrA*-S83L) (25), which increased MIC to NOR by more than 10-fold. As predicted, the survival of the NOR-resistant *E. coli* under combination treatment was suppressed in the wt background but not in the tolerant strain (Fig. 4E), similarly to the DAP and RIF combination for the *S. aureus*

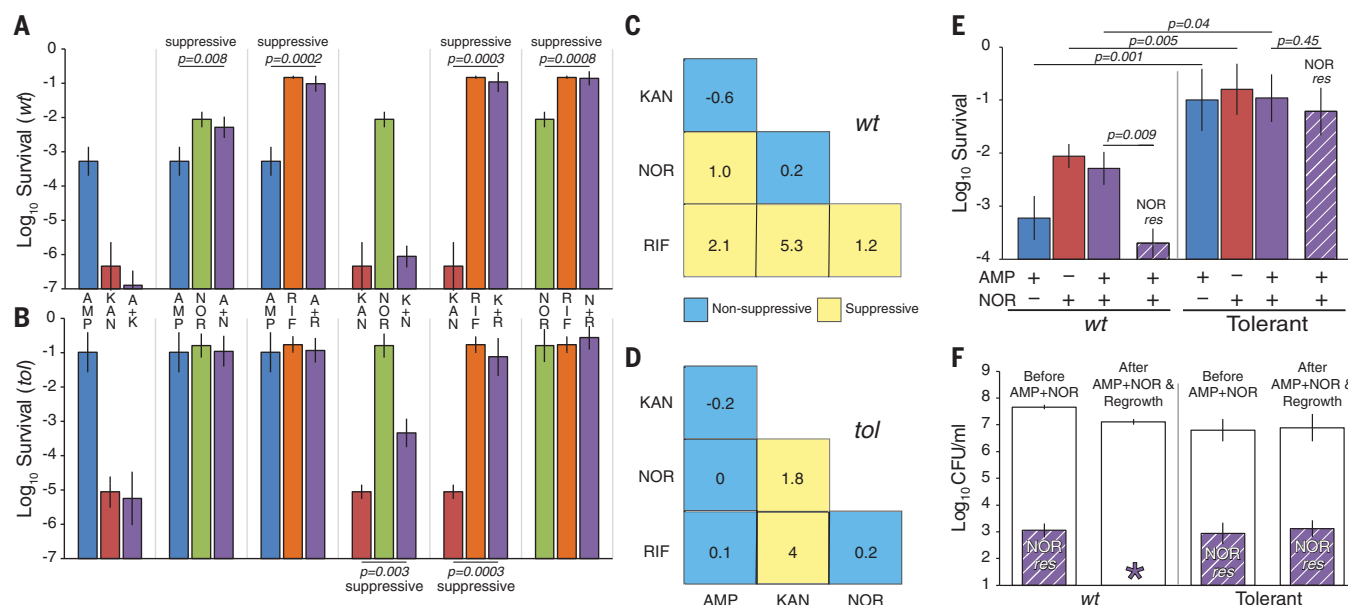


Fig. 4. Tolerance promotes resistance in other suppressive combinations.

(A to D) All six possible combination treatments for antibiotics from four different classes: AMP (50 $\mu\text{g}/\text{ml}$), KAN (kanamycin, 30 $\mu\text{g}/\text{ml}$), NOR (1 $\mu\text{g}/\text{ml}$), and RIF (200 $\mu\text{g}/\text{ml}$) for [(A) and (C)] *E. coli* KLY (wt) and [(B) and (D)] its tolerant derivative KLY *metG*^T. Survival was measured after 4 hours. The numbers in (C) and (D) represent the suppression factor (see fig. S8). *P* values in (A) and (B) were estimated with Student's *t* test. (E) Survival after 4 hours of the wt strain, tolerant strain, and their NOR-resistant derivative (*gyrA* S83L) (patterned fill) under combination treatment of AMP and NOR. Survival data are presented as the means \pm SD from at least three biological replicates. The *P* value for ANOVA *F* test of the interaction

effect of NOR resistance in wt or tolerant background under AMP and NOR in combination is 2.8×10^{-6} . *P* values for the pairwise comparison data were estimated with Student's *t* test. (F) Competition experiments for sensitive (empty bars) and NOR-resistant mutant (patterned fill). Around 10^3 NOR-resistant mutants (*gyrA* S83L) were mixed with their parental strains ($\sim 10^7$) (wt, KLY; and tolerant, KLY-*metG*^T). The mixed populations were killed with combination treatment of AMP and NOR then regrown overnight. The NOR-resistant population went extinct in the wt background but survived in the tolerance background. Asterisk indicates below detection limit (<10 CFU/ml). Data are presented as the means \pm SD from at least three biological replicates.

clinical strains (Fig. 3A). We repeated the assay for the rescue of resistance mutations by tolerance under the combination NOR and AMP and found that tolerance could rescue NOR resistance mutations that would otherwise go extinct in the wt background (Fig. 4F; $P = 0.0003$). We conclude that rescue of resistance mutations by tolerance is a general phenomenon that may have crucial implications for the evolution of resistance in patients treated with combinations of antimicrobials.

Our analysis of strains isolated from blood infections revealed a notable similarity to in vitro experiments. In both, the rapid evolution of tolerance was identified as a major survival factor, followed by the emergence of resistance. However, in contrast to the in vitro evolution results (where a single drug was used), our study shows how tolerance promotes the evolution of resistance under combination treatments that are expected to prevent resistance.

Despite the drawbacks of using suppressive combination treatment, this strategy can be effective at preventing the evolution of resistance (21, 24) and may explain the motivation for the empirical use of such treatments in patients (23, 26). But it does need to be deployed before tolerance to those drugs has established. Diagnostic tools for detecting

the emergence of tolerance under treatment would provide crucial information for guiding combination treatments (11, 27). Moreover, combination treatments such as DAP and RIF may be effective at preventing the evolution of tolerance, which has been shown to underlie difficult-to-treat infections in immunocompromised patients (12). Designing combination therapies that account for tolerance or persistence (28) may be especially relevant for the treatment of tuberculosis, where tolerance has been suggested to be a major factor for survival of the pathogen (29) and where the prevention of the de novo evolution of resistance in patients is crucial (30). The generality of the mechanism by which tolerance promotes resistance suggests that it is relevant not only to de novo evolution of resistance by mutations (31, 32) but also to other mechanisms for acquiring resistance, such as horizontal gene transfer. Our study could also apply to the recognition of the effect of drug tolerance on the outcome of anticancer combination treatments (33–35).

REFERENCES AND NOTES

- O. Fridman, A. Goldberg, I. Ronin, N. Shores, N. Q. Balaban, *Nature* **513**, 418–421 (2014).
- L. Mechler et al., *Antimicrob. Agents Chemother.* **59**, 5366–5376 (2015).
- B. Van den Bergh et al., *Nat. Microbiol.* **1**, 16020 (2016).

- I. Levin-Reisman et al., *Science* **355**, 826–830 (2017).
- C. Walsh, *Nature* **406**, 775–781 (2000).
- A. Brauner, O. Fridman, O. Gefen, N. Q. Balaban, *Nat. Rev. Microbiol.* **14**, 320–330 (2016).
- A. Brauner, N. Shores, O. Fridman, N. Q. Balaban, *Biophys. J.* **112**, 2664–2671 (2017).
- S. Handwerker, A. Tomasz, *Annu. Rev. Pharmacol. Toxicol.* **25**, 349–380 (1985).
- B. R. Levin, D. E. Rozen, *Nat. Rev. Microbiol.* **4**, 556–562 (2006).
- N. Q. Balaban, J. Merrin, R. Chait, L. Kowalik, S. Leibler, *Science* **305**, 1622–1625 (2004).
- O. Gefen, B. Chelok, J. Strahilevitz, N. Q. Balaban, *Sci. Rep.* **7**, 41284 (2017).
- E. S. Honsa et al., *mBio* **8**, e02124-16 (2017).
- C. Vulin, N. Leimer, M. Huemer, M. Ackermann, A. S. Zinkernagel, *Nat. Commun.* **9**, 4074 (2018).
- V. Dengler Haunreiter et al., *Nat. Commun.* **10**, 1149 (2019).
- M. D. LaFleur, Q. Qi, K. Lewis, *Antimicrob. Agents Chemother.* **54**, 39–44 (2010).
- E. Tuomanen, R. Cozens, W. Tosch, O. Zak, A. Tomasz, *J. Gen. Microbiol.* **132**, 1297–1304 (1986).
- A. J. Lee et al., *Proc. Natl. Acad. Sci. U.S.A.* **115**, 4069–4074 (2018).
- Y. Katayama et al., *Antimicrob. Agents Chemother.* **61**, e00452-e17 (2017).
- A. J. O'Neill, T. Huovinen, C. W. G. Fishwick, I. Chopra, *Antimicrob. Agents Chemother.* **50**, 298–309 (2006).
- I. C. McCall, N. Shah, A. Govindan, F. Baquero, B. R. Levin, *Antimicrob. Agents Chemother.* **63**, e02360-18 (2019).
- N. Singh, P. J. Yeh, *J. Antibiot.* **70**, 1033–1042 (2017).
- E. Jawetz, J. B. Gunnison, R. S. Speck, V. R. Coleman, *AMA Arch. Intern. Med.* **87**, 349–359 (1951).
- W. E. Rose, A. D. Berti, J. B. Hatch, D. G. Maki, *Antimicrob. Agents Chemother.* **57**, 3450–3452 (2013).
- R. Chait, A. Crane, R. Kishony, *Nature* **446**, 668–671 (2007).
- S. Bagel, V. Hullen, B. Wiedemann, P. Heisig, *Antimicrob. Agents Chemother.* **43**, 868–875 (1999).
- S. Rieg, W. V. Kern, A. Soriano, *Lancet* **392**, 554–555 (2018).
- M. Perros, *Science* **347**, 1062–1064 (2015).

28. B. P. Conlon *et al.*, *Nature* **503**, 365–370 (2013).
29. N. K. Dutta *et al.*, *Sci. Adv.* **5**, eaav2104 (2019).
30. N. R. Cohen, M. A. Lobritz, J. J. Collins, *Cell Host Microbe* **13**, 632–642 (2013).
31. K. Sieradzki, T. Leski, J. Dick, L. Borio, A. Tomasz, *J. Clin. Microbiol.* **41**, 1687–1693 (2003).
32. M. M. Mwangi *et al.*, *Proc. Natl. Acad. Sci. U.S.A.* **104**, 9451–9456 (2007).
33. S. Pearl Mizrahi, O. Gefen, I. Simon, N. Q. Balaban, *Cell Cycle* **15**, 3442–3453 (2016).
34. K. Kochanowski, L. Morinishi, S. Altschuler, L. Wu, *Curr. Opin. Syst. Biol.* **10**, 1–8 (2018).
35. M. V. Blagosklonny, *Leukemia* **13**, 2031–2035 (1999).

ACKNOWLEDGMENTS

We thank A. O'Neill for providing the strains 8325-4 and derivatives R23 (*rpoB* S486L) and R35 (*rpoB* S464P) and

J. Strahilevitch, M. V. Assous, I. Levin-Reisman, A. Brauner, S. P. Mizrahi, and O. Fridman for discussions and suggestions. Ethics approval of this work was granted by the Shaare Zedek Medical Center ethics committee (#0277-17-SZMC). **Funding:** The work was supported by the European Research Council (Consolidator grant no. 681819), the Israel Science Foundation (grant no. 492/15), and the Minerva Foundation. J.L. acknowledges support from the HUJI-CSC scholarship program. **Author contributions:** Conceptualization, J.L., O.G., and N.Q.B.; Methodology, J.L., O.G., and N.Q.B.; Investigation, J.L. and M.B.-M.; Writing – original draft, J.L. and N.Q.B.; Writing – review & editing, J.L., O.G., and N.Q.B.; Funding acquisition, N.Q.B.; Resources, M.B.-M. and I.R.; Supervision, N.Q.B. **Competing interests:** N.Q.B. and O.G. submitted U.S. patent application 62/244,809, which covers the fabrication of the Tdtest technique utilized in this paper (II). I.R., J.L., and M.B.-M. declare no competing interests. **Data and materials availability:** The accession number for the sequencing data is National Center for Biotechnology Information

BioProject PRJNA503808. Code for ScanLag is available at <http://bio-site.phys.huji.ac.il/Materials>. The clinical strains are available under a material transfer agreement from MBM under a material agreement with Shaare Zedek Hospital.

SUPPLEMENTARY MATERIALS

science.sciencemag.org/content/367/6474/200/suppl/DC1
Materials and Methods
Supplementary Text
Figs. S1 to S8
Tables S1 to S3
References (36–48)

[View/request a protocol for this paper from Bio-protocol.](#)

6 June 2019; accepted 20 November 2019
10.1126/science.aay3041

SIGNAL TRANSDUCTION

Glucose-dependent control of leucine metabolism by leucyl-tRNA synthetase 1

Ina Yoon¹, Miso Nam², Hoi Kyoung Kim¹, Hee-Sun Moon¹, Sungmin Kim¹, Jayun Jang³, Ji Ae Song³, Seung Jae Jeong¹, Sang Bum Kim¹, Seongmin Cho³, YounHa Kim³, Jihye Lee¹, Won Suk Yang¹, Hee Chan Yoo⁴, Kibum Kim^{4,5}, Min-Sun Kim^{2,*}, Aerin Yang⁶, Kyukwang Cho⁶, Hee-Sung Park⁶, Geum-Sook Hwang², Kwang Yeon Hwang⁷, Jung Min Han^{4,5}, Jong Hyun Kim^{1,†,§}, Sunghoon Kim^{1,3,†,§}

Despite the importance of glucose and amino acids for energy metabolism, interactions between the two nutrients are not well understood. We provide evidence for a role of leucyl-tRNA synthetase 1 (LARS1) in glucose-dependent control of leucine usage. Upon glucose starvation, LARS1 was phosphorylated by Unc-51 like autophagy activating kinase 1 (ULK1) at the residues crucial for leucine binding. The phosphorylated LARS1 showed decreased leucine binding, which may inhibit protein synthesis and help save energy. Leucine that is not used for anabolic processes may be available for catabolic pathway energy generation. The LARS1-mediated changes in leucine utilization might help support cell survival under glucose deprivation. Thus, depending on glucose availability, LARS1 may help regulate whether leucine is used for protein synthesis or energy production.

Cells integrate information on nutrient availability to survive under environmental stresses (1). Glucose and energy homeostasis is tightly regulated by metabolic organs (2). In muscle cells deprived of glucose, activity of anabolic pathways is decreased, and proteins are broken down to supply amino acids to oxidation pathways (3). However, it remains to be determined how amino acids are directed to anabolic or catabolic pathways under various conditions. Mechanistic target of rapamycin complex 1 (mTORC1) is a master regulator of anabolic pathways in response to nutrients (4). Rag guanosine triphosphatases (GTPases) are proposed to stimulate mTORC1 in response to both glucose and amino acids (5). Leucyl-tRNA synthetase 1 (LARS1) covalently couples leucine to its cognate tRNAs using adenosine triphosphate (ATP). LARS1 also senses intracellular leucine and helps convert RagD^{GTP} to RagD^{GDP}

(GDP, guanosine diphosphate) (6–8). The function of LARS1 as both a leucine sensor and an ATP consumer led us to explore its possible role mediating glucose-dependent mTORC1 signaling.

We examined the GTP- or GDP-binding status of Rag GTPases. In the presence of glucose, Rag GTPases mainly existed in active form for mTORC1 activation (fig. S1A). Glucose-induced activation of mTORC1 was decreased in cells transfected with small interfering RNAs (siRNAs) for RagA and RagB, or RagC and RagD (fig. S1B). Overexpression of inactive or active RagB and RagD heterodimers inhibited or activated mTORC1, respectively, regardless of glucose availability (fig. S1, C and D).

We monitored contribution of LARS1 on mTORC1 activity, which was sensitive to the amount of LARS1 in the presence of both glucose and leucine, but not in the presence of leucine alone, suggesting that LARS1 senses leucine with the aid of glucose (fig. S2). Because leucine-to-mTORC1 activation is triggered by the binding of LARS1 and RagD (6), we investigated whether glucose might affect this interaction. In cells stimulated with glucose, LARS1 was enriched in lysosomes and localized with lysotracker (Fig. 1, A and B). Fluorescence resonance energy transfer (FRET) and coimmunoprecipitation (co-IP) experiments showed enhanced interaction of overexpressed and tagged LARS1 and RagD in glucose-rich conditions (Fig. 1, C and D). In transgenic (TG), wild-type (WT), and heterozygous (HET) mouse embryonic fibroblasts (MEFs), glucose-induced ribosomal protein S6 kinase (S6K) phosphorylation was positively correlated with the amount of LARS1 (Fig. 1E). However, alanyl-, isoleucyl-, and valyl-tRNA synthetases (AARS1, IARS1, and VARS1) did not show a similar effect (Fig. 1, F and G, and fig. S3), implying

that LARS1 may be a specific positive mTORC1 regulator by glucose as well as leucine. S6K phosphorylation was sustained longer in cells overexpressing Myc-LARS1 after glucose withdrawal, whereas it was more rapidly lost in cells depleting LARS1 (Fig. 1H).

Although RagA mediates glucose-induced mTORC1 activation (5), the association of LARS1 and RagD was still enhanced in response to glucose in cells overexpressing RagA^{GTP} (fig. S4). Although the mTORC1 pathway is inactivated by tuberous sclerosis complex 2 (TSC2) in glucose starvation (9), TSC2 knockout (KO) MEFs deprived of glucose still showed decreased S6K phosphorylation, indicating the existence of another regulation mechanism (fig. S5A). The mTORC1 activity was still positively correlated with the amount of LARS1 in TSC2 KO MEFs (fig. S5B). These results are consistent with glucose-induced activation of mTORC1 through the LARS1-RagD pathway.

Because glucose seemed to regulate leucine sensing ability of LARS1, we investigated post-translational modification of LARS1. LARS1 was phosphorylated on serine in cells deprived of glucose (fig. S6A). Through siRNA-based screening (10–12), suppression of adenosine 5'-monophosphate-activated protein kinase (AMPK) or Unc-51 like autophagy activating kinase 1 (ULK1) decreased LARS1 phosphorylation (fig. S6, B and C). ULK1 is activated by AMPK and is constitutively active when overexpressed (11, 13). Overexpression of ULK1 increased LARS1 phosphorylation in cells even without active AMPK (fig. S6D). LARS1 pulled down ULK1 kinase domain *in vitro* (fig. S7A) and is phosphorylated *in vitro* by ULK1 WT, but not by catalytically inactive mutant (K46I) (fig. S7B) (14), indicating that ULK1 might directly phosphorylate LARS1. LARS1 was identified as a possible ULK1-interacting protein (15) and potential member of an autophagy network by mass spectrometry (MS) (16). Co-IP and FRET experiments showed that the association of overexpressed and tagged LARS1 and ULK1 was increased in cells deprived of glucose (Fig. 2, A and B, and fig. S7C). However, AARS1 was not bound to ULK1 (Fig. 2C), indicating some specificity of LARS1 and ULK1 interaction.

We focused on LARS1 S391 and S720, which are evolutionally conserved, as residues possibly phosphorylated by ULK1 on the basis of three criteria: LARS1 fragments phosphorylated *in vitro*, phosphorylated residues identified by MS, and consensus sequence predicting ULK1 substrates (13) (fig. S8, A to D). Although LARS1 Ser³⁹¹→Ala (S391A) and S720A showed decreased autoradiograph intensity compared with WT in *in vitro* kinase assay, S391A was phosphorylated less than S720A but similarly to 2SA (S391A/S720A) (Fig. 2D), which made us speculate that phosphorylation of S391 might be a prerequisite for that of S720. S391

¹Medicinal Bioconvergence Research Center and College of Pharmacy, Seoul National University, Seoul 08826, Republic of Korea. ²Integrated Metabolomics Research Group, Western Seoul Center, Korea Basic Science Institute, Seoul 03759, Republic of Korea. ³Department of Molecular Medicine and Biopharmaceutical Sciences and Graduate School for Convergence Technologies, Seoul National University, Seoul 08826, Republic of Korea. ⁴Yonsei Institute of Pharmaceutical Sciences, College of Pharmacy, Yonsei University, Incheon 21983, Republic of Korea. ⁵Department of Integrated OMICS for Biomedical Science, Yonsei University, Seoul 03722, Republic of Korea. ⁶Department of Chemistry, Korea Advanced Institute of Science and Technology, Yuseong-gu, Daejeon 34141, Republic of Korea. ⁷Division of Biotechnology, College of Life Sciences and Biotechnology, Korea University, Seongbuk-gu, Seoul 02841, Republic of Korea.

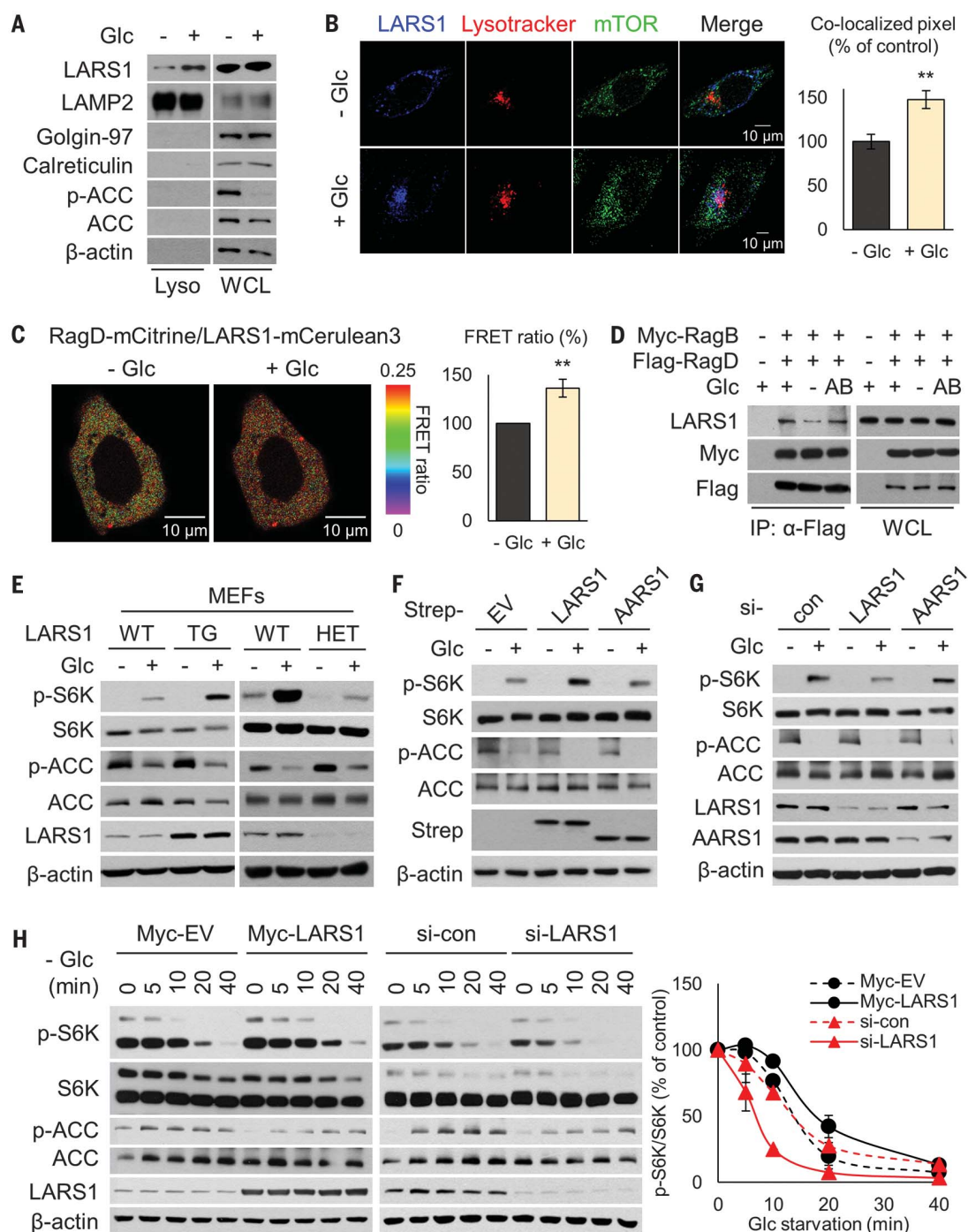
*Present address: Food Analysis Center, Korea Food Research Institute, Wanju 55365, Republic of Korea. †Present address: Nextgen Bioscience, Seongnam 13494, Republic of Korea.

‡These authors contributed equally to this work.

§Corresponding author. Email: kimjohn@biocon.snu.ac.kr (J.H.K.); sungkim@biocon.snu.ac.kr (S.K.)

Fig. 1. Glucose induces the interaction of LARS1 and RagD for mTORC1 activation.

(A) LARS1 located in lysosome was determined by immunoblot in human embryonic kidney 293T (HEK293T) cells. Glc, glucose; Lyso, lysosome; WCL, whole cell lysates; ACC, acetyl-CoA carboxylase; p, phosphorylation. (B) Localization of LARS1 with lysotracker was monitored by immunofluorescence in Hela cells ($n \geq 16$; unpaired t test; $^{**}P < 0.01$; mean \pm SEM). (C) The interaction of overexpressed and tagged LARS1 and RagD in response to glucose was monitored by live FRET assay in CHO-K1 cells. The ratio of the fluorescence intensity mCitrine-RagD to mCerulean3-LARS1 with the excitation at 457 nm was measured ($n = 4$ per group; unpaired t test; $^{**}P < 0.01$; mean \pm SEM). (D) LARS1-RagD interaction in response to glucose was determined by co-IP in HEK293T cells. AB, add back. (E) Glucose-dependent mTORC1 activities estimated from S6K phosphorylation in LARS1 WT, TG, and HET MEFs. (F and G) The glucose-dependent mTORC1 activities were also determined by up-regulation (F) and down-regulation (G) of LARS1 and AARS1. Strep, strep-tag; EV, empty vector; si, small interfering RNAs; con, nontarget control. (H) The effect of LARS1 on the remaining mTORC1 activity under glucose starvation was observed in HEK293T cells.



phosphorylation seemed to induce conformational changes based on circular dichroism (CD) and limited proteolysis. Although LARS1 WT, S391A, and S391E had similar secondary structure compositions, tertiary structure was different in S391E (Fig. 2E and fig. S9). We made an antibody specific to phosphoLARS1 (S720). It was validated by immunoblotting purified LARS1 with S720 phosphorylation (17) and by LARS1 phosphorylated in cells deprived of glucose (Fig. 2, F and G, and fig. S10). ULK1 phos-

phorylated S720 of LARS1 WT and S391E but not that of S391A (Fig. 2H). ULK1 suppression using siRNAs and SBI-0206965 (13) decreased LARS1 S720 phosphorylation (Fig. 2, I and J). Thus, ULK1 may phosphorylate LARS1 at S391 first and then S720 in glucose deprivation.

Because LARS1 S720 is located within a KMSKS motif, which is crucial for ATP binding (fig. S8D) (18), we tested the effect of LARS1 phosphorylation on ATP binding. LARS1 mutants with mutations at S720 (S720 mutants)

had decreased ATP-binding affinity, whereas S391 mutants still bound to ATP (fig. S11A). Leucine bound to LARS1 better in the presence of ATP, which is consistent with the result that LARS1 S720 mutants had decreased leucine-binding capability (fig. S11B and Fig. 3A). Furthermore, leucine did not bind to five additional mutants substituting S720 for Asp, Val, Asn, Cys, or Arg (fig. S11C), suggesting that serine is critical for the binding of leucine as well as ATP. We monitored catalytic activity of

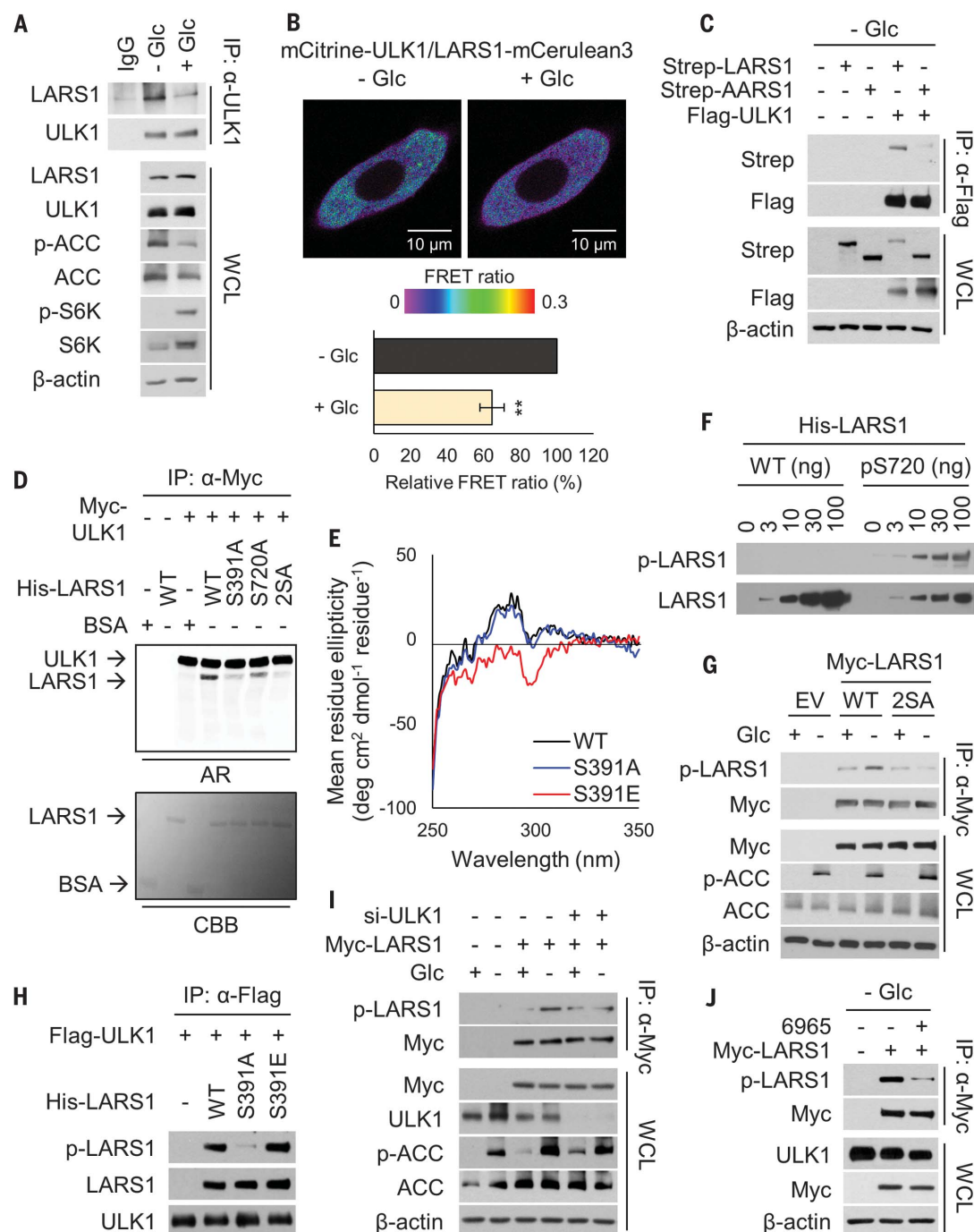


Fig. 2. Glucose starvation-dependent phosphorylation of LARS1 by ULK1. (A) Co-IP of LARS1 with ULK1 in response to glucose was monitored in HEK293T cells. IgG, immunoglobulin G. (B) The interaction of LARS1 with ULK1 in response to glucose was determined by live FRET assay in CHO-K1 cells ($n = 3$ per group; unpaired t test; $**P < 0.01$; mean \pm SEM). (C) Co-IP of ULK1 with LARS1 or AARS1 was determined in HEK293T cells. (D) In vitro kinase assay using [32 P]ATP. Radioactive labeling of ULK1 and LARS1 was determined by autoradiography. BSA, bovine serum albumin; AR, autoradiograph; CBB, Coomassie brilliant blue. S, serine; A, alanine. (E) Near-ultraviolet CD spectrum of His-LARS1 WT and mutants. E, glutamate. (F) Immunoblot of purified His-LARS1 WT and pS720. (G) Glucose starvation-induced LARS1 S720 phosphorylation in HEK293T cells. (H) Immunoblot of S720 phosphorylation after kinase assay using LARS1 WT and mutants. (I and J) Phosphorylation of LARS1 S720 with the suppression of ULK1 by siRNAs (I) or inhibitor (J) was determined in HEK293T cells. 6965, SBI-0206965.

LARS1. Leu-AMP and Leu-tRNA production of LARS1 2SE (S391E/S720E) and S720E were blocked, whereas LARS1 S391A and S391E showed comparable activity to WT. 2SA and S720A retained ~10% of WT activity, implying a possible weak interaction with leucine (fig. S11D and Fig. 3B). Cells overexpressing LARS1 2SE and S720E showed reduced leucine incorporation (fig. S11E). Thus, ULK1-mediated LARS1 phosphorylation appears to reduce ATP and leucine binding, leading to inhibition of leucylation.

We investigated mTORC1-stimulating activity of LARS1. LARS1 mutants showed reduced translocation to lysosome (fig. S12A), and 2SE and S720E did not interact with RagD, whereas 2SA and S720A showed weak binding. LARS1 S391 mutants also showed weaker interaction compared with WT despite its leucine-binding capability (Fig. 3C and fig. S12, A and B). LARS1 mutants did not restore S6K phosphorylation completely, whereas WT did. It was more decreased in cells expressing 2SE and S720E than the other mutants (Fig. 3D). Weaker effects

of 2SA and S720A might reflect incomplete blocking of LARS1 and leucine binding. Cells expressing LARS1 mutants showed decreased cell size and increased autophagy compared with WT-expressing cells, as measured by forward scattering, amounts of microtubule-associated protein 1 light chain 3 (LC3)-phosphatidylethanolamine conjugate (LC3 II), and green fluorescent protein (GFP)-LC3 puncta formation (fig. S12, C to G, and Fig. 3E). Thus, changing leucine binding capability of LARS1 may regulate leucylation and

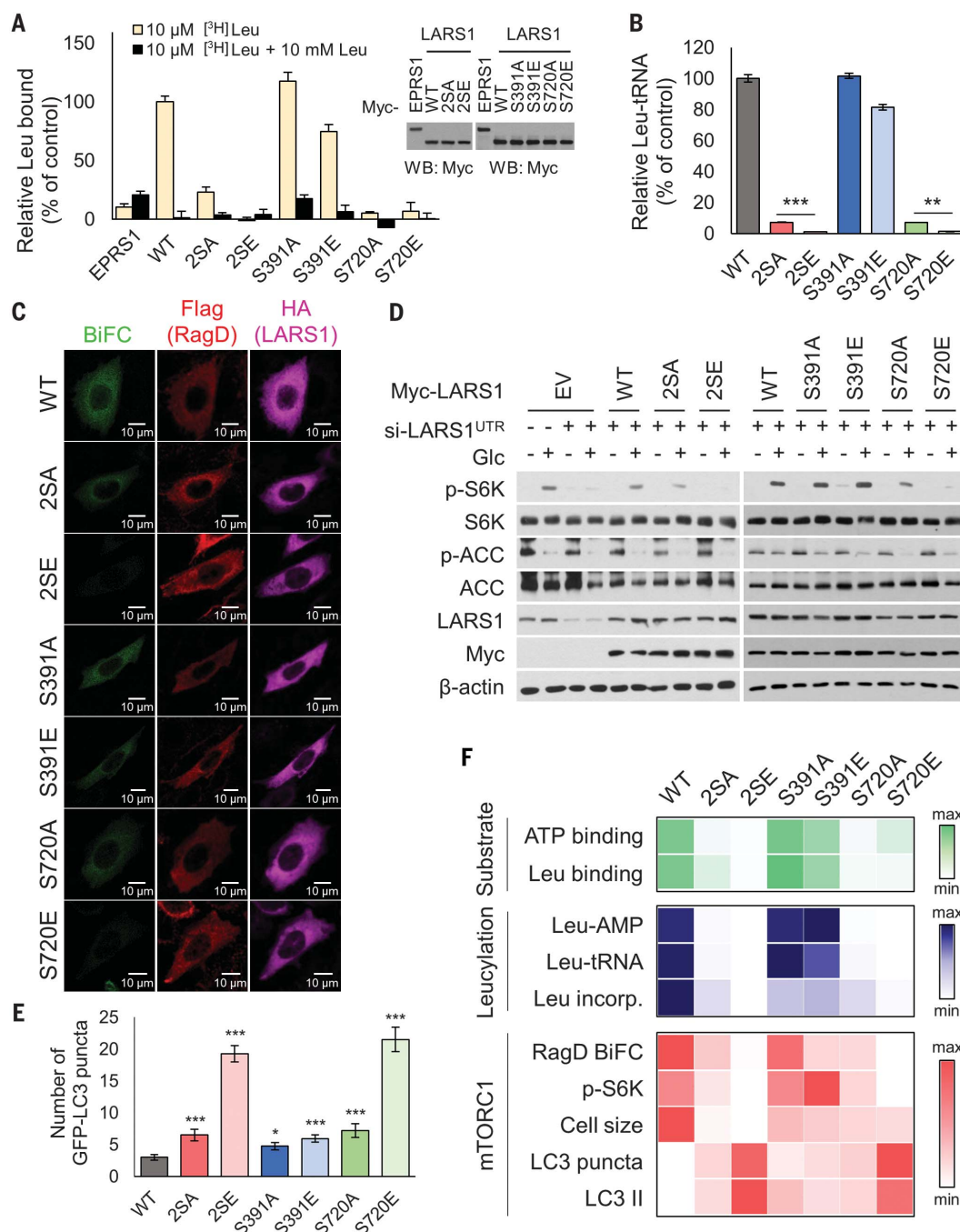


Fig. 3. Effects of LARS1 phosphorylation on catalytic and noncatalytic activities for protein synthesis.

(A) The amount of leucine bound to LARS1 WT and mutants was quantified. The abundance of EPRS1, LARS1 WT, and mutants was determined by immunoblot ($n = 3$ per group; unpaired t test; mean \pm SEM). EPRS1, glutamyl-prolyl-tRNA synthetase 1; WB, Western blot. (B) The catalytic activity of LARS1 WT and mutants was determined by Leu-tRNA production ($n = 3$ per group; mean \pm SEM). (C) The interaction of LARS1 WT and mutants with RagD was determined by bimolecular fluorescence complementation (BiFC) in CHO-K1 cells. (D) The effect of LARS1 WT and mutants on mTORC1 activation was estimated by phosphorylation of S6K in HEK293T cells. (E) The effect of LARS1 WT and mutants on the formation of GFP-LC3 puncta was evaluated in HEK293T cells ($n \geq 51$; mean \pm SEM). (F) The contribution of LARS1 WT and mutants on substrate binding, leucylation activity, and mTORC1 stimulation activity was summarized as a heat map. Experimental detail in figs. S11 and S12. Unpaired t test; * $P < 0.05$, ** $P < 0.01$, *** $P < 0.001$.

mTORC1-dependent physiology under glucose starvation (Fig. 3F).

Because autophagy contributes to starvation responses and is regulated by mTORC1 and ULK1 (19), we examined functional relationship of LARS1 and autophagy. LARS1 negatively affected the autophagy response to glucose deprivation (fig. S13, A and B). Conversely, when inhibiting autophagy with bafilomycin A, LARS1 phosphorylation and LARS1-mediated mTORC1 regulation were still observed to be dependent on glucose availability (fig. S13, C to E).

Amino acids are used not only as building blocks for protein synthesis but also as a carbon source for energy production (3), and leucine catabolism is inhibited by glucose (20). Therefore, we examined the direction of leucine usage in glucose deprivation. We used rhabdomyosarcoma (RD) cell lines, for high expression of leucine catabolic enzymes (LCEs) in muscle (27). Leucine increased ATP concentration and decreased cytotoxicity in cells deprived of glucose (fig. S14). mRNAs of some LCEs were more abundant in the absence of glucose (fig. S15, A and B). Suppression of LCEs

decreased ATP concentration and increased cytotoxicity under glucose restriction (fig. S15, C to E), implying the significance of leucine catabolism in glucose starvation.

To monitor the effect of LARS1 phosphorylation on leucine catabolism, the fraction of 13 C-labeled citrate and malate converted from 13 C₆-leucine was determined (fig. S16A). These fractions were increased in cells expressing LARS1 2SE compared with WT, suggesting an increased leucine contribution to tricarboxylic acid cycle intermediates (Fig. 4, A and B, and fig. S16, B and C). Investigation of glutamine

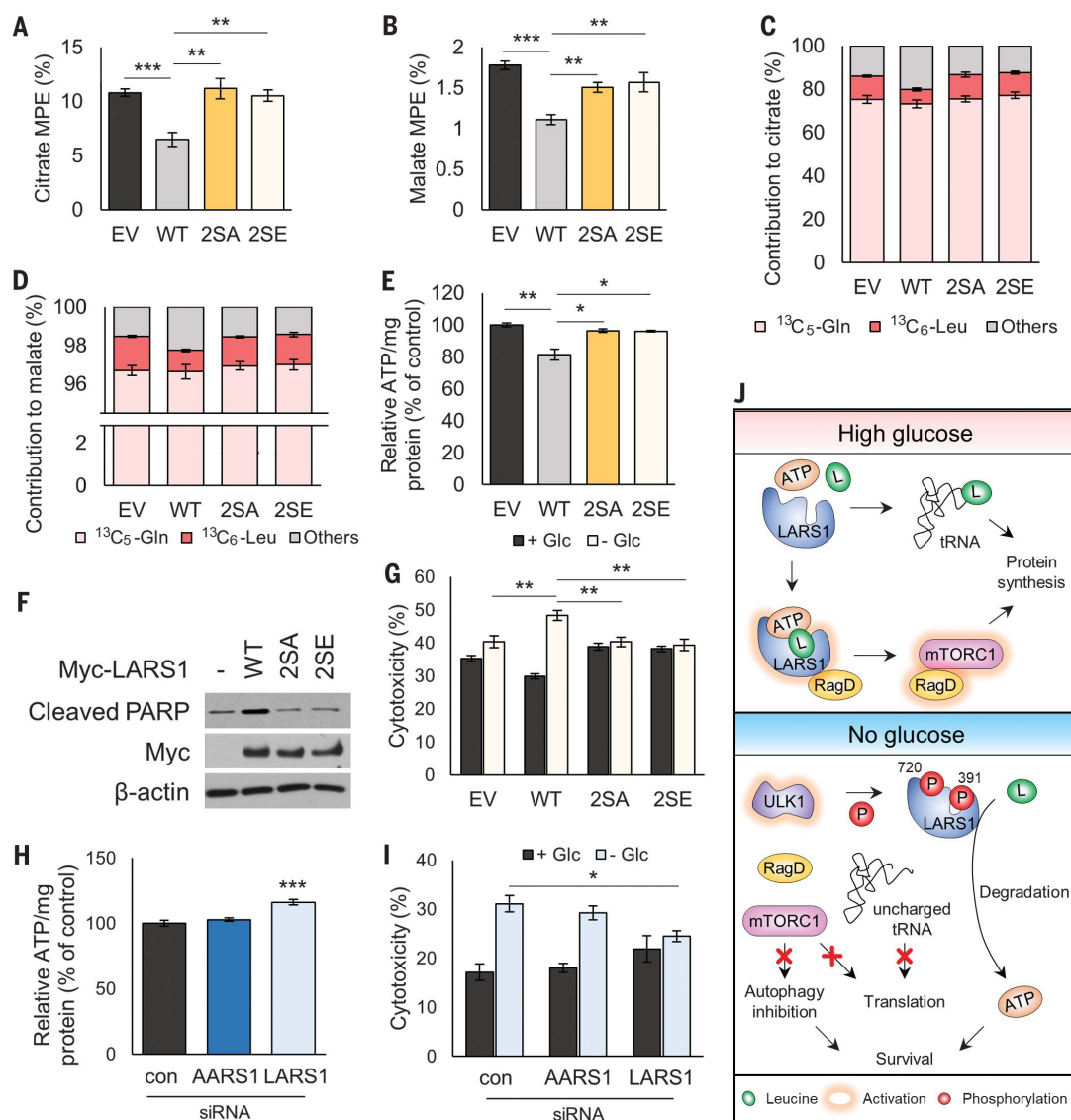


Fig. 4. LARS1 phosphorylation makes leucine more available for catabolism.

(A to D) RD cells stably expressing LARS1 WT and mutants (RD^{LARS1} stable cells) were transfected with siLARS1^{UTR} to suppress endogenous LARS1 and incubated with $^{13}\text{C}_6$ -leucine or $^{13}\text{C}_5$ -glutamine. The fraction of ^{13}C -labeled citrate and malate was measured by liquid chromatography-mass spectrometry ($n \geq 3$; mean \pm SEM). MPE, molar percent enrichment. The contribution to total citrate or malate from leucine and glutamine was visualized in (C) and (D). (E) ATP levels were determined in RD^{LARS1} stable cells with siLARS1^{UTR} using luminescence assay ($n = 3$ per group; mean \pm SEM). (F and G) RD^{LARS1} stable cells were transfected with siLARS1^{UTR} and glucose starvation-induced cell death was determined by the PARP cleavage and LDH assay ($n = 5$ per group; mean \pm SEM). (H) The amount of ATP in RD cells starved of glucose was quantified by luminescence assay ($n = 6$ per group; mean \pm SEM). (I) Cytotoxicity was determined by LDH assay in RD cells ($n = 5$ per group; mean \pm SEM). (J) Schematic model of LARS1 roles in the control of glucose-dependent leucine metabolism. Unpaired t test; * $P < 0.05$, ** $P < 0.01$, *** $P < 0.001$.

degradation (fig. S17A) (22) indicated that oxidative glutamine metabolism was decreased in cells expressing LARS1 WT compared with 2SE as monitored by m+4 citrate and m+4 malate (fig. S17, B and C) (23). When analyzing the source of total citrate and malate, the contribution of leucine seemed to be the second most common (Fig. 4, C and D).

ATP concentration was increased in cells expressing LARS1 2SE compared with WT under glucose deprivation (Fig. 4E). Monitoring the poly(ADP-ribose) polymerase (PARP) cleavage and activity of lactate dehydrogenase (LDH) showed that cytotoxicity was decreased in cells expressing LARS1 mutants (Fig. 4, F and G). Whereas AARS1 did not show the similar effect (Fig. 4, H and I), both the fraction of leucine-derived citrate and malate and the ATP concentration were increased and cytotoxicity was decreased by the depletion of LARS1 and VARS1 (fig. S18). Thus, although leucine regu-

lates the mTORC1 pathway through specific LARS1 and RagD interaction, three branched-chain amino acids (BCAAs) appear to be similarly important for protecting cells under glucose starvation because degradation of one BCAA is positively correlated with that of others (21, 24).

Because nutrient deprivation induces cell death caused by metabolic imbalance, understanding metabolic changes is crucial (3, 25, 26). We propose that LARS1 mediates defense under glucose starvation by rebalancing leucine metabolism. Upon sensing leucine in the presence of glucose, LARS1 supports translation by leucylating tRNA and by activating mTORC1. However, in the absence of glucose, LARS1 phosphorylated by ULK1 loses its leucine binding capability, decreasing both activities, thus leading to the inhibition of protein synthesis and activation of autophagy. In this way, phosphorylated LARS1 may

save ATP consumption and allow leucine to be used for ATP generation, which together provide the tolerance against glucose starvation (Fig. 4J).

In muscle, the major energy source changes from glucose to ketone bodies during starvation (27). Because leucine is a potent mTORC1 activator and is an exclusively ketogenic amino acid (28), changing leucine metabolism might help defend against glucose starvation in muscle.

REFERENCES AND NOTES

1. P. B. Soeters, *Nestle Nutr. Inst. Workshop Ser.* **82**, 17–25 (2015).
2. J. D. Rabinowitz, E. White, *Science* **330**, 1344–1348 (2010).
3. A. Valerio, G. D'Antona, E. Nisoli, *Aging* **3**, 464–478 (2011).
4. R. A. Saxton, D. M. Sabatini, *Cell* **168**, 960–976 (2017).
5. A. Efeyan et al., *Nature* **493**, 679–683 (2013).
6. J. M. Han et al., *Cell* **149**, 410–424 (2012).
7. J. H. Kim et al., *Nat. Commun.* **8**, 732 (2017).
8. M. Lee et al., *Proc. Natl. Acad. Sci. U.S.A.* **115**, E5279–E5288 (2018).

9. K. Inoki, T. Zhu, K. L. Guan, *Cell* **115**, 577–590 (2003).
10. S. Horman *et al.*, *Curr. Biol.* **12**, 1419–1423 (2002).
11. F. McAlpine, L. E. Williamson, S. A. Tooze, E. Y. Chan, *Autophagy* **9**, 361–373 (2013).
12. S. Shin *et al.*, *Mol. Cell* **59**, 382–398 (2015).
13. D. F. Egan *et al.*, *Mol. Cell* **59**, 285–297 (2015).
14. E. Y. Chan, A. Longatti, N. C. McKnight, S. A. Tooze, *Mol. Cell. Biol.* **29**, 157–171 (2009).
15. A. D. Rouillard *et al.*, *Database* **2016**, baw100 (2016).
16. C. Behrends, M. E. Sowa, S. P. Gygi, J. W. Harper, *Nature* **466**, 68–76 (2010).
17. H. S. Park *et al.*, *Science* **333**, 1151–1154 (2011).
18. J. J. Burbaum, P. Schimmel, *J. Biol. Chem.* **266**, 16965–16968 (1991).
19. J. Kim, M. Kundu, B. Viollet, K. L. Guan, *Nat. Cell Biol.* **13**, 132–141 (2011).
20. D. Shao *et al.*, *Nat. Commun.* **9**, 2935 (2018).
21. J. T. Brosnan, M. E. Brosnan, *J. Nutr.* **136** (suppl.), 207S–211S (2006).
22. C. Yang *et al.*, *Mol. Cell* **56**, 414–424 (2014).
23. B. Kim, J. Li, C. Jang, Z. Arany, *EMBO J.* **36**, 2321–2333 (2017).
24. R. Paxton, R. A. Harris, *Arch. Biochem. Biophys.* **231**, 48–57 (1984).
25. A. Y. Choo *et al.*, *Mol. Cell* **38**, 487–499 (2010).
26. G. Leprévier *et al.*, *Cell* **153**, 1064–1079 (2013).
27. J. M. Argilés, N. Campos, J. M. Lopez-Pedrosa, R. Rueda, L. Rodríguez-Mañas, *J. Am. Med. Dir. Assoc.* **17**, 789–796 (2016).
28. M. G. Carlson, W. L. Snead, P. J. Campbell, *Am. J. Clin. Nutr.* **60**, 29–36 (1994).

ACKNOWLEDGMENTS

We thank H.-S. Jeong for supplying AMPK γ 1 null 293A cells.

Funding: This work was supported by the Global Frontier Project grant [NRF-M3A6A4-2010-0029785 (Sunghoon Kim), NRF-2014M3A6A4075060 (H.-S.P.), NRF-2015M3A6A4076702 (G.-S.H.), and NRF-2013M3A6A4044795 (K.Y.H.)] of the National Research Foundation funded by the Ministry of Science and ICT (MSIT) of Korea; the Korea Basic Science Institute (T39720) (G.-S.H.); and the Basic Science Research Program through the National Research Foundation of Korea funded by the Ministry of Education [2018R1A6A1A03023718 (J.M.H.)]. **Author contributions:** I.Y. and J.H.K. conceived of and designed the

experiments, collected and analyzed data, and wrote the manuscript. M.N., H.K.K., H.-S.M., Sunghoon Kim, J.J., J.A.S., S.J.J., S.B.K., S.C., Y.K., J.L., W.S.Y., H.C.Y., K.K., M.-S.K., A.Y., K.C., H.-S.P., G.-S.H., and K.Y.H. collected and analyzed data. J.M.H. conceived of and designed the experiments. Sunghoon Kim conceived of and designed the experiments, wrote the manuscript, and gave final approval for this study. **Competing interests:** The authors declare no competing interests. **Data and materials availability:** All data are available in the manuscript or the supplementary materials.

SUPPLEMENTARY MATERIALS

science.sciencemag.org/content/367/6474/205/suppl/DC1
Materials and Methods
Figs. S1 to S18
References (29–33)

[View/request a protocol for this paper from Bio-protocol.](#)

24 May 2018; resubmitted 20 March 2019
Accepted 14 November 2019
Published online 28 November 2019
10.1126/science.aau2753

PALEOANTHROPOLOGY

Age control of the first appearance datum for Javanese *Homo erectus* in the Sangiran area

Shuji Matsu'ura^{1*}, Megumi Kondo², Tohru Danhara³, Shuhei Sakata⁴, Hideki Iwano³, Takafumi Hirata⁵, Iwan Kurniawan⁶, Erick Setiyabudi⁶, Yoshihiro Takeshita⁷, Masayuki Hyodo^{8,9*}, Ikuko Kitaba^{8,10}, Masafumi Sudo¹¹, Yugo Danhara³, Fachroel Aziz⁶

The chronology of the World Heritage Site of Sangiran in Indonesia is crucial for the understanding of human dispersals and settlement in Asia in the Early Pleistocene (before 780,000 years ago). It has been controversial, however, especially regarding the timing of the earliest hominin migration into the Sangiran region. We use a method of combining fission-track and uranium-lead dating and present key ages to calibrate the lower (older) Sangiran hominin-bearing horizons. We conclude that the first appearance datum for the Sangiran hominins is most likely ~1.3 million years ago and less than 1.5 million years ago, which is markedly later than the dates that have been widely accepted for the past two decades.

The first appearance datum of *Homo erectus* in the Far East, a hominin species that originated in equatorial Africa or perhaps the Caucasus region of Eurasia (1–3), is important for modeling early human dispersals across Asia after the first out-of-Africa migration. Since the mid-1990s, researchers have believed that eastern Asia's oldest hominin remains date back to 1.7 to 1.8 million years ago (Ma) (4–7), about half a million years earlier than previously thought (8–11). Despite uncertainties (12), this chronology and its consequences have been widely recognized as one of paleoanthropology's basic paradigms: *H. erectus* expanded rapidly to eastern Asia (1, 13) after its first appearance at ~1.85 Ma. Furthermore, combined with chronological revisions of *H. erectus* sites in China, different dispersal dynamics have been suggested for southeastern and northeastern Asia (14, 15): an earlier (>1.5 Ma) *H. erectus* dispersal along a southern route to equatorial southeast Asia and a later (after ~1.3 Ma) dispersing population along a northerly route to northeast Asia. Although the hypothesis of a later dispersal to northeastern Asia disagrees with current Chinese hominin fossil chronolo-

gies (6, 7), an early dispersal into southeast Asia has been based on evidence from the Sangiran area (Indonesia), where, on the basis of ⁴⁰Ar/³⁹Ar geochronology, it has been proposed that *H. erectus* dates to ~1.6 Ma (5). However, other ⁴⁰Ar/³⁹Ar ages (16, 17) and a newly refined magnetic polarity stratigraphy of the Sangiran area (18) have failed to support this chronology. This calls for reevaluation of the 1.6 Ma Sangiran *H. erectus* age. We report U-Pb and fission-track dates of volcaniclastic layers in and just above the Grenzbank zone, a key bed of the lower Sangiran hominin-bearing horizons. We also present dates of a marker tuff lying below the hominin-bearing horizons. Our results provide reliable age control points to infer the first appearance datum for Javanese *H. erectus* in Sangiran.

Sangiran in Central Java (Fig. 1A) is one of the most productive sites in paleoanthropology. It has produced a steady stream of *H. erectus* finds since 1936, now totaling >100 hominin specimens. However, it lacks an accepted chronostratigraphy. Geologically, the Sangiran area is a domelike structure, extending 8 km north-south and 4 km east-west (Fig. 1B). The dome is truncated by erosion, exposing a concentric pattern of strata, with older strata surrounded by younger strata (19) (Fig. 1B). The exposed sediments, >300 m thick, are divided into four units (19). The marine Puren Formation lies at the base (Fig. 1C). The overlying Sangiran Formation consists of the Lower Lahar (volcanic breccia) at its lowermost part and the black clay. The latter comprises shallow marine to lagoonal sediments and overlying lacustrine sediments that are partly pedogenized. The Sangiran Formation is overlain by the Bapang Formation, the base of which is known as the Grenzbank zone—a fossiliferous unit of carbonate-cemented gravelly sands. The Bapang Formation is further overlain by the Pohjar Formation (Fig. 1C). The upper two formations are primarily fluvial sediments

intercalating many layers of pumice, volcanic ash, and lahar.

Previous lithostratigraphic and geochemical investigations have revealed that the hominin-bearing horizons of the Sangiran area could range from the Upper Tuff of the Bapang Formation down to Tuff 11 of the uppermost Sangiran Formation (19) or plausibly to the lower levels in the Upper Sangiran Formation (8, 20) (Fig. 1C). A systematic investigation of the chronostratigraphy of this sequence was first conducted in the late 1970s to early 1990s, including fission-track dating and magnetostratigraphic analysis, which suggested a hominin time span of ~0.8 to 1.1 Ma (10, 19) or possibly to ~1.3 Ma (8). However, in 1994, a substantially older ⁴⁰Ar/³⁹Ar date of 1.66 Ma was reported for pumices presumed to overlie the two allegedly oldest hominin remains (4). Although this date has been questioned because of the uncertain stratigraphic relationship between the dated pumice and the hominin specimens (5, 21, 22), Larick *et al.* (5) subsequently reported a series of hornblende ⁴⁰Ar/³⁹Ar dates that supported the older chronology and placed the Sangiran hominin-bearing sequence from >1.5 to ~1.0 Ma. The widely cited age of >1.5 Ma derives from a date of 1.51 ± 0.08 Ma (5) for a pumice lens lying a few meters above the Grenzbank zone at the base of the Bapang Formation (Fig. 1C and Fig. 2). However, other pumice and tuff samples collected from the lowermost part of the Bapang Formation have produced a group of notably younger hornblende ⁴⁰Ar/³⁹Ar dates of 0.8 to 0.9 Ma (16, 17). One of the samples yielded a date of ~1.5 Ma; however, this has been provisionally considered to relate to natural reworking (17). These 0.8 to 0.9 Ma dates—centering around 0.88 Ma—are, in turn, consistent with the newly refined magnetostratigraphy (18), which securely establishes the Matuyama-Brunhes polarity transition within the Upper Tuff complex of the Bapang Formation and constrains the age of the uppermost hominin-bearing sediments to ~0.79 Ma. Thus, the controversy over the long (older) and short (younger) chronologies for the Sangiran hominins is ongoing (15, 18, 23). Further studies are needed to resolve this issue and to better understand the biogeographic origins and evolution of Javanese *H. erectus*.

To solve this long-standing chronological controversy, we applied a method of combining fission-track and U-Pb dating on zircon grain populations taken from the lowermost Bapang section—which directly contains the former sampling location of the ⁴⁰Ar/³⁹Ar 1.51 ± 0.08 Ma (5) sample—and also on zircon grains taken from a tuff that could potentially provide a maximum age for the Sangiran hominins. Zircon is commonly observed in volcanic rocks and is a markedly robust mineral. The U-Pb zircon method has been

¹Department of Anthropology, National Museum of Nature and Science, Tsukuba City, Ibaraki 305-0005, Japan.

²Laboratory of Physical Anthropology, Ochanomizu University, Bunkyo-ku, Tokyo 112-8610, Japan. ³Kyoto Fission-Track Corporation, Ltd., Omiya, Kita-ku, Kyoto 603-8832, Japan. ⁴Earthquake Research Institute, University of Tokyo, Bunkyo-ku, Tokyo 113-0032, Japan. ⁵Geochemical Research Center, University of Tokyo, Bunkyo-ku, Tokyo 113-0033, Japan. ⁶Centre for Geological Survey, Bandung 40122, Indonesia. ⁷Institute of Education, Shinshu University, Nagano City, Nagano 380-8544, Japan. ⁸Research Center for Inland Seas, Kobe University, Nada-ku, Kobe 657-8501, Japan. ⁹Department of Planetology, Faculty of Science, Kobe University, Nada-ku, Kobe 657-8501, Japan. ¹⁰Research Centre for Palaeoclimatology, Ritsumeikan University, Kusatsu City, Shiga 525-8577, Japan. ¹¹Institute of Geosciences, University of Potsdam, 14476 Golm, Germany.

*Corresponding author. Email: matsu-ur@js2.so-net.ne.jp (S.M.); mhyodo@kobe-u.ac.jp (M.H.)

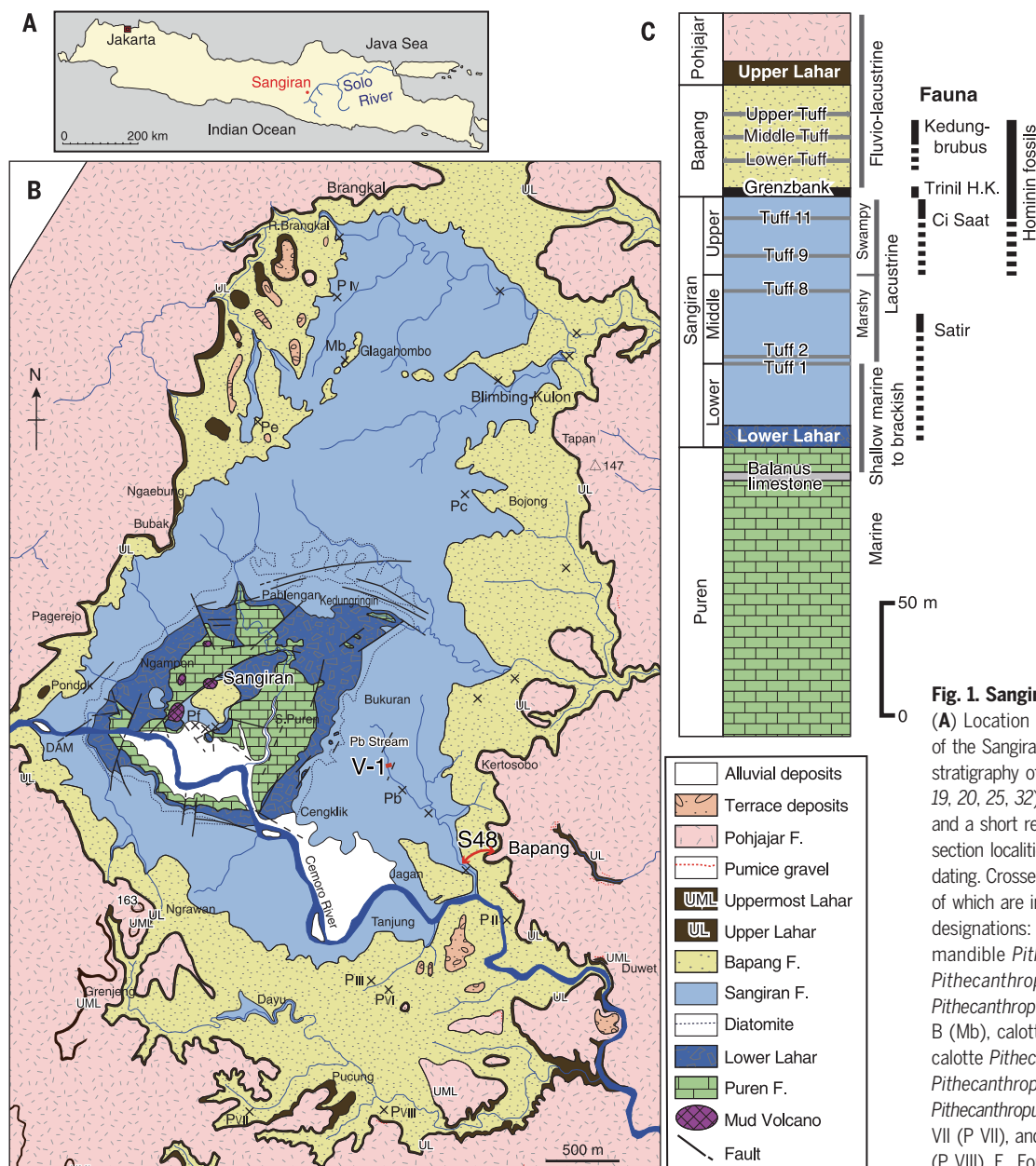


Fig. 1. Sangiran location and stratigraphy.

(A) Location of Sangiran. (B) Geological map of the Sangiran area (after 19). (C) Generalized stratigraphy of the Sangiran area (after 19, 20, 25, 32). In (B), a thick red arrow (S48) and a short red line (V-1) show the columnar section localities involved with samples for dating. Crosses show *H. erectus* fossil sites, some of which are indicated with registered designations: mandible *Pithecanthropus* B (Pb), mandible *Pithecanthropus* C (Pc), mandible *Pithecanthropus* E (Pe), mandible *Pithecanthropus* F (Pf), mandible *Meganthropus* B (Mb), calotte *Pithecanthropus* II (P II), calotte *Pithecanthropus* III (P III), cranium *Pithecanthropus* IV (P IV), calotte *Pithecanthropus* VI (P VI), calotte *Pithecanthropus* VII (P VII), and cranium *Pithecanthropus* VIII (P VIII). F., Formation.

recently improved in dating young Quaternary samples (24). The U-Pb and fission-track methods are complementary because they can be applied to the same zircon grain population. Note that closure temperatures for fission-track and U-Pb chronometry on zircons are $\sim 240^\circ\text{C}$ and $>900^\circ\text{C}$, respectively (24). Because zircon variably crystallizes before eruption (24), U-Pb ages indicate the timing of crystallization, whereas the fission-track age closely reflects the timing of eruption.

We collected samples for dating from two tephra horizons at the type site of the middle to lower levels of the Bapang Formation near the Bapang Village [columnar section site S48 (Fig. 1B); fig. S1, A and G]. Tuff sample BP-

LMTCL-1 was collected from the yellowish white tuffaceous sand layer immediately above the Grenzbank zone, whereas pumice sample BP-GB-BC-P1 was taken from the bottom part of the bluish gray clay layer intercalated in the Grenzbank zone (Fig. 2 and fig. S1, A to D). We also collected sample Pb-T8 from the yellowish white tuff (Tuff 8) at the V-1 section site (Fig. 1B and fig. S1, E to G). Tuff 8 is a marked tephra that lies slightly below the base of the Upper Sangiran Formation (Fig. 1C and Fig. 2), i.e., stratigraphically underlying the hominin-bearing sediments.

Analytical results are summarized in Fig. 3. Tuff sample BP-LMTCL-1 yielded numerous colorless and euhedral zircon grains that sug-

gest proximal magmatic sources. To obtain a robust fission-track date from younger zircons with low spontaneous track density (table S1), we measured >1600 grains and calculated cumulative grain plateau ages (fig. S2). The weighted mean of two plateau ages was 0.884 ± 0.031 Ma (table S1). As mentioned earlier, it is necessary to consider the time difference of crystallization and eruption. Zircons usually crystallize over an extended period of time in a magma reservoir, and individual crystals potentially have various, prolonged durations of growth (24). The U-Pb age distribution of crystal faces of 75 grains from sample BP-LMTCL-1 is shown in Fig. 3, corresponding to crystallization before and around eruption, with

a weighted average age of 0.991 ± 0.005 Ma. The lower tail (younger ages) of the U-Pb age distribution is consistent with the fission-track date of 0.884 ± 0.031 Ma, supporting the interpretation that the lower end of the U-Pb age range approximates the eruption

age. These results for the tuff that lies just above the Grenzbank zone demonstrate that the Grenzbank zone is close to 0.9 Ma.

As for the pumice sample BP-GB-BC-P1, taken from within the Grenzbank zone, the number of zircon grains was comparatively

fewer and reliable fission-track dating was not possible. We note that the zircon grains included some reddish detrital ones that dated from ~4 to ~90 Ma (24). After excluding xenocrystals, weighted averaging of the U-Pb ages from the zircon crystal faces provided a 0.971 ± 0.009 Ma date (Fig. 3). Notably, the U-Pb age distributions of the two tephra units (BP-GB-BC-P1 and BP-LMTCL-1) correspond well with each other (Fig. 3), suggesting similar crystallization and eruption times, which demonstrates that the Grenzbank zone is close to 0.9 Ma. This is consistent with the recently confirmed absence of the Jaramillo subchronozone in the Bapang Formation (18), indicating an age younger than 0.99 Ma.

Sample Pb-T8 from Tuff 8, located several meters stratigraphically below the base of the Upper Sangiran Formation (which plausibly corresponds to the first appearance datum for the Sangiran hominins), yielded zircons suggesting proximal magmatic sources (24). Although the number of grains was comparatively fewer, higher spontaneous track density (higher uranium content) allowed reliable fission-track dating, producing a plateau age of 1.345 ± 0.108 Ma (table S1). We consider this date to represent the eruption age of Tuff 8. In our U-Pb dating of the same zircon assemblage, we aimed to estimate a maximum limit of the eruption age and hence analyzed the inner crystal zones, which likely represent pre-eruptive crystallization regions (24). The weighted mean of 1.688 ± 0.010 Ma for the grain U-Pb ages reflects an average timing of crystallization before eruption. The lowermost (youngest) tail of the U-Pb age distribution overlaps with the $+2\sigma$ range (1.56 Ma) of the Tuff 8 fission-track date (Fig. 3), implying that the maximum possible age of Tuff 8 is ~1.55 Ma.

The Grenzbank zone, located at the base of the Bapang Formation, is a key bed of the Sangiran hominin-bearing horizons. The above results for the Grenzbank zone (~0.9 Ma) contradict the widely cited bulk hornblende sample $^{40}\text{Ar}/^{39}\text{Ar}$ date of 1.51 Ma (5) for the pumice-rich layer lying a few meters above the Grenzbank zone (Fig. 2). They are consistent with previous $^{40}\text{Ar}/^{39}\text{Ar}$ determinations, centering around 0.88 Ma, on single hornblende grains (16, 17) of pumice and tuff sampled at another locality of the lowermost Bapang Formation. The Larick *et al.*'s (5) notably older $^{40}\text{Ar}/^{39}\text{Ar}$ date may be provisionally considered to relate to inherited hornblende grains or possible reworking of epiclastic pumice balls.

The majority of the Sangiran hominin fossils were found by chance by local inhabitants, sometimes recovered without precise provenance. Despite this problem, geological and geochemical surveys (8, 19, 20), as mentioned earlier, have shown that the hominin specimens could derive from sediments between

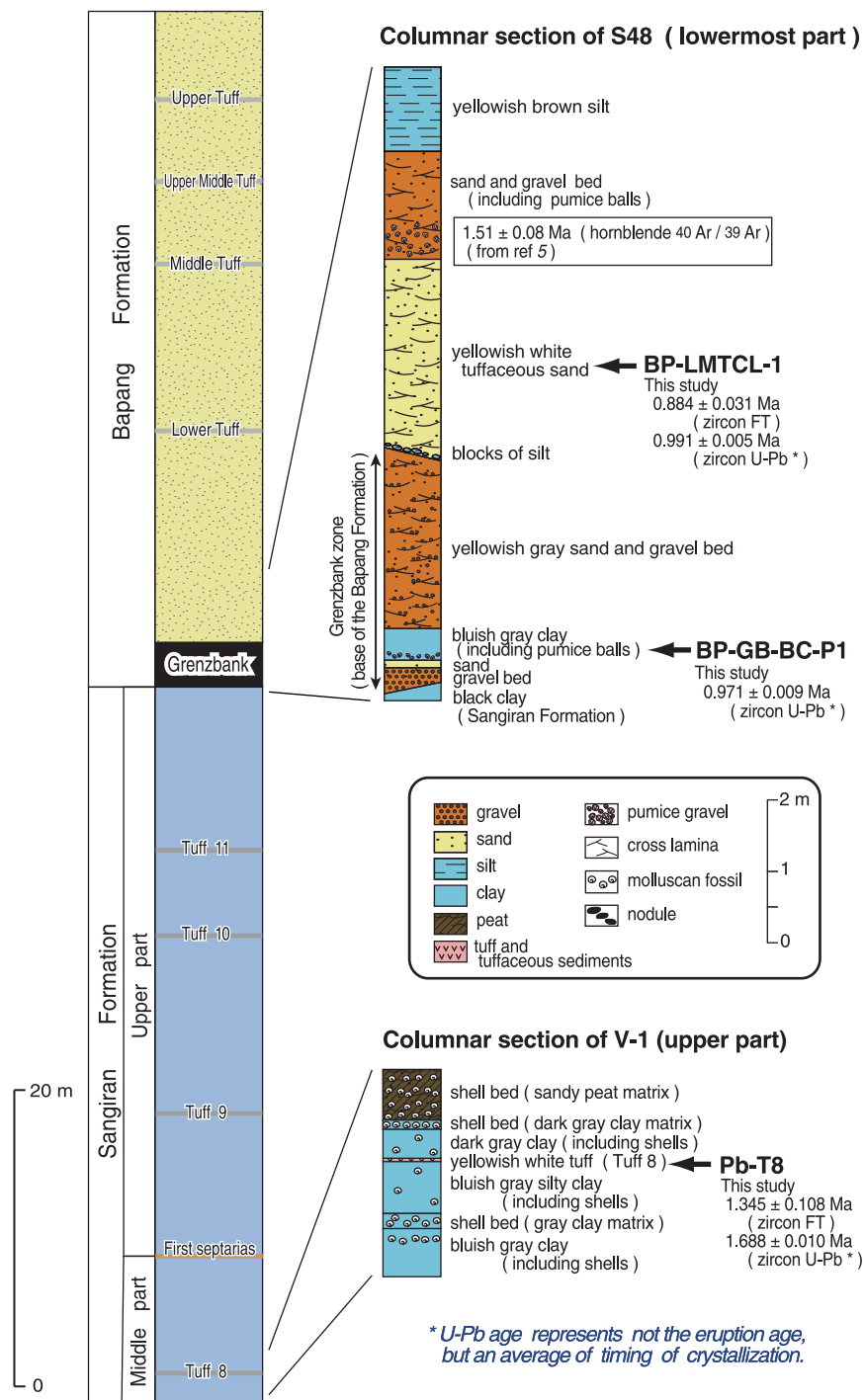


Fig. 2. Geological columnar sections showing the stratigraphic levels of the tephra samples treated in this study (BP-LMTCL-1, BP-GB-BC-P1, and Pb-T8). For the locations and photographs of the sampling sites, see fig. S1. Note that the U-Pb age represents an average of timing of zircon crystallization, which commonly occurs substantially before eruption, and that the deposition time of the unit layer is younger than the U-Pb age (24) (see Fig. 3). FT, fission-track.

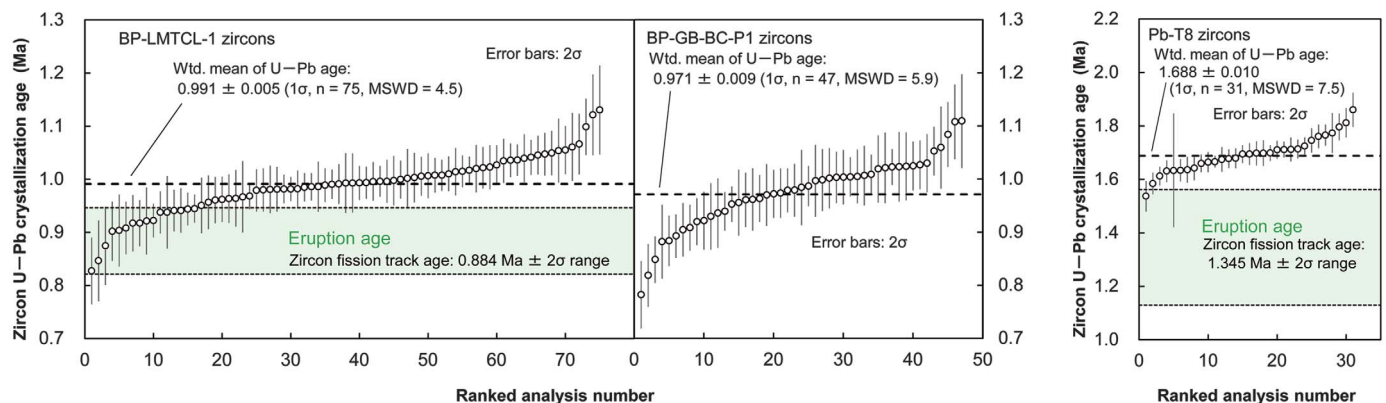


Fig. 3. Zircon fission-track age for BP-LMTCL-1 and Pb-T8 and the U-Pb age results of zircon grains for BP-LMTCL-1, BP-GB-BC-P1, and Pb-T8. Data for the fission-track age results are available in table S1, and data for the U-Pb age results are in table S5. The closure temperature ($\sim 240^\circ\text{C}$) of zircon fission-track chronometry is much lower than that ($>900^\circ\text{C}$) of U-Pb systematics. The weighted mean of grain U-Pb ages signifies an average of timing of crystallization

which variably occurs before eruption (24), where the fission-track date should represent the eruption age. Note that the 2σ ranges of the weighted mean U-Pb ages of BP-LMTCL-1 and BP-GB-BC-P1 overlap considerably, and the two groups of grain U-Pb ages show statistically comparable overall crystallization distributions ($P = 0.483$, two-sample, two-sided Kolmogorov-Smirnov test). Wtd., weighted; n , number of grains; MSWD, mean square weighted deviation.

the Upper Tuff of the Bapang Formation and the upper part of the Sangiran Formation (Fig. 1C). The Sangiran *H. erectus* materials, hitherto variously referred to as *Pithecanthropus* and *Meganthropus*, are tentatively divided into chronologically older and younger groups in light of paleontologic and stratigraphic contexts (8, 25–27).

The chronologically younger group includes crania *Pithecanthropus* III (Sangiran 3), VI (Sangiran 10), VII (Sangiran 12), and VIII (Sangiran 17); Skull IX; and mandibles Sb 8103 and Ng 8503. This group is derived from the Bapang Formation above the Grenzbank zone, mainly from sediments near the Middle Tuff (Fig. 1C) (8, 19), and it is associated with the Kedung Brubus fauna (25). Currently, the uppermost datum of the Sangiran hominin fossils has been stratigraphically placed at just below the Upper Middle Tuff (18) (Fig. 2); this stratigraphic level lies a few meters below the Matuyama-Brunhes transition and is dated to ~ 0.79 Ma (18).

The chronologically older group includes crania *Pithecanthropus* II (Sangiran 2) and IV (Sangiran 4); crania Sangiran 27 and 31; frontal Bp 9408; maxilla Bpg 2001.04; mandibles *Pithecanthropus* B (Sangiran 1b), C (Sangiran 9), and F (Sangiran 22); mandibles Bk7905 and Bk8606; and mandible *Meganthropus* B (Sangiran 8). The provenience of this group, based on hominin remains with known stratigraphic positions, ranges from the Grenzbank zone (the basal layer of the Bapang Formation, now dated to ~ 0.9 Ma) to Tuff 11 of the uppermost Sangiran Formation, but it plausibly goes down to lower levels in the Upper Sangiran Formation (8, 19, 20). This group is associated with the Trinil H.K. (Trinil Haupt Knochenschicht) fauna and the Ci Saat fauna (25) (Fig. 1C).

Magnetostratigraphy (10, 18) has suggested that the Jaramillo subchronozone lies in the uppermost Sangiran Formation with the lower boundary of the zone (1.07 Ma) near Tuff 11. We estimate the base of the Upper Sangiran Formation—i.e., the plausible first appearance datum (FAD) for the Sangiran hominins (20)—as follows. Using the chronological brackets of 0.884 Ma (the tuff immediately overlying the Grenzbank zone) and 1.345 Ma (Tuff 8), the base of the Upper Sangiran Formation (Fig. 1C and Fig. 2) is estimated to be 1.27 Ma, assuming a constant depositional rate during this stratigraphic interval. This age estimate is also concordant with the stratigraphic position of Tuff 8 relative to the age of the Lower Lahar lying at the basal Sangiran Formation (Fig. 1C). The latter has been dated at ~ 1.7 Ma by $^{40}\text{Ar}/^{39}\text{Ar}$ dating of single hornblende grains (22) or ~ 1.9 Ma by $^{40}\text{Ar}/^{39}\text{Ar}$ dating of bulk sample hornblendes (28). Considering that the maximum possible age of Tuff 8 is ~ 1.55 Ma, the FAD for the Sangiran hominins is best considered to be either ~ 1.27 or <1.45 Ma.

Some consequences of the short chronology supported by this work include paleoenvironmental context that relates to adaptation and evolution of Javanese *H. erectus*. The Sangiran hominins have been shown to comprise two morphologically distinguishable groups—in mandibular, dental, and cranial morphology (23, 26, 27)—with the top of the Grenzbank zone being the stratigraphic and temporal boundary. The older hominin group, although highly variable, displays relatively primitive features that are comparable in morphology to the 1.4 to 1.7 Ma African *H. erectus* (*Homo ergaster*) (27). The younger hominin group is comparatively advanced, showing a larger neurocranial size and a degree of dentognathic

reduction comparable to Middle Pleistocene Chinese *H. erectus* (23).

It is well known that the global climate underwent a fundamental change between ~ 1.2 and 0.7 Ma, the mid-Pleistocene transition (MPT), when there was a shift from low-amplitude 41-kyr (thousand years) to high-amplitude 100-kyr climate cycles accompanied by more intensive global glaciation and exposure of continental shelf (29, 30). The MPT is characterized by the first major cooling phase at about 900 kyr ago, associated with a rapid increase in global ice volume in marine isotope stage (MIS) 22 (29, 30), initiating successive major glaciations. These climatic dynamics profoundly affected the biota and environment. Our estimated age of the Grenzbank zone is approximately at the onset of MIS 22 (~ 900 to 866 kyr ago). It is therefore possible that the morphological changes observed between the older and younger Sangiran hominin assemblages are associated with some drastic change induced by MIS 22. Although in situ dynamic microevolution within the same *H. erectus* population is conceivable (23), a new immigration event might have been the dominant source of the observed morphological changes. MIS 22 marks the first time in the Pleistocene that the sea level dropped ~ 120 m below the present level (30) and exposed the Sunda shelf around the Indonesian archipelago more widely than before, forming a large landmass. The Kedung Brubus fauna, associated with the younger group of Sangiran hominins, suggests massive interchange with the Asian continent (25). To the contrary, the Ci Saat and Trinil H.K. faunae associated with the older hominin group are more insular in character, albeit indicating some connection with the mainland.

Concerning the FAD of *H. erectus* in the Sangiran area, our results provide a probable FAD of ~1.3 Ma and a maximum possible FAD of ~1.45 Ma. Another hominin specimen that has been contended to be the earliest Javanese *H. erectus* is the Mojokerto skull from the Peking site in East Java. This skull is now concluded to be less than ~1.49 Ma on the basis of fission-track age determinations (37). Thus, the hominin dispersal into Java is resolved to be <1.5 Ma. The comparative primitive morphology of the Javanese *H. erectus* of the older chronological group may represent either primitive retentions (27) or derived features independently acquired in this hominin lineage.

In conclusion, our results provide important evidence that supports the short (younger) chronology. The Grenzbank zone is securely anchored at ~0.9 Ma, and our best estimate for the first hominin colonization into the Sangiran area is ~1.3 Ma (or <1.5 Ma), both much later than the estimate that has been widely accepted for more than two decades.

REFERENCES AND NOTES

1. B. Wood, *Proc. Natl. Acad. Sci. U.S.A.* **108**, 10375–10376 (2011).
2. S. C. Antón, *Curr. Anthropol.* **53** (Suppl. 6), S278–S298 (2012).
3. G. P. Rightmire, M. S. Ponce de León, D. Lordkipanidze, A. Margvelashvili, C. P. E. Zollikofer, *J. Hum. Evol.* **104**, 50–79 (2017).
4. C. C. Swisher 3rd et al., *Science* **263**, 1118–1121 (1994).
5. R. Larick et al., *Proc. Natl. Acad. Sci. U.S.A.* **98**, 4866–4871 (2001).
6. R. X. Zhu et al., *J. Hum. Evol.* **55**, 1075–1085 (2008).
7. H. Tu, G. Shen, D. Granger, X. Yang, Z. Lai, *Quat. Geochronol.* **41**, 174–179 (2017).
8. S. Matsu'ura, *Bull. Natl. Sci. Mus. Tokyo. Ser. D* **8**, 1–53 (1982).
9. G. G. Pope, J. E. Cronin, *J. Hum. Evol.* **13**, 377–396 (1984).
10. M. Hyodo, N. Watanabe, W. Sunata, E. E. Susanto, H. Wahyono, *Anthropol. Sci.* **101**, 157–186 (1993).
11. M. Hyodo et al., *J. Hum. Evol.* **43**, 27–41 (2002).
12. R. Dennell, in *Out of Africa I: The First Hominin Colonization of Eurasia*, J. G. Fleagle, J. J. Shea, F. E. Grine, A. L. Baden, R. E. Leakey, Eds. (Springer, 2010), pp. 247–273.
13. S. C. Antón, R. Potts, L. C. Aiello, *Science* **345**, 1236828 (2014).
14. R. L. Ciochon, E. A. Bettis 3rd, *Nature* **458**, 153–154 (2009).
15. Y. Zaim et al., *J. Hum. Evol.* **61**, 363–376 (2011).
16. H. Saleki, G. Féraud, F. Sémah, C. Falguères, A. -M. Sémah, T. Djubiantono, Datations radiométriques des couches à *Homo erectus* de Kabuh à Ngebung (Sangiran, Java central, Indonésie). *Actes du XIIIe Congrès UISPP Forlì Italie 2*, **63**–74 (1998).
17. C. Falguères et al., *Quat. Int.* **416**, 5–11 (2016).
18. M. Hyodo et al., *Proc. Natl. Acad. Sci. U.S.A.* **108**, 19563–19568 (2011).
19. N. Watanabe, D. Kadar, Eds., *Quaternary Geology of the Hominid Fossil Bearing Formations in Java* (Geological Research and Development Centre, Bandung, 1985).
20. B. Brasseur, F. Sémah, A.-M. Sémah, T. Djubiantono, *Quat. Int.* **376**, 84–100 (2015).
21. J. de Vos, P. Sondaar, *Science* **266**, 1726–1727 (1994).
22. F. Sémah, H. Saleki, C. Falguères, G. Féraud, T. Djubiantono, *J. Archaeol. Sci.* **27**, 763–769 (2000).
23. Y. Kaifu, F. Aziz, H. Baba, in *Homo erectus in Indonesia: Recent Progress of the Study and Current Understanding*, F. Aziz, H. Baba, Eds. (Centre for Geological Survey, Bandung, 2013), pp. 43–64.
24. Materials and methods are available as supplementary materials.
25. J. de Vos, P. Y. Sondaar, G. D. van den Bergh, F. Aziz, *Cour. Forschungsinst. Senckenberg* **171**, 129–140 (1994).
26. Y. Kaifu et al., *Am. J. Phys. Anthropol.* **128**, 709–726 (2005).
27. Y. Kaifu, E. Indriati, F. Aziz, I. Kurniawan, H. Baba, in *Asian Paleanthropology: From Africa to China and Beyond*, C. J. Norton, D. R. Braun, Eds. (Springer, 2010), pp. 143–157.
28. E. A. Bettis III et al., *Palaeogeogr. Palaeoclimatol. Palaeoecol.* **206**, 115–131 (2004).
29. P. U. Clark et al., *Quat. Sci. Rev.* **25**, 3150–3184 (2006).
30. H. Elderfield et al., *Science* **337**, 704–709 (2012).
31. M. J. Morwood, P. O'Sullivan, E. E. Susanto, F. Aziz, *Aust. Archaeol.* **57**, 1–4 (2003).
32. B. Brasseur, "Dynamique et histoire des dépôts du Pléistocène inférieur et moyen ancien dans le dôme de Sangiran (Java central, Indonésie)," thesis, Muséum National d'Histoire Naturelle (2009).

ACKNOWLEDGMENTS

This chronological research was done under the auspices of the Centre for Geological Survey (CGS, formerly Geological Research and Development Centre) in Bandung, Indonesia. We thank the successive directors of CGS for continued support and courtesy lasting more than 25 years. This joint research project was conducted partly under the general agreement of cooperation between CGS and the National Museum of Nature and Science, Tokyo (NMNS). We thank H. Baba and Y. Kaifu of NMNS for consideration and help. Special thanks to the late Sudijono of CGS for long-term collaboration since the 1970s. We owe a very important debt to the late H. Kumai of Osaka City University, without whose enormous amount of work and instruction this project would not have been possible. We are also grateful to N. Watanabe (deceased) and D. Kadar, who made a beginning of Indonesia-Japan research cooperation in this field. **Funding:** This study was partially supported by the Japan Society for the Promotion of Science (grants 13440255, 15403015, 18200053, and 22320154) and by NMNS (fund no. 6503). **Author contributions:** S.M. and F.A. planned and coordinated the original chronological project with I.Ku., M.H., and M.K.; T.D., T.H., M.K., F.A., and S.M. planned dating analyses; F.A., I.Ku., M.H., M.K., Y.T., E.S., I.Ki., H.I., S.S., T.D., T.H., M.S., Y.D., and S.M. performed research; T.D., H.I., S.S., M.K., Y.D., T.H., and M.S. undertook dating experiments; and S.M. prepared the manuscript, with input from H.I., S.S., T.D., Y.T., and M.H., including tables and figures, with additional contributions from other authors. **Competing interests:** The authors declare no competing interests. **Data and materials availability:** The data that support the findings of this study are available in the paper and supplementary materials.

SUPPLEMENTARY MATERIALS

science.sciencemag.org/content/367/6474/210/suppl/DC1
Materials and Methods
Figs. S1 to S5
Tables S1 to S5
References (33–88)

22 July 2018; resubmitted 18 September 2019
Accepted 18 November 2019
10.1126/science.aau8556



High-Pressure Reactor Array

Asynt has developed a novel high-pressure reactor array that integrates directly with their Integrity 10 Reaction Station, enabling scientists to undertake up to 10 independently pressurized reactions (up to 100 barg [bar gauge]) in parallel. The Integrity 10 is designed to carry out parallel reactions, each with independent temperature control between

-30°C and +150°C, making it perfect for design of experiments (DoE) testing. Integrity 10 maximizes efficiency and saves precious fume hood space. The system is manufactured as standard from durable 316 Stainless Steel, but Asynt can also fabricate it from exotic alloys such as Hastelloy or Inconel.

Asynt

For info: +44-(0)-1638-781709

www.asynt.com/product/integrity-10-high-pressure-module

3D Cell Culture Scaffolds

Mimetix scaffolds mimic the extracellular matrix, providing an ideal architectural environment to support the growth of cells in 3D. They are created by electrospinning medical-grade polymer poly(L-lactide) (PLLA) into microfibers, which are highly consistent with regard to fiber diameter and pore size, resulting in excellent reproducibility of cell-based assays. Mimetix aligned microfiber scaffolds provide a physical structure for the 3D culture of cells from tissues such as the central nervous system, skeletal muscle, and heart, where orientation influences cell growth and behavior. The Mimetix scaffold is incorporated into standard SBS footprint well-plate frames (12- and 96-well) with bases having superior optical clarity and minimal base distortion. The aligned scaffolds are thin enough to allow microscopic imaging. Mimetix scaffolds are available in two formats: Aligned (parallel fibers with a scaffold depth of 2 μ m–4 μ m) and Randomly Oriented (mimics the extracellular matrix with a scaffold depth of 50 μ m).

AMS Biotechnology

For info: 617-945-5033

www.amsbio.com/mimetix.aspx

Microscopy Camera

Andor Technology (Andor) announces the launch of Sona 4.2B-6, a new model in the ultrasensitive back-illuminated Sona microscopy camera series. The 4.2B-6 provides a superbly balanced combination of sensitivity, speed, and resolution, suiting it perfectly to the needs of the most challenging microscopy applications. The new camera features a 4.2-megapixel sensor format with a 6.5- μ m pixel size. This format is suited to obtaining maximum resolution from the commonly used 60x and 40x objective lens magnifications. The 4.2B-6 also features a low-noise mode that uses correlated multisampling to reduce noise while maintaining frame rates and the low exposure times that are vital for studying live cells. Dynamic cellular processes can be captured by its high-speed imaging capabilities—up to an impressive 74 fps for full-range 16-bit images. This camera is important for the growing number of applications that use measurements over time or change in fluorescence intensity levels to make determinations on rates, con-

centrations, or spatial position, such as fluorescence resonance energy transfer, ion signaling, gene expression analysis, or localization-based superresolution.

Andor Technology

For info: 978-402-6776

www.andor.com/sona

Food Sample Tracker

The Ziath Track and Trace starter kit contains everything an organization needs to start up and maintain enhanced food-sample integrity, tracking, and audit trails. The new starter kit combines top-quality 2D-coded sample storage tubes, 48-position Society for Biomolecular Screening (SBS) format tube racks, and a high-performance single-tube 2D barcode scanner. Also included is the Ziath Samples sample management software, which allows you to organize your food sample inventory, making setting up a traceable record of food samples very straightforward.

Ziath

For info: 858-880-6920

www.ziath.com

Custom Beamsplitters

Optical Surfaces supplies single-to-OEM quantities of high-precision, custom beamsplitters to a growing number of spectroscopy, interferometry, and imaging instrument manufacturers worldwide. The optimal beamsplitter can take on many forms, including cubes, plates, hexagons, pentagons, polarizing, nonpolarizing, or wedge designs, in a wide variety of reflection/transmission ratios and substrates depending upon your application. Drawing on over 50 years of experience, our technical experts can advise you on the key beamsplitter parameters to consider, including wavelength range, physical size, and polarization—and if used in an interferometer, path-length and phase-matching requirements. Optical Surfaces' custom beamsplitters offer outstanding flatness and parallel specifications, and are typically manufactured to a surface accuracy of $\lambda/20$ p-v (peak to valley) at 633 nm, a surface quality of 10/5, and microroughness of less than 1.2 nm rms (root mean square). Supplied mounted or unmounted, they can be enhanced with an extensive range of coatings designed to operate at your required angle of incidence.

Optical Surfaces

For info: +44-(0)-208-668-6126

www.optisurf.com

Portable GC/MS

HAPSITE ER is the only person-portable gas chromatograph/mass spectrometer (GC/MS) that requires minimal training to deliver qualitative and quantitative lab-quality results—in the field, in less than 10 min. All the operator has to do is push a button to begin identifying and quantifying volatile organic compounds, toxic industrial chemicals, toxic industrial materials, chemical warfare agents, and select semi-volatile organic compounds. HAPSITE ER can identify analytes in the ppm (parts per million)–ppt (parts per trillion) range. The GC column provides sharp chromatography and excellent resolution. During the quantitation process, the front panel clearly displays what chemicals are present, their concentration, and access to information regarding the degree of danger—to help make quick decisions affecting life, health, and public safety.

Inficon

For info: 610-524-6633

www.inficon.com

Electronically submit your new product description or product literature information! Go to www.sciencemag.org/about/new-products-section for more information.

Newly offered instrumentation, apparatus, and laboratory materials of interest to researchers in all disciplines in academic, industrial, and governmental organizations are featured in this space. Emphasis is given to purpose, chief characteristics, and availability of products and materials. Endorsement by *Science* or AAAS of any products or materials mentioned is not implied. Additional information may be obtained from the manufacturer or supplier.



Clinical Research Medical Director

Description: The Clinical Research Medical Director will be responsible for leading and expanding the Clinical Research Institute at St. Elizabeth Healthcare.

Requirements: • MD/DO, PharmD, or PhD • Minimum of 7 to 10 years of research experience • Preferred Qualifications:

MPH Experience: • Experience authoring research papers for peer review journals • Public speaking experience at conferences/symposia • Experience with specialty medications or devices

Responsibilities include: • Implement program vision and strategy • Establish short and long-range goals for growth • Lead intra/inter-departmental teams • Driving physician activation/participation • Educating physicians on the impact/value of clinical research • Mentor and coach primary investigators to address specific clinical needs and implement best practices to conduct clinical research • Chair the Clinical Research Institute Governance Board • Ensure compliance/alignment with protocols, guidelines, applicable regulations, and standard operating procedures • Monitors designated operating and capital budgets • Participate in development opportunities to increase the visibility of the Clinical Research Institute and generate funding support

About St. Elizabeth Healthcare: We are a four-hospital, 1,000 bed community health system in a market of 400,000 people. St. Elizabeth is home to a Family Medicine Residency Program and, in partnership with the University of Kentucky and Northern Kentucky University, a medical school. Through our affiliations with the Mayo Clinic Care Network and the University of Kentucky Markey Cancer Center, collaboration with both organizations exists for clinical, educational and research purposes. Please contact Michele Kenner at Michele.Kenner@stelizabeth.com to learn more about this opportunity to direct an emerging world class clinical research program in the Greater Cincinnati area.



Two-year postdoctoral fellowships at Masaryk University

Masaryk University in Brno, Czech Republic, seeks exceptional and motivated applicants to join its best research teams.

Twenty-three fellowships are available. Complete information including research areas, eligibility criteria and the application procedure can be found at www.postdoc.muni.cz.

The application deadline is **29th February 2020**. Interviews are expected to take place shortly afterwards.

Masaryk University is a leading Central European research university and an equal opportunities employer.

MASARYK
UNIVERSITY

MUNI

FIND YOUR HAPPIER PLACE.

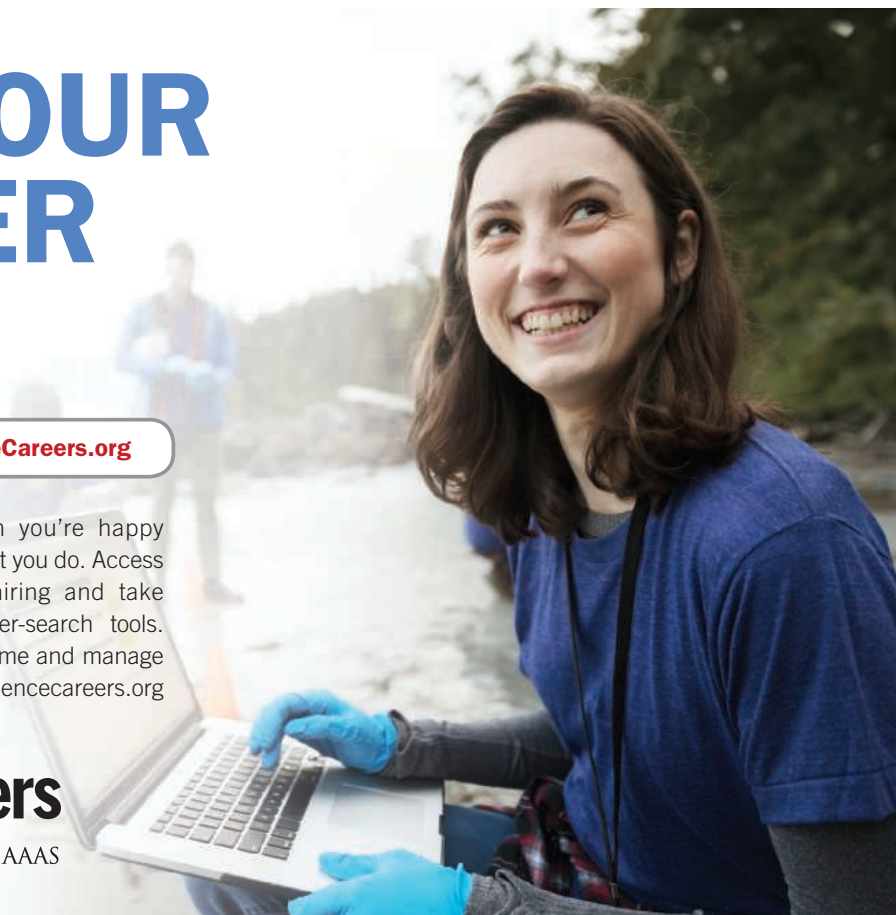


Find your next job at ScienceCareers.org

There's scientific proof that when you're happy with what you do, you're better at what you do. Access career opportunities, see who's hiring and take advantage of our proprietary career-search tools. Get tailored job alerts, post your resume and manage your applications all in one place: sciencecareers.org

ScienceCareers

FROM THE JOURNAL SCIENCE AAAS



10 ways that Science Careers can help advance your career

1. Register for a free online account on **ScienceCareers.org**.
2. Search thousands of job postings and find your perfect job.
3. Sign up to receive e-mail alerts about job postings that match your criteria.
4. Upload your resume into our database and connect with employers.
5. Watch one of our many webinars on different career topics such as job searching, networking, and more.
6. Download our career booklets, including Career Basics, Careers Beyond the Bench, and Developing Your Skills.
7. Complete an interactive, personalized career plan at “my IDP.”
8. Visit our Employer Profiles to learn more about prospective employers.
9. Research graduate program information and find a program right for you.
10. Read relevant career advice articles from our library of thousands.

Visit **ScienceCareers.org**
today — all resources are free



ScienceCareers

FROM THE JOURNAL SCIENCE  AAAS

SCIENCECAREERS.ORG

myIDP:
A career plan customized
for you, by you.

For your career in science, there's only one

Science

Features in myIDP include:

- Exercises to help you examine your skills, interests, and values.
- A list of 20 scientific career paths with a prediction of which ones best fit your skills and interests.
- A tool for setting strategic goals for the coming year, with optional reminders to keep you on track.
- Articles and resources to guide you through the process.
- Options to save materials online and print them for further review and discussion.
- Ability to select which portion of your IDP you wish to share with advisors, mentors, or others.
- A certificate of completion for users that finish myIDP.



Visit the website and start planning today!
myIDP.sciencecareers.org

ScienceCareers In partnership with: AAAS



By Lila Westreich

A refreshing change

Midway through grad school, a friend asked me to volunteer as a barback—a bartender's assistant—at the opening gala for a film festival. I was hesitant at first, having never worked behind a bar. But I said yes, lured by the offer of free tickets to the festival. I spent an evening running around like a chicken with its head cut off: slicing fruit, replacing liquor bottles, and doing other menial tasks. By the end of the night, I was tired and sweaty and I'd dropped an expensive bottle of vodka. But I felt incredible—in awe of how much fun I had—and I went home and slept better than I had in years. The event forced me to reflect on what brings me happiness and a clear state of mind. It was a turning point in my grad school experience.

I got into my doctoral program on a technicality. On my application, I'd checked the box for "Ph.D." not knowing that a master's degree was a prerequisite. My adviser—who interviewed me over the phone—misread my undergraduate record and thought I had a graduate degree under my belt, so I was admitted to the Ph.D. program. He welcomed me into his lab even after finding out about the error. But it left me feeling like I had a lot to prove.

I got off to a running start. My adviser had 3 years of funding to cover my stipend and tuition. I threw myself into reading every paper I could find and thinking about how to test scientific questions no one had yet delved into. And I was awarded a grant to help fund some expensive genetics labwork.

But 4 years later, I felt lost. I barely passed my qualifying exam. A manuscript I spent a year working on was rejected outright, without peer review, and I was running out of funding. My mood was in the gutter. I told my therapist at the time, "The more people are interested in what I study, the angrier I am that they care and I don't." I dreamed about quitting my program, moving back home, and working at the bike shop that had employed me during college. Then came the barback gig.

After we finished cleaning up the bar that night, I was handed festival tickets and an envelope with my cut of the tips—close to \$40. It felt wrong to be compensated while having so much fun. I grinned as we snuck upstairs to watch the gala attendees finish their drinks and to steal shrimp from the serving bowls.

The next day, I tried to figure out why I loved this short-lived experience so much. I realized it was because the



"The demands of the job were exactly what I was missing from my Ph.D. program."

demands of the job were exactly what I was missing from my Ph.D. program. It was physically exhausting, the tasks I was responsible for were simple and could be completed in a short time, and I knew without a doubt when I succeeded and when I failed. My mind was blissfully blank all night. At that point, I had not had a break from thinking as hard as I possibly could for 4 years. I had never come up for air, and I was completely unaware of the toll it was taking on my mental health.

Since then, I've tried to give my mind more breaks. When I start to feel overwhelmed—when an experiment fails, a mistake sets me back a month, or funding falls through—I make a point of doing things that allow me to feel successful in other ways. I learn how to play a new

song on the piano. I go for a run. I volunteer for an organization that I care deeply about, performing basic tasks such as stapling papers and shredding documents. The simplicity of these activities brings a peace of mind that I never find in academia. They help clear my head, preparing me to dive back into the graduate work that both excites and exhausts me.

I don't think I'll ever be a professional barback. But I'll never forget the lessons I learned that night. Graduate school takes a lot of work and skill, but it doesn't exercise all the muscles of your brain, body, or spirit. Sometimes it's OK—even necessary—to find other, decidedly unscientific, ways to fill your cup. ■

Lila Westreich is a Ph.D. candidate at the University of Washington, Seattle. Do you have an interesting career story to share? Send it to SciCareerEditor@aaas.org.